High kinetic inductance-based microwave photon detection

Ognjen Stanisavljević

To cite this version:

Ognjen Stanisavljević. High kinetic inductance-based microwave photon detection. Quantum Physics [quant-ph]. Université Paris-Saclay, 2024. English. NNT : 2024UPASP038 . tel-04655464

HAL Id: tel-04655464
https://theses.hal.science/tel-04655464

Submitted on 22 Jul 2024

High kinetic inductance-based microwave photon detection

Un détecteur à haute inductance cinétique de photon micro-onde

Thèse de doctorat de l'université Paris-Saclay

École doctorale n° 564, physique en l'Ile-de-France (PIF)
Spécialité de doctorat: Physique
Graduate School: Physique. Référent: Faculté des sciences d'Orsay

Thèse préparée au **Laboratoire de Physique des Solides** (Université Paris-Saclay, CNRS), sous la direction de **Julien BASSET**, Maître de conférences, et le co-encadrement de **Jérôme ESTEVE**, Chargé de recherche

Thèse soutenue à Paris-Saclay, le 13 juin 2024, par

Ognjen STANISAVLJEVIĆ

Composition du jury

Membres du jury avec voix délibérative

Sophie GUERON Directrice de recherche, LPS, Université Paris-Saclay, CNRS	Présidente
Ville MAISI Professeur Assistant, Université de Lund, Suède	Rapporteur & examinateur
Nicolas ROCH Chargé de recherche (HDR), Institut Néel, CNRS, Grenoble	Rapporteur & examinateur
Joachim ANKERHOLD Professeur, Université d'Ulm, Allemagne	Examinateur
Max HOFHEINZ Professeur, Université de Sherbrooke, Canada	Examinateur

THESE DE DOCTORAT

NNT: 2024UPASP038

Acknowledgements

A while ago, a friend I have not seen in a long time messaged me that he is back in Belgrade for a week. Unbeknownst to me at the time, our lunch together would be a start of my almost five-year long journey in France, culminating in this thesis that is in front of you. As I have greatly enjoyed my time in Orsay, it feels appropriate to start this acknowledgment by saying a big thank you to Marko. And also, see you soon.

There are many other people to whom I owe a great deal, and without whom this work would not exist, starting with Marco Aprili, who invited me to the NS2 group for an internship, and taught me the basics of superconductivity and low temperature physics. And more than physics, taught me a great deal about research and how to evaluate it.

I am also incredibly grateful to my advisors, Julien and Jérôme. They have supported me along every step of my PhD, both professionally and personally. During the last three years, I have learned from you a lot more than I can fit in a couple of sentences. I hope I will be able to carry on in my carrier with as much passion and rigour as you. And I am especially grateful for showing me how fun physics can be, and helping me overcome my college memories of electrodynamics, the one area of physics I once upon a time said to myself I wanted nothing to do with.

A big thank you to Julien, Freek, Alexandra, Charis, and Sylvie for making the NS2 group an enjoyable work environment ever since my arrival. And of course, my PhD colleagues Sara, Clément, Paulino, Naila, and many more, who have made the days in the lab infinitely more entertaining compared to the lonely first days of my PhD during the pandemic.

I would also like to thank Sophie Gueron, Max Hofheinz, Joachim Ankerhold, and especially Ville Maisi and Nicolas Roch for accepting to be in my thesis jury, and making the defense a very pleasant experience with their comments and suggestions.

Undoubtedly, none of this would happen without the support of my family and friends. Thank you to Daniel for being an amazing housemate and a friend, I have enjoyed discovering Paris with you. Thanks to Aleksandar, Dusan, and Marko again for many a night spent together, I hope I have not complained too much. Thanks to Danilo, Pavle and Jelena for making all my returns to Serbia unforgettable, and especially Lazar for always finding me a place to stay.

Thank you to Jovana, Jelena and Ana for their unwavering friendship, even in the hardest of times. And thank you to Marko and Radosav for all the coffees we had, followed by various discussions on very important topics.

And finally, I would like to thank my mother Mirjana, to whom I dedicate this thesis, for believing in me and always letting me find my own way through life. I could have never done this without your endless love and support.

Introduction

In this thesis, we present the work done towards building a highly efficient single microwave photon detector. Photon detection has been a fruitful area of research ever since the discovery of photoelectric effect in the late nineteenth century. Over one hundred years of improvement has lead to developments in numerous different areas, including biomedical imaging, scattering experiments and single molecule detection. Especially, optical photon detectors are indispensable tools in various quantum technologies and applications, from fundamental tests of quantum mechanics, to quantum communication and computation. The first optical photon detectors were based on photomultiplier tubes [1]. In these devices, a single electron expelled from a photocathode due to photoelectric effect, is multiplied through secondary emission, resulting in measurable current. Over time, the photomultiplier tubes have been replaced by solid-state detectors, such as avalanche photodiodes [2] due to better quantum efficiency, especially at infrared wavelengths, culminating in detectors sensitive enough to detect single photons — single-photon avalanche diodes [3, 4, 5]. SPADs are semiconductor based devices that rely on reversely biased p-n junctions. The bias voltage is greater than the junction breakdown voltage. Thus, even a single charge carrier entering the junction depletion layer can trigger an avalanche effect leading to a sustained macroscopic current. However, the energy of the photons that can be detected using these detectors is fundamentally limited by the value of the semiconducting gap, which is 1.1 eV for silicon, corresponding to the wavelength of 1100 nm, or the frequency of 300 THz, although narrower gap semiconductors such as HgCdTe are used for infrared photon detection [6].

A possible way to extend the detection range of photon detectors is to substitute the semiconductors with superconductors, as the superconducting gap of a material such as aluminium is 10^4 times smaller than a typical semiconductor gap. Many single photon detectors, such as transition edge sensors [7], or tunnel junction based optical photon detectors [8] are based on superconductors. The most widely used superconducting detectors are the nanowire single photon detectors [9, 10], and microwave kinetic inductance detectors [11]. In SNSPDs, the absorbed photon breaks the Cooper pairs, and creates local normal state hotspots in the nanowire. These hotspots are then identified by measuring the voltage drop across the nanowire. The SNSPDs are characterized by low dark counts, quantum efficiency close to unity, and an excellent time resolution [12].

On the other hand, the MKIDs rely on monitoring the resonance frequency of a microwave cavity. When the incident photons of energy $\hbar\omega > 2\Delta$ are absorbed by the resonator, they break the Cooper pairs, leading to changes in the kinetic inductance of the resonator, and its impedance. These changes are then reflected in the resonance frequency and width. In addition to their high quantum efficiency, and low dark counts, the main advantage of MKIDs is their scalability, and they are widely used in astronomy from optical and near-IR range [13], down to millimeter wavelengths [14].

What is common for all these superconducting photon detectors is that they rely on the energy of the detected photon to overcome the superconducting gap Δ. Thus, the energy of detected photons is determined by the material used to fabricate the device. Frequency range of these detectors typically starts at 100 GHz, and extends up to several THz, but practical continuous single microwave photon detectors, in the 1 - 30 GHz range, are still lacking. Extending the same detection principle to the microwave frequency range fails due to absence of materials with gap corresponding to microwave photons, which carry 10^5 times less energy compared to visible ones. However, an efficient microwave detector would be of substantial utility in microwave quantum optics [15], quantum cryptography [16], sensing [17, 18], and axion search [19, 20, 21]. Therefore, the fabrication of microwave photon detectors remains an intense area of research. There have been several recent efforts exploiting superconducting quantum circuits [22] in different ways — whether by entangling the microwave photon with a qubit [23, 24], utilizing quantum criticality [25] or a Josephson mixer [26, 27].

In this work, we build on the idea of a microwave photon detector based on the photoelectric effect. Rather than relying solely on the energy of the incident photon to break the Cooper pairs in a superconductor, our detector is based on photo-assisted tunneling through a superconducting tunnel junction biased just below the superconducting gap. Thus, the difference in energy between the microwave photon, and the gap, is provided by the voltage source. Due to their nonlinearity, superconducting tunnel junctions, or Josephson junctions, have been an essential component of superconducting quantum circuits since the inception of the field [28]. Examples of devices built using Josephson junctions include qubits such as transmons [29], quantum limited amplifiers [30], and more. When coupled to microwave resonators, Josephson junctions can be used as sources of non-classical light [31, 32, 33] and entangled microwave beams [34]. Similar devices can be operated as photomultipliers, and show promise for microwave photon counting [35].

In recent years, realizing single microwave photon detectors based on inelastic tunneling has been an active area of research, and noticeable progress has been made, particularly using photo-assisted tunneling through double quantum dots [36, 37, 38]. Although the experiments are promising, these devices suffer from low quantum efficiency, caused by the mismatch between the photo-assisted tunneling rate and the photon input rate.

Elastic Quasiparticle Tunneling

In contrast to the Josephson junction devices listed above, which exploit Cooper pair transport for their operation, our detector is based on quasiparticle tunneling through a superconducting junction. Quasiparticle tunneling across an SIS junction is depicted in figure 1a. The two superconducting electrodes are represented by their density of states, with the tunneling barrier shown in grey. When the junction bias voltage is lower than the superconducting gap, there are no available states for the quasiparticle to tunnel into, and no current flows. At high bias, the ohmic behaviour is recovered. The quasiparticle tunneling is described by the Hamiltonian

$$H_T = T \sum_{k,q} c^{\dagger}_{R,q} c_{L,k} + h.c. \tag{1}$$

where c_L and c_R are electronic annihilation operators for left and right junction electrodes respectively and T is tunneling amplitude inversely proportional to the junction resistance. By considering the tunneling as a weak perturbation, current through the junction can be calculated using the Fermi's golden rule. The resulting current-voltage characteristic, shown in figure 1b, is non-linear due to the gap in the density of states.

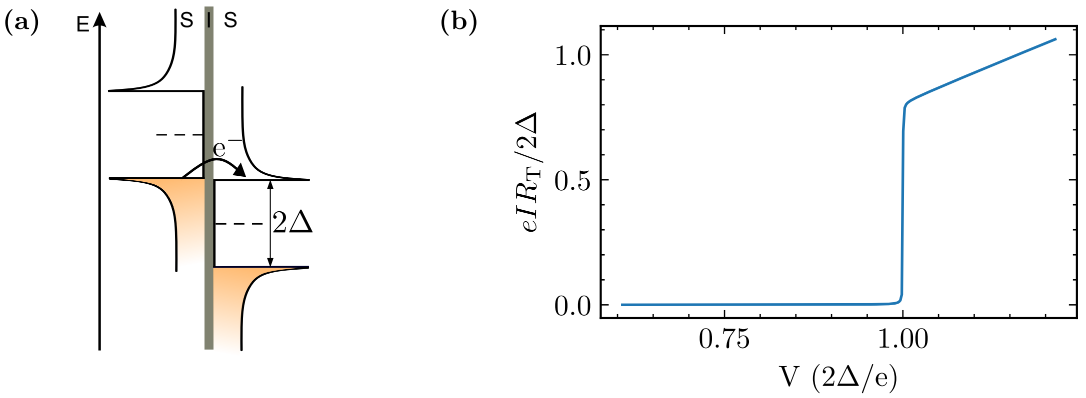

Figure 1: a) Illustration of quasiparticle tunneling through an SIS junction b) Quasiparticle branch of the $I(V)$ characteristic for an SIS junction of tunneling resistance R_{T} calculated from the Hamiltonian 1.

Inelastic Quasiparticle Tunneling

When the junction is irradiated by photons, the current-voltage characteristic of the junction is modified by an onset of inelastic processes, in which a quasiparticle gains the energy to tunnel across the junction by absorbing photons [39]. This process is shown in figure 2a. To include the inelastic processes into the quasiparticle tunneling description we modify the Hamiltonian 1 [40]:

$$H_T = T\sum_{k,q} c^{\dagger}_{R,q} c_{L,k} e^{i\frac{e}{\hbar}\Phi_J} + h.c. \tag{2}$$

with Φ_J being the flux at the junction. By using the commutation relation for the charge and flux $[\Phi_J, Q_J] = i\hbar$ we note that

$$e^{i\frac{e}{\hbar}\Phi_J} Q_J e^{-i\frac{e}{\hbar}\Phi_J} = Q_J - e \tag{3}$$

and we recognize $e^{i\frac{e}{\hbar}\Phi_J}$ as the charge translation operator. This operator changes the charge on the junction by e for every tunneling event, and its dynamics depends on the circuit in which the junction is embedded. We assume that the tunnel junction is coupled to a single electromagnetic mode of frequency ω_1. The flux Φ_J can then be rewritten in terms of its ladder operators a and $a^{\dagger}$, resulting in

$$H_T = T\sum_{k,q} c^{\dagger}_{R,q} c_{L,k} e^{i\lambda(a+a^{\dagger})} + h.c. \tag{4}$$

where λ is the coupling parameter. If we model the mode as a lumped element LC-circuit, the flux threading the inductor is $\sqrt{\hbar Z_c/2}(a + a^{\dagger})$. Comparing this with the previous equation, we have for the coupling parameter

$$\lambda = \sqrt{\pi \frac{Z_c}{R_{\mathrm{K}}}} \tag{5}$$

where $R_{\mathrm{K}} = h/e^2 = 25.813\,\mathrm{k}\Omega$ is the quantum of resistance and $Z_c = \sqrt{L/C}$ is the characteristic impedance of the resonator mode. Knowing the Hamiltonian, we can calculate the current through the junction, with the inelastic tunneling included. A typical current-voltage characteristic of a junction irradiated by light is shown in figure 2b. Compared to the $I(V)$ in absence of radiation, there is a subgap current step in bias voltage range $eV \in [2\Delta - \hbar\omega_1, 2\Delta]$, corresponding to the photo-

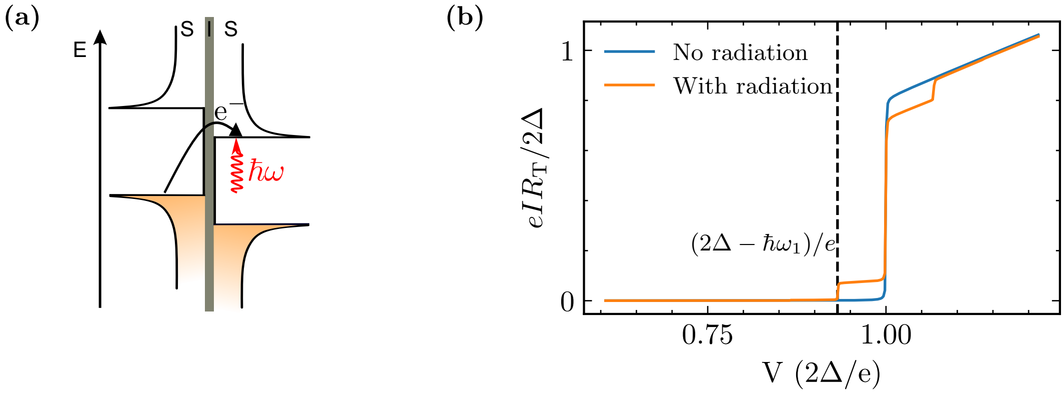

Figure 2: a) Photo-assisted quasiparticle tunneling across an SIS junction b) Calculated current-voltage characteristics of an SIS junction of resistance R_T: current in absence of electromagnetic radiation is shown in blue. Current through the junction irradiated by light of frequency ω_1 is in orange

assisted tunneling. Additionally, there is a step of the same width above the superconducting gap. This reduction in tunneling current is known as dynamical Coulomb blockade, and appears due to quantum vacuum fluctuations [40]. Heights of the steps in current depend on the coupling between the resonator and the junction. To highlight this dependence, we assume that the resonator was initially in state $|1\rangle$, and look at the rate of the inelastic process corresponding to photon absorption. This rate is proportional to the overlap between wave functions $\psi_1(Q_J)$ and $\psi_0(Q_J - e)$, shown in figure 3. Resonators fabricated using conventional superconductors such as aluminium or niobium have characteristic impedances of $\sim 100\,\Omega$, corresponding to $\lambda \ll 1$. In this case, the rates of the inelastic processes are small, and the system stays close to equilibrium. In contrast, if characteristic impedance is increased the inelastic tunneling rate rises, and for $\lambda \sim 1$ prevails over the elastic one.

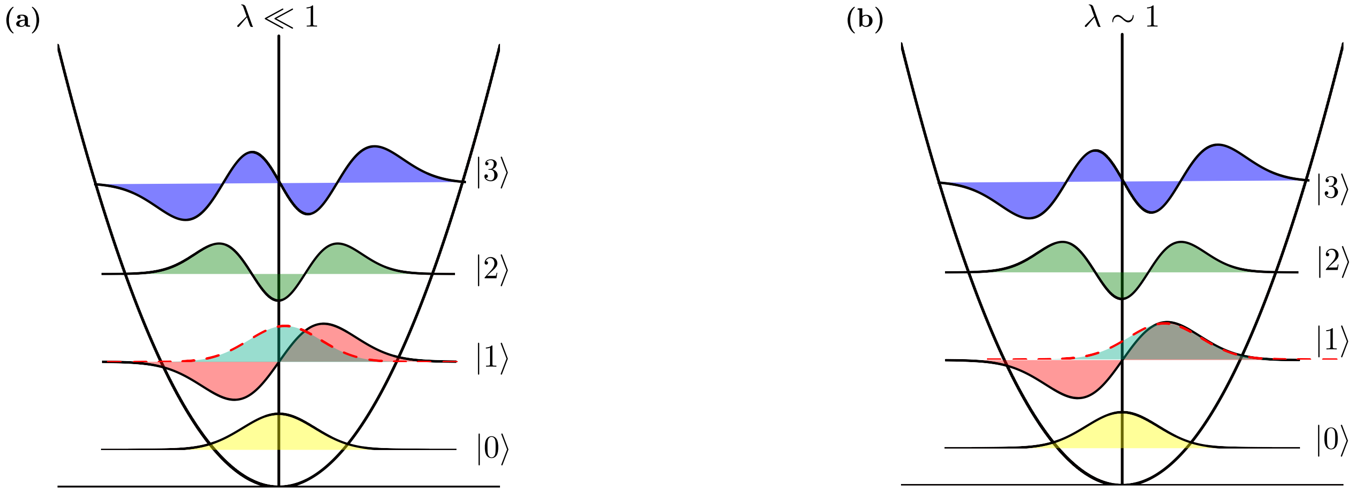

Figure 3: Matrix element corresponding to the single photon inelastic process. The matrix element is calculated as overlap of a wave function of state $|1\rangle$ (shown in red), and the ground state wave function displaced in x-axis by λ (shown in light blue with dashed red outline). This overlap is shown in weak coupling limit $\lambda \ll 1$ in a), and in strong coupling case in b).

Additionally, this picture holds for processes involving multiple photons per tunneling event.

While they can be safely neglected in weak coupling case, they play a prominent role in the dynamics of the system for $\lambda \sim 1$.

Photon Detector design

In figure 2b, we observe that the current below the superconducting gap appears only if the electromagnetic radiation is present. We exploit this fact by utilizing the tunneling current for photon detection. Photo-assisted tunneling through a tunnel junction has already been harnessed for detecting electromagnetic radiation, e.g. through the use of SIS mixers in astronomy, at frequencies on the order of 100 GHz [41], or for noise measurements at microwave frequencies [42]. In this work, we lower the operation frequency of quasiparticle tunneling based detectors to the 4 - 8 GHz band, and design the detector with the eventual goal of single microwave photon detection in mind.

The scheme of our proposed detector is shown in figure 4. It consists of a resonator galvanically coupled to a $Z_0 = 50\,\Omega$ transmission line, which is then connected to the rest of the experimental setup. To detect photons of wavelength w, the resonator length is set to $w/4$. It is terminated by a voltage biased superconducting tunnel junction of tunneling resistance R_T. The junction is biased such that the absorption of the incident photons through photo-assisted tunneling is energetically permitted, but no current flows in absence of microwaves. These conditions are fulfilled for bias voltages $eV \in [2\Delta - \hbar\omega_1, 2\Delta]$. The characteristic impedance Z_c of the resonator is comparable to the quantum of resistance, so that the coupling parameter satisfies $\lambda \sim 1$, in order to increase the inelastic tunneling rate. Fabricating these high characteristic impedance resonators has been an important avenue of research recently, and several different directions have been taken: utilizing Josephson junction chains [43], spiral resonators [31], or different high kinetic inductance materials such as NbN [44]. In this work, we use granular aluminium. Thin films fabricated in grAl are characterized by resistivity several orders of magnitude higher compared to pure aluminium. The high resistivity translates into low Cooper pair density when grAl is in the superconducting state at low temperature. Consequently, grAl has high kinetic inductance in the superconducting state. It has already been shown that grAl is suitable for making high quality factor resonators [45], and it allows us to produce resonators of characteristic impedance $Z_c > 5\,\mathrm{k}\Omega$.

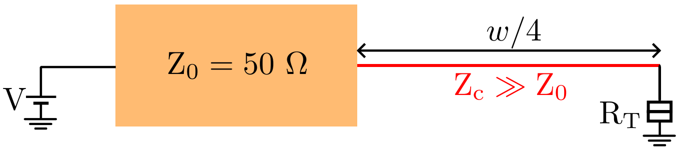

Figure 4: Photon to electron converter scheme. To detect photons of wavelength w, a $w/4$ resonator, shown in red, is terminated on one side by a voltage biased superconducting tunnel junction. Characteristic impedance Z_c of the resonator is comparable to the quantum of resistance. The resonator is galvanically coupled to the rest of the circuit through a $50\,\Omega$ line

Thesis Overview

The quasiparticle tunneling in junctions coupled to the electromagnetic environment, such as a resonator mode is usually described by $P(E)$ theory [40]. In this theory, the environment influence is calculated from quantum fluctuations of the phase at junction electrodes. $P(E)$ has been widely successful in predicting inelastic tunneling rates [46, 47]. However, one of the core assumptions in

$P(E)$ theory is that the electromagnetic modes stay in thermal equilibrium. As we consider strong coupling to the modes of high quality factor, this assumption cannot be made. In this case, rates of different processes start to depend on the state of the resonator, and the comprehensive description of the system must take this fact into account. Therefore, we treat the junction electrodes as equilibrium bath for the cavity mode, and derive the Lindblad master equation and use the obtained resonator reduced density matrix to calculate the transport through the junction. This theoretical description of the junction-resonator system is the topic of Chapter 1. Particularly, we discuss the conditions needed to achieve high photon to electron conversion quantum efficiency in these devices. These considerations are then used to propose a photon detector design.

In Chapter 2, we experimentally characterize our photon detector. We measure the photo-assisted current for different microwave pumping powers to obtain the efficiency of the detector. The calibration method based on the theoretical description of the device is devised, and used to extract the quantum efficiency of 0.83, significantly better than the highest obtained so far in similar devices. Other detector figures of merit, such as dark count and noise equivalent power, are also discussed.

The third chapter is devoted to the technical details of the microwave photon detection experiments. Firstly, the sample parameters are given in more detail. Then, the setup that allows us to conduct both microwave and dc measurements is shown. The dc chain calibration, allowing for precise photo-assisted current measurement is also specified.

In Chapter 4, the behaviour of our photo detector in response to thermal radiation is discussed. We show that the thermal photo-assisted current measurements are in agreement with the estimated near-ideal quantum efficiency of our detector. Additionally, we show how the same device can be used to effectively cool down the resonator mode. By measuring the emission at resonator frequency, we calculate the mean resonator population as function of temperature and junction bias, and show that our theory adequately explains the data at all temperatures without any free parameters.

Chapter 5 is dedicated to the preliminary work on extending the photon detector described in chapters 1 and 2 to the single microwave photon detection regime. To detect individual tunneling events, we switch from measuring the photo-assisted current to counting charge. We use a radio-frequency single-electron transistor (RF-SET) for charge detection [48]. RF-SETs have been commonly widely used charge detection experiments, with bandwidths on the order of 100 MHz and sensitivity reaching $0.9 \cdot 10^{-6}\,\mathrm{e}/\sqrt{\mathrm{Hz}}$ [49]. For the tunnelled quasiparticle to be detected by the RF-SET, it needs to be confined to a small island. Thus, we propose a single microwave photon detector design based on two capacitively coupled RF-SETs, shown in figure 5. One RF-SET is

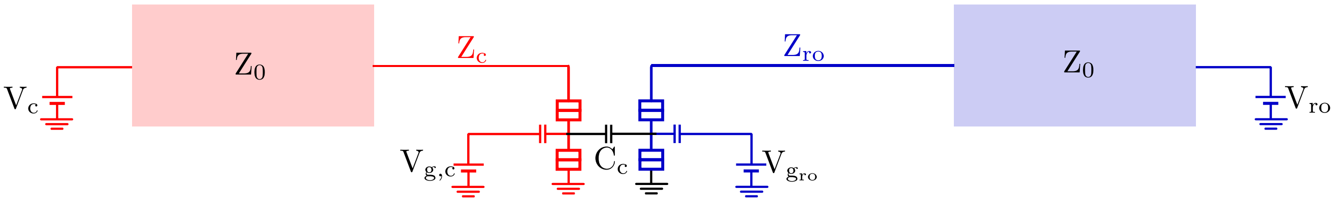

Figure 5: Single microwave photon detector design based on two capacitively couple RF-SETs. One RF-SET, shown in red, is used as a photon-to-electron converter, relying on inelastic quasiparticle tunneling. When the incident photon enters the converter resonator, it is absorbed by the junction, resulting in the change of the SET island charge. This change is detected by the capacitively coupled readout RF-SET shown in blue.

used as a photon-to-electron converter. When the incident photon enters the converter resonator, it is absorbed by the junction, resulting in the change of the SET island charge. The characteristic impedance of the converter SET resonator is on the order of resistance quantum, in order to boost the inelastic tunneling. The detector SET is coupled to a readout RF-SET through a capacitor C_c, so that the change in the island charge, and hence the microwave photon, is detected.

We start by describing the fabricated sample, and the experimental setup. We then use the reflectometry measurements to characterize the two RF-SETs. We measure the charge noise of the readout RF-SET and show that it is as low as $5 \cdot 10^{-5}\,\mathrm{e}/\sqrt{\mathrm{Hz}}$. We demonstrate the coupling of the two RF-SETs by measuring the tunneling through the photon-to-electron converter with the readout RF-SET. However, the lifetime of the tunnelled quasiparticles on the converter SET island was too short to detect individual tunneling events. We also measure the microwave emission of the RF-SET, and show that unlike for the single junction coupled to the resonator, the emission does not monotonically increase with increasing bias voltage. We develop a classical master equation model, and succeed in reproducing the emission data.

Chapter 1

Microwave Photon Detection Via Photo-assisted Tunneling in SIS Junctions

In this chapter, we give the theoretical description of the quasiparticle tunneling in a superconducting junction coupled to a single microwave mode. We start by considering a tunnel junction coupled to a transmission line resonator, and derive the expression for the coupling parameter. We then discuss the tunneling rates corresponding to different inelastic processes, and the Lindblad master equation for a resonator coupled to an SIS junction described as a bath in equilibrium. The steady state solution of this equation is used to calculate the photo-assisted current, and show that there is a bias voltage range below the superconducting gap where this current is proportional to resonator population. We then derive the formula for quantum efficiency of photon to electron conversion. Finally, we present the proposed design of a highly efficient microwave photon detector based on photo-assisted quasiparticle tunneling.

1.1 Resonator - junction Coupling

In contrast to the lumped element case presented in the Introduction, the resonators that we consider consist of transmission lines of finite length (see figure 4). To rewrite the tunneling Hamiltonian 2 in terms of mode ladder operators for a distributed cavity, we start from the Lagrangian of a transmission line of length L, characterized by the inductance per unit length l, and capacitance per unit length c [50]:

$$\mathcal{L} = \int_0^L \mathrm{d}x \left(\frac{c}{2} \partial_t^2 \Phi - \frac{1}{2l} \partial_x^2 \Phi \right) \tag{1.1}$$

where $\Phi(x,t)$ is the magnetic flux. The Euler-Lagrange equation corresponding to this Lagrangian is

$$v_p^2 \partial_x^2 \Phi - \partial_t^2 \Phi = 0 \tag{1.2}$$

where $v_p = 1/\sqrt{lc}$ is the phase velocity. To look for solutions, we separate the temporal and spatial dependence:

$$\Phi(x,t) = \phi(t)\varphi(x) \tag{1.3}$$

If we assume for the time dependence $\phi_n(t) = e^{-i\omega t}$, the equation 1.2 becomes

$$-\partial_x^2 \varphi(x) = k^2 \varphi(x) \tag{1.4}$$

where $k = \omega/v_p$ In our experiments, the resonators are galvanically coupled to the feedline (figure 4). Therefore the appropriate boundary conditions are

$$\varphi(0) = 0, \qquad \partial_x \varphi(x = L) = 0. \tag{1.5}$$

The boundary condition at $x = 0$ reflects the coupling of the mode to the $50\,\Omega$ line, while the one at $x = L$ is the open circuit boundary condition, and corresponds to maximum voltage. The equation 1.4, and the boundary conditions above, define an eigenvalue problem. The solutions are the normal modes of the system ϕ_n, φ_n:

$$\Phi(x,t) = \sum_n \phi_n(t)\varphi_n(x). \tag{1.6}$$

The time dependent solutions are $\phi_n(t) = e^{-i\omega_n t}$, while the spatial normal modes for a quarter-wavelength resonator are:

$$\varphi_n(x) = \cos\Big(k_n x - (2n+1)\frac{\pi}{2}\Big), n \in \mathbb{N} \tag{1.7}$$

where the amplitude of all the modes at $x = x_j$ is 1, and $k_n = \omega_n \sqrt{lc} = (2n+1)\pi/2L$. The normal modes satisfy the following orthogonality relations:

$$\int_0^L \mathrm{d}x \varphi_n(x)\varphi_m(x) = \frac{L}{2}\delta_{nm} \tag{1.8}$$

$$\int_0^L \mathrm{d}x (\partial_x \varphi_n(x))(\partial_x \varphi_m(x)) = \frac{k_n}{2}\delta_{nm}. \tag{1.9}$$

In terms of normal modes, the Lagrangian 1.1 is

$$\mathcal{L} = \frac{\tilde{C}}{2} \sum_n \left(\partial_t \phi_n^2 - \omega_n^2 \phi_n^2\right) \tag{1.10}$$

where $\tilde{C} = cL/2$. The conjugate momentum to the mode amplitude ϕ_n is $Q_n = \tilde{C}\partial_t \phi_n$, and the Hamiltonian is then

$$H = \sum_n \frac{Q_n^2}{2\tilde{C}} + \frac{\tilde{C}}{2}\omega_n^2 \phi_n^2. \tag{1.11}$$

It represents a sum of independent harmonic oscillators. We quantize it by introducing the ladder operators a_n for each mode:

$$H = \sum_n \hbar\omega_n \left(a_n^\dagger a_n + \frac{1}{2}\right) \tag{1.12}$$

where

$$Q_n = i\sqrt{\frac{\hbar \tilde{C}\omega_n}{2}}(a_n^\dagger - a_n), \qquad \phi_n = i\sqrt{\frac{\hbar}{2\tilde{C}\omega_n}}(a_n^\dagger + a_n). \tag{1.13}$$

The flux at the junction position due to mode n is then

$$\phi_n \varphi(x_j) = \sqrt{\frac{2\hbar Z}{(2n+1)\pi}}(a_n^\dagger + a_n) \tag{1.14}$$

with $Z = \sqrt{l/c}$ being the impedance of the transmission line. Comparing this with equation 2, we can write

$$e^{i\frac{e}{\hbar}\Phi_{J,n}} = e^{i\lambda(a_n + a_n^\dagger)} \tag{1.15}$$

with the coupling parameter $\lambda = \sqrt{\pi Z_c / R_\mathrm{K}}$, and the characteristic impedance of the n-th mode, for the $\lambda/4$ resonator case, is

$$Z_c = \frac{4Z}{(2n+1)\pi}. \tag{1.16}$$

Impact of the Junction Capacitance on the Resonator Modes

The junction connected at the end of the resonator changes the mode frequencies, as well as their characteristic impedances Z_c, compared to the case considered above. The resonance frequencies ω_n are obtained by including the junction in transfer matrix calculations (see appendix C) as a lumped capacitor C_j.

To determine the characteristic impedance of mode ω_n, we repeat the calculation presented above, generalized to the case where transmission line capacitance or inductance are not constant, but rather depend on position (see e.g. [51]). Mode characteristic impedance in this general case is given by

$$Z_c = \frac{1}{\omega_n \tilde{C}_n} \tag{1.17}$$

where $\tilde{C}_n$ is proportional to the distributed line capacitance:

$$Z_c = \frac{1}{\omega_n}\left(\int_0^L \mathrm{d}x\; c(x)\left|\varphi_n(x)\right|^2\right)^{-1} \tag{1.18}$$

This value depends on the normalization of mode amplitudes φ_n. We fix the normalization by comparing equation 1.18 to the case discussed above. To recover the quarter-wavelength resonator formula, normalization $|\varphi_n(x_j)| = 1$ is required.

For the case of a junction C_j connected to the end of a transmission line characterized by lineic capacitance c, the equation 1.18 results in

$$Z_c = \frac{1}{\omega_n}\left(c\int_0^L \mathrm{d}x\; \left|\varphi_n(x)\right|^2 + C_j\right)^{-1}. \tag{1.19}$$

Thus, connecting the junction to the resonator reduces the characteristic impedance of its modes.

1.2 Quasiparticle Tunneling Rates

In the previous section, we have derived the coupling parameter expression for a transmission line resonator coupled to a junction, and showed that the tunneling Hamiltonian can be written as

$$H_T = T\sum_{k,q} c^{\dagger}_{R,q} c_{L,k} e^{i\lambda(a+a^{\dagger})} + h.c. \tag{1.20}$$

with $\lambda = \sqrt{\pi Z_c/R_{\mathrm{K}}}$. We now use the Fermi's golden rule to calculate the tunneling rates from this Hamiltonian.

1.2.1 Elastic Tunneling

First, let us consider the Hamiltonian 1, describing the tunneling through the junction in absence of any high impedance environment. The forward tunneling rate calculated using the Fermi's golden rule is

$$\overrightarrow{\gamma}(V) = \frac{1}{e^2 R_{\mathrm{T}}}\int_{-\infty}^{\infty} \mathrm{d}E\, n_L(E) n_R(E+eV) f(E)(1 - f(E+eV)) \tag{1.21}$$

where n_L and n_R are the densities of states of the left and right junction electrodes, and $f(E)$ is the Fermi-Dirac distribution. To get the net current flowing through the junction, we need to take into account the tunneling in both directions:

$$I(V) = e(\overrightarrow{\gamma}(V) - \overleftarrow{\gamma}(V)). \tag{1.22}$$

The tunneling rate $\overleftarrow{\gamma}(V)$ can be calculated using the same procedure as the one presented above, resulting in

$$\overleftarrow{\gamma}(V) = \overrightarrow{\gamma}(-V). \tag{1.23}$$

The current voltage characteristic is then

$$I(V) = \frac{1}{eR_{\mathrm{T}}}\int_{-\infty}^{\infty} \mathrm{d}E\, n_L(E) n_R(E+eV)(f(E) - f(E+eV)). \tag{1.24}$$

where the superconducting density of states in both junction electrodes is given by (see e.g. [52])

$$n(E) = \mathrm{Re}\left(\frac{E + i\Gamma}{\sqrt{(E + i\Gamma)^2 - \Delta^2}}\right) \tag{1.25}$$

with Δ being the superconducting gap, and Γ the Dynes parameter, describing the tail of the $I(V)$ below the superconducting gap. For aluminium, the superconducting gap is $\Delta \approx 200\,\mu\mathrm{eV}$. Typical values of Dynes parameter for aluminium are $\Gamma/\Delta = 10^{-4} - 10^{-6}$ [53], and reported values are as low as $\Gamma/\Delta = 1.6 \cdot 10^{-7}$ [54]. Unless otherwise noted, in calculations presented in this thesis, the Dynes parameter is set to $\Gamma = 10\,\mathrm{neV}$, corresponding to $\Gamma/\Delta = 5 \cdot 10^{-5}$. Restricting the bias voltage to positive values close to the superconducting gap, we can neglect the reverse tunneling, and the approximation

$$I(V) \approx e\overrightarrow{\gamma}(V) \tag{1.26}$$

is valid for all practical purposes.

1.2.2 Inelastic Tunneling

To calculate the inelastic tunneling rates mediated by photon absorption or emission into the resonator mode, we start by writing the charge translation operator in terms of quantum jump operators A_l:

$$e^{i\lambda(a+a^\dagger)} = \sum_l A_l \tag{1.27}$$

The jump operator A_l creates l photons in the resonator for $l > 0$, or removes $-l$ photons from the resonator if $l < 0$. In the Fock state basis we have [55]

$$A_l = \sum_{n\geq 0} |n+l\rangle \langle n+l| \, e^{i\lambda(a+a^\dagger)} \, |n\rangle \langle n| \, , l \geq 0 \tag{1.28}$$

For $l < 0$, the quantum jump operators are defined through $A_{-l} = (-1)^l A_l^\dagger$. Matrix elements of these operators can be calculated from [56]

$$\langle n+l| \, A_l \, |n\rangle = \left(\frac{n!}{(n+l)!}\right)^{1/2} (i\lambda)^l e^{-\lambda^2/2} L_n^{(l)}(\lambda^2), \; l \geq 0 \tag{1.29}$$

where $L_n^{(l)}$ are generalized Laguerre polynomials.

Following the same calculation as in the elastic case, we can calculate the tunneling rates corresponding to different inelastic processes. If we assume that the initial state of the resonator is $|n\rangle$, and the final state is $|n+l\rangle$, the tunneling rate corresponding to this process given by the Fermi golden rule is

$$\kappa_{n,n+l} = \left|\langle n+l| \, e^{i\lambda(a+a^\dagger)} \, |n\rangle\right|^2 \overrightarrow{\gamma}(V - l\hbar\omega_1/e) \tag{1.30}$$

where ω_1 is the frequency of the resonator mode coupled to the junction.

Single Photon Tunneling Rates

Tunneling rates $\kappa_{n,n-1}$ corresponding to single photon absorption, for two values of λ, are shown in figure 1.1. Firstly, we consider the weak coupling case shown in 1.1a. For a given junction voltage bias, rate $\kappa_{n,n-1}$ grows linearly with n, in a manner similar to a standard loss channel. This linear growth can be derived from equations 1.29 and 1.30. The tunneling rate $\kappa_{n,n-1}$ calculated from these equations is

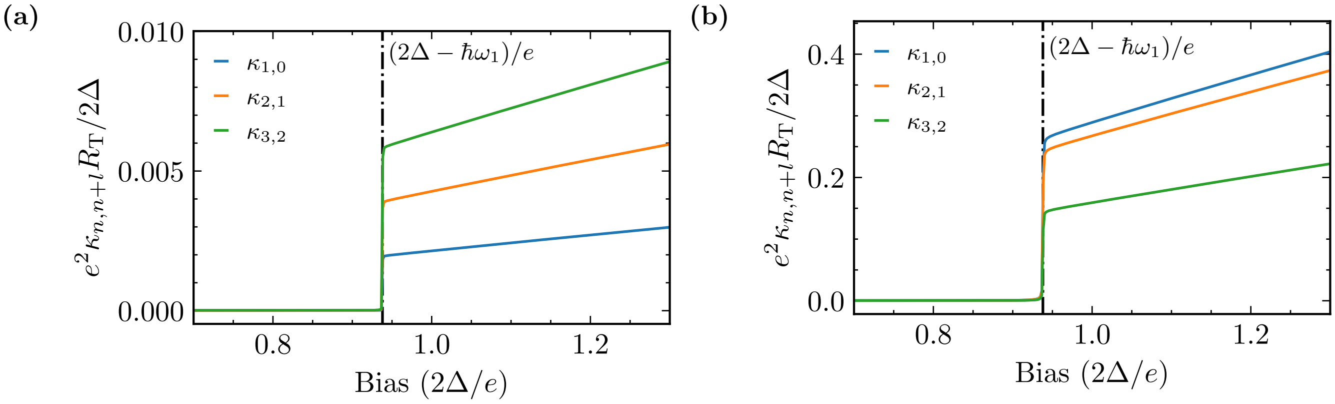

Figure 1.1: Inelastic tunneling rates corresponding to single photon absorption as functions of bias for different initial resonator states. Superconducting gap is $\Delta = 200\,\mu$eV, while the photon frequency is $\omega = 2\pi \times 6\,$GHz. (a) $\lambda = 0.05$ corresponding to conventional resonator characteristic impedance (b) $\lambda = 0.8$, corresponding to our experiment. Note the difference in y-axis.

$$\kappa_{n,n-1} = \frac{1}{n}\lambda^2 e^{-\lambda^2}\left(L^1_{n-1}(\lambda^2)\right)^2 \overrightarrow{\gamma}(V + \hbar\omega_1/e) \tag{1.31}$$

where the first few associated Laguerre polynomials are

$$\begin{aligned} L^1_0(\lambda^2) &= 1 \\ L^1_1(\lambda^2) &= 2 - \lambda^2 \\ L^1_2(\lambda^2) &= \frac{1}{2}(6 - 6\lambda + \lambda^2). \end{aligned} \tag{1.32}$$

In the limit $\lambda \ll 1$, we have

$$L^1_n(0) = n + 1 \tag{1.33}$$

and the single-photon absorption tunneling rate is

$$\kappa_{n,n-1} = n\lambda^2 e^{-\lambda^2}\overrightarrow{\gamma}(V + \hbar\omega_1/e) \tag{1.34}$$

For $\lambda \sim 1$, the picture is markedly different. The inelastic rates are two orders of magnitude higher compared to the $\lambda \ll 1$ case. Additionally, $L^1_n(\lambda^2)$ decreases with increasing n for $\lambda \sim 1$, thus decreasing the tunneling rates (figure 1.1b).

Multi-photon Process Rates

To further highlight the differences between the two regimes, we consider the inelastic tunneling rates involving multiple photons. Rates corresponding to transitions $|n\rangle \rightarrow |0\rangle$ are

$$\kappa_{n,0} = \frac{1}{n!}\lambda^{2n} e^{-\lambda^2} \overrightarrow{\gamma}(V + l\hbar\omega_1/e) \tag{1.35}$$

Tunneling rates $\kappa_{n,0}, n = 1, 2, 3$ for two values of λ are shown in figure 1.2. The sharp increase in rates happens at the bias voltage $eV = 2\Delta - n\hbar\omega_1$. Below this value, the tunneling rates are very small, and mostly set by the Dynes parameter ($\Gamma/\Delta = 5 \cdot 10^{-5}$ in our case). For $\lambda \ll 1$ (figure 1.2a), the multiphoton processes can be safely neglected due to the exponential dependence on n (equation 1.35). On the other hand, for $\lambda \sim 1$, the multi-photon inelastic tunneling rates are comparable to the single photon process ones. Thus, they need to be taken into account to accurately calculate steady state of the resonator, and the current flowing through the junction.

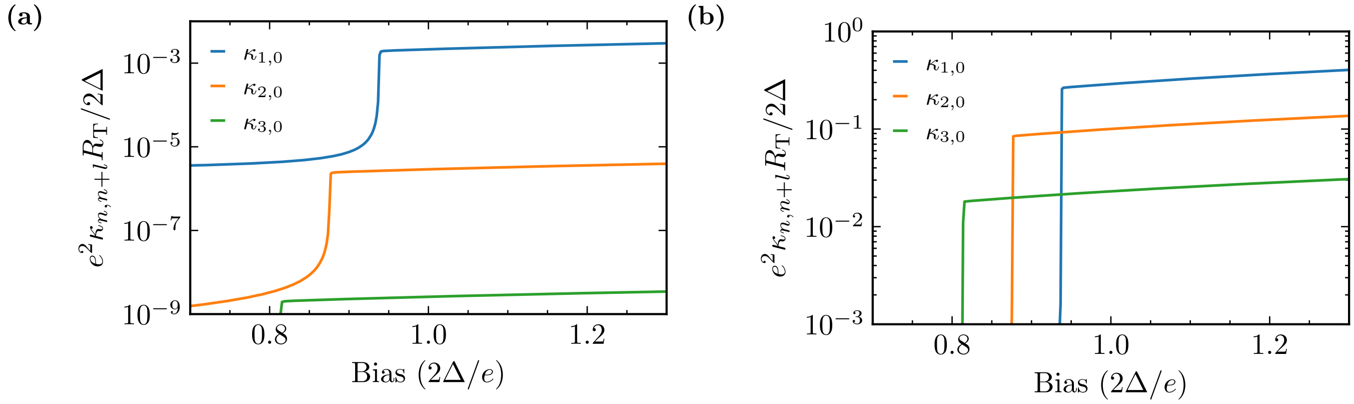

Figure 1.2: Inelastic tunneling rates corresponding to transitions $|n\rangle \rightarrow |0\rangle$ as function of bias for different initial resonator states. Superconducting gap is $\Delta = 200\,\mu\mathrm{eV}$, while the photon frequency is $\omega = 2\pi \times 6\,\mathrm{GHz}$. (a) $\lambda = 0.05$ corresponding to conventional resonator characteristic impedance (b) $\lambda = 0.8$, corresponding to our experiment.

1.3 Photo-Assisted Current

The inelastic tunneling rates, and therefore the current flowing through the junction, depend on the number of photons in the resonator. To calculate the photo-assisted current, one has to determine the resonator state first. To do so, we use a quantum master equation. Detailed quantum master equation derivation is given in [55].

1.3.1 Resonator-junction Quantum Master Equation

In Markov approximation, the evolution of the reduced density matrix of an open quantum system coupled to a bath is [57]:

$$\dot{\rho} = -\frac{1}{\hbar^2}\int_0^\infty \mathrm{d}\tau \mathrm{Tr}_\mathrm{B}\left[H_I(t)H_I(t-\tau)\rho(t) \otimes \rho_B - H_I(t)\rho(t) \otimes \rho_B H_I(t-\tau) + \mathrm{h.c.}\right] \tag{1.36}$$

where $\mathrm{Tr}_\mathrm{B}[\ldots]$ is the trace over bath degrees of freedom. In our case, the system is the resonator mode, while the superconducting tunnel junction leads represent the bath. The resonator and the junction are coupled by the tunneling Hamiltonian, which in the interaction frame reads

$$H_I(t) = T\sum_{k,q} c^\dagger_{R,q}(t)c_{L,k}(t)e^{i\lambda(a(t)+a^\dagger(t))}e^{ieVt/\hbar} + \mathrm{h.c.} \tag{1.37}$$

where the summation goes over the quasiparticle energies in the two junction electrodes. In terms of the quantum jump operators, we have

$$H_I(t) = \sum_l A_l e^{il\omega_1 t}B_l(t) \tag{1.38}$$

where $B_l(t)$ are bath operators, and ω_1 is the resonator mode frequency. If we assume that the bath is stationary, and apply the rotating wave approximation to eliminate rapidly oscillating terms, the quantum master equation can be written as

$$\dot\rho = -\frac{1}{\hbar^2}\int_0^\infty \mathrm{d}\tau \sum_l T^2\left[A_lA_l^\dagger\rho(t)K(\tau)e^{il\omega_1\tau} - A_l\rho(t)A_l^\dagger K(\tau)e^{il\omega_1\tau} + \mathrm{h.c.}\right] \tag{1.39}$$

where $K(\tau)$ is the bath memory function

$$K(\tau) = \sum_{k,q}\langle c^\dagger_{R,q}c_{R,q}c_{L,k}c^\dagger_{L,k}\rangle e^{i\tau(\omega_q-\omega_k)}e^{ieV\tau/\hbar} + \mathrm{h.c.}. \tag{1.40}$$

Averaging $\langle\ldots\rangle$ is performed over the equilibrium bath state. We define the real and imaginary part of the single sided bath memory function Fourier transform at $l\omega_1$ as

$$\frac{T^2}{\hbar^2}\int_0^\infty \mathrm{d}\tau K(\tau)e^{il\omega_1\tau} = \gamma_l + i\epsilon_l. \tag{1.41}$$

Using the identity

$$\int_0^\infty \mathrm{d}\tau e^{i\sigma\tau} = \pi\delta(\sigma) + i\mathcal{P}\frac{1}{\sigma} \tag{1.42}$$

with $\mathcal{P}$ being the Cauchy principal value, we recognize the real part of the bath memory function Fourier transform as the shifted current-voltage characteristic of the junction:

$$\gamma_l = \frac{1}{e}I(V + l\hbar\omega_1/e) \tag{1.43}$$

where we have neglected the reverse tunneling. Then, due to causality, ϵ_l is proportional to the Kramers-Kronig transform I^{KK} of the junction current-voltage characteristic. The master equation is then

$$\dot\rho = \sum_l -\frac{i}{2e}I^{\mathrm{KK}}(V + l\hbar\omega_1/e)[A_lA_l^\dagger,\rho] + \frac{1}{e}I(V + l\hbar\omega_1/e)(2A_l^\dagger\rho A_l - \{A_lA_l^\dagger,\rho\}). \tag{1.44}$$

The first term in the equation amounts to shifting of resonator eigenstates, and can be absorbed into the system Hamiltonian. This shift due to coupling to the junction bath is called Lamb shift in analogy with atomic physics. It is described in detail in [58, 59].

To finalize the description of our system, the microwave drive is added. Together with the Lamb shift, it constitutes the Hamiltonian part of the dynamics of the resonator:

$$H = H_{\mathrm{D}} + H_{\mathrm{LS}} \tag{1.45}$$

$$H_{\mathrm{D}} = i\eta(a - a^{\dagger}) - \delta a^{\dagger} a \tag{1.46}$$

$$H_{\mathrm{LS}} = \frac{1}{2e}\sum_{l=-\infty}^{l=\infty} I^{\mathrm{KK}}(V + l\hbar\omega_1/e) A_l A_l^{\dagger}, \tag{1.47}$$

where H_{D} is the microwave drive, with η being the pumping strength and δ drive detuning. H_{LS} describes the Lamb shift of the resonator. The master equation governing the time evolution of the reduced resonator density matrix ρ is then

$$\dot{\rho} = -i[H, \rho] + \frac{1}{e}\sum_{l=-\infty}^{\infty} I(V + l\hbar\omega_1/e)\mathcal{D}[A_l^{\dagger}](\rho) + \kappa\mathcal{D}[a](\rho) \tag{1.48}$$

where $\mathcal{D}[F](\rho) = F\rho F^{\dagger} - \frac{1}{2}\{F^{\dagger}F, \rho\}$. The first term in the master equation describes the usual unitary dynamics. The second term corresponds to the photon exchange with the junction, and the final term is the coupling to the thermal bath, characterized by the damping rate κ. To find the stationary resonator density matrix, we solve the equation

$$\dot{\rho} = 0. \tag{1.49}$$

After obtaining the steady state density matrix, the photo-assisted current is given by

$$I_{\mathrm{PAT}} = \sum_{l\neq 0} I(V - l\hbar\omega_1/e)\,\mathrm{Tr}\left(A_l^{\dagger} A_l \rho\right). \tag{1.50}$$

To obtain the total current, we add the elastic tunneling contribution:

$$I = \sum_{l} I(V - l\hbar\omega_1/e)\,\mathrm{Tr}\left(A_l^{\dagger} A_l \rho\right). \tag{1.51}$$

We will use this equation to compare the calculated tunneling current to the experimental data.

1.3.2 Low Power Limit: Photon Detection

In general, the equation 1.49 needs to be solved numerically. However, in the limit of interest for single photon detection, a concise analytical solution exists. We assume the microwave drive is weak, so that the mean resonator population satisfies $\langle n_{\mathrm{res}}\rangle \ll 1$. Additionally, the Lamb shift is neglected, and the bias voltage is fixed to $eV = 2\Delta - \hbar\omega_1/2$. At this voltage bias, the dominant inelastic process is the single photon absorption. To solve the master equation, the resonator Hilbert space is truncated to two states. The reduced density matrix ρ is

$$\rho = \begin{pmatrix} \rho_{00} & \rho_{01} \\ \rho_{10} & \rho_{11} \end{pmatrix}. \tag{1.52}$$

The annihilation operator a is given by

$$a = \begin{pmatrix} 0 & 1 \\ 0 & 0 \end{pmatrix}. \tag{1.53}$$

From equation 1.29, and the identity $L_0^k(x) = 1$, the single photon junction loss operator is

$$A_1 = i\lambda e^{-\lambda^2/2} a \tag{1.54}$$

where a is the annihilation operator. The quantum master equation reduces to

$$0 = -[H_\mathrm{D}, \rho] + (\kappa_j^{(1)} + \kappa)\mathcal{D}[a](\rho) \tag{1.55}$$

where $\kappa_j^{(1)} = \lambda^2 e^{-\lambda^2} I(2\Delta + \hbar\omega_1/2e)$ is the one photon junction loss rate, and κ is the damping rate. The resonator excited state population is given by the density matrix element ρ_{11}. To leading order in η, the solution of master equation is:

$$\rho_{11} = \frac{4\eta^2}{4\delta^2 + \kappa_\mathrm{tot}^2} \tag{1.56}$$

where $\kappa_\mathrm{tot} = \kappa_j^{(1)} + \kappa$ is the total resonator loss. From equation 1.50, the photo-assisted current is

$$I_\mathrm{PAT} = e\rho_{11}\kappa_j^{(1)} = \frac{4\eta^2\kappa_j^{(1)} e}{4\delta^2 + (\kappa + \kappa_j^{(1)})^2} \tag{1.57}$$

or in terms of resonator population

$$I_\mathrm{PAT} = e\langle n_\mathrm{res}\rangle \kappa_j^{(1)}. \tag{1.58}$$

Providing that the resonator population satisfies $\langle n_\mathrm{res}\rangle \ll 1$, the photo-assisted current through the junction is proportional to the number of photons in the resonator. Thus, by measuring current, we monitor the number of photons in the cavity, and our device acts as a microwave photon detector.

1.3.3 Multi-photon Processes and Detector Saturation

When the microwave drive power is increased, the photo-assisted current due to multi-photon tunneling processes cannot be neglected, leading to saturation in the detector. We demonstrate the saturation effect by estimating the current stemming from two-photon losses in the weak pumping limit. The calculation involving higher order processes is analogous.

We restrict the resonator Hilbert space to the three lowest levels, and fix the bias voltage to $V = (2\Delta - 3\hbar\omega_1/2)/e$, such that one-photon losses are negligible. The resonator density matrix is

$$\rho = \begin{pmatrix} \rho_{00} & \rho_{01} & \rho_{02} \\ \rho_{10} & \rho_{11} & \rho_{12} \\ \rho_{20} & \rho_{21} & \rho_{22} \end{pmatrix} \tag{1.59}$$

and the annihilation operator is

$$a = \begin{pmatrix} 0 & 1 & 0 \\ 0 & 0 & \sqrt{2} \\ 0 & 0 & 0 \end{pmatrix}. \tag{1.60}$$

The junction voltage bias is set such that single photon absorption is not allowed, so we only consider the two photon loss proportional to

$$A_2 = -\frac{\lambda^2}{\sqrt{2}} e^{-\lambda^2/2} \begin{pmatrix} 0 & 0 & 1 \\ 0 & 0 & 0 \\ 0 & 0 & 0 \end{pmatrix}. \tag{1.61}$$

The master equation is then:

$$0 = -[H_\mathrm{D}, \rho] + I(2\Delta/e + 3\hbar\omega_1/2e)\mathcal{D}[A_2^\dagger](\rho) + \kappa\mathcal{D}[a](\rho) \tag{1.62}$$

where κ is the damping rate. Solving this equation, we get for the probability to find the resonator in the second excited state to the leading power in η:

$$\rho_{22} = \frac{32\eta^4}{(4\delta^2 + \kappa^2)(16\delta^2 + (\kappa_j^{(2)} + 2\kappa)^2)} \tag{1.63}$$

where

$$\kappa_j^{(2)} = \frac{\lambda^4}{2} e^{-\lambda^2} I(2\Delta/e + 3\hbar\omega_1/2e)/e \tag{1.64}$$

is the two-photon junction loss rate. Knowing the density matrix element ρ_{22}, we can calculate the photo-assisted tunneling current through the junction:

$$I_\mathrm{PAT}^{(2)} = e\rho_{22}\kappa_j^{(2)}. \tag{1.65}$$

The current is no longer proportional to the square of the pumping strength η, but rather $I_\mathrm{PAT} \propto \eta^4$. In case of zero drive detuning, and assuming $\kappa_j^{(2)} \ll \kappa$, the photo assisted current is

$$I_\mathrm{PAT}^{(2)} \approx \frac{\langle n_\mathrm{res}\rangle^2}{2}\kappa_j^{(2)} e. \tag{1.66}$$

Thus, when $I_\mathrm{PAT}^{(1)}$ and $I_\mathrm{PAT}^{(2)}$ are of the same order of magnitude, monitoring the current flowing through the junction no longer corresponds to measuring the number of photons in the resonator. To obtain a quantitative estimation of this saturation effect, we need to solve the master equation 1.49 numerically, which is done later. However, from

$$\frac{\kappa_j^{(2)}}{\kappa_j^{(1)}} \approx \frac{\lambda^2}{2} \tag{1.67}$$

we note that the detector saturates at lower photon flux for higher λ. For $\lambda \sim 1$, we expect to observe saturation effects when $\langle n_\mathrm{res}\rangle$ is on the order of unity.

Similar calculation to the one shown above, for bias voltage $eV = 2\Delta - 5\hbar\omega_1/2$, results in the three-photon absorption current of:

$$I_{\mathrm{PAT}}^{(3)} = \frac{96\eta^6 \kappa_j^{(3)} e}{(4\delta^2 + \kappa^2)^2 (36\delta^2 + (\kappa_j^{(3)} + 3\kappa)^2)} \tag{1.68}$$

where the junction loss rate is

$$\kappa_j^{(3)} = \frac{\lambda^6}{6} e^{-\lambda^2} I(2\Delta/e + 5\hbar\omega_1/2e)/e. \tag{1.69}$$

As expected, the photo-assisted current is proportional to ϕ^3.

1.4 Towards a Practical Photon Detector: Device Parameters

In the previous section, we have shown that the resonator-junction system acts as a photodetector. Now, we are going to use the formalism developed above to estimate the performance of such a device. For the detector to be of practical use, it is necessary to combine high detection efficiency with low dark counts. These requirements put constraints on device parameters. Below, we show the conditions that need to be satisfied for these requirements to be fulfilled. Firstly, we calculate the quantum efficiency of photon to electron conversion in a resonator-junction system coupled to a transmission line. Then, we discuss how to minimize the detector dark current.

1.4.1 Quantum efficiency: Rate Matching

Photoelectric conversion quantum efficiency χ is defined as the ratio of the resulting electron flux ϕ_e to the incident photon flux ϕ:

$$\chi = \frac{\phi_e}{\phi} = \frac{I_{\mathrm{PAT}}}{e\phi}. \tag{1.70}$$

The proposed photon detector is shown in figure 1.3. The photons are fed into the resonator with the rate κ_c, set by the mismatch between the impedances of the feedline $Z_0 = 50\,\Omega$, and the resonator, and converted into electrons through inelastic tunneling, characterized by rate κ_j. In an ideal case, each incident photon is absorbed by the junction, and converted into an electron resulting in quantum efficiency of unity.

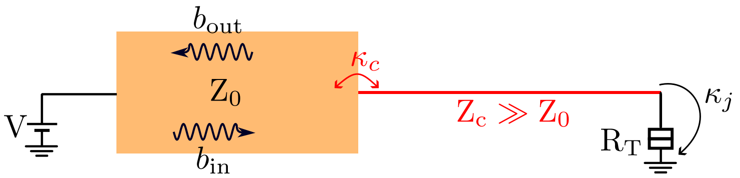

Figure 1.3: Proposed detector scheme. Incident photons, characterized by the field b_{in} are fed into the resonator with rate κ_c set by the mismatch between the impedances of the feedline $Z_0 = 50\,\Omega$, and the the resonator. The reflected signal is given by the field b_{out}. Inelastic tunneling rate is κ_j.

The power absorbed by the device is given by $1 - |S_{11}(\omega)|^2$, where S_{11} is the reflection coefficient defined as the ratio of ingoing and outgoing electromagnetic fields:

$$S_{11} = \frac{b_{\text{out}}}{b_{\text{in}}}. \tag{1.71}$$

For a single mode resonator, the reflection coefficient is given by (see appendix A)

$$S_{11}(\delta) = 1 - \frac{\kappa_c}{\frac{\kappa_{\text{tot}}}{2} + i\delta} \tag{1.72}$$

where κ_c is the coupling rate, κ_{tot} are total resonator losses, and $\delta = \omega - \omega_1$ is the detuning compared to resonance frequency. Aside from the coupling to the experimental setup, additional losses present in the system are due to tunneling through the junction, κ_j, and spurious resonator losses κ_i:

$$\kappa_{\text{tot}} = \kappa_c + \kappa_j + \kappa_i \tag{1.73}$$

In the rest of this chapter, we discuss the linear regime described in section 1.3.2, and consider that the junction loss rate is due to single-photon loss $\kappa_j = \kappa_j^{(1)}$, dropping the superscript.

Absorption is highest for zero detuning, and writes:

$$1 - |S_{11}(0)|^2 = \frac{4(\kappa_i + \kappa_j)\kappa_c}{(\kappa_i + \kappa_j + \kappa_c)^2} \tag{1.74}$$

This expression has a maximum at

$$\kappa_i + \kappa_j = \kappa_c, \tag{1.75}$$

when the coupling rate equals the sum of junction and intrinsic loss rates. This condition is equivalent to impedance matching for maximizing power transfer.

However, only the photons absorbed by the junction are converted to electrons. Thus, the presence of spurious losses κ_i reduces the conversion quantum efficiency compared to total absorption. To estimate the efficiency of the photon to electron conversion process, we assume the photo-assisted tunneling current to be

$$I_{\text{PAT}} = e\langle n_{\text{res}}\rangle \kappa_j \tag{1.76}$$

The current is related to the incident photon flux ϕ by $I_{\text{PAT}} = \chi e \phi$, where χ is quantum efficiency. By taking the resonator population to be

$$\langle n_{\text{res}}\rangle = 4\eta^2/(\kappa_i + \kappa_j + \kappa_c)^2 \tag{1.77}$$

where $\eta = \sqrt{\phi\kappa_c}$ is the microwave pumping strength, we get

$$\chi = \frac{4\kappa_j\kappa_c}{(\kappa_i + \kappa_j + \kappa_c)^2} \tag{1.78}$$

Quantum efficiency has a maximum at

$$\kappa_j = \kappa_c + \kappa_i, \tag{1.79}$$

which is slightly different from the maximum of absorption given by the rate matching condition due to the presence of spurious losses κ_i.

1.4.2 Minimizing the Dark Current: Strong Coupling Regime

In the previous section we have shown that high photon-to-electron conversion can be achieved by tuning the junction loss rate to the value of the coupling between the resonator and the feedline. A priori, this matching condition can be satisfied regardless of the value of the coupling parameter λ. We now include the consideration of dark current in the device design, and show that by using strong coupling regime $\lambda \sim 1$ we reduce the potential dark rate of our detector.

The dark rate set by the current flowing through the junction biased at the operating voltage $eV = 2\Delta - \hbar\omega_1/2$ when no microwave drive is applied. This current is determined by the junction Dynes parameter Γ and its tunneling resistance R_T. The current-voltage characteristic in the vicinity of the detector operating point calculated using equation 1.24 is shown in figure 1.4 for two different values of Dynes parameter. The junction tunneling resistance is fixed to $R_\mathrm{T} = 1.6\,\mathrm{M\Omega}$. The subgap current is inversely proportional to the Dynes parameter. Thus, by minimizing it, e.g. through careful shielding of the sample [54], and the proper choice of the material (e.g. choosing aluminium instead of niobium), we minimize the detector dark rate.

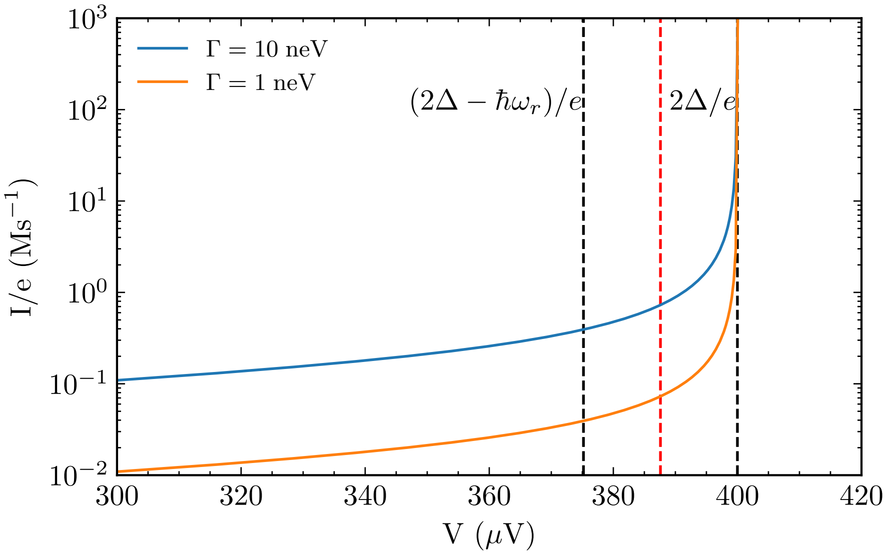

Figure 1.4: Junction current-voltage characteristic below the superconducting gap calculated from equation 1.24 for junction tunnel resistance $R_\mathrm{T} = 1.6\,\mathrm{M\Omega}$ (blue) and two value of Dynes parameter — 10 neV (blue curve) and 1 neV (orange curve). The temperature of both junction electrodes is set to 30 mK. Red dashed line represents the operating voltage bias of the detector.

Additionally, the current flowing through the junction scales inversely with the resistance, thus making high resistance junctions desirable for minimization of subgap current. To demonstrate how junction resistance can be maximized by choosing high coupling parameter λ, we consider the single-photon absorption rate

$$\kappa_j = \lambda^2 e^{-\lambda^2} I(V + \hbar\omega_1). \tag{1.80}$$

For a fixed junction resistance, this rate is set by the resonator-junction coupling parameter through the matrix element $\lambda^2 e^{-\lambda^2}$. Its evolution with λ is shown in figure 1.5. It reaches the maximum for $\lambda = 1$, and at values more than two orders of magnitude higher than for commonly used resonators with characteristic impedances $Z_C \sim 100\,\Omega$. Therefore, for strong coupling $\lambda \sim 1$, junctions fulfilling the rate matching condition $\kappa_j = \kappa_c$ for a given coupling rate are 100 times more resistive compared to the standard weak coupling case, making the use of strong coupling crucial for minimizing dark current in our detector.

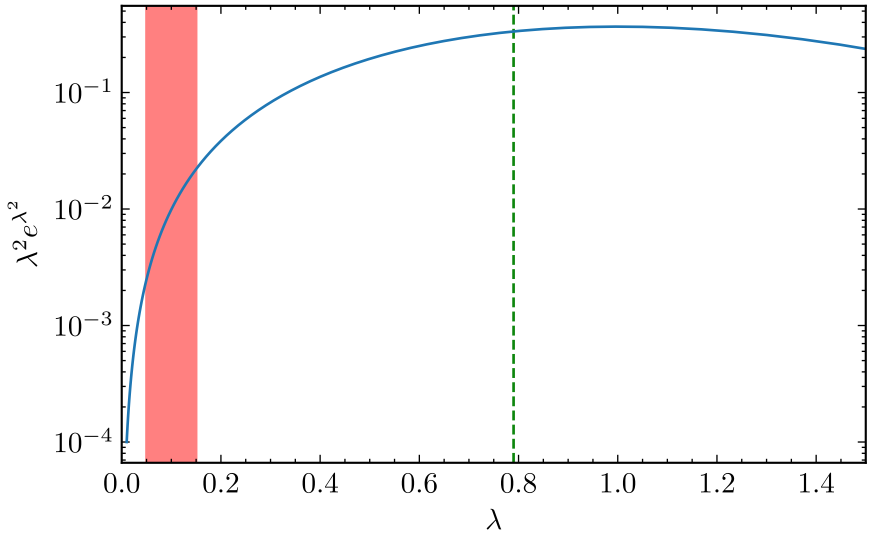

Figure 1.5: Matrix element $\left|\langle 0| e^{i\lambda(a+a^\dagger)} |1\rangle\right|^2$ as function of coupling parameter λ. Red shaded area corresponds to conventionally used resonators, while green dashed line is our experiment.

1.5 Sample Design

We have shown the requirements that our device needs to satisfy to be utilized as a practical photon detector: rate matching to achieve high quantum efficiency, and high coupling in order to minimize dark counts. Now we discuss the design of such a device. We start by designing the resonator. In order to achieve high characteristic impedance, we fabricate the resonator using granular aluminium. Granular aluminium (grAl for short) is a material that consists of aluminium islands surrounded by amorphous aluminium–oxide, and is a promising material for high impedance, high quality factor resonators [60, 45]. GrAl is fabricated by evaporating aluminium in oxygen atmosphere. Resistivity of grAl films increases with increasing oxygen content, which we control by tuning the oxygen pressure during evaporation. Fabrication details can be found in appendix B. Room temperature resistivity of fabricated grAl films are $\rho_{\mathrm{grAl}} = 800 - 2000\,\mu\Omega\mathrm{cm}$ and sheet resistance $R_\square = 400 - 1000\,\Omega/\square$, which is orders of magnitude higher than for pure aluminium. When its resistivity is low enough, grAl is a superconductor at low temperatures, and exhibits a superconductor to insulator transition at a resistivity on the order of $10\,000\,\mu\Omega\mathrm{cm}$ [61].

According to Mattis-Bardeen theory in the dirty limit and at zero temperature, the kinetic inductance of a superconducting film is [62]

$$L_\square = \frac{\hbar R_\square}{\pi \Delta}, \tag{1.81}$$

where Δ is the superconducting gap, and $R_\square$ is the sheet resistance in the normal state. The kinetic inductance in the superconducting state is directly proportional to the resistance in the normal state. This is a consequence of small Cooper pair density when the normal state resistivity is high. For fixed supercurrent, if Cooper pair density is small, their velocity, and thus their kinetic energy, needs to be higher, resulting in high kinetic inductance. GrAl superconducting gap was measured from tunneling spectroscopy to be $\Delta_{\mathrm{grAl}} = 330\,\mu\mathrm{eV}$ (significantly higher compared to the pure aluminium superconducting gap of approximately $200\,\mu\mathrm{eV}$). Hence, the kinetic inductance of typical grAl films with $R_\square = 400 - 1000\,\Omega/\square$ is 250 - 650 pH/□. The full study of achievable kinetic inductance in grAl films is in progress in the group, and the highest value reached so far is 5 nH/□ close to the SIT.

1.5.1 Resonator Design

The resonator is made in microstrip geometry. We target the coupling rate $\kappa_c/2\pi = 50 - 100\,\mathrm{MHz}$ and fundamental resonance frequency in the 4 - 8 GHz band. The coupling rate is set by the impedance mismatch between the resonator and the $50\,\Omega$ feedline. Thus, the κ_c requirement translates into the the target characteristic impedance close to $5\,\mathrm{k}\Omega$, and the coupling parameter $\lambda \approx 0.8$.

To determine the resonator properties we perform electromagnetic simulations with Sonnet software, as well as analytic calculations using transfer matrix method (appendix C). Comparison of a quarter wavelength resonator reflection spectrum simulated using Sonnet and the transfer matrix method is shown in figure 1.6. In Sonnet simulations, grAl kinetic inductance is the only free parameter, and we choose it so that it corresponds to a typical fabricated grAl nanowire $L_\square = 600\,\mathrm{pH}/\square$. The same kinetic inductance value is used for the transfer matrix calculations. Geometric contribution to the total inductance is negligible. Capacitance per unit length is chosen such that the phase velocity matches the Sonnet simulation. Therefore, resonance frequency will be identical for both methods. From figure 1.6b, we see that the frequency of the fundamental resonator mode is $\omega_1 = 2\pi \times 7.4\,\mathrm{GHz}$. A value close to the upper limit of the measurement band is chosen, because we expect the resonance frequency to decrease significantly in the presence of the tunnel junction.

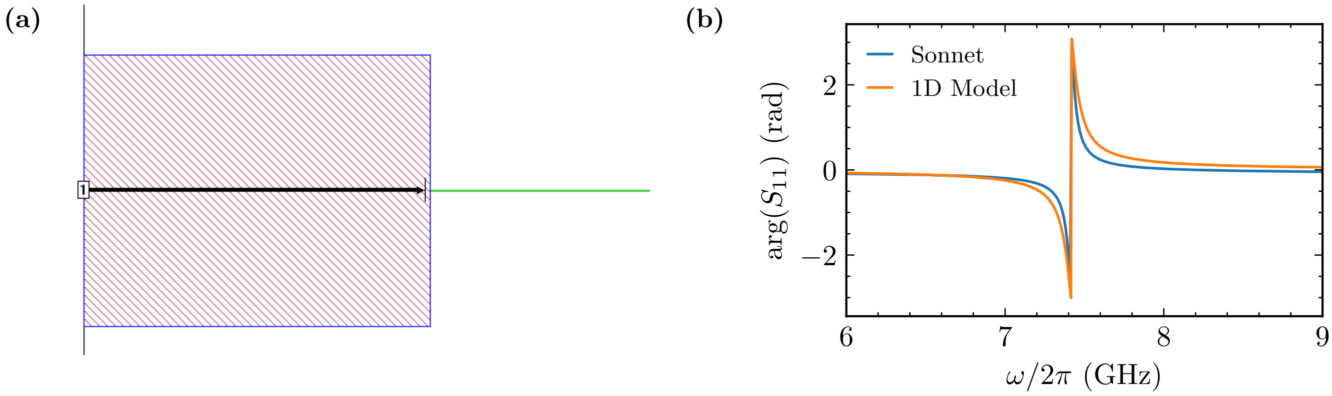

Figure 1.6: (a) Image of the Sonnet circuit used for simulating the resonator. The $50\,\Omega$ feedline is in red, while the grAl cavity is green. (b) Reflection spectrum of a quarter-wavelength resonator simulated using Sonnet software (blue) and transfer matrix model (orange). We note the discrepancy between the resonance widths.

We fit the resonance spectrum to equation 1.72, assuming that the only loss in the system is due to coupling to the transmission line, and extract the coupling rate. Fit results are given in

Method	$\kappa_c/2\pi$ (MHz)
Sonnet	52
T matrix	95

Table 1.1: Comparison of resonator coupling rates calculated from Sonnet simulations and transfer matrix method

table 1.1. There is a disagreement between the two methods. One possible explanation for the discrepancy is the width mismatch between the aluminium feedline (220 µm wide) and the grAl resonator ($\sim$ 700 nm wide), which is not captured by the 1D transfer matrix method. Therefore, we cannot rely solely on the 1D model calculations to estimate the coupling rate.

The typical junction size in our devices is on the order of 150 nm × 150 nm. Using the standard value of capacitance per unit area $100\,\mathrm{fF}\,\mu\mathrm{m}^{-2}$, we expect junction capacitance $C_j \sim 2\,\mathrm{fF}$. The fundamental mode resonance frequency and characteristic impedance of a resonator discussed above as functions of junction capacitance are shown in figure 1.7.

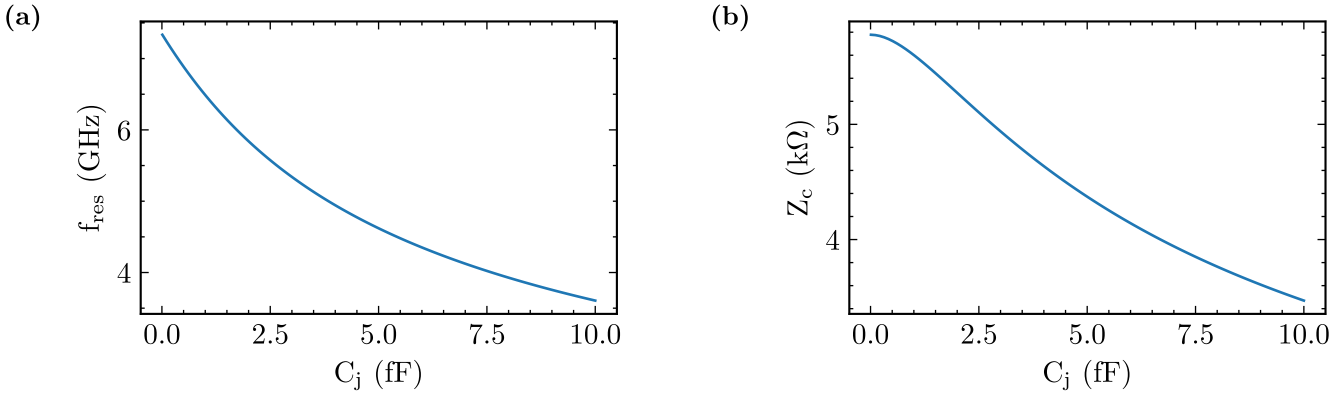

Figure 1.7: Effect of the junction on resonator properties in transfer matrix method. (a) Resonance frequency of the fundamental resonator mode function of junction capacitance. (b) Characteristic impedance of the fundamental resonator mode as function of junction capacitance.

1.5.2 Rate Matching: Setting the Junction Resistance

As discussed in section 1.4.1, for the detector to have high photon-to-electron conversion efficiency, the rate matching condition (equation 1.79) needs to be fulfilled. The coupling rates measured in previous experiments with similar devices are $\kappa_c = 2\pi \times 70 - 80\,\mathrm{MHz}$, and we tune the junction loss rate to satisfy the rate matching condition.

We set the operating bias to the middle of voltage range $eV \in [2\Delta - \hbar\omega_1, 2\Delta]$. From equation 1.80, the rate corresponding to single photon loss is

$$\kappa_j = \lambda^2 e^{-\lambda^2} I(2\Delta/e + \hbar\omega_1/2e). \tag{1.82}$$

The current flowing through the junction is inversely proportional to its tunneling resistance R_T. Thus, by choosing the suitable resistance, junction loss can be matched to the coupling rate. This rate is approximately

$$\kappa_j = \lambda^2 e^{-\lambda^2} \frac{2\Delta + \hbar\omega_1/2}{eR_\mathrm{T}} \tag{1.83}$$

For κ_c in the middle of the range cited above, and resonance frequency $\omega_1 = 2\pi \times 6\,\mathrm{GHz}$, we obtain the target tunnel resistance $R_\mathrm{T} \approx 1.5\,\mathrm{M\Omega}$.

We illustrate the rate matching condition, and the quantum efficiency of our proposed photon-to-electron converter estimated from equation 1.78 in figure 1.8. For bias voltages satisfying $eV > 2\Delta - \hbar\omega_1$ rates are closely matched, and we notice a plateau where detection efficiency is close to unity, meaning that we can operate our detector anywhere in this bias range, reducing the sensitivity to small shifts in loss rates and voltage noise.

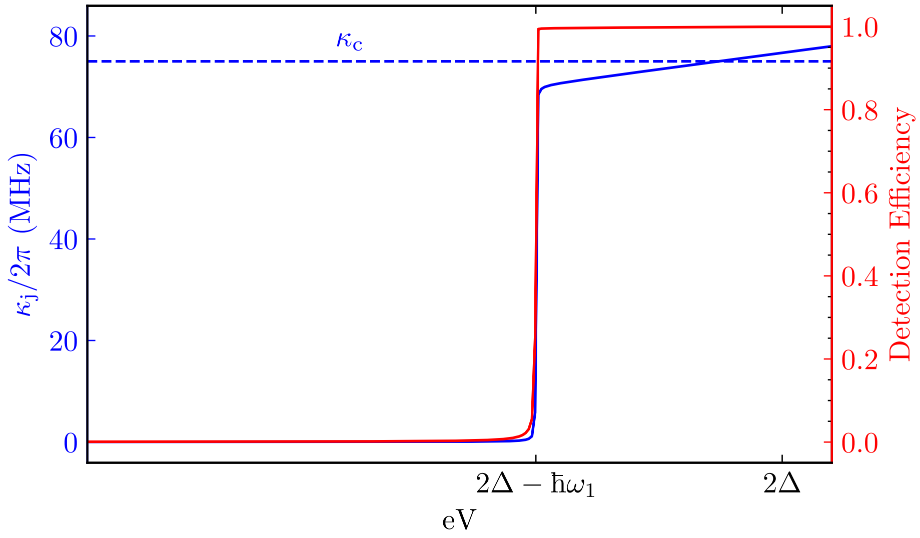

Figure 1.8: Single-photon absorption loss rate (equation 1.80) in blue, and the conversion efficiency estimated from equation 1.78 as functions of bias voltages for the resonator described in section 1.5.1 coupled to a $1.5\,\mathrm{M\Omega}$ junction. For bias voltages satisfying $eV > 2\Delta - \hbar\omega_1$ rates are closely matched, and we notice a plateau where detection efficiency is close to unity. We have neglected intrinsic losses in this calculation.

1.5.3 Conclusion

To conclude on the sample design, we summarize the parameters of our proposed device in table 1.2. We target the fundamental mode resonance frequency of $\omega_1 = 2\pi \times 6\,\mathrm{GHz}$, to be in the middle of our 4 - 8 GHz measurement band, and the detector bandwidth in the 50 - 100 MHz range. To enhance the inelastic tunneling rate κ_j, and minimize the dark detector current, we propose a high characteristic impedance resonator of $Z_c \approx 5\,\mathrm{k\Omega}$, resulting in the strong coupling between the resonator and the junction ($\lambda \approx 0.8$). The coupling rate between this resonator and the feedline, setting the detector bandwidth, is estimated to be $\kappa_c \approx 2\pi \times 75\,\mathrm{MHz}$. To satisfy the rate matching condition (equation 1.79), we target the junction resistance close to $1.5\,\mathrm{M\Omega}$. The proposed device should have conversion efficiency near unity, and low dark counts ($10^4\,\mathrm{s}^{-1}$) in the whole bias range $eV \in [2\Delta - \hbar\omega_1, 2\Delta]$.

Device Parameter	Value
ω_1	$2\pi \times 6\,\mathrm{GHz}$
κ_c	$2\pi \times 75\,\mathrm{MHz}$
Z_c	$5\,\mathrm{k\Omega}$
λ	0.8
R_T	$1.5\,\mathrm{M\Omega}$

Table 1.2: Target sample parameters for the proposed microwave photon-to-electron converter.

1.6 Conclusion

We have outlined the theoretical description of the junction-resonator system — we treat the junction as a Markovian bath at equilibrium, and derive the quantum master equation governing the time evolution of the reduced density operator of the resonator. The obtained steady state resonator density matrix is then used to calculate the current flowing through the junction in presence of a coherent microwave drive. When the mean number of photons in the resonator is significantly less than one, and for junction bias voltages in range $eV \in [2\Delta - \hbar\omega_1, 2\Delta]$, the photo-assisted current is proportional to the resonator population, and the device can be used for photon detection.

For a photon-detector to be used in measurements it needs to have high quantum efficiency, and minimal dark counts. We have shown that these constraints can be satisfied in our sample: by tuning the junction resistance one can match the one photon inelastic tunneling rate to the coupling rate of the resonator to the feedline, resulting in quantum efficiency nearing unity, and utilizing high coupling between the resonator and the junction to increase the inelastic tunneling, allows the use of high resistance junctions, minimizing the subgap current, and therefore the dark count.

Finally, we have proposed a design fulfilling the conditions listed above. The resonator is designed with the help of electromagnetic field simulations. The target parameters are frequency $\omega_1 = 2\pi \times 6\,\mathrm{GHz}$, and characteristic impedance $Z_c = 5\,\mathrm{k\Omega}$. Impedance mismatch between the resonator and the $50\,\Omega$ feedline results in the coupling rate $\kappa_c \approx 2\pi \times 75\,\mathrm{MHz}$. We then determine the junction resistance needed to match the junction loss rate to the coupling rate. The resulting tunneling resistance is $R_\mathrm{T} \approx 1.5\,\mathrm{M\Omega}$. Such a device should have photon to electron conversion efficiency approaching one, as well as low dark current (on the order of $10^4\,\mathrm{s}^{-1}$).

Chapter 2

Experimental Characterization of the Microwave Photon Detector

---

In this chapter we implement a photon detector device proposed in Chapter 1, and present the results of the experiments characterizing its performance. We start with reflection spectroscopy measurements, presented in section 2.1. Close to the superconducting gap, we observe a sharp increase in absorption close to resonance frequency. This additional photon absorption is attributed to the inelastic tunneling through the junction. By fitting the measured reflection spectra, we estimate different resonator loss rates, allowing us to obtain a quantum efficiency estimate for the photon-to-electron conversion. The assessed quantum efficiency is 0.85, significantly higher than the highest reported number for photodetectors based on inelastic tunneling [36].

To confirm that the absorbed photons result in charge flow, we apply the microwave drive and measure the current flowing through the junction as function of bias voltage and drive power. The photo-assisted current measurements are presented in section 2.2. We observe a photo-assisted current strictly proportional to the resonator population, in agreement with the predictions. Additionally, photo-assisted current due to multi-photon absorption is measured, and it is shown that it aligns with the theoretical calculations.

The detector quantum efficiency estimated from spectroscopy measurements is verified by carefully calibrating the microwave circuit, and measuring the dependence of photo-assisted current on incident microwave power. The calibration procedure is discussed in setion 2.3. It relies on measuring the photo-assisted current due to multi-photon processes as function of applied drive power, and fitting it to the quantum master equation model outlined in chapter 1 with attenuation between the microwave source and the sample as the only free parameter. The quantum efficiency obtained through this calibration procedure is in agreement with the estimate based on the measured resonator loss rates.

Finally, we estimate other figures of merit for the detector, namely the dark current and 1 dB and 3 dB compression points. These results are presented in section 2.4. The measured detector dark count is on the order of $10^5\,\mathrm{s}^{-1}$. We discuss its origin, and show that it can be explained by a residual photon population in the resonator.

2.1 Reflection Spectroscopy

The first experiments we discuss are the spectroscopy measurements of the fundamental resonator mode. The simplified measurement setup is shown in figure 2.1. The microwave measurements are performed in a reflection setup, using a VNA (see Chapter 3 for detailed experimental setup). Measuring the resonator spectra allows us to obtain the resonator loss rates. and estimate the expected photon-to-electron conversion quantum efficiency.

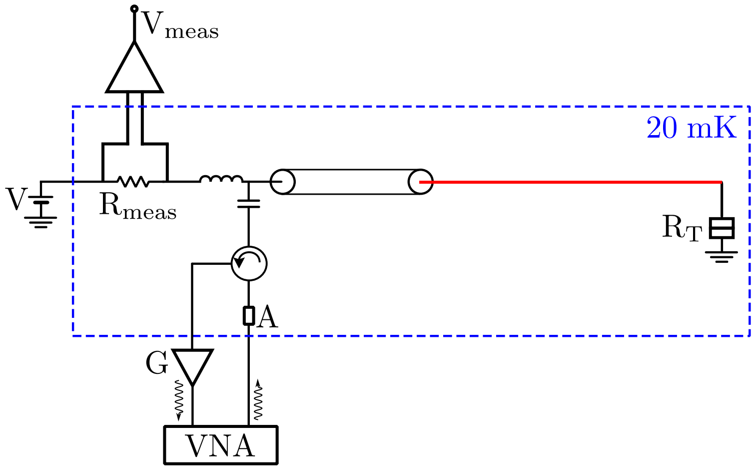

Figure 2.1: Simplified scheme of the measurement setup. The microwave measurements are done in a reflection setup. The current flowing through the junction is measured by monitoring the voltage drop across the resistor R_{meas} connected in series with the sample at low temperature. The VNA is used as a room temperature microwave source. The microwave excitation is attenuated by factor A before reaching the sample.

2.1.1 Reflection Evolution with Junction Bias Voltage

Firstly, we measure the reflection spectra at different junction biases close to the superconducting gap. The measurements are shown in figure 2.2. In the phase of the reflected signal (figure 2.2a), we observe a resonance at $\omega_1 = 2\pi \times 5.5\,\mathrm{GHz}$, corresponding to the fundamental mode of the resonator. In the modulus (figure 2.2b), at low bias we observe a slight dip in the reflected signal, meaning

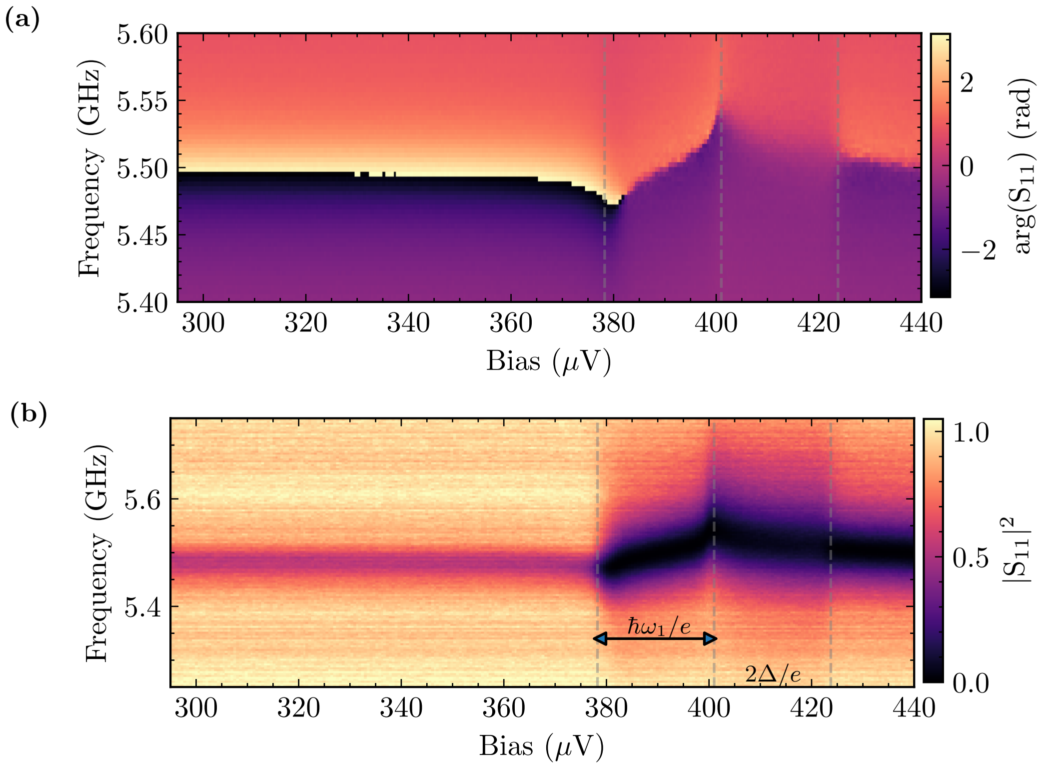

Figure 2.2: (a) Phase of reflected signal as function of junction bias and frequency. (b) Same dependence for the absolute value of reflection. Microwave excitation power is $P = -142\,\mathrm{dBm}$.

that the losses are small. As the junction bias approaches the superconducting gap, there is a sharp drop in reflection at resonance, and for bias voltages $V > (2\Delta - \hbar\omega_1)/e = 379\,\mu\mathrm{V}$, we have almost perfect absorption. Two vertical cuts of the bias-spectra map are shown in figure 2.3, highlighting the increase in absorption close to the superconducting gap.

In addition to the increase in absorption, we notice a shift in resonance frequency in the vicinity of the superconducting gap. This is the Lamb shift predicted by the quantum master equation (see section 1.3.1), and measured in detail in e.g. [59].

Fitting the resonator spectra

To estimate the loss rates κ_c, κ_j and κ_i, we fit each reflection spectrum to the formula

$$S_{11}(\omega) = ae^{i\alpha}\left(1 - \frac{2(Q_l/|Q_c|)e^{i\phi}}{1 + 2iQ_l(\omega/\omega_1 - 1)}\right) \tag{2.1}$$

where ω_1 is the resonance frequency, Q_l is the loaded quality factor, and Q_c is the coupling quality factor. Expression in parentheses describes the resonator itself, and is equivalent to equation 1.72 with complex κ_c, while the prefactor appears due to imperfections in measurement setup — a describes the losses in microwave chain, while α describes the phase shift. The parameter ϕ is set by impedance mismatches in the circuit. The fitting procedure follows [63], and we will outline it here on the example of the cavity reflection spectrum taken at $V_{\mathrm{bias}} = 300\,\mu\mathrm{V}$ shown in figure 2.3.

In order to correct for the distortion due to imperfect microwave lines, all measured VNA spectra are normalized to a reference trace. The reference trace is taken using the same experimental

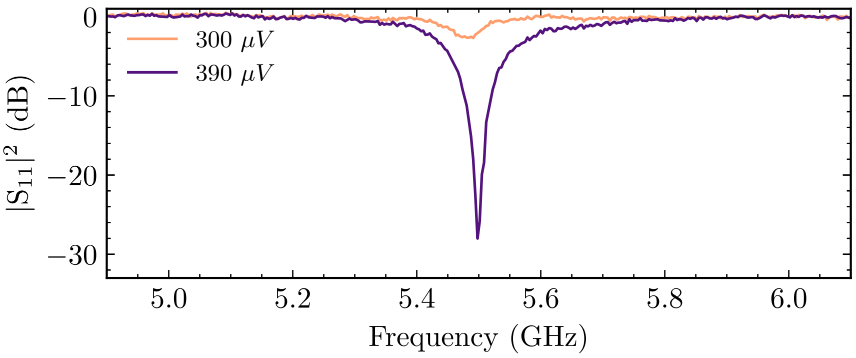

Figure 2.3: Two reflection spectra at different junction biases. Well below the superconducting gap ($V = 300\,\mu\text{V}$) we see a small dip at resonance, while for $V = 390\,\mu\text{V}$ there is nearly perfect absorption at resonance — $|S_{11}|^2 \approx -30\,\text{dB}$.

configuration, at temperature $T \approx 1.5\,\text{K}$. Due to grAl kinetic inductance being significantly higher at this temperature, the resonator frequency is low enough so that close to the base experiment temperature resonance frequency, all the power is reflected, and we measure only the microwave chain. This normalized trace, shown in figure 2.4 for junction bias voltage $V = 300\,\mu\text{eV}$, is described by equation 2.1.

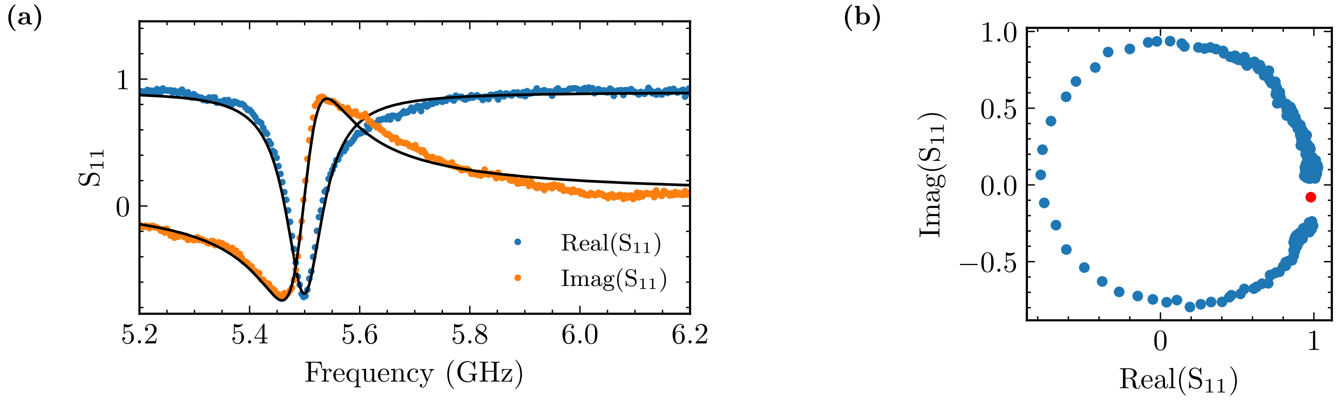

Figure 2.4: (a) Real and imaginary parts of the resonator spectrum measured at junction bias voltage $V_{\text{bias}} = 300\,\mu\text{V}$. Solid black lines represent the fit to equation 2.1. (b) Reflection spectrum close to resonance frequency shown in complex plane. The off-resonant point P is shown in red.

The resonance data outline a circle in the complex plane (figure 2.4). The radius r of the resonance circle is set by the ratio of the loaded quality factor to the coupling quality factor:

$$r = \frac{Q_l}{|Q_c|}. \tag{2.2}$$

However, before obtaining the two quality factors, the rescaling of the data due to the measurement setup needs to be taken into account. Rescaling parameters a and α are determined from the position of the off-resonant point P. As seen from equation 2.1, the point $P = 1$ is the invariant of the resonator model. When the frequency is far from resonance, it falls on the resonance circle regardless of the parameters Q_c, Q_l or ϕ. Thus, its position in the complex plane is fixed by a and α.

To find the off-resonant point, a circle is fitted to the data. The data is then translated so that the centre of the resonance circle is at the origin, and the unwrapped phase of the translated data is fitted to

$$\theta(\omega) = \theta_0 + 2\arctan\left(2Q_l\left(1 - \frac{\omega}{\omega_1}\right)\right) \tag{2.3}$$

From the fit, we extract the resonance frequency ω_1, loaded quality factor Q_l, and the offset phase θ_0. The off-resonant point P is then determined from:

$$P = x_c + r_0\cos(\beta) + i(y_c + r_0\sin(\beta)) \tag{2.4}$$

where x_c, y_c, and r_0 are resonance circle parameters, and $\beta = ((\theta_0 - \pi) \mod 2\pi) - \pi$. The environment loss and phase shift are given by $a = |P|$ and $\alpha = \arg(P)$. This procedure is done once, and parameters a, and α are fixed for all the measurements, as they depend only on the microwave measurement chain.

After the off-resonant point is determined, the data are rescaled so that $P = 1$, and another circle fit is performed. Now that the data is in its canonical form, the coupling quality factor is given by the radius of the fitted circle r_0:

$$Q_c = \frac{Q_l}{r_0} \tag{2.5}$$

and the internal quality factor is

$$Q^{-1} = Q_l^{-1} - Q_c^{-1} \tag{2.6}$$

The coupling loss rate κ_c is given by $\kappa_c = \omega_1/Q_c$, while the other losses are given by $\kappa = \omega_1/Q$. A typical fit is shown in figure 2.4a.

Loss rates bias dependence

The loss rates extracted using the fitting procedure outlined above on the data shown in figure 2.2 are shown in figure 2.5. In terms of the extracted loss rates, the equation 1.72 can be rewritten as:

$$S_{11} = 1 - \frac{\kappa_c}{\frac{\kappa+\kappa_c}{2} + i(\omega - \omega_1)} \tag{2.7}$$

where κ_c is the coupling loss, while κ describes all the other losses present in the system. The coupling loss rate is weakly dependent on the junction bias, and its value is $\kappa_c = 2\pi \times 71\,\mathrm{MHz}$. The other loss rate κ is constant below the gap. At bias voltage $eV = 2\Delta - \hbar\omega_1$ it rises from $2\pi \times 9.5\,\mathrm{MHz}$ to $2\pi \times 75\,\mathrm{MHz}$, and then stays constant in the bias range $2\Delta - \hbar\omega_1 < eV < 2\Delta$. This loss rate has two contributions — junction induced losses κ_j, and internal losses of the resonator κ_i:

$$\kappa = \kappa_i + \kappa_j. \tag{2.8}$$

We expect κ_j to be negligible well below the superconducting gap. Thus, we attribute this loss rate to voltage independent internal resonator losses κ_i. The bias voltage dependence of these loss rates are shown in figure 2.5b. The internal resonator loss rate is $\kappa_i = 2\pi \times 9.5\,\mathrm{MHz}$, and corresponds to the internal quality factor $Q_i = \omega_1/\kappa_i = 579$.

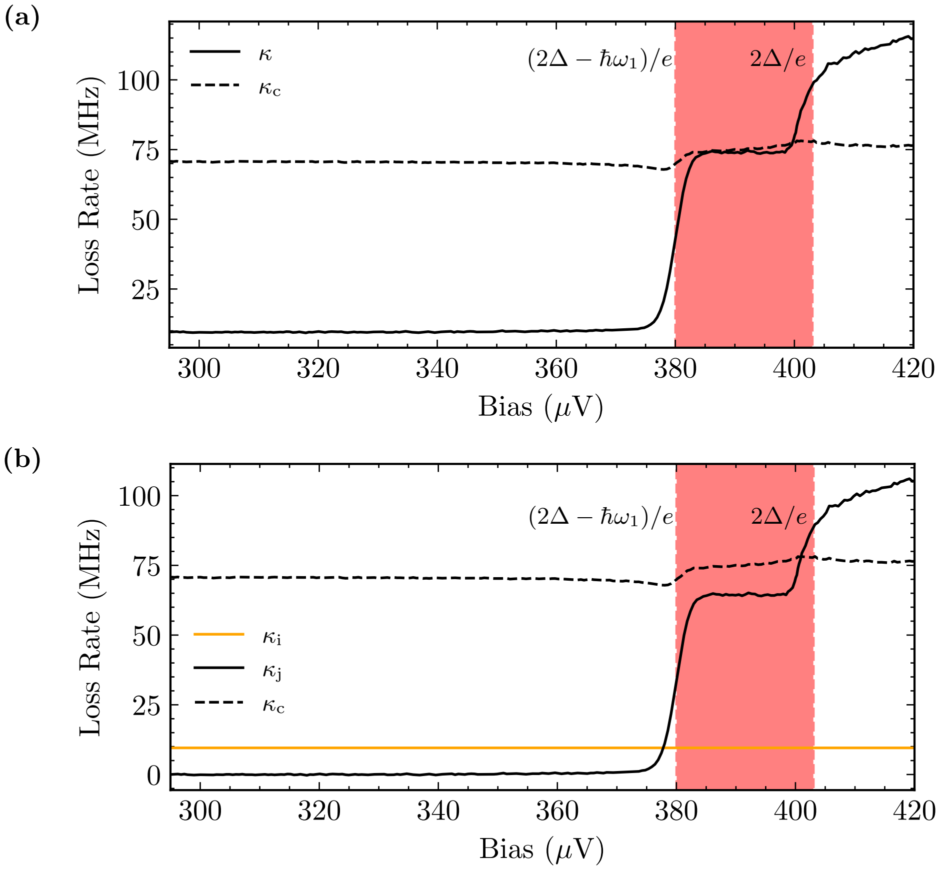

Figure 2.5: (a) Coupling rate κ_c and other losses κ as functions of junction bias voltage (b) The loss rate κ can be separated into internal loss rate of the resonator κ_i independent of bias voltage, and junction loss rate κ_j

Microwave absorption and conversion quantum efficiency

After obtaining the three resonator loss rates κ_c, κ_j and κ_i, we calculate the microwave absorption

$$1 - |S_{11}(0)|^2 = \frac{4(\kappa_i + \kappa_j)\kappa_c}{(\kappa_i + \kappa_j + \kappa_c)^2} \tag{2.9}$$

and the expected quantum efficiency of microwave photon-to-electron conversion

$$\chi = \frac{4\kappa_j \kappa_c}{(\kappa_i + \kappa_j + \kappa_c)^2}. \tag{2.10}$$

The absorption probability and quantum efficiency for different junction biases are shown in figure 2.6. Inside the gap, the absorption is approximately 0.4 due to the internal resonator losses. For voltages $eV > 2\Delta - \hbar\omega_1$, where the photo-assisted quasiparticle tunneling is allowed, absorption increases to unity. At the same bias voltage, the quantum efficiency rises from 0 to 0.85. Especially, over the whole bias voltage range $eV \in [2\Delta - \hbar\omega_1, 2\Delta]$, we expect quantum efficiency $\chi > 0.85$. Above $eV = 2\Delta$, the conversion efficiency stays high, however the large current flowing though the junction due to the elastic process makes this range unusable for photon-detection.

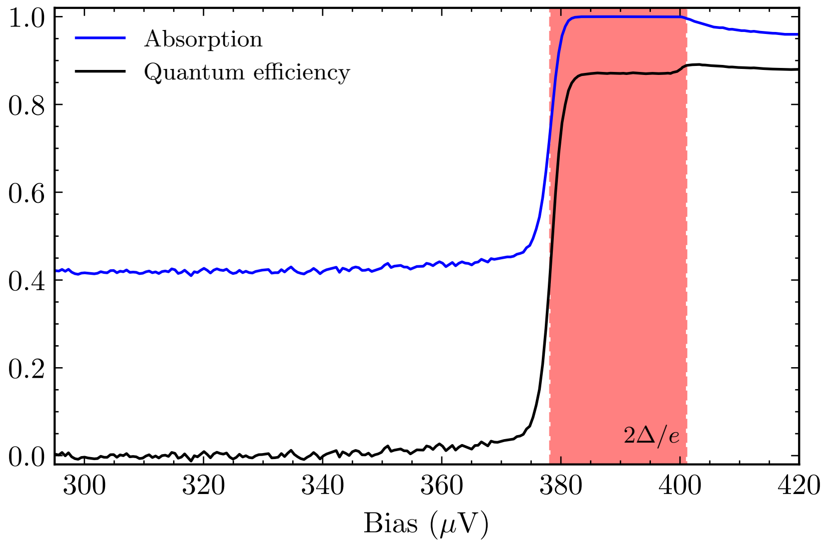

Figure 2.6: Absorption given by equation 1.74 (blue) and expected quantum efficiency given by 1.78 (black) as functions of junction bias. The range of voltage biases suitable for photon detection experiments, characterized by high quantum efficiency and low dark count, is shaded in red.

2.1.2 Resonator Loss Rates at High Excitation Power

The cavity reflection spectra change when the applied microwave power is increased due to the appearance of multi-photon processes. To highlight the multi-photon absorption, we compare the reflection spectra as function of junction bias voltage for two different powers: $P = -138\,\mathrm{dBm}$ and $P = -118\,\mathrm{dBm}$ in figure 2.7, These two powers correspond to mean resonator populations $\langle n_{\mathrm{res}} \rangle = 0.016$ and $\langle n_{\mathrm{res}} \rangle = 1.6$ respectively when the junction is biased well below the superconducting gap. At higher resonator population, additional absorption is present below the gap.

The bias voltage threshold for a process where n photons are absorbed per tunneling event is

$$eV > 2\Delta - n\hbar\omega_1 \tag{2.11}$$

Therefore, we expect the subgap absorption to appear as a series of steps. The junction loss rate and coupling rate as function of bias voltage for the two excitation powers cited above, extracted from the reflection spectra fits, are presented in figure 2.8. The dashed lines in the figures correspond to junction voltages $eV = 2\Delta - n\hbar\omega_1, n = 0, 1, 2, 3$. When the mean resonator population is on the order of unity, tunneling processes involving several photons are distinguishable in the junction loss rates. These processes cause reduction of detection efficiency as the incident microwave power increases, and lead to the saturation of the detector. Additionally, a small change in the coupling rate is observed close to the superconducting gap.

2.2 Photo-assisted Tunneling Current

With the help of spectroscopy measurements, we have demonstrated the high photon absorption when the junction is biased just below the superconducting gap. The quantum efficiency of photon-to-electron conversion is predicted to be high in this bias voltage range.

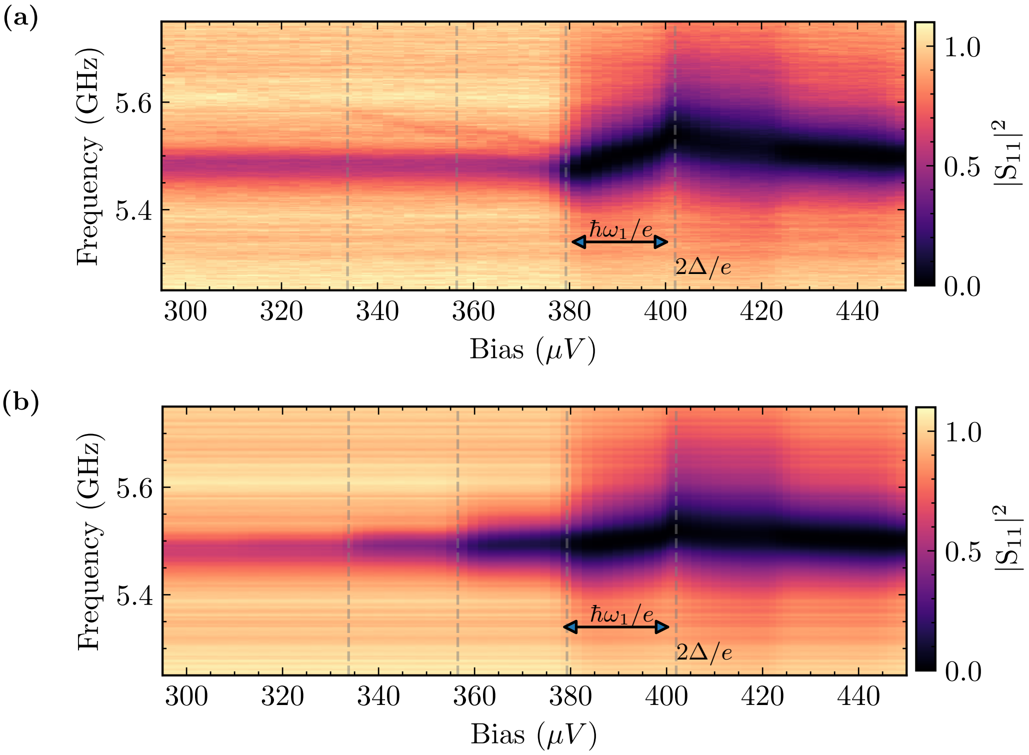

Figure 2.7: Resonator spectra as function of junction bias for two different microwave excitation powers. (a) $P = -138\,\mathrm{dBm}$ (b) $P = -118\,\mathrm{dBm}$

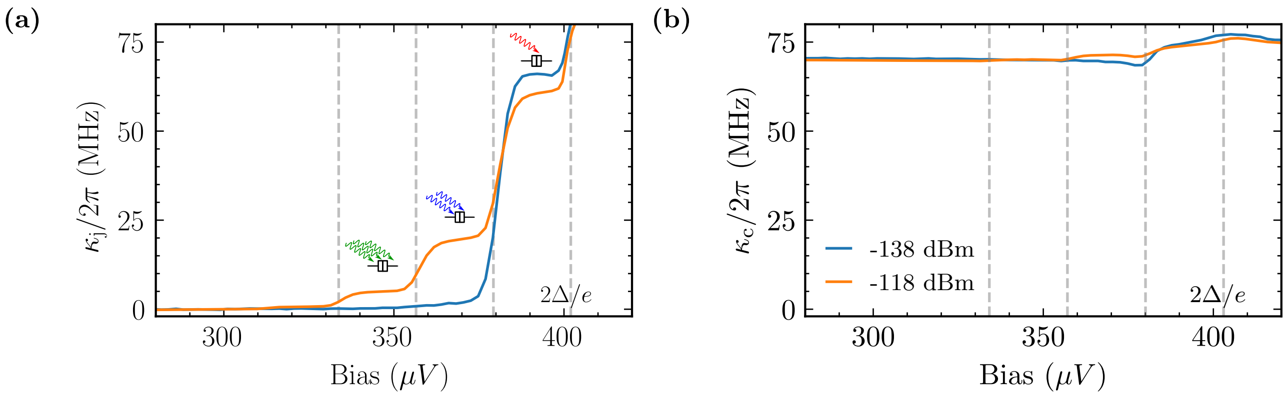

Figure 2.8: (a) Junction loss rate (b) Coupling rate as function of junction bias voltage for different microwave excitation power. Grey dashed lines correspond to voltages $eV = 2\Delta - n\hbar\omega_1, n = 0, 1, 2, 3$

We now turn to measuring the current response of our detector to coherent excitation, in order to confirm that the photon absorption results in charge flowing through the junction. We present the photo-assisted current measurements as function of microwave pumping strength and frequency, and devise a calibration method that relies on these measurements. We use the calibration procedure to verify the detector quantum efficiency estimate obtained from reflection spectroscopy.

The current flowing though the junction is measured by monitoring the voltage drop across a $R_\mathrm{meas} = 51\,\mathrm{k\Omega}$ resistor connected in series with the sample (see figure 2.1). We keep the microwave setup fixed across all our measurements, and use the VNA as a room temperature microwave source. The VNA calibration is verified by measuring its output power (see Chapter 3). Unless otherwise mentioned, the pump frequency corresponds to the resonator frequency well below the superconducting gap. The microwave power cited is always the one at the sample, and is estimated using the calibration presented in section 2.3.1.

The current flowing through the junction as a function of voltage bias below the superconducting gap for different microwave pumping powers is shown in figure 2.9. We notice a plateau in subgap current (blue curve in figure 2.9). The width of the plateau is $\hbar\omega_1/e$, as expected for a photo-assisted tunneling process. As the pumping strength rises further (figure 2.9), one notices two steps, and eventually three steps in the current below the superconducting gap. As discussed earlier, these steps correspond to multiphoton tunneling processes. We will use their non-linear evolution with power to calibrate our photodetector. But firstly, we discuss the single photon process in more detail.

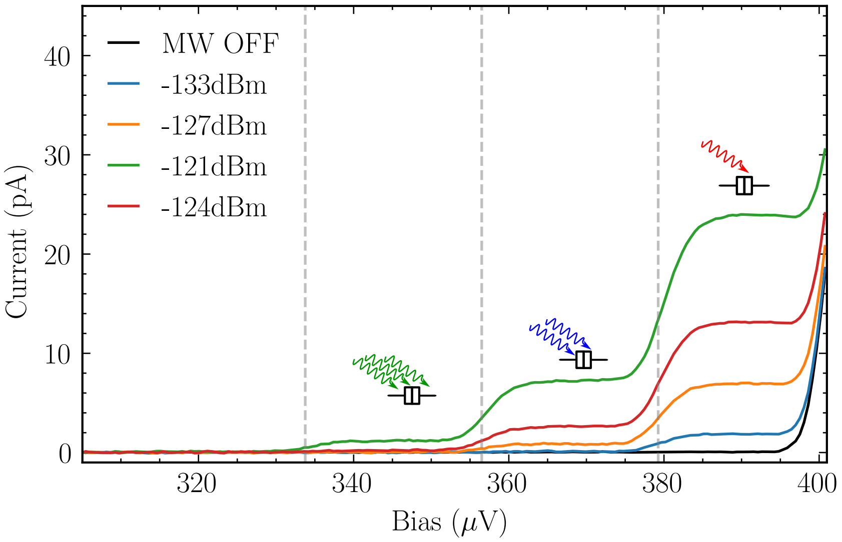

Figure 2.9: Current through the junction as function of bias voltage for different microwave pumping powers. Grey dashed lines represent bias voltages $eV = 2\Delta - n\hbar\omega_1, n = 1, 2, 3$, and represent the energy thresholds for processes involving the absorption of n photons per tunneling event.

2.2.1 Single Photon Process

For low microwave power, the photons absorbed by the junction result in an inelastic tunneling current in voltage bias span $eV > 2\Delta - \hbar\omega_1$. The evolution of the current with applied microwave power and frequency, and bias voltage in low power range is shown in figure 2.10. We show the photo-assisted current, i.e. the difference in current with pumping, and with no microwave drive applied:

$$I_{\text{PAT}} = I(\eta) - I(\eta = 0), \tag{2.12}$$

where η is the pumping strength. A peak in photo-assisted current at resonance frequency ω_1 (figure 2.10a) is observed. A line-cut at $\omega = 2\pi \times 5.5\,\text{GHz}$ is shown in figure 2.11. Above $eV = 2\Delta$, the photo-assisted current is negative— the rise in current due to the photon absorption is negated by the suppression of the elastic process for the excited resonator states. This phenomenon can be

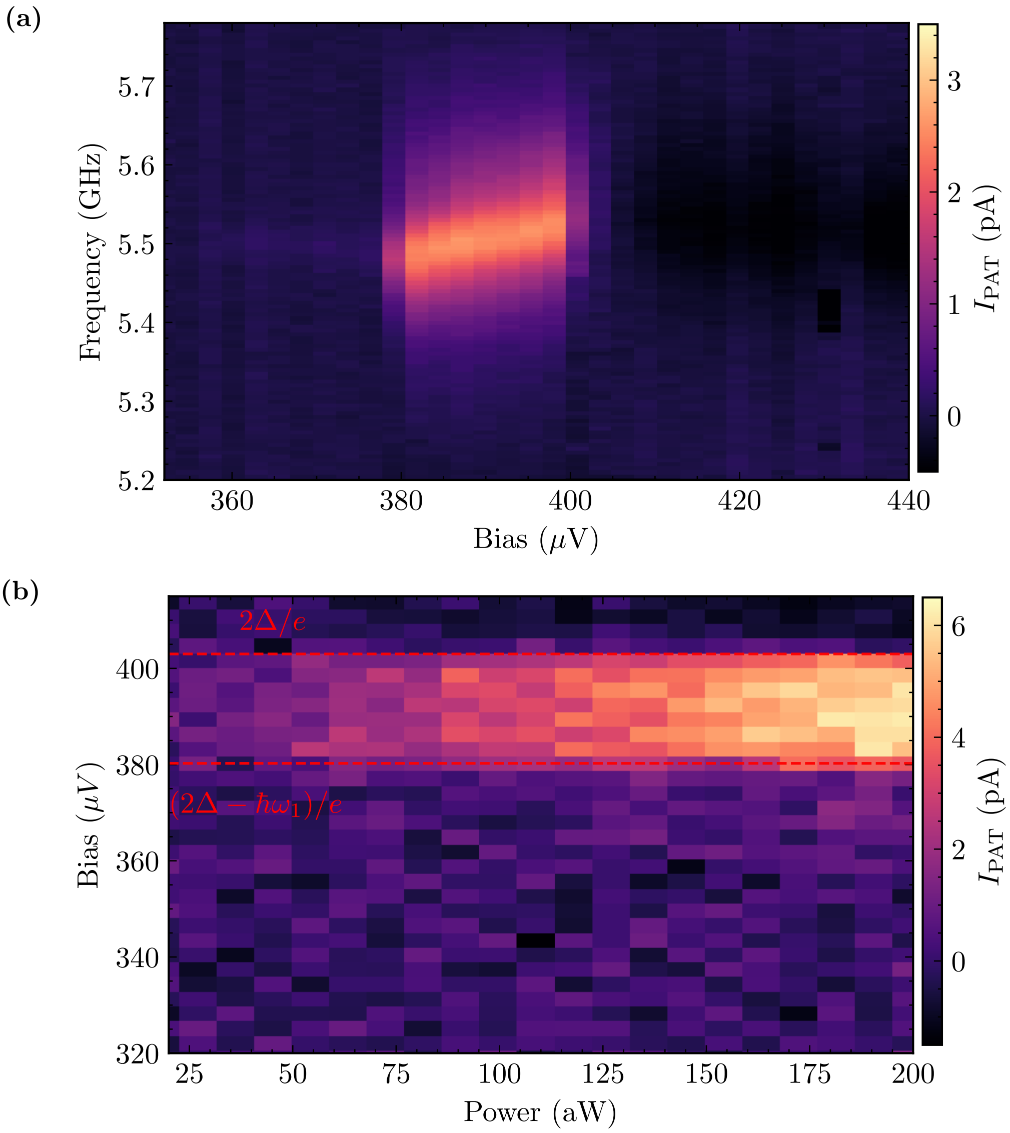

Figure 2.10: (a) Photo-assisted tunneling current as function of junction bias voltage and frequency of applied microwave drive. The excitation power is fixed to $P = -131.5\,\mathrm{dBm} = 71\,\mathrm{aW}$ (b) Photo-assisted tunneling current as function of junction bias voltage and applied microwave power. The excitation frequency is fixed to $\omega_1 = 5.5\,\mathrm{GHz}$

demonstrated using the formalism derived in Chapter 1: we assume that the drive is weak, so that the state of the resonator can be described by a mixture of vacuum and the one photon Fock state. Photo-assisted current at $eV = 2\Delta + \hbar\omega_1/2$ is then:

$$I_{\mathrm{PAT}}(2\Delta + \hbar\omega_1/2) = \langle n_{\mathrm{res}}\rangle\kappa_{1,0}e + (1 - \langle n_{\mathrm{res}}\rangle)\kappa_{0,0}e + \langle n_{\mathrm{res}}\rangle\kappa_{1,1}e - \kappa_{0,0}e. \tag{2.13}$$

The first term represents the photo-assisted process, while the next two terms are the elastic processes corresponding to two lowest resonator states. The last term represents the current without any microwave drive. The emission processes are energetically forbidden. Inserting the corresponding rates (equation 1.30), and assuming that $I(2\Delta + 3\hbar\omega_1/2) \approx I(2\Delta + \hbar\omega_1/2)$, where $I(V)$ is the

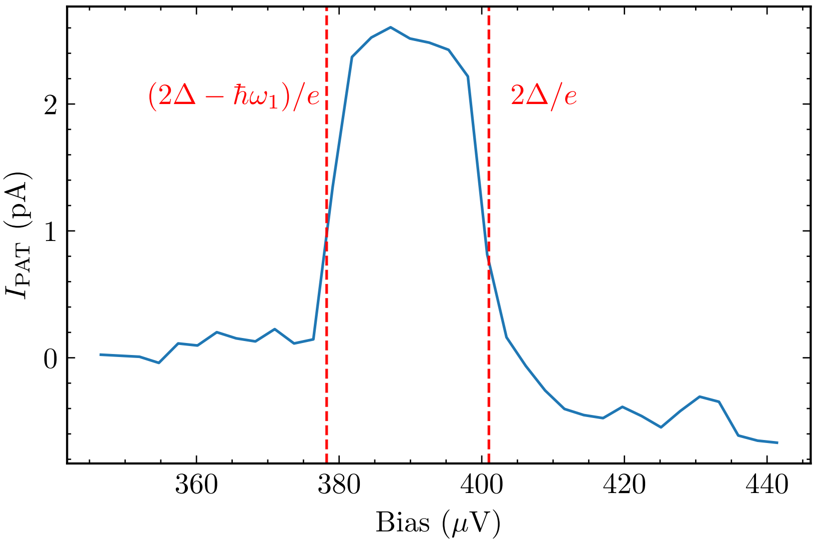

Figure 2.11: Photo-assisted current as function of junction bias for excitation power $P = -131.5\,\mathrm{dBm}$ and frequency $\omega = 2\pi \times 5.5\,\mathrm{GHz}$. PAT current is maximal for $eV \in [2\Delta - \hbar\omega_1, 2\Delta]$. Above the superconducting gap, the photo-assisted current is negative.

current-voltage characteristic of the junction in absence of the environment, we get

$$I_{\mathrm{PAT}}(2\Delta + \hbar\omega_1/2) = \langle n_{\mathrm{res}}\rangle \lambda^2 e^{-\lambda/2}(\lambda^2 - 1) I(2\Delta + \hbar\omega_1/2) \tag{2.14}$$

where λ is the coupling parameter. Indeed, for $\lambda < 1$, corresponding to our experiment, $I_{\mathrm{PAT}} < 0$ holds. To get the quantitative agreement with the experimental data, the PAT current needs to be calculated from the quantum master equation 1.49.

For fixed drive frequency, the photo-assisted current rises with microwave power (figure 2.10b). The measured photo-assisted current junction bias dependence has a step-like structure, in agreement with the expectations.

To probe the subgap current in more detail, we set the junction bias voltage to $V = (2\Delta - \hbar\omega_1/2)/e = 391.6\,\mu\mathrm{V}$ and measure the current as function of applied power and frequency.

PAT Current frequency dependence

The drive frequency dependence is shown in figure 2.12. For the presented microwave powers, the resonator population is low enough so that the multi-photon processes are negligible. Therefore, the photo-assisted current is proportional to the resonator population, and we expect its frequency dependence to have a Lorentzian shape. We fit the trace taken at the lowest drive strength (red points in figure 2.12) to the equation:

$$I = I_{\mathrm{dark}} + I_{\mathrm{max}} \frac{(\kappa/2)^2}{(\omega - \omega_1)^2 + (\kappa/2)^2} \tag{2.15}$$

where I_{dark} is the dark current, I_{max} is the current at resonance frequency and κ specifies the width. The fit is shown in figure 2.12 (black solid line). The fit results are $I_{\mathrm{dark}} = (44.9 \pm 0.8)\,\mathrm{fA}$, $I_{\mathrm{max}} = (0.274 \pm 0.003)\,\mathrm{pA}$ and $\kappa/2\pi = (146 \pm 3)\,\mathrm{MHz}$. The fit is good and the loss rate $\kappa = \kappa_{\mathrm{tot}} = \kappa_c + \kappa_i + \kappa_j$

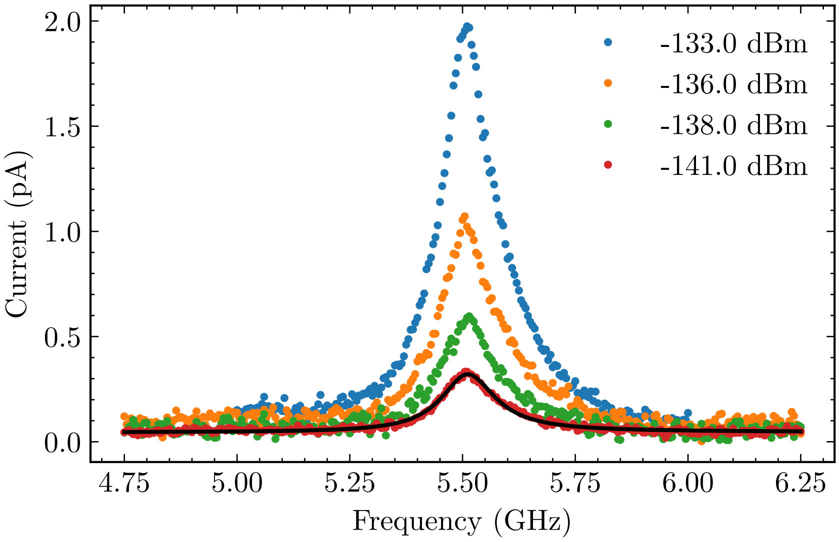

Figure 2.12: Current through the junction at $eV = 2\Delta - \hbar\omega_1/2$ as function of microwave drive frequency for different applied powers. A Lorentzian shape is observed, with peak current value increasing with rising drive power. The data corresponding to the lowest power (red points) is fitted to a Lorentzian, and the fit is shown in black solid line.

is in agreement with the VNA measurements.

PAT Current versus microwave power

To measure the evolution of current with applied power, we fix the drive frequency to resonance. The current - power data is shown in figure 2.13. For low excitation power, the current saturates at $I_{\mathrm{dark}} = 55\,\mathrm{fA}$. This value is slightly different when compared to the one extracted from the Lorentzian fit of the photo-assisted current frequency dependence. This is due to systematic uncertainties. The value of dark current is discussed in detail in section 2.4.1. When the photon flux rises, the current starts increasing linearly with power. This linear regime extends up to $P \approx -119\,\mathrm{dBm}$, corresponding to the $1\,\mathrm{dB}$ compression point of the detector. At high pump power, the current deviates from the linear behaviour as a consequence of multi-photon absorption.

2.2.2 Higher Order Processes

At $\langle n_{\mathrm{res}} \rangle \sim 1$, the multiphoton absorption processes lead to saturation of the detector, and reduced quantum efficiency. However, multiphoton processes are a useful resource for calibrating the detector. In this section, we explore these processes in more detail. Firstly, we show the measurement of photo-assisted current as function of drive frequency at different bias voltages below the gap.

Multi-photon tunneling current as function of detuning

The current is measured at four junction bias voltages given in table 2.1. These voltages correspond to values

$$eV = 2\Delta - (2n-1)\hbar\omega_1/2, n = 1,2,3,4 \tag{2.16}$$

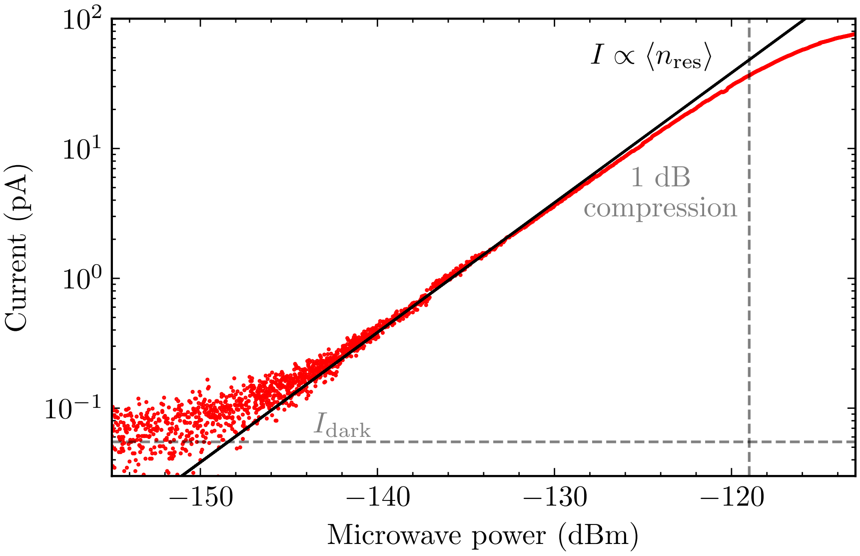

Figure 2.13: The total current flowing through the junction as a function of microwave power measured at junction bias $eV = 2\Delta - \hbar\omega_1/2$, and resonant drive. Solid black line represents the linear detector behaviour. The saturation at low excitation power is due to the dark current. At high enough pump power, the current deviates from linear behaviour due to multi-photon processes. This deviation is characterized by the 1 dB compression point (grey dashed line).

n	V (µV)
1	388
2	366
3	343
4	321

Table 2.1: Junction bias voltages corresponding to values $eV = 2\Delta - (2n-1)\hbar\omega_1/2, n = 1, 2, 3, 4$. Current measured at these values of bias voltage is shown in figures 2.14 and 2.15.

and they are chosen such that at least n photons are absorbed per tunnelling event. For each measurement, the drive power is fixed such that the current at resonance is approximately 2 pA, well below the saturation current, and higher order processes than the one considered have negligible contribution. The measurements are shown in figure 2.14. As the number of photons absorbed per tunneling event rises, the width of the current peak decreases. To estimate this width, we fit the current - frequency data to equation 2.15. Extracted widths are given in table 2.2. As discussed in the previous section, the single photon process width aligns with the resonance width at the specified voltage bias. However, for the multi-photon absorption, this is not the case. The current peak width is significantly smaller, as expected for a nonlinear process.

Additionally, we can see that for multiphoton processes, especially for three and four photon cases (figures 2.14c and 2.14d respectively), the current spectra are not Lorentzian. The fit overestimates the current at the sides of the peak. As the absorption at origin of tunneling current is due to multi-photon loss, the deviation from Lorentzian shape is expected. Instead, to accurately describe these processes, we use the master equation formalism presented in section 1.3.1.

As discussed in section 1.3, the detuning dependence of the photo-assisted tunneling current due

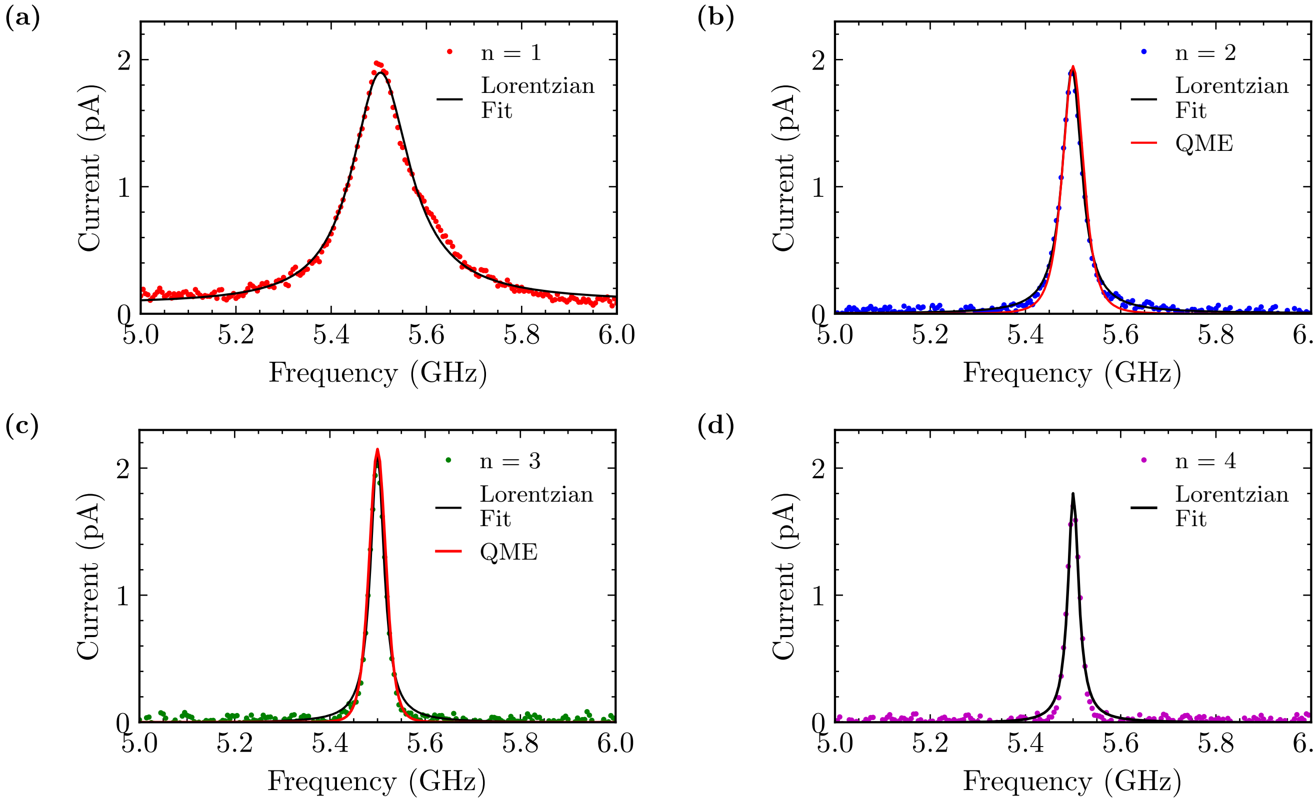

Figure 2.14: Total current flowing through the junction as function of drive frequency for junction bias voltages $eV = 2\Delta - (2n-1)\hbar\omega_1/2, n = 1, 2, 3, 4$. The Lorentzian fits for each dataset are shown in black solid lines, while the weak pumping limit solutions for $n = 2$ (equation 1.65), and $n = 3$ (equation 1.68) are shown in red solid lines in the corresponding panels.

to different absorption processes is

$$\begin{aligned}
I^{(1)}_{\text{PAT}} &= \frac{4\eta^2\kappa_j^{(1)}e}{4\delta^2 + (\kappa + \kappa_j^{(1)})^2} \\
I^{(2)}_{\text{PAT}} &= \frac{32\eta^4\kappa_j^{(2)}e}{(4\delta^2 + \kappa^2)(16\delta^2 + (\kappa_j^{(2)} + 2\kappa)^2)} \\
I^{(3)}_{\text{PAT}} &= \frac{96\eta^6\kappa_j^{(3)}e}{(4\delta^2 + \kappa^2)^2(36\delta^2 + (\kappa_j^{(3)} + 3\kappa)^2)} \\
\text{with } \kappa_j^{(n)} &= \frac{e^{-\lambda^2}\lambda^{2n}}{n!}\frac{I(2\Delta/e + (2n-1)\hbar\omega/2e)}{e}
\end{aligned} \tag{2.17}$$

where $I(V)$ is the bare current-voltage characteristic of the junction, and $\kappa = \kappa_i + \kappa_c$ is the resonator damping.

The comparison of the quantum master equation prediction and the experimental data for the detuning dependence of the current is shown in figures 2.14b and 2.14c, for the two-photon, and the three-photon absorption respectively. We have not computed the current-frequency dependence for $n = 4$, as it was too computationally intensive. The data is better described by the quantum

n	$\kappa/2\pi$ (MHz)
1	146
2	48
3	34
4	27

Table 2.2: Current versus frequency Lorentzian fit widths (figure 2.14) for different junction bias voltages

master equation theory (solid red lines) than by the Lorentzian fits shown in solid black lines.

Evolution of photo-assisted current with microwave power

We now turn to the photo-assisted current evolution with drive power. We set the detuning to $\delta = 0$ and measure the current at four junction bias voltages given in table 2.1. The photo-assisted current as function of microwave drive power is shown in figure 2.15. For low excitation power, the photo-assisted current has a constant slope in a log-log plot, corresponding to a power law behaviour, with the exponent depending on the particular process. The power law dependence is

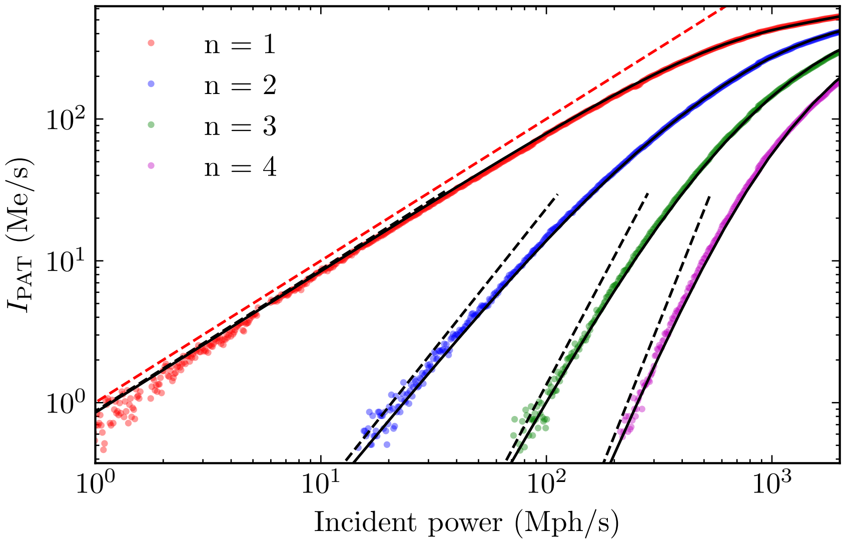

Figure 2.15: Photo-assisted tunneling current as a function of microwave power measured at junction bias $eV = 2\Delta - (2n-1)\hbar\omega_1/2, n = 1, 2, 3, 4$, and resonant drive. Dashed black lines represent the weak pumping limit quantum master equation solutions (equations 2.18 - 2.21), while the solid black lines are the predictions obtained by solving the quantum master equation numerically. The red dashed line represents the ideal photon to electron conversion, with quantum efficiency equal to one. The sample parameters are set to their ab initio values, and it is assumed that the incident power at the sample stage is known.

observed in weak pumping limit quantum master equation solutions for zero detuning:

$$I^{(1)}_{\mathrm{PAT}} = \frac{4\eta^2\kappa_j^{(1)}e}{(\kappa+\kappa_j^{(1)})^2} \tag{2.18}$$

$$I^{(2)}_{\mathrm{PAT}} = \frac{32\eta^4\kappa_j^{(2)}e}{\kappa^2(2\kappa+\kappa_j^{(2)})^2} \tag{2.19}$$

$$I^{(3)}_{\mathrm{PAT}} = \frac{96\eta^6\kappa_j^{(3)}e}{\kappa^4(3\kappa+\kappa_j^{(3)})^2} \tag{2.20}$$

$$I^{(4)}_{\mathrm{PAT}} = \frac{512\eta^8\kappa_j^{(4)}e}{3\kappa^6(4\kappa+\kappa_j^{(4)})^2} \tag{2.21}$$

We have added the solution for bias voltage $eV = 2\Delta - 7\hbar\omega_1/2$, which was calculated only for $\delta = 0$. By examining the master equation solutions, we note that $I^{(n)}_{\mathrm{PAT}} \propto \eta^{2n} \propto \phi^n$, where ϕ is the incident photon flux, reproducing the power law behaviour.

The weak pumping limit quantum master equation solutions are shown in black dashed lines in figure 2.15. The sample parameters are fixed to their ab initio values. Detailed calculation of these parameters is given in Chapter 3. Junction-resonator coupling parameter $\lambda = 0.785$ is calculated using the transfer matrix method. Resonator damping rate $\kappa = \kappa_c + \kappa_i = 2\pi \times 80.5\,\mathrm{MHz}$ is taken from the microwave spectroscopy measurements. The effective junction resistance is $R_{\mathrm{T}} = 1.75\,\mathrm{M\Omega}$, and the pumping strength η is calculated based on the calibration procedure presented in section 2.3. Comparing them to the experimental data, we note that the weak pumping limit is experimentally accessible only for the first-order process (red points). Thus, if we want to reproduce the current due to multiphoton absorption, we need to solve the master equation 1.49 numerically.

To solve the master equation 1.49 for an arbitrary microwave drive power, we use the python QuTiP library [64, 65]. Resulting calculations for the ab initio sample parameters are shown in solid black lines in figure 2.15. There is an excellent agreement between the data and theory over the whole range of applied drive power, confirming the good understanding of photon-to-electron conversion in our system.

In the calculations presented in this section, the incident power at the sample stage is treated as a free parameter, and a fit to the experimental data is performed. Fitting the four photo-assisted current measurements over the wide pump power range allows us to determine the incident power at the sample with low uncertainty. We discuss this fitting procedure in detail in the following section.

2.3 Power Calibration

Until now, we have assumed that the incident microwave power at the sample is known. In this section, we present the calibration procedure used to determine the attenuation between the room temperature microwave source and the sample, which is then used to calculate the pumping strength. The calibration is based on fitting the photo-assisted current to the master equation model. We then compare the results to other calibration methods commonly used throughout the literature.

2.3.1 Current-Power Dependence Calibration

As mentioned in the previous section, after fixing the sample parameters, the remaining quantity needed to be determined to solve the master equation is the pumping strength $\eta = \sqrt{\phi/\kappa_c}$, where ϕ is the photon flux. The flux is reduced by an unknown factor A, representing the attenuation between the microwave source and the sample. One possible method of obtaining A is fitting the photo-assisted current calculated from the quantum master equation 1.49 to the experimental data. From the weak pumping limit solutions (equations 2.18–2.21), the photo-assisted current at junction bias voltage $eV = 2\Delta - (2n-1)\hbar\omega_1/2$ is proportional to η^{2n}. As $A \propto \eta^2$, fitting the four current versus microwave power traces is equivalent to fitting A, A^2, A^3 and A^4 simultaneously with only one free parameter, allowing us to precisely determine A. In all calculations, the resonator Hilbert space is truncated to 20 photons, and the microwave power range used in fitting is restricted such that the mean resonator population is $\langle n_{\text{res}} \rangle < 5$. The resulting fit is shown in figure 2.15 (solid black lines). There is excellent agreement between the measured data and the quantum master equation fit with attenuation A being the lone free parameter in this fitting procedure. The result of the fit is $A = 106.97\,\text{dB}$. Once the attenuation between the microwave source and the sample is determined, the quantum efficiency can be directly obtained from the linear increase of the photo-assisted tunneling current with photon flux. The obtained quantum efficiency is $\chi = 0.83$. This quantum efficiency is in agreement with our predictions based on spectroscopy measurements.

Quantum Efficiency Error Estimation

The statistical error in the attenuation estimated using the fitting procedure outlined in the preceding section is negligible. The main source of error are the systematic errors that enter the calibration procedure. Especially, it is not possible for us to determine the effective tunneling resistance R_{T} with high precision, as it includes the dynamical Coulomb blockade effects of the higher modes. The properties of higher resonator modes cannot be determined experimentally, and we have to rely on the transfer matrix model calculations.

In order to estimate the uncertainty in quantum efficiency, we let the coupling parameter λ and effective resistance R_{T} be free parameters in the calibration procedure. For each value of λ and R_{T}, we calculate the photo-assisted current, and repeat the fitting procedure described in the previous section to obtain the optimal attenuation. Then, we calculate the reduced residual sum

$$\chi_r^2(\lambda, R_{\text{T}}) = \frac{\sum (I_{\text{PAT}}^{\text{exp}} - I_{\text{PAT}}(A_{opt}, \lambda, R_{\text{T}}))^2}{N_{DOF}} \tag{2.22}$$

for each fit. The number of degrees of freedom N_{DOF} is calculated by subtracting the number of free parameters in the fitting procedure from the number of points in the experimental dataset. The optimal parameters are chosen by minimizing the residual sum. By using this fitting procedure, we obtain $\lambda = 0.76$, $R_{\text{T}} = 1.90\,\text{M}\Omega$ and $A = 106.7\,\text{dB}$ resulting in quantum efficiency $\chi = 0.79$. The reduced residual sum as function of λ and R_{T} is shown in figure 2.16. With the three free parameters, the reduced residual sum is below 2, indicating that it can be used to estimate the error bar on the fit parameters. The standard deviation of attenuation results in the region satisfying

$$\chi_r^2 < 2\min(\chi_r^2) \tag{2.23}$$

(red ellipse in figure 2.16) determines the 1σ error bar. Finally, we get for the attenuation between

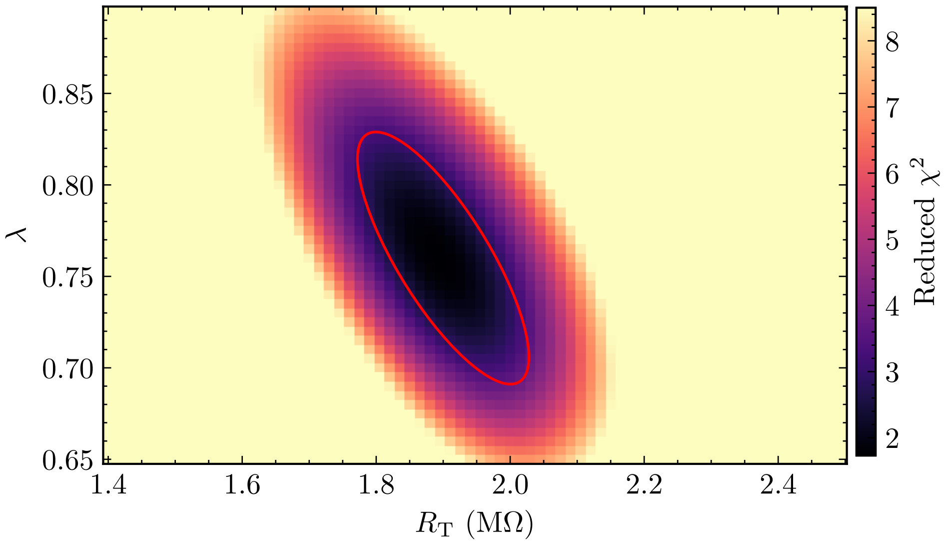

Figure 2.16: Reduced residual sum as function of junction-resonator coupling and junction resistance. The red ellipse encircles the region where χ_r^2 stays below two times its minimal value, and is used to determine the standard error in attenuation.

the microwave source and the sample

$$A = (107.0 \pm 0.3)\,\mathrm{dB} \tag{2.24}$$

resulting in quantum efficiency

$$\chi = (0.83 \pm 0.05). \tag{2.25}$$

2.3.2 Other Calibration Methods

We now compare the calibration method presented in the previous section to other commonly used methods.

Cable attenuation estimate

A crude calibration method consists of estimating the attenuation of every microwave component and cable in the RF chain to obtain the total attenuation. This means directly measuring the attenuation or gain of all room temperature components, such as cables and amplifiers. Gain of the low temperature amplifier is also directly measured. Attenuators are considered to be at their nominal value. Circulator insertion loss is taken from the datasheet, while the diplexer loss was measured at room temperature. All this, together with a reference VNA trace away from resonance, can be used to determine the total attenuation of microwave cables inside the fridge. This includes the total attenuation of input and measurement lines. We suppose that input and output lines are identical, and assume for the attenuation of the input line half of this measured value. Putting together all the measurements, we obtain $A = 106\,\mathrm{dB}$. The value is only 1 dB lower than the value extracted using the quantum master equation fit. This method relies on many assumptions, and cannot be considered reliable. Additionally, the uncertainty in the determined attenuation is not easy to quantify.

Shot noise calibration

Another calibration method relies on measuring the junction current shot noise power spectral density. At voltage bias values high above the superconducting gap, the junction exhibits ohmic behaviour, meaning that the current through the junction is proportional to bias voltage. In this regime, the shot noise power emitted by the junction in a bandwidth BW centered around the resonance frequency is [33]

$$P = \frac{4\lambda^2 \kappa_c \hbar\omega_1}{e(\kappa_c + \omega_1 \lambda^2 R_\mathrm{N}/\pi R_\mathrm{K})} I(V - \hbar\omega_1/e) \times BW \tag{2.26}$$

where R_N is the normal state resistance of the junction. This is also predicted by the master equation calculations (see section 4.3.2).

We measure the emitted power in a 5 MHz bandwidth around resonance for junction bias voltages between 1.3 mV and 1.8 mV. As expected, the emitted power is directly proportional to bias voltage, and by extracting the slope of this linear dependence and comparing it to equation 2.26, we extract the attenuation

$$A = (107 \pm 1)\,\mathrm{dB} \tag{2.27}$$

This is compatible with the results obtained using two previously discussed calibration methods. During the measurement, it was noticed that a very high junction bias is needed for the junction to exhibit linear behaviour. In this bias range, the sample properties may be altered by heating, or other out-of-equilibrium effects. Therefore, although more trustworthy than just the microwave components estimate, this method is not as reliable as the current-power measurement based calibration presented above.

2.4 Detector figures of merit

We have measured the photo-assisted current and shown that our photo-detector has quantum efficiency near unity, limited by the internal quality factor of the grAl cavity. However, in order for the detector to be of practical use, there are additional properties that need to be considered. In this section, we show the measurements of these detector figures of merit.

2.4.1 Dark current

To determine the dark current, we measure the current flowing through the junction as function of bias voltage at base temperature of the experiment, and without any microwave drive. The measurements are shown in figure 2.17 The measured dark current in the bias voltage range $eV \in [2\Delta - \hbar\omega_1, 2\Delta]$ is

$$I_\mathrm{dark} = (55 \pm 5)\,\mathrm{fA} \tag{2.28}$$

resulting in the dark count rate of $340\,\mathrm{ks}^{-1}$ for the bandwidth of 150 MHz. The origin of the dark current is not fully understood. However, its step-like voltage dependence indicates that the dark current is not caused by the rounding of the junction $I(V)$, but is due to a non-equilibrium population of the two lowest resonator modes corresponding to $\langle n_\mathrm{res} \rangle = 1 \cdot 10^{-3}$ and $\langle n_\mathrm{res} \rangle = 2 \cdot 10^{-4}$ at ω_1 and ω_2 respectively. Several different steps can be taken to reduce the photon population, such

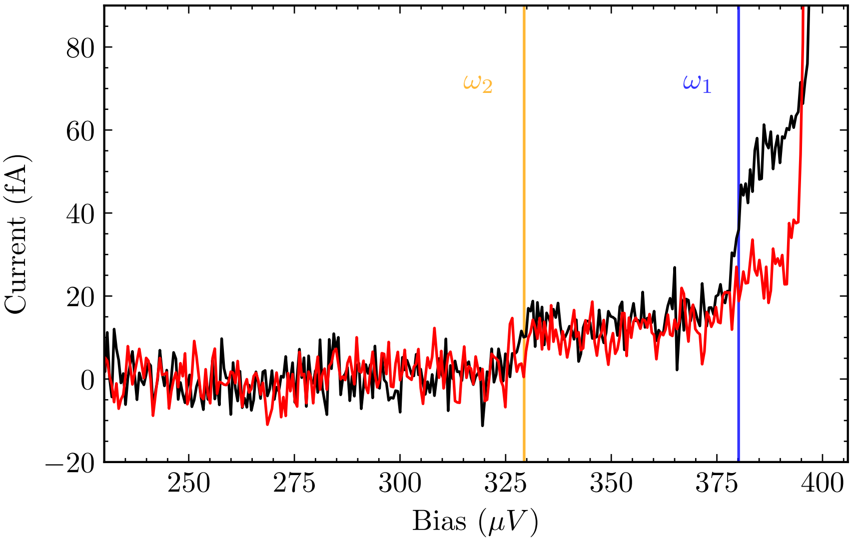

Figure 2.17: Current as function of junction bias without the microwave drive. The solid black line is the measurement taken in the same cooldown and setup as all the results presented in this chapter. Solid red line represents the measurement taken in a subsequent cooldown after sealing the sample holder with indium. The vertical lines correspond to bias voltages $2\Delta - \hbar\omega_n, n = 1, 2$

as using more shielding and filtering the lines. We show in figure 2.17 the dark current measurement using the same setup, but performed in a subsequent cooldown, after sealing the sample holder box using indium wire (red trace).

We measure a reduction in dark current to be

$$I_{\text{dark}} = (26 \pm 4)\,\text{fA}. \tag{2.29}$$

The dark current data was taken using the lock-in measurement setup outlined in section 3.1.2. To achieve the precision needed, the data was averaged over several days, and it is sensitive to fluctuations in gain, and especially voltage amplifier input impedance, for which we correct. As a confirmation of low dark current, we show the measurement taken with a high impedance voltage amplifier. The resulting data, without any corrections for amplifier impedance is shown in figure 2.18. The current just below the gap is $I \approx 300\,\text{fA}$. However, a linear current - voltage dependence can be seen below the gap. The resistance corresponding to the slope of the subgap current is greater than $2\,\text{G}\Omega$. At impedances this high, leakage currents cannot be neglected. Due to high current noise of the amplifier, the subgap impedance cannot be determined with required precision, and we use these measurements only to estimate the upper limit on the dark current.

2.4.2 Noise Equivalent Power

In addition to quantum efficiency, and dark current, noise equivalent power, as a measure of photodetector sensitivity, represents a key figure of merit. The noise equivalent power (NEP) is the incident power that can be detected with signal to noise ratio equal to unity in a bandwidth of 1 Hz. We estimate the NEP from the noise of our current measurements. The current noise for the lock-in

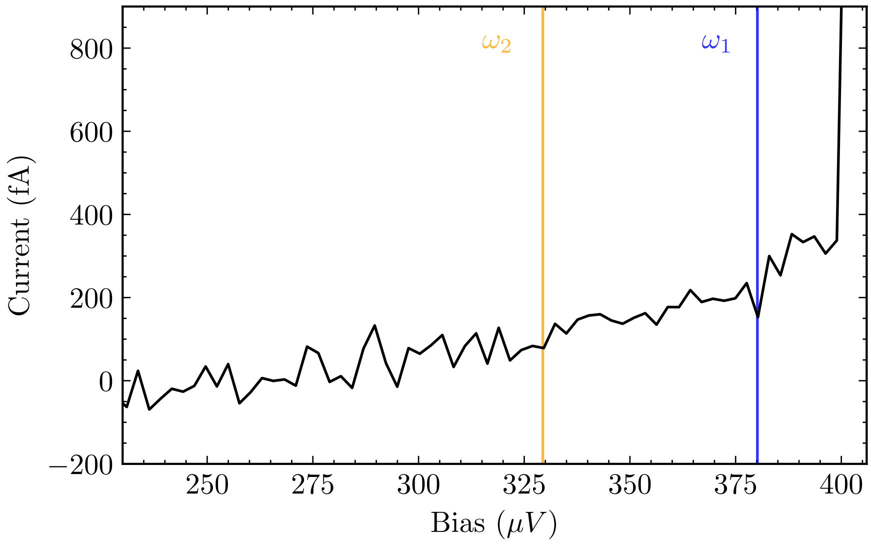

Figure 2.18: Current as function of junction bias without the microwave drive measured using the high impedance voltage amplifier. The vertical lines correspond to bias voltages $2\Delta - \hbar\omega_n, n = 1, 2$

measurement setup, is approximately $120\,\mathrm{fA}/\sqrt{\mathrm{Hz}}$. The corresponding NEP is then calculated from

$$\mathrm{NEP} = \frac{i_n}{e}\hbar\omega_1 \tag{2.30}$$

resulting in $2.7\,\mathrm{aW}/\sqrt{\mathrm{Hz}}$. This NEP is four orders of magnitude above the current state of the art detectors [27]. However, our experiment was not designed with the purpose of reaching low NEP. One could readily reduce the NEP by adapting the setup to use a low temperature HEMT amplifier [66], instead of measuring the current by monitoring the voltage drop across the resistor connected in series with the sample using a room temperature voltage amplifier. This would result in a current noise of $1\,\mathrm{fA}/\sqrt{\mathrm{Hz}}$, with the equivalent NEP of $2.3 \cdot 10^{-20}\,\mathrm{W}/\sqrt{\mathrm{Hz}}$, thus approaching the state of the art.

2.4.3 Detector Saturation

All the detector properties are calculated in the low microwave drive limit. As the microwave power increases, the detector saturates when $\langle n_{\mathrm{res}} \rangle$ is on the order of unity, and multiphoton processes can no longer be neglected (see figure 2.15). This saturation is quantified by 1 dB and 3 dB compression points. For our detector, these compression points are $P_{1\,\mathrm{dB}} = 340\,\mathrm{Mph/s}$ and $P_{3\,\mathrm{dB}} = 1\,\mathrm{Gph/s}$.

2.5 Conclusion

We have presented the measurements characterising our photon-to-electron converter. The resonator properties were determined through microwave spectroscopy. From the resonator loss rates, we estimated the photon to electron conversion quantum efficiency to be $\chi > 0.85$, which is an order of magnitude greater than in other detectors based on inelastic tunneling.

To confirm the quantum efficiency estimate, we measure the evolution of photo-assisted current with junction bias voltage and microwave drive power and frequency. These measurements are well explained by the quantum master equation formalism presented in Chapter 1, indicating good understanding of the photon to electron conversion mechanism in our device. The same formalism is used to devise the calibration procedure relying on fitting the photo-assisted current measured as function of applied microwave power to the theoretical model. This calibration yields the quantum efficiency $\chi = (0.83 \pm 0.05)$, confirming the assessment based on the microwave spectroscopy measurement.

The other detector figures of merit are also estimated. In particular, the dark electron rate is shown to be $160\,\mathrm{ks}^{-1}$.

Chapter 3

Experimental Setup and Sample Characterization

In the previous chapters, we have described the working mechanism behind our photon detector, and then experimentally characterized it through radio-frequency and DC measurements. We now give the technical details of the experiment, as well as the calculations used to extract the sample parameters given in Chapters 1 and 2.

3.1 Experimental Setup

The sample is fabricated on a silicon wafer (the fabrication details are in appendix B), and consists of a 5.5 GHz resonator terminated by a superconducting tunnel junction. The wafer is glued using PMMA to a sample holder box containing a printed circuit board. The chip is bonded to the printed circuit board using AlSi wires. The sample holder box is then tightly closed, and fixed to the mixing chamber plate of a Bluefors SD dilution refrigerator with the base temperature 20 mK. The 50 Ω microstrip transmission lines on the PCB are connected to the experimental setup through SMA ports. Images of the experimental setup are shown in figure 3.2.

The detailed schematic of the setup is in figure 3.3. It combines the dc and microwave measurement lines. Firstly, we will describe the setup used for high frequency measurements allowing us to perform reflection measurements in the 4 - 8 GHz band. Secondly, we will outline the dc setup, which we use to bias the tunnel junction, as well as to measure the current flowing through the sample.

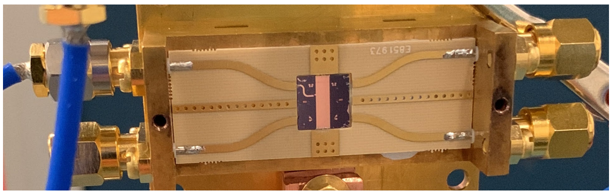

Figure 3.1: The sample holder box with the sample in the centre. The sample is bonded to the transmission lines on the printed circuit board using AlSi wires.

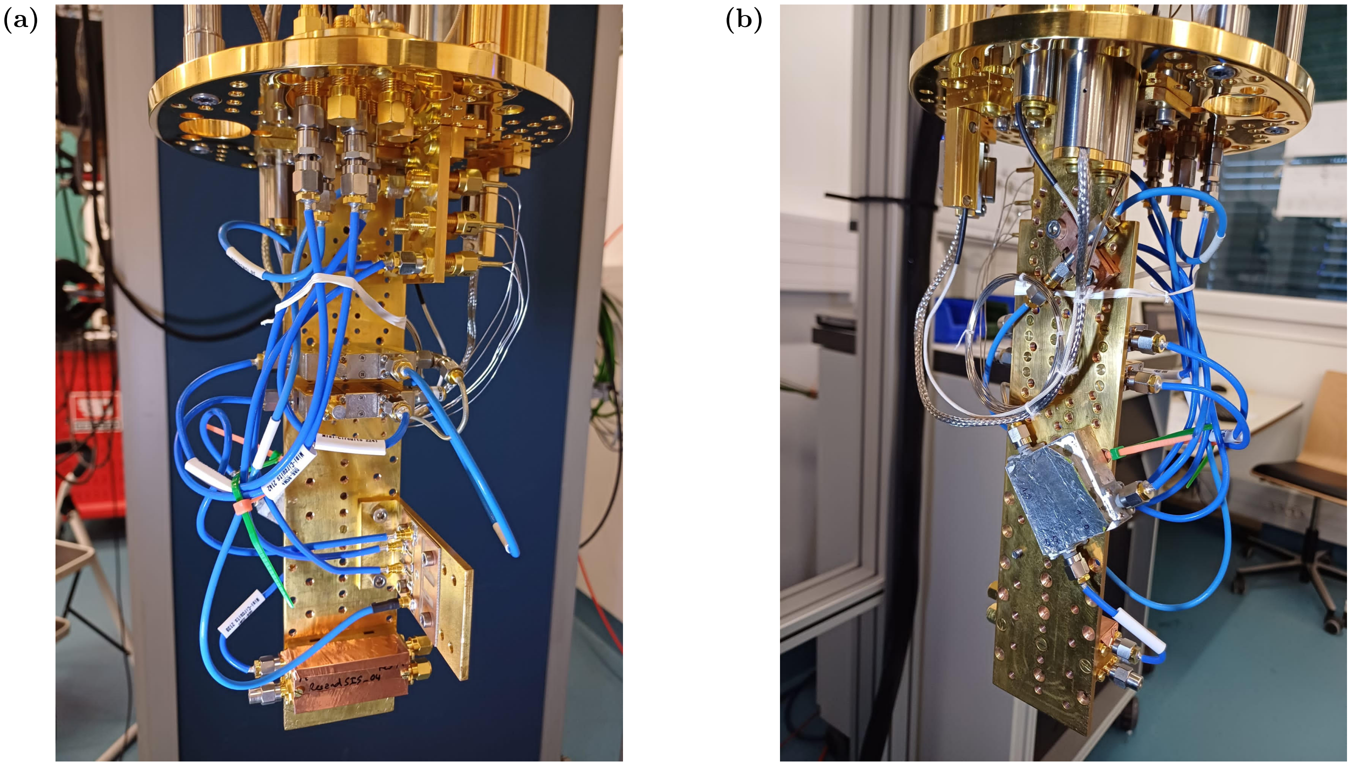

Figure 3.2: Low temperature experimental (a) Tightly closed sample holder box is in the bottom of the image. Above it, the plate containing the printed circuit board with the surface mounted biasing circuit components is visible. The biasing circuit is connected to the rest of the setup with SMPX cables. The two double circulators connected in series are fixed to the upper part of the mixing chamber plate (b) A diplexer and an attenuator are fixed to the back side of the mixing plate.

3.1.1 Microwave Setup

In figure 3.3, the microwave setup is shown in red. Both the input and detection lines are $50\,\Omega$ coaxial cables. To eliminate the unwanted thermal photons, the input line is strongly attenuated. The total attenuation of the line is $-90\,\mathrm{dB}$. We can compute the expected photon population at low temperature from the following [67]: if the attenuation at stage T_i is $A_{\mathrm{T_i}}$, then the photon number $n_{th,i}$ at this stage is given by the photon number at the previous stage $n_{th,i-1}$ attenuated by $A_{\mathrm{T_i}}$, and the photons emitted by the attenuator, which is the black body radiation at temperature T_i

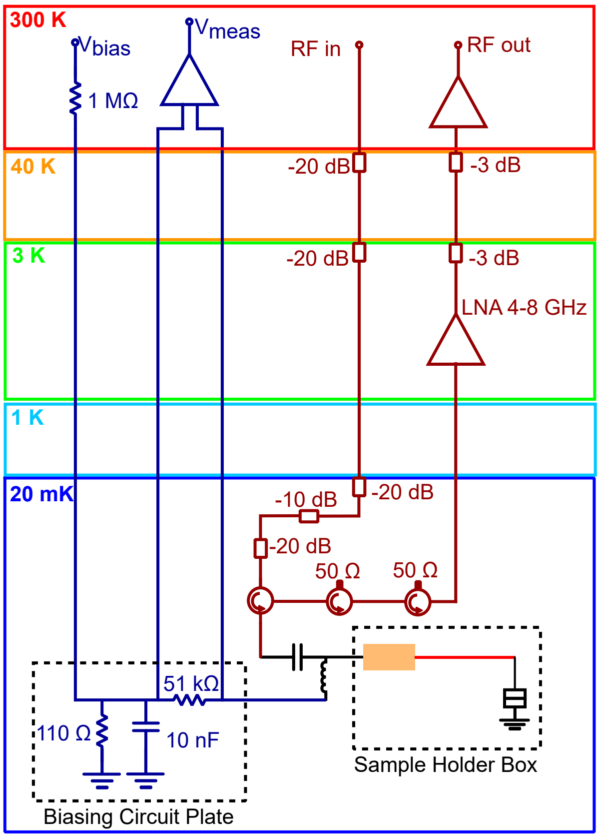

Figure 3.3: Detailed measurement setup used for photon-to-electron conversion experiments. Microwave part of the setup is shown in red, while the DC setup is in blue

scaled by $(1 - A_{\mathrm{T_i}})$. We then have

$$n_{th,i} = A_{\mathrm{T_i}} n_{th,i-1} + (1 - A_{\mathrm{T_i}}) n_{\mathrm{BE}}(T_i, \omega) \tag{3.1}$$

where $n_{\mathrm{BE}}(T, \omega)$ is the Bose-Einstein factor at temperature T, and frequency ω. By performing this calculation, we note that the majority of unwanted thermal photons come from the 1 K stage. For this reason the attenuation at 20 mK stage is -50 dB. This is realized by fixing three attenuators to the mixing chamber plate, and making sure they are properly anchored for good thermalization. From equation 3.1, we get the thermal population at resonance frequency of $n_{th} = 1.2 \cdot 10^{-4}$, and an equivalent temperature close to 29 mK.

After the microwave excitation is reflected from the sample, it is directed to the output line through a series of circulators. It is first amplified by a Low Noise Factory LNF-LNC4_8C cryogenic HEMT amplifier. The gain of the amplifier was independently measured in a separate cooldown to be 37 dB, while the noise temperature is 1.5 K. To prevent the amplifier noise from reaching the sample, we stack two double circulators in series: looking from the sample we have LNF 4 - 8 GHz double-junction circulator, with a typical isolation of 40 dB, in series with an LNF 4 - 12 GHz double-junction circulator, with 30 dB of isolation. Taking the amplifier noise as black body radiation at 1.5 K, and 70 dB of isolation, the photon number at resonator frequency at the sample stage due to the amplifier is $2.4 \cdot 10^{-6}$, which should have negligible impact on our measurements. Two -3 dB attenuators are added on the input line — at 3 K stage, and 40 K stage to eliminate standing waves in the line. At room temperature, the signal is further amplified by two Mini-Circuits ZX60-83LN-S+ low noise amplifiers in series.

Microwave spectra are measured using a Rohde&Schwarz ZVA vector network analyzer connected to RF in and RF out ports in figure 3.3. The same VNA is also used as the microwave source for photo-assisted current measurements. In these experiments we vary the microwave power by more than three orders of magnitude. We use Rohde&Schwarz FSV3000 spectrum analyzer to calibrate the VNA power over this range. This is done by connecting the output port of the VNA directly to the spectrum analyzer, and measuring the power. The results of this measurement are shown in figure 3.4. The VNA is well calibrated, but there are several jumps in power (circled in red in the figure). These jumps correspond to the change of the physical attenuation inside the VNA. By carrying out a calibration relying on data in figure 3.4, we correct for these jumps in our measurements.

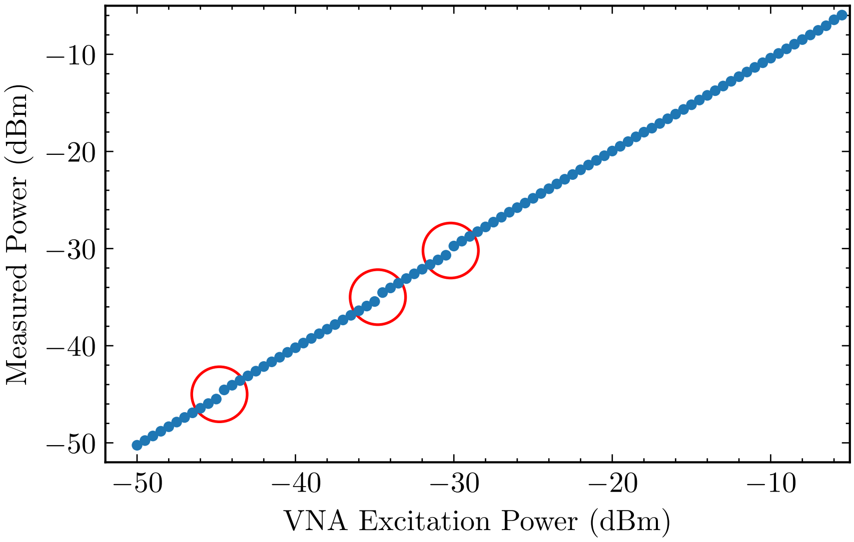

Figure 3.4: VNA power calibration measurement. The jumps in power circled in red are due to change in the internal VNA attenuators

3.1.2 Low-frequency measurement setup

Low-frequency part of the setup is shown in blue in figure 3.3. It allows us to voltage bias the junction, and measure the DC current flowing through it. The junction is biased using a voltage divider, which consists of a 1.009 MΩ resistor at room temperature, and a resistor at 20 mK. Its resistance at low temperature is measured to be 109.3 Ω by fixing the width of current steps in figure 2.9 to $V_{\text{step}} = \hbar\omega_1/e$, allowing us to precisely determine the junction bias voltage. To filter the high frequency voltage noise, we add a 10 nF capacitor in parallel with the divider resistor, making a low-pass filter with a 150 kHz cut-off.

Current through the sample is determined by measuring the voltage drop across a $R_{\text{meas}} = 51\,\text{k}\Omega$ resistor placed in series with the sample. Together with the other low temperature circuit components, this resistor is soldered to a printed circuit board, which is then anchored to the fridge by using a metal plate (see figure 3.2a). The circuit is connected to the room temperature setup using thermocoax cables. Each cable has a capacitance of $C_{\mathrm{TC}} = 1.5\,\mathrm{nF}$, and resistance $R_{\mathrm{TC}} = 170\,\Omega$. At room temperature, the voltage signal is first amplified with a differential voltage amplifier, then further amplified and filtered using a Stanford Research Systems SR560 filter, and measured with a Stanford Research Systems SR830 lock-in amplifier (see figure 3.5). We have used two differential voltage amplifiers in our experiments. The first is a home-made device based on an Analog Devices AD8421 chip. It was chosen for its low voltage noise density of $3\,\mathrm{nV}/\sqrt{\mathrm{Hz}}$ and its high input impedance greater than $1\,\mathrm{G}\Omega$. The drawback of this amplifier is its high current noise density $200\,\mathrm{fA}/\sqrt{\mathrm{Hz}}$. When both sources of noise are taken into account, we expect $\delta I = \sqrt{(200\,\mathrm{fA}/\sqrt{\mathrm{Hz}})^2 + (3\,\mathrm{nV}/\sqrt{\mathrm{Hz}}/R_{\mathrm{meas}})^2} = 210\,\mathrm{fA}/\sqrt{\mathrm{Hz}}$.

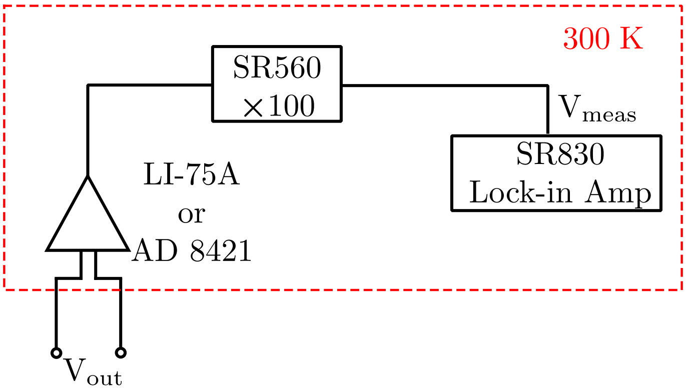

Figure 3.5: Room temperature circuit used for measuring the current flowing through the sample. The voltage V_{out} across the resistor connected in series with the sample at low temperature is first amplified by a differential amplifier. We have used two different amplifiers in our experiments: the first is based on the Analog Devices AD8421 chip, while the second one is the NF Corporation LI-75A. The signal is then further amplified by an SR560 filter with a gain of 100, and measured with a SR830 lock-in amplifier.

We also use an NF corporation LI-75A preamplifier. Both its current and voltage noise density are low, and according to the datasheet, we expect current noise density of $\delta I = 40\,\mathrm{fA}/\sqrt{\mathrm{Hz}}$, which is 5 times lower compared to the AD amplifier. For this reason we choose to use the NF LI-75A differential amplifier for all our measurements unless otherwise noted. However, its nominal input impedance is $100\,\mathrm{M}\Omega$, and must be taken into account, especially when measuring the dark current.

3.1.3 Current Measurement Chain Calibration

Measuring the amplifier impedance

Below the superconducting gap, the current flowing through the junction is small, and the LI-75A amplifier input impedance is lower than the resistance of our sample. For this reason, we measure the input impedance in a separate cooldown by replacing the sample with an open circuit, and take this impedance into account when calculating the current flowing through the sample. The measured input impedance is $Z_{\mathrm{in}} = (94.8 \pm 0.2)\,\mathrm{M}\Omega$. This amplifier input impedance fluctuates during the measurements, with a time scale of several days. To correct for this during the cooldowns with the sample, we measure a current voltage characteristic well below the gap, and use these measurements to extract the amplifier impedance.

Low frequency circuit gain calibration

The gain of the room temperature dc measurement chain shown in figure 3.5, with the LI-75A differential amplifier characterized by the nominal gain of 100, and the resistance R_{meas} at low temperature were independently calibrated. For calibrating the dc gain, we short the measurement circuit at low temperature, in place of the sample. The temperature dependence of the voltage measurement gain G_{dc} is shown in figure 3.6. The gain is close to its nominal value of 10 000, and shows good temperature stability.

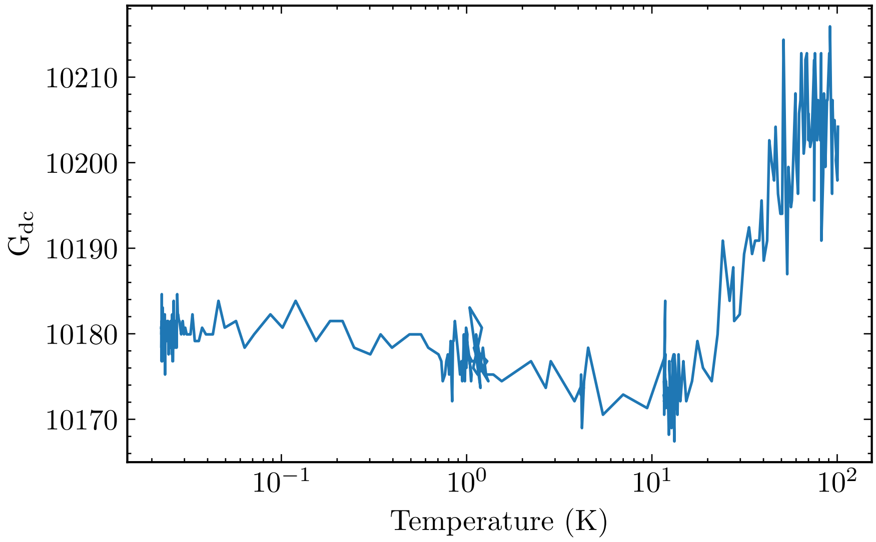

Figure 3.6: Gain of the dc measurement chain as function of temperature

To measure R_{meas}, we measure the current through the measurement circuit using a room temperature current amplifier. The current amplifier is connected to the low temperature circuit using another thermocoax cable. Using this procedure, we get $R_{\text{meas}} = (51.63 \pm 0.01)\,\text{k}\Omega$. Thus, if the voltage measured with the lock-in amplifier is V_{meas}, the current flowing through the sample is

$$I = \frac{V_{\text{meas}}}{G_{\text{dc}} R_{\text{meas}}}. \tag{3.2}$$

3.1.4 Low Frequency Circuit Bandwidth

We use two types of components that allow us to combine dc and microwave signals. First one is bias-tee, as shown in figure 3.3. Bias-tees separate the frequency bands by using an inductor in the low frequency branch, and a capacitor in the high frequency one. Bias-tees have capacitors in the range of 0.1 - 1 μF. Combined with the measurement resistor R_{meas}, this restricts the bandwidth of the circuit to $\sim$ 10 Hz, which is low. Therefore, instead of a bias tee, we use a diplexer. The diplexer used in the experiments combines signals coming from two ports: a dc to 1 GHz port, and a 1 - 8 GHz port into a single dc – 8 GHz band. The capacitance of the low frequency diplexer port is measured to be 0.1 nF. Thus, the measurement bandwidth is limited by the thermocoax capacitance C_{TC} to 2 kHz.

3.1.5 Subgap Current Measurement

The dc measurement chain characterization presented above is performed to ensure that the current measurements, especially below the superconducting gap, are precise. When no microwave drive is applied, the subgap current is expected to be small — on the order of 10 - 100 fA from the theoretical calculations. Thus, to increase the signal to noise ratio, the measurements are done in lock-in configuration. To measure the current at V_{bias}, the sample is biased by a square wave of maximum voltage V_{bias}, and the minimum value is $V_{\text{ref}} = 220\,\mu\text{V}$. The same waveform is used as the lock-in amplifier reference. Its frequency is 12 Hz. The current at the same frequency is then measured using a lock-in amplifier (see figure 3.5). By constantly switching between the measurement bias value, and the reference value V_{ref}, we eliminate the influence of amplifier gain drifts over the course of a measurement. The lock-in measures the response to a sine wave, and we account for the square wave excitation. Such a measurement using the LI-75A differential amplifier is shown in blue in figure 3.7. The sharp rise in current is observed, corresponding to the superconducting gap $\Delta = 201\,\mu\text{eV}$. Below the gap, the current rises linearly with bias voltage. This current is attributed to a leakage through the voltage amplifier, due to its low value of input impedance when compared to the junction resistance. To correct for the presence of the amplifier, we fit the current-voltage dependence between 200 and 300 µV to a linear function and extract the input impedance under the assumption that no current flows though the sample. The obtained input impedance is then fixed for all the subsequent measurements. All photo-assisted current measurements presented in Chapter 2 are subjected to this correction. The corrected $I(V)$ measurement is shown in figure 3.7 in orange.

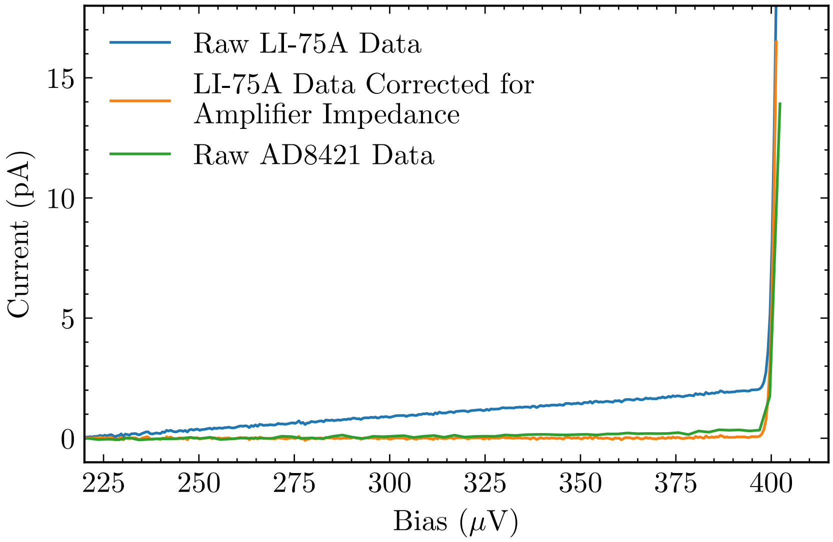

Figure 3.7: Current-voltage characteristic of the junction below the superconducting gap. The data measured with the LI-75A differential amplifier is shown in blue, while the data measured with the AD8421 based differential amplifier is shown in green. LI-75A data (blue curve) corrected for input impedance of the voltage amplifier is shown in orange.

To confirm that the subgap current is due to the leakage to the amplifier, we switch to the high impedance AD8421 based device, and measure the subgap current (green curve in figure 3.7). Indeed, the subgap current is greatly reduced.

3.2 Sample Characterisation

We now turn our attention from the experimental setup to the measurements used to evaluate the sample parameters. The sample is shown in figure 3.8. The grAl microstrip resonator is 180 µm long and 720 nm wide. It is galvanically coupled to the 50 Ω line, which can be seen in orange in the left of the picture. On the right, we see the tunnel junction, and the patch used to connect the junction to the resonator. The junction dimensions are 120 nm × 140 nm.

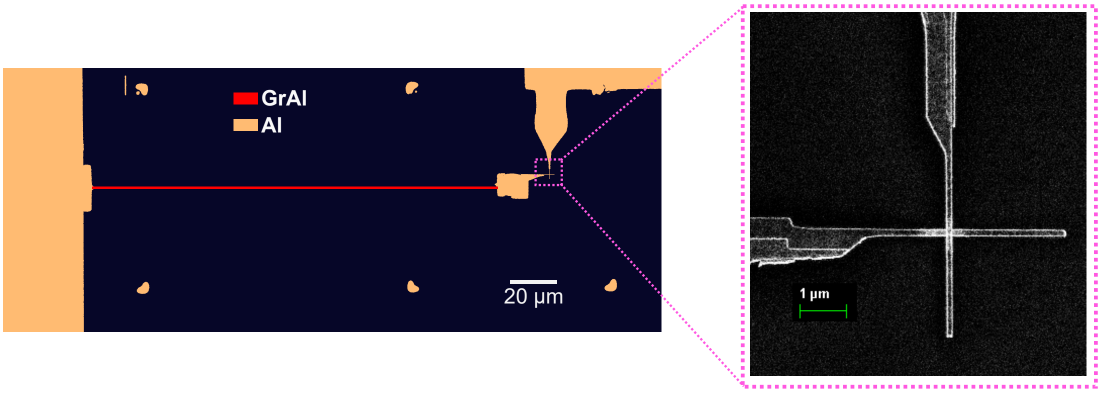

Figure 3.8: Picture of the sample. Optical picture showing the grAl resonator in red and aluminium in orange. The grAl microstrip resonator is 180 µm long and 720 nm wide. A scanning electron micrograph of the junction is shown on the right. The junction dimensions are 120 nm × 140 nm

Firstly, the mode structure of the sample is calculated using the experimental measurements and the transfer matrix model simulations. We then further characterize the fundamental resonator mode. Finally, we determine the junction parameters from dc current measurements. All the measurements were done using the setup presented in the previous section, and at 20 mK unless otherwise mentioned.

3.2.1 Mode structure

We use grAl sheet resistance measurements to evaluate the characteristic impedance of the resonator modes. To obtain the grAl sheet resistance, we measure the total resistance of the sample as function of temperature, shown in figure 3.9. The resistance of the sample is the sum of grAl nanowire and junction resistances. During the measurement, the junction was biased at 1 mV, far above the superconducting gap. At this bias, the junction behaves as a normal tunnel junction of resistance R_T at all temperatures, so we observe only the superconducting transition of grAl, close to $T = 2\,\mathrm{K}$. We take the resistance of the resonator to be the difference in total sample resistances just before this transition (labelled in blue in figure 3.9), and just after (labelled in orange). The grAl wire resistance is then $(243 \pm 3)\,\mathrm{k}\Omega$. Combined with the wire dimensions, the sheet resistance is $R_\square = (970 \pm 20)\,\Omega/\square$. From equation 1.81, we obtain kinetic inductance of $L_\square = (618 \pm 10)\,\mathrm{pH}/\square$. Granular aluminium superconducting gap is $\Delta_\mathrm{grAl} = 330\,\mu\mathrm{eV}$, measured from tunnel spectra of grAl/AlOx/Al tunnel junctions. We use this value in transfer matrix simulations.

To determine the junction capacitance, we vary it in the simulations until the model reproduces the frequencies of the two lowest modes. The fundamental mode frequency $\omega = 5.50\,\mathrm{GHz}$ is extracted from microwave measurements (section 2.1). The frequency of the second lowest mode is determined

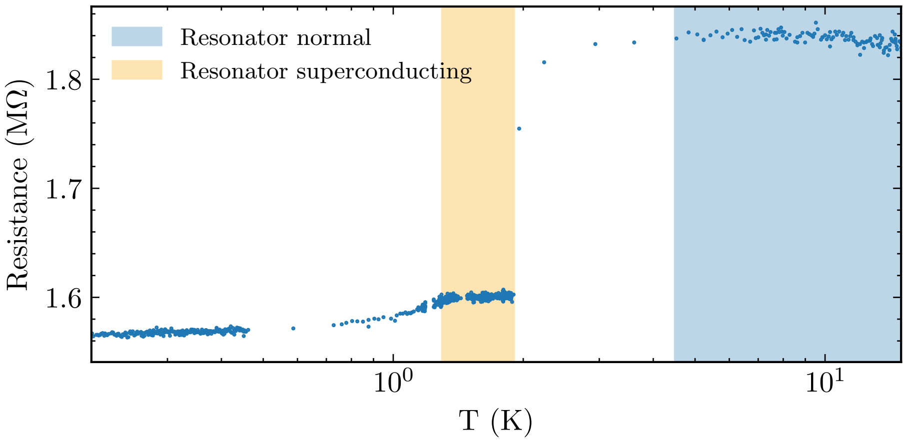

Figure 3.9: Total Sample resistance as function of temperature. We observe the superconducting transition of grAl close to $T_{c,grAl} \approx 2\,\mathrm{K}$, followed by the aluminium superconducting transition at 1.4 K characterized by a kink in sample resistance

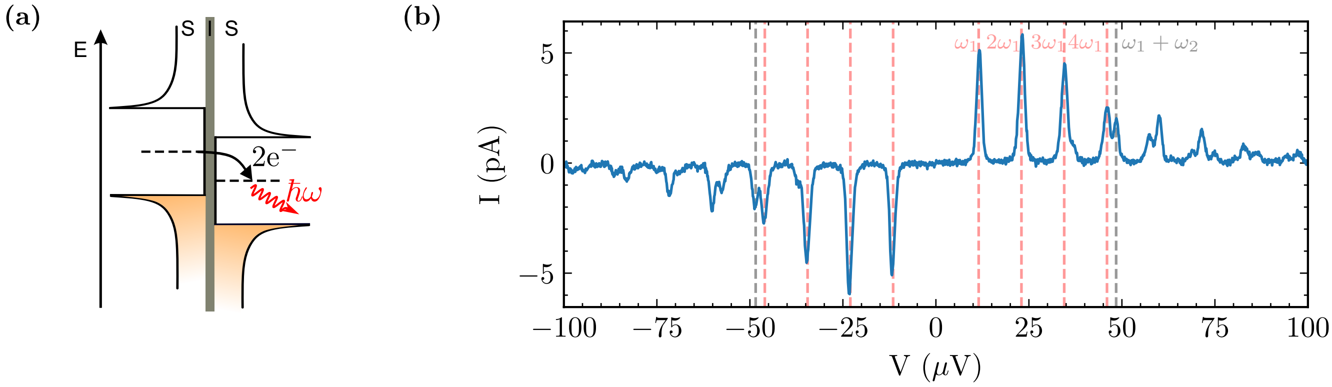

Figure 3.10: (a) Inelastic Cooper pair tunneling principle. The excess Cooper pair energy provided by the voltage bias is emitted to the resonator (b) Current - voltage characteristic of the junction close to zero voltage bias. Peaks in current due to inelastic Cooper pair tunneling are visible.

from inelastic Cooper pair tunneling. This process is depicted in figure 3.10a. The inelastic tunneling is only possible when the energy provided by the voltage bias can be emitted into resonator modes (see e.g. [47]). In figure 3.10b, we identify several peaks in current, to which we attribute the resonant conditions indicated by the dashed lines. We conclude that the frequency of the second resonator mode is $\omega_2 = 2\pi \times 17.87\,\mathrm{GHz}$. Capacitance needed in the transfer matrix calculations to reproduce the two mode frequencies is $C_\mathrm{j} = 2.6\,\mathrm{fF}$. It is compatible with the junction size, and the size of the pad used for patching the junction to the resonator.

The parameters given above are then used to calculate the resonance frequencies and spatial dependence of the modes (see appendix C). When the spatial dependence of the modes is known, the corresponding characteristic impedance is calculated from the equation 1.19. The mode structure of the sample is shown in table 3.1.

Mode	$\omega/2\pi$ (GHz)	Z_c (kΩ)	λ
1	5.52	5.09	0.79
2	17.86	0.77	0.31
3	31.56	0.20	0.16
4	45.84	0.07	0.09
5	60.37	0.03	0.06
6	75.01	0.02	0.05
7	89.71	0.01	0.04

Table 3.1: Sample modes, their characteristic impedances and coupling parameters

3.2.2 Determining the Junction Resistance

To obtain the normal state tunnel resistance of the junction, its current-voltage characteristic is measured at bias voltages $V = 1 - 2\,\mathrm{mV}$, far above the superconducting gap. In this bias voltage range, the ohmic behaviour of the tunnel junction is recovered, and the extracted resistance is $1.53\,\mathrm{M\Omega}$.

Effective junction resistance in the single mode model

In the master equation description presented in chapters 1 and 2, we have considered a single mode resonator. However, the fabricated resonator has several modes, the properties of which are given in table 3.1. As we consider only the experiments in which the fundamental resonator mode is pumped, and the junction is biased below the superconducting gap so that the tunneling processes involving photon emission are forbidden, we may assume that the higher modes stay in vacuum. The presence of these spectator modes renormalizes the tunneling rates:

$$\varkappa_{n,n+l} = \prod_{m\neq 1} \left| \langle 0| \, e^{i\lambda_m (a_m + a_m^\dagger)} \, |0\rangle \right|^2 \left| \langle n+l| \, e^{i\lambda (a+a^\dagger)} \, |n\rangle \right|^2 \overrightarrow{\gamma}(V - l\hbar\omega/e) \tag{3.3}$$

As the renormalization factor is common for all the rates, it amounts to an effective junction resistance

$$R_{\mathrm{T}} = \prod_{m\neq 1} | \langle 0| \, e^{i\lambda_m (a_m + a_m^\dagger)} \, |0\rangle |^2 \times 1.53\,\mathrm{M\Omega} = e^{-(\lambda_2^2 + \lambda_3^2 + \ldots)} \times 1.53\,\mathrm{M\Omega} \tag{3.4}$$

The effective resistance is $R_{\mathrm{T}} = 1.75\,\mathrm{M\Omega}$, and this value is used in all photo-assisted current calculations unless noted otherwise.

3.3 Conclusion

In this chapter we have discussed the setup of the experiment used to characterize our photon detector. The experiment is designed to allow measuring the microwave properties of the resonator and the dc current flowing through the junction simultaneously. Both the microwave source, and the dc measurement chain are calibrated, to ensure the precision in photo-assisted current measurements required for accurate estimation of the detector quantum efficiency and dark current.

The device parameters used for theoretical calculations in Chapter 2 were also presented. The two lowest mode frequencies of the resonator are extracted form the inelastic Cooper pair tunneling current measurements. These results are then used to determine the parameters for transfer matrix calculations, and the mode structure up to the resonator superconducting gap is obtained. The junction properties, such as the superconducting gap Δ, and normal state tunneling resistance R_{T} are deduced from its current - voltage characteristic.

Chapter 4

Thermal Photo-assisted Current and Out-of-Equilibrium Noise Spectroscopy

In this chapter, we present the response of the photon detector device described in previous chapters to thermal radiation. When the temperature is increased, the mean population of the resonator rises, resulting in a thermal photo-assisted current flowing through the junction. We measure this current, and confirm the high photon to electron conversion efficiency estimated in Chapter 2. We use the rate equation formalism to describe the current flowing through the junction, and show good agreement with the experimental data.

As a consequence of the photon absorption by the junction, the mean resonator population is expected to be lower than in thermal equilibrium when the junction is biased below the superconducting gap. Thus, the junction effectively cools down the resonator. The use of similar systems for active cooling has already been demonstrated both in theory [68], and experimentally [69, 70, 71], and it is claimed that these devices could find widespread applications in quantum technologies, e.g. in qubit initialization or reset. We probe this effect by measuring the power emitted by the sample close to resonance frequency. This allows us to calculate the evolution of mean resonator population with temperature and junction bias voltage, and quantify the effective cooling for the junction bias voltages satisfying $eV < 2\Delta + \hbar\omega_1$.

Above the superconducting gap, the inelastic processes where the quasiparticle tunnels while emitting energy into the resonator become possible. The effect of photon emission on the conductance of a junction coupled to an electromagnetic mode has been studied in numerous experiments, starting with [46], and the emitted power in such systems has also been studied in case of a normal tunnel junction [72]. We extend this to the case of the superconducting junction, and high coupling $\lambda \sim 1$, taking the junction far from equilibrium. Through input-output theory, we show that the quantity probed by measuring emission in such experiments is the population of the resonator. The mean resonator population measurements are in quantitative agreement with the rate equation predictions. Additionally, we show, theoretically and experimentally, that non thermal states in the resonator are created by the inelastic tunneling processes. We also identify a narrow bias region where emission spectrum displays a peculiar non-Lorentzian lineshape.

4.1 Thermal Photo-assisted Tunneling Current

At a temperature T, all dissipative elements of the circuit (see figure 3.3), such as attenuators, emit black body radiation. At the fundamental frequency ω_1 of the resonator, this radiation is characterized by the Bose-Einstein occupation factor $n_{\mathrm{BE}}(\omega_1, T)$. Hence, by changing the temperature of the fridge, we can tune the incident thermal radiation on the sample. We then measure the current flowing through the junction at different temperatures. Resulting current-voltage characteristics are shown in figure 4.1. As the temperature is increased, a photo-assisted current appears below the gap. At low enough temperature, there is only one step in bias voltage span $V \in [2\Delta - \hbar\omega_1, 2\Delta]$, corresponding to the one photon inelastic tunneling process. When the temperature is raised further, more steps emerge, and above 300 mK, inelastic current due to two and three photon processes is visible.

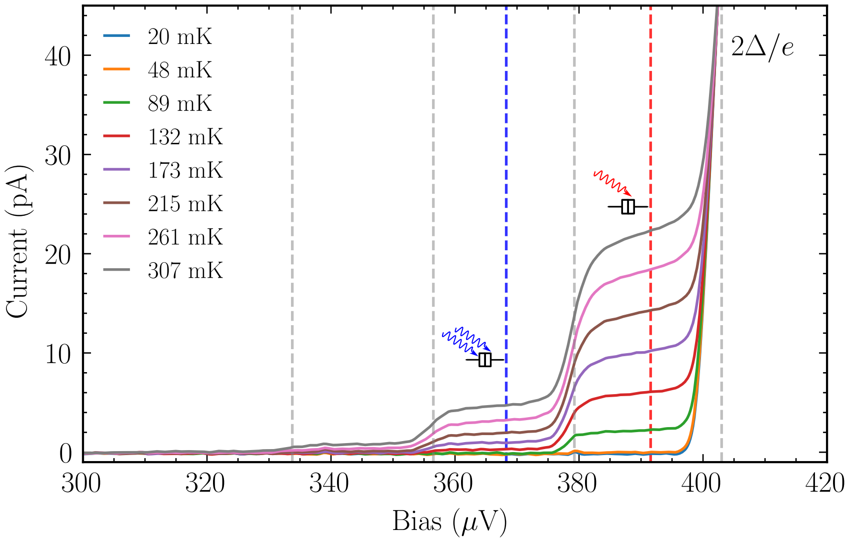

Figure 4.1: Current through the junction as a function of bias voltage for different fridge temperatures. The subgap steps correspond to the processes where different number of photons are absorbed per tunneling event. Voltage threshold for each process is marked by a dashed grey line. Red and blue dashed lines mark the voltages where one and two photon tunneling currents were measured

4.1.1 Single photon tunneling current

We compare the measured current to a simple model, making several assumptions. The multi-photon processes are neglected, and only the ground state and the first excited state of the resonator are considered. Additionally, we assume the probability for the excited state to be occupied is small: $p(1) = \langle n_{\mathrm{res}} \rangle \ll 1$. It is also supposed that both the coupling loss and intrinsic loss channels of the resonator couple to a thermal bath at temperature T_{fridge}. Junction is presumed to be a bath at zero temperature. These assumptions are summarized in the model illustration in figure 4.2.

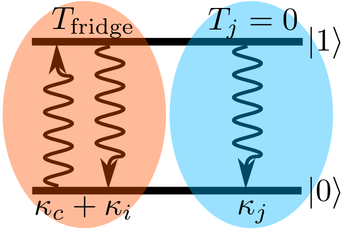

Figure 4.2: Schematic of the model used to explain the thermal photo-assisted current. Junction is presumed to be a zero temperature bath. The coupling loss and intrinsic loss channels of the resonator are assumed to be coupled to a thermal bath at temperature T_{fridge}.

The evolution of the mean resonator population is then given by

$$\frac{\mathrm{d}}{\mathrm{d}t}\langle n_{\mathrm{res}}\rangle = -(\kappa_c+\kappa_i)(n_{\mathrm{BE}}(\omega_1, T_{\mathrm{fridge}})+1)\langle n_{\mathrm{res}}\rangle - \kappa_j\langle n_{\mathrm{res}}\rangle + (\kappa_c+\kappa_i)n_{\mathrm{BE}}(\omega_1, T_{\mathrm{fridge}})(1-\langle n_{\mathrm{res}}\rangle). \tag{4.1}$$

The steady state solution of the equation 4.1 is:

$$\langle n_{\mathrm{res}}\rangle = \frac{\kappa_c + \kappa_i}{\kappa_c + \kappa_i + \kappa_j} n_{\mathrm{BE}}(\omega_1, T_{\mathrm{fridge}}). \tag{4.2}$$

The resulting photo-assisted tunneling current is:

$$I_{\mathrm{PAT}} = e\frac{\kappa_j(\kappa_c + \kappa_i)}{\kappa_c + \kappa_i + \kappa_j} n_{\mathrm{BE}}(\omega_1, T_{\mathrm{fridge}}) = e\frac{\xi}{2} n_{\mathrm{BE}}(\omega_1, T_{\mathrm{fridge}}) \tag{4.3}$$

where $\xi = 2\kappa_j(\kappa_c + \kappa_i)/(\kappa_c + \kappa_i + \kappa_j)$ is the thermal photo-assisted tunneling current rate.

We expect this prediction to hold for temperatures satisfying $n_{\mathrm{BE}}(\omega_1, T_{\mathrm{fridge}}) \ll 1$. If we take the $n_{\mathrm{BE}}(\omega_1, T_{\mathrm{fridge}}) < 0.1$, the rate equation solution 4.3 should agree with the experiment up to 110 mK.

The theoretical prediction, together with the current through the junction measured at junction bias $eV = 2\Delta - \hbar\omega_1/2$ (red dashed line in figure 4.1) is shown in figure 4.3. Above 40 mK there is good agreement between the data and the rate equation solution, once again confirming the highly efficient photon to electron conversion in our circuit. The measured current is slightly above the theoretical prediction. This discrepancy could be due to the sample temperature being higher than the thermometer reading. A temperature increase of 3 mK eliminates the difference between the measured current and the calculation. As the temperature is lowered, the current saturates at 55 fA, corresponding to the detector dark current discussed in section 2.4.1.

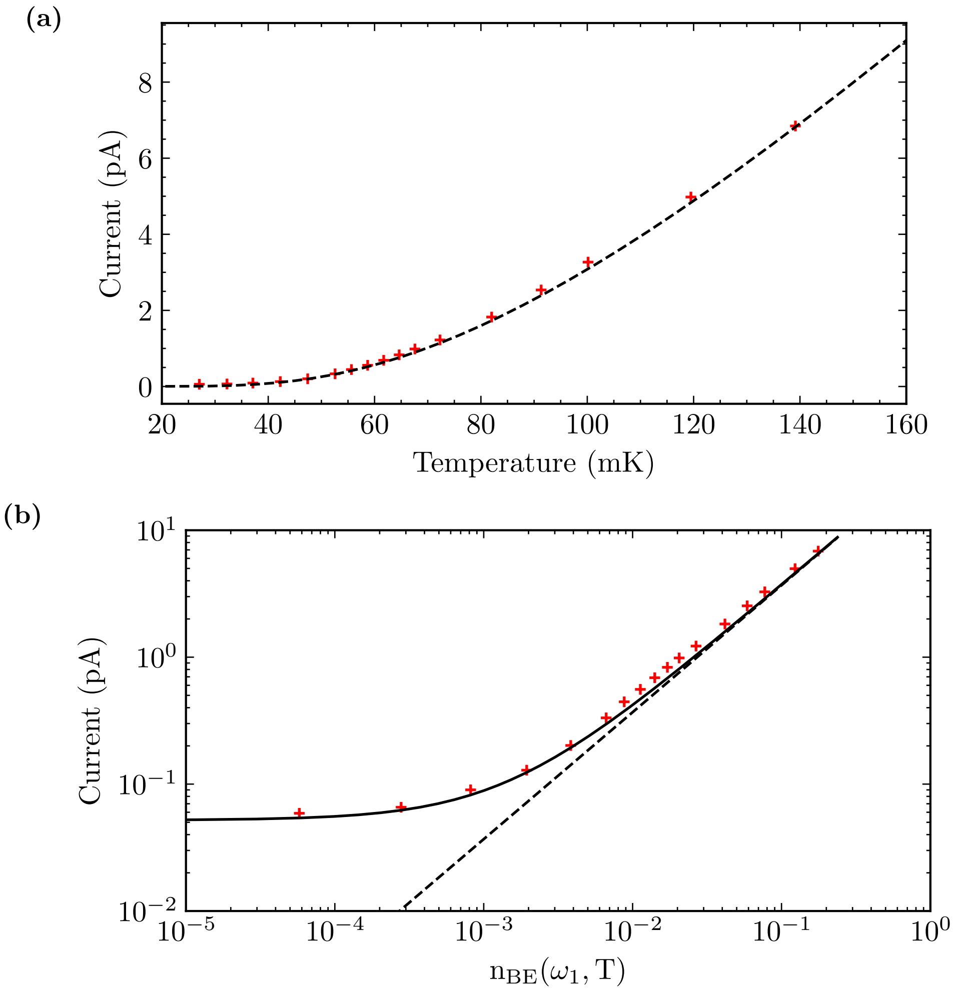

Figure 4.3: (a) Current at junction bias voltage $eV = 2\Delta - \hbar\omega_1/2$ (red dashed line in figure 4.1) as a function of temperature. The black dashed line is the low temperature rate equation prediction (equation 4.3). (b) Same measurement as in (a) plotted in terms of the Bose–Einstein occupation number and current in logarithmic scale. The black dashed line is the low temperature rate equation prediction, while the solid line is the fit to equation 4.7.

Thermal photo-assisted current calibration

The current versus temperature measurement can be used as an alternative method to calibrate the photon detector. From equation 2.7, we can write at zero detuning:

$$1 - |S_{11}| = \frac{2\kappa_c}{\kappa_{tot}} \tag{4.4}$$

where $\kappa_{tot} = \kappa_c + \kappa_i + \kappa_j$ is the total resonator loss. The quantum efficiency is then

$$\chi = \frac{2\kappa_j}{\kappa_{\mathrm{tot}}}(1 - |S_{11}|). \tag{4.5}$$

The previous equation can be rewritten in terms of thermal photo-assisted current rate as:

$$\chi = \left(1 - \sqrt{1 - 2\xi/\kappa_{\text{tot}}}\right)(1 - |S_{11}|) \tag{4.6}$$

The thermal current rate can be determined from fitting the current - temperature data to equation 4.3, with added dark current:

$$I = I_{\text{dark}} + e\frac{\xi}{2}n_{\text{BE}}(\omega_1, T_{\text{fridge}}) \tag{4.7}$$

The fit is shown in figure 4.3b. The fit results are $I_{\text{dark}} = (52 \pm 2)\,\text{fA}$ and $\xi = 2\pi \times (80 \pm 2)\,\text{MHz}$. Total resonator loss κ_{tot} can be determined either from microwave measurements, or by measuring the current at the bias voltage $eV = 2\Delta - \hbar\omega_1/2$ as function of the frequency of a microwave pump tone (section 2.2.1). Absolute value of the reflected signal $|S_{11}|$ is estimated directly by measuring the reflected power at resonance frequency.

The measured values $\xi = 2\pi \times (80 \pm 2)\,\text{MHz}$ and $\kappa_{\text{tot}} = 2\pi \times (146 \pm 3)\,\text{MHz}$ are compatible with $\chi \approx 1$. However, there is large uncertainty due to not precisely knowing the temperature of the sample, which can be different from the thermometer reading.

4.1.2 Classical Master Equation Model

The simple rate equation model detailed above correctly describes the tunneling through the junction only for $\langle n_{\text{res}} \rangle \ll 1$. To extend the description to all temperatures we must take multiple photon processes into account. In the experiments discussed in this chapter, the coherent microwave drive is substituted for an incoherent thermal excitation. The absence of coherence simplifies the description of the system, as the resonator state is fully described by a diagonal density matrix in the Fock basis. This makes finding the resonator steady state significantly less computationally intensive, allowing us to extend the model to include multiple resonator modes. Including higher modes is crucial to accurately describe the current through the junction above the superconducting gap, or at higher temperatures, as in these conditions, these modes cannot be assumed to be in vacuum.

For the sake of clarity, we will detail the single-mode model, and then expand it to the multimode case. The probability $p(n)$ corresponds to the probability to find the resonator in state n. The equation governing the time evolution of this probability is

$$\begin{aligned}\dot{p}(n) = &-\sum_{l=-n,l\neq 0}^{\infty} \kappa_{n,n+l}p(n) + \sum_{l=-n,l\neq 0}^{\infty} \kappa_{n+l,n}p(n+l) \\ &+(\kappa_c + \kappa_i)n_{\text{th}}p(n-1) + (\kappa_c + \kappa_i)(n_{\text{th}}+1)p(n+1) - (\kappa_c + \kappa_i)(2n_{\text{th}}+1)p(n)\end{aligned} \tag{4.8}$$

The first two terms in the equation represent the photon exchange between the resonator and the junction. The rate $\kappa_{n,n+l}$ describes the transition from state $|n\rangle$ to state $|n+l\rangle$. For the single mode case, it is given by equation 1.30. Terms in the second row of equation 4.8 couple the resonator to the thermal bath. As mentioned previously, we assume that the intrinsic loss channel couples to the bath at fridge temperature. The state of the resonator is described by the probability vector $\vec{P} = \begin{pmatrix} p(0) & p(1) & \dots & p(n) & \dots \end{pmatrix}$. Its time evolution is given by the equation 4.8, which can be written in matrix form as:

$$\frac{\mathrm{d}\vec{P}}{\mathrm{d}t} = K\vec{P} \tag{4.9}$$

where K is the rate matrix. Off-diagonal elements of the rate matrix $(K)_{ij}, i \neq j$ are given by the total transition rates from state $|j\rangle$ to state $|i\rangle$. Diagonal elements $(K)_{ii}$ are given by the negative sum of all transition rates away from state $|i\rangle$. We are interested in the stationary solutions of the master equation. Therefore, we look for the non-trivial solutions of the equation

$$K\vec{P} = 0 \tag{4.10}$$

We consider 20 lowest resonator states and calculate the rate matrix K. It is shown in figure 4.4 for one junction bias below (390 µeV) and one bias voltage above the superconducting gap (800 µeV). We note that the rates corresponding to processes involving photon emission (these rates are given by the elements below the main diagonal of the rate matrix shown in figure 4.4) are non-zero only for the junction biased above the superconducting gap. To find the solution of the equation 4.10 we solve

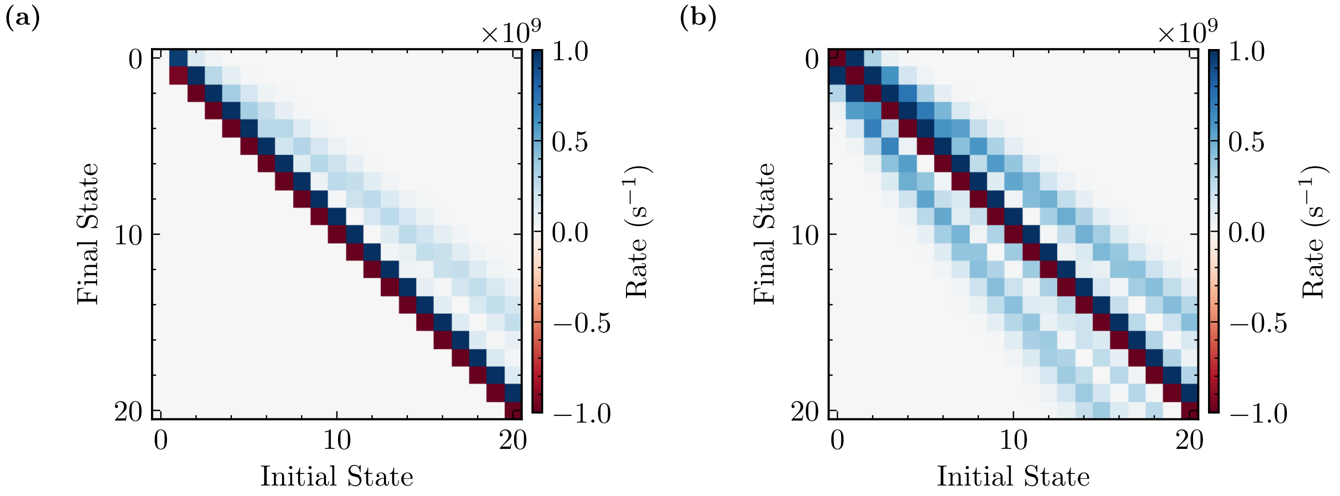

Figure 4.4: Rate matrix K for junction bias voltage (a) 390 μV (b5) 800 μV

$$(K + \epsilon\Sigma)\vec{P} = \begin{pmatrix}\epsilon & 0 & 0 & \dots\end{pmatrix}^T \tag{4.11}$$

where

$$\Sigma = \begin{pmatrix} 1 & 1 & 1 & \dots \\ 0 & 0 & 0 & \dots \\ \vdots & \vdots & \vdots & \ddots \end{pmatrix} \tag{4.12}$$

and ϵ is a parameter chosen to be significantly smaller than the transition rates (in the calculations we set $\epsilon = 10^3\,\mathrm{s}^{-1}$).

When the stationary state of the resonator is known, the mean resonator population is calculated through

$$\langle n_{\mathrm{res}} \rangle = \sum_n np(n) \tag{4.13}$$

and the tunneling current through the junction is

$$I = e\sum_n p(n)\left(\sum_{l\neq 0}\kappa_{n,n+l} + \left|\langle n|\, e^{i\lambda(a+a^\dagger)}\,|n\rangle\right|^2 I(V)\right) \tag{4.14}$$

The second term represents the elastic process contribution, which does not appear in the master equation.

This master equation description can be extended to a multimode resonator in a straightforward manner. Let us consider a system consisting of two modes of frequencies ω_1, and ω_2. The resonator state is $\vec{P} = \begin{pmatrix} p(0,0) & p(0,1) & \ldots & p(1,0) & p_2(1,1) & \ldots \end{pmatrix}$. As an example, we calculate the transition rate for the two photon process $|0,0\rangle \to |1,1\rangle$: as the two modes are independent, the displacement operator matrix element corresponding to the this process is the product of the two matrix elements associated with single mode processes:

$$\left|\langle 1,1|\, e^{i\lambda_1(a_1+a_1^\dagger)+i\lambda_2(a_2+a_2^\dagger)}\,|0,0\rangle\right|^2 = \left|\langle 1|\, e^{i\lambda_1(a_1+a_1^\dagger)}\,|0\rangle\right|^2\left|\langle 1|\, e^{i\lambda_2(a_2+a_2^\dagger)}\,|0\rangle\right|^2. \tag{4.15}$$

The tunneling rate is then

$$\left|\langle 1,1|\, e^{i\lambda_1(a_1+a_1^\dagger)+i\lambda_2(a_2+a_2^\dagger)}\,|0,0\rangle\right|^2 I(V-\hbar\omega_1/e-\hbar\omega_2/e)/e. \tag{4.16}$$

Analogously, for the case of several independent modes, the inelastic tunneling rate from state $|n_1, n_2, \ldots\rangle$ to $|n_1+l_1, n_2+l_2, \ldots\rangle$ is then

$$\kappa_{(n_k)}^{(n_k+l_k)} = \prod_k \left|\langle n_k+l_k|\, e^{i\lambda(a_k+a_k^\dagger)}\,|n_k\rangle\right|^2 I(V-\sum_k l_k\hbar\omega_k/e)/e \tag{4.17}$$

where k is the index counting the resonator modes. Knowing the tunneling rates, we can calculate the resonator population and the tunneling current by generalizing the equations 4.13 and 4.14 in a straightforward manner.

Reproducing the base temperature I(V)

To check the validity of this model, we compare the $I(V)$ calculated for the base temperature of the fridge to the experimental data. In figure 4.5, we compare the experiment to the one-mode and two-mode master equation models. Sample parameters are fixed to the ab initio values (see Chapter 2 for details) in both calculations. The junction normal state resistance R_T used is not the effective resistance, but rather the one directly measured. We see that the one mode calculation overestimates the tunneling current close to the superconducting gap. As the blockade effects of higher resonator modes are not included, this discrepancy between the data and the theory is expected. In the case of the quantum master equation calculation, we corrected for it by renormalizing the junction resistance. In contrast, the agreement between the two-mode model and the experiment is good at all voltage biases.

Temperature dependence of the photo-assisted current

We now focus on the subgap behaviour of the tunneling current with temperature. One and two photon processes are considered, corresponding to the current measured at $eV = 2\Delta-(2n+1)\hbar\omega_1/2, n =$

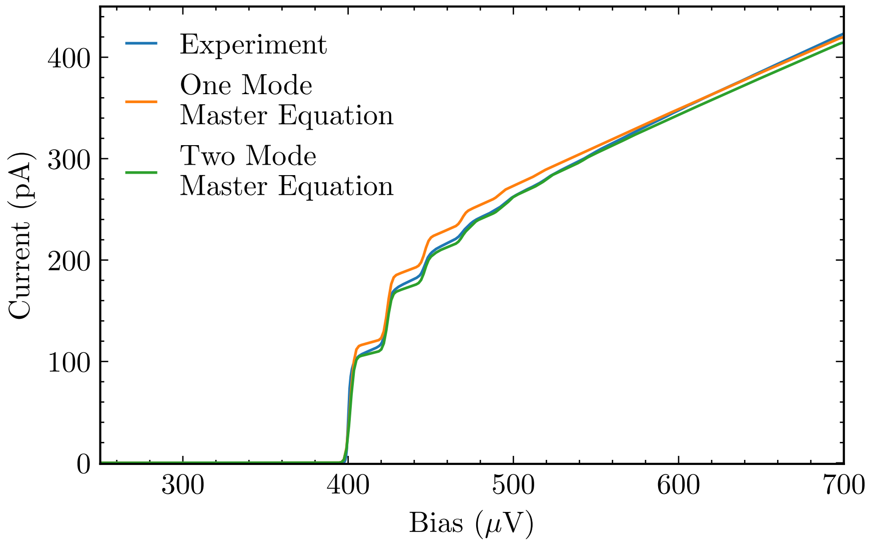

Figure 4.5: Comparison of the junction $I(V)$ measured at base temperature of the experiment and the classical rate equation calculations for a single mode (shown in orange) case, and two-mode (shown in green) model.

$0, 1$ (red and blue dashed lines in figure 4.1). In figure 4.6, we compare the experimental data to the rate equation model presented in section 4.1.1 and the two-mode classical master equation. As

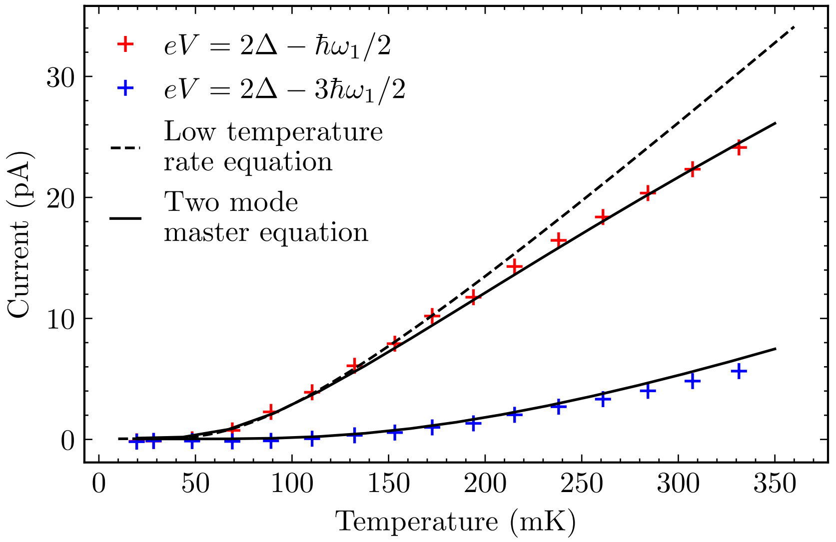

Figure 4.6: Current through the junction at bias voltage $eV = 2\Delta - \hbar\omega_1/2$ (red) and $eV = 2\Delta - \hbar\omega_1/2$ (blue). Dashed line represents the rate equation prediction (equation 4.3), while solid lines are master equation calculations taking the two lowest frequency modes from table 3.1. Dynes parameter is fixed to 10 neV in all calculations.

expected, for temperatures above 200 mK, the low temperature rate equation model overestimates the current. At the same temperatures, the two-photon process starts to contribute significantly to the total tunneling current, leading to a saturation effect. On the other hand, the two-mode master equation reproduces these effects very well. The classical master equation predictions are given in solid black lines. We again see an excellent agreement with the experiments without any free parameters.

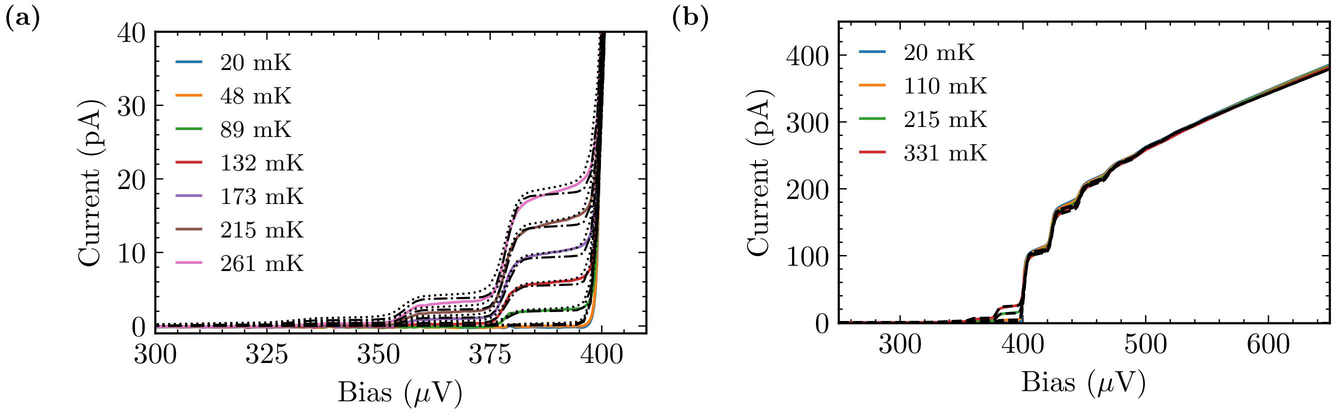

Figure 4.7: (a) Subgap junction current-voltage characteristics for different temperatures. The two-mode master equation calculation is in black. In calculations represented by dash-dotted lines, Dynes parameter is fixed to $\Gamma_0 = 10\,\text{neV}$, while for the dotted lines, the Dynes parameter is considered to be temperature dependent (see equation 4.18). (b) Current through the junction for a wider span of bias voltages and different temperatures. The two-mode master equation prediction is shown in black. The experiment is well reproduced by the theory for all bias voltages and temperatures simultaneously.

The current flowing through the junction is shown in figure 4.7a for the whole subgap voltage bias range. Experimental data is in solid coloured lines, while the master equation calculations are shown in black. The dash-dotted black lines correspond to current calculated with Dynes parameter fixed to $\Gamma_0 = 10\,\text{neV}$ (dash-dotted black lines in figure 4.7a). We observe good agreement with the experimental data.

However, it can be further improved by including the temperature dependence of the Dynes parameter (dotted lines in figure 4.7a):

$$\Gamma = \Gamma_0 \left(1 + \frac{T}{T_0}\right) \tag{4.18}$$

where $T_0 = 20\,\text{mK}$ is the base temperature of the fridge. Especially, the slope of photo-assisted current steps is better reproduced when the Dynes parameter is considered to be temperature dependent. This slope in current steps is absent in current-voltage characteristics measured while at base temperature for similar values of photo-assisted current (see figure 2.9), confirming that it comes from additional subgap states, rather than out-of-equilibrium effects.

4.1.3 Conclusion

To conclude our discussion on the tunneling current, we present the current-voltage characteristics over a wide range of junction bias values in figure 4.7b for several different temperatures. The experimental data is compared to the two-mode master equation calculation. The theory aligns with the experiment at all junction biases and temperatures simultaneously, without any free parameters, reaffirming our understanding of the photon-to-electron conversion in the resonator-junction system.

4.2 Out-of-equilibrium Emission: A Measure of Resonator Population

We now shift our focus to out-of-equilibrium noise measurements. We measure the power emitted by the sample close to the fundamental resonance frequency. By measuring the emission at resonance, we directly probe the resonator population, as shown in section 4.2.1. This allows us to study several phenomena, such as the cooling of the resonator mode by the junction through photo-assisted tunneling, or the dynamical Coulomb blockade of shot noise. These measurements are compared to the theoretical calculation based on the classical master equation model outlined in the previous section.

4.2.1 Input-Output Theory for a Harmonic Oscillator: Correlation Functions

The power spectral density measured by a spectrum analyzer is given by the Fourier transform of the squared outgoing field $|b_{\mathrm{out}}(t)|^2$ (see figure 1.3). We relate this quantity to the resonator population $\langle n_{\mathrm{res}}\rangle = \langle a^\dagger a\rangle$ with the help of input-output theory, starting from the equation A.14 relating the ingoing and outgoing electromagnetic fields:

$$b_{\mathrm{out}}(t) = b_{\mathrm{in}}(t) + \sqrt{\kappa_c}a(t). \tag{4.19}$$

where κ_c is the resonator coupling rate. We assume the input field $b_{\mathrm{in}}(t)$ to be in thermal state characterized by fridge temperature T_{fridge}. The equation 4.19 is true regardless of the character of ingoing and outgoing fields.

We are interested in the outgoing field correlation function $\langle b^\dagger_{\mathrm{out}}(t)b_{\mathrm{out}}(t')\rangle$, assuming that the input field $b_{\mathrm{in}}(t)$ is in a thermal state. Detailed derivation of this correlation function is given in [57], resulting in

$$\langle b^\dagger_{\mathrm{out}}(t)b_{\mathrm{out}}(t')\rangle = \kappa_c(n_{\mathrm{BE}}+1)\langle a^\dagger(t)a(t')\rangle - \kappa_c n_{\mathrm{BE}}\langle a(t')a^\dagger(t)\rangle + n_{\mathrm{BE}}\delta(t-t') \tag{4.20}$$

where n_{BE} is the Bose-Einstein occupation number at the resonance frequency, and κ_c is the resonator coupling rate. The output spectrum in the frame rotating at resonator frequency is then given by

$$S_{\mathrm{out}}(\delta) = \kappa_c(n_{\mathrm{BE}}+1)S_{a^\dagger a}(\delta) - \kappa_c(n_{\mathrm{BE}})S_{aa^\dagger}(-\delta) + n_{\mathrm{BE}} \tag{4.21}$$

where δ is the detuning compared to the resonator frequency. The power spectral density $S_{AB}(\delta)$ is defined as

$$S_{AB}(\delta) = \int_{-\infty}^{\infty} \mathrm{d}\tau\langle A(t+\tau)B(t)\rangle e^{-i\delta\tau} = 2\int_0^{\infty} \mathrm{Re}\left\{\langle A(\tau)B(0)\rangle e^{-i\delta\tau}\right\} d\tau. \tag{4.22}$$

We have assumed that all processes are stationary.

Power spectral density $P(\delta)$ measured using a spectrum analyzer is given by

$$P(\delta) = \hbar\omega_1 \times G \times S_{\text{out}}(\delta), \tag{4.23}$$

where G is the gain of the microwave measurement chain, determined from the photon detector calibration procedure described in section 2.3.

To extract the mean resonator population, we integrate the power spectral density:

$$\int_{-\infty}^{\infty} \mathrm{d}\delta S_{\text{out}}(\delta) = \kappa_c(n_{\text{BE}} + 1)\langle n_{\text{res}}\rangle - \kappa_c n_{\text{BE}}(\langle n_{\text{res}}\rangle + 1) + S_{th} \tag{4.24}$$

where $S_{th} = \int \mathrm{d}\delta\, n_{\text{BE}}$ is the thermal radiation corresponding to the last term in equation 4.21. The integrated power spectral density is then

$$\int_{-\infty}^{\infty} \mathrm{d}\delta S_{\text{out}}(\delta) = \kappa_c(\langle n_{\text{res}}\rangle - n_{\text{BE}}) + S_{th}. \tag{4.25}$$

Therefore, by measuring the integrated power spectral density, we obtain the mean resonator population $\langle n_{\text{res}}\rangle$ from

$$\int_{-\infty}^{\infty} \mathrm{d}\delta P(\delta) = \hbar\omega_1 \times G \times (\kappa_c(\langle n_{\text{res}}\rangle - n_{\text{BE}}) + S_{th}) \tag{4.26}$$

Additionally, if the resonator state is assumed to be thermal, the detailed balance is satisfied:

$$S_{a^\dagger a}(\delta) = \frac{\langle n_{\text{res}}\rangle}{\langle n_{\text{res}}\rangle + 1} S_{aa^\dagger}(-\delta) \tag{4.27}$$

and the output spectrum is

$$S_{\text{out}}(\delta) = \kappa_c(\langle n_{\text{res}}\rangle - n_{\text{BE}}) f(\delta) + n_{\text{BE}} \tag{4.28}$$

where $f(\delta)$ is defined as $f(\delta) = S_{a^\dagger a}(\delta)/\langle n_{\text{res}}\rangle$. For a thermal state, $f(\delta)$ is a Lorentzian function given by

$$f(\delta) = \frac{4\kappa_{\text{tot}}}{4\delta^2 + \kappa_{\text{tot}}} \tag{4.29}$$

where κ_{tot} are the total resonator losses.

4.3 Out-of-Equilibrium Emission as Function of Temperature

In the previous section, we have shown that measuring the power emitted by the sample at resonance frequency allows us to probe the mean population of the resonator $\langle n_{\text{res}}\rangle$. Now we show the results of these experiments. We measure the evolution of emission spectra with junction bias at different temperatures. The measurements are performed in a lock-in configuration - similar to the one described in 3.1.2 for measuring the photo-assisted current. The junction is biased by a square wave with reference value set at $V_{\text{ref}} = 220\,\mu\text{V}$, and frequency 12 Hz. A continuous wave measurement over 10 periods of the bias signal is carried out, and the measurement result is obtained by multiplying the trace by a sine wave at the bias frequency. Thus, we effectively measure the excess emitted power spectral density ΔP compared to the reference voltage bias well bellow the superconducting gap. This procedure corrects for the imperfections in microwave lines and eliminates the noise added by the amplification chain. We assume that the resonator is in equilibrium when the junction is biased far below the superconducting gap. Consequently, by performing the lock-in measurement, the thermal background S_{th} is subtracted, and the integrated excess power spectral density ΔP is related to the mean resonator population $\langle n_{\mathrm{res}} \rangle$ through

$$\int_{-\infty}^{\infty} \mathrm{d}\delta \Delta P(\delta) = \hbar\omega_1 \times G \times (\kappa_c(\langle n_{\mathrm{res}} \rangle - n_{\mathrm{BE}})). \tag{4.30}$$

Thus, zero excess emitted power results in $\langle n_{\mathrm{res}} \rangle = n_{\mathrm{BE}}$, and $\Delta P < 0$ corresponds to $\langle n_{\mathrm{res}} \rangle < n_{\mathrm{BE}}$. The gain G is calculated by subtracting the VNA trace baseline value at resonance frequency from the attenuation given by 2.24, resulting in $G = 69.1\,\mathrm{dB}$.

The measured spectra as function of junction bias at different temperatures are shown in figure 4.8. Above the superconducting gap, we observe the increase in emission with rising junction bias. This increase is weakly dependent on temperature. However, just below the superconducting gap, we observe negative excess emission corresponding to photon absorption due to photo-assisted tunneling, amounting to an effective cooling of the resonator mode, as demonstrated in [69, 71] using SIN junctions.

We use the emission data presented in figure 4.8 to calculate the mean population of the resonator using equation 4.30. The evolution of the resonator population with junction bias and temperature is shown in figure 4.9. At low junction bias, the resonator is at thermal equilibrium. When the junction bias approaches $eV = 2\Delta - \hbar\omega_1$, we observe a dip in resonator population. The dip corresponds to photon absorption through inelastic quasiparticle tunneling, and it gets more pronounced with rising temperature. For temperatures above 200 mK we also observe absorption due to multi-photon processes at voltages $eV < 2\Delta - \hbar\omega_1$. Above $eV = 2\Delta + \hbar\omega_1$, the resonator population rises above the equilibrium value n_{BE} due to photon emission by the junction.

To describe the bias dependence of the emitted spectra, we use the two-mode classical master equation described in section 4.1.2. Predicted resonator population for ab initio sample parameters is shown in dashed lines in figure 4.9. As with the photo-assisted current, we observe good agreement between the experiment and theory, validating our theoretical description of the experiments (section 4.2.1). The resonator population is reproduced in the whole junction bias range without any free parameters.

4.3.1 Effective Cooling of the Resonator Mode

First, we focus on the resonator population for junction bias values below the superconducting gap, and explore the resonator cooling effect in more detail. Active cooling in superconducting circuits is a dynamic area of research, and several protocols have been recently developed, e.g. using beam-splitter interaction [73] or photo-assisted tunneling through SIN junctions [71].

We fix the junction bias to $eV = 2\Delta - \hbar\omega_1/2$, where the effective cooling power is maximal and measure the evolution of the resonator population with temperature. The experimental data is shown in figure 4.10. The mean resonator population is reduced to approximately half its equilibrium value. The experimental data is compared to the two level model outlined in section 4.1.1 (solid black line in figure 4.10). The resonator population just below the superconducting gap is given by equation 4.2. Unlike for photo-assisted current, the low temperature approximation aligns well with the experimental data even in presence of multiphoton losses, up to 330 mK.

We define an effective temperature based on the resonator mean population. For the highest

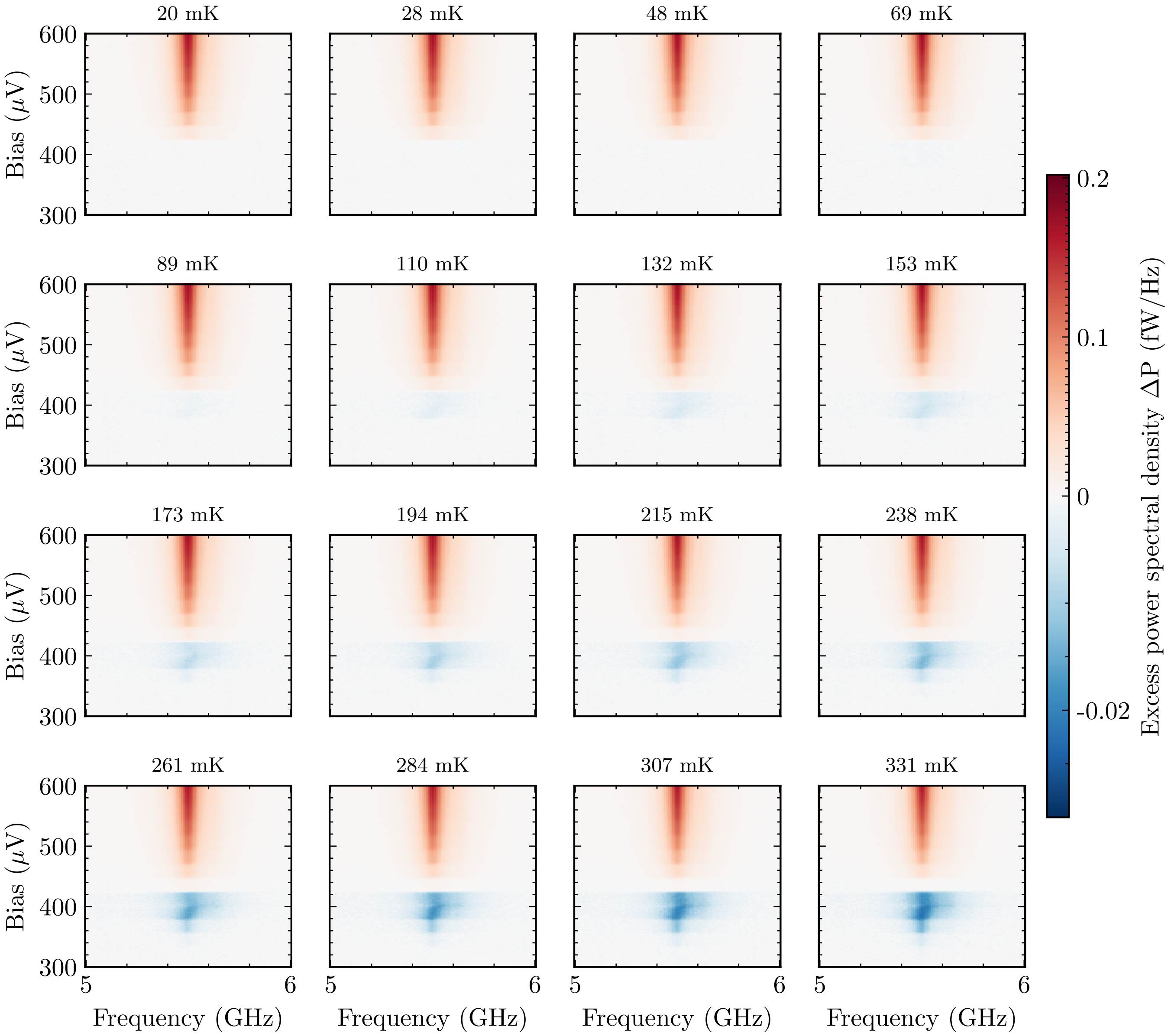

Figure 4.8: Excess emitted power spectral density ΔP as function of frequency and junction bias voltage for different temperatures. Zero excess power corresponds to equilibrium black-body radiation n_{BE} and $\Delta P < 0$ to $\langle n_{\mathrm{res}} \rangle < n_{\mathrm{BE}}$.

measured fridge temperature 330 mK, the effective resonator temperature when the junction is biased at $eV = 2\Delta - \hbar\omega_1/2$ is approximately 100 mK lower than the fridge temperature. This effective cooling power can be improved by tuning the device parameters. From equation 4.2, we note that the mean resonator population is inversely proportional to the junction loss rate κ_j, and conversely, directly proportional to the junction resistance. Thus, by coupling the identical resonator to a ten times more transparent junction, the cooling power could be greatly increased. The effective resonator population as function of environment temperature in this case is presented in blue in figure 4.10. In this case, the effective resonator temperature is kept below 100 mK, or

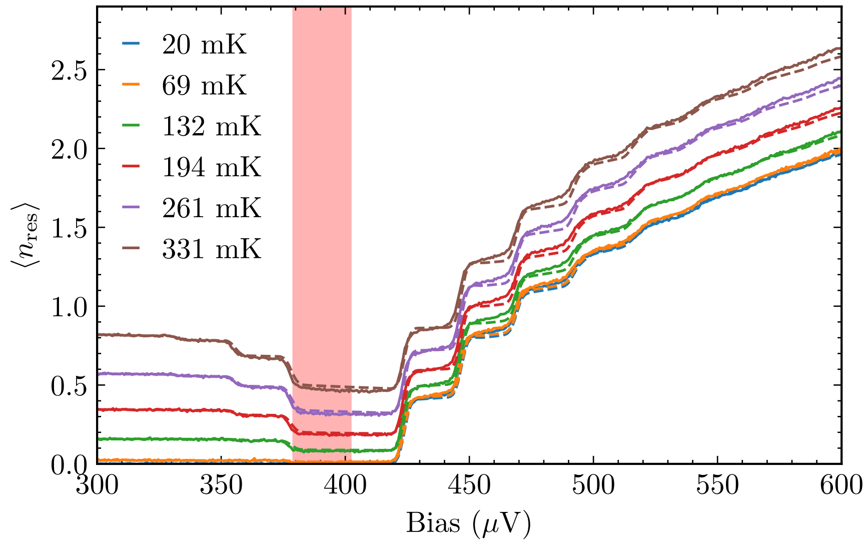

Figure 4.9: Mean resonator population as function of junction bias voltage for different temperatures. The solid lines represent the experimental data, while the dashed lines are two-mode classical master equation predictions for ab initio sample parameters. Subgap voltage bias span $eV \in [2\Delta - \hbar\omega_1, 2\Delta]$ corresponding to maximum cooling power is highlighted in red.

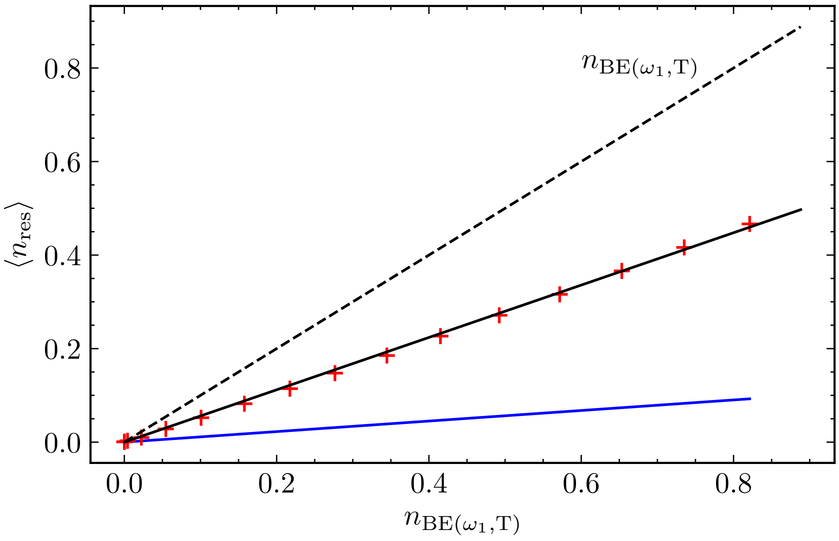

Figure 4.10: Mean resonator population at voltage bias $eV = 2\Delta - \hbar\omega_1/2$ as function of equilibrium occupation number $n_{\text{BE}}(\omega_1, T)$ represented by the dashed black line. Solid black line represents the rate equation model prediction (equation 4.2), while the blue line is the prediction for the mean population of the same resonator coupled to a 150 kΩ superconducting tunnel junction (ten times less resistive than the junction in our device).

$\langle n_{\text{res}} \rangle \ll 1$, even if the environment temperature is above 300 mK. A similar effect has already been demonstrated in a device using SIN junction in [71], where not only the mean resonator population was measured, but also the occupation probability of different Fock states.

Effective Temperature of the Junction

As we have shown above, by further reducing the κ_c/κ_j ratio, one could additionally decrease the resonator population when the junction is biased just below the gap. However, at some point the junction can no longer be approximated as a zero-temperature bath. A priori, the effective temperature of an SIS junction biased below $eV = 2\Delta$ is very low due to absence of the excitations in the system. To estimate it, we modify the rate equation model from section 4.1.1 to include the junction as a bath with finite effective temperature T_j. An analogous calculation for mean resonator population results in

$$\langle n_{\mathrm{res}} \rangle = \frac{(\kappa_c + \kappa_i) n_{\mathrm{BE}}(\omega_1, T) + \kappa_j n_j}{\kappa_c + \kappa_i + \kappa_j} \tag{4.31}$$

where $n_j = n_{\mathrm{BE}}(\omega_1, T_j)$ is the effective population due to the junction. We compare the mean resonator population at junction bias $eV = 2\Delta - \hbar\omega_1/2$ as function of temperature to this model in figure 4.11. Despite the long averaging times, the signal is too noisy to reliably determine the effective junction temperature. However, based on the equation 4.31, we claim $n_j < 8 \cdot 10^{-4}$. This temperature is lower than the normal metal junction temperatures reported in [71]. Thus, use of these devices for active cooling of superconducting circuits seems promising.

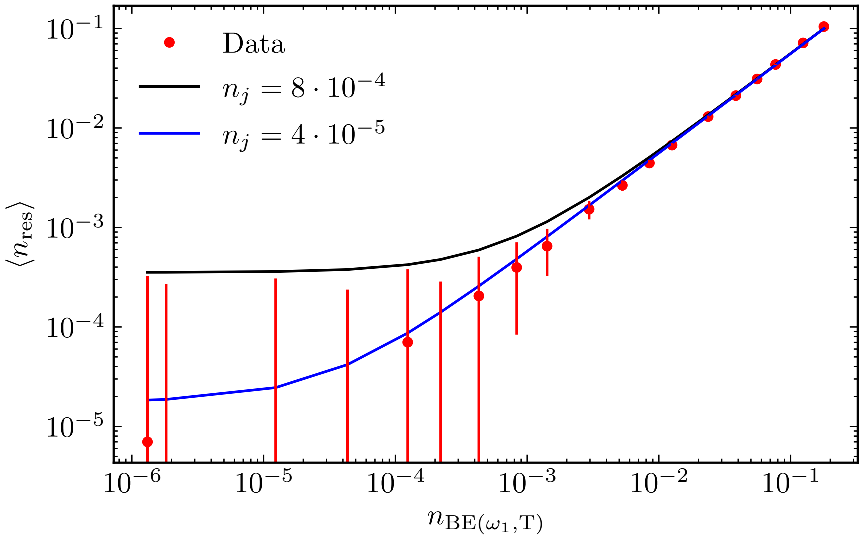

Figure 4.11: Mean resonator population at $eV = 2\Delta - \hbar\omega_1/2$ as function of fridge temperature. Solid lines represent the rate equation model with finite effective junction temperature (equation 4.31) for $n_j = 8 \cdot 10^{-4}$ corresponding to $T_j = 37\,\mathrm{mK}$ (black) and $n_j = 4 \cdot 10^{-5}$ corresponding to $T_j = 26\,\mathrm{mK}$ (black). Based on this calculation we estimate the junction temperature to satisfy $n_j < 8 \cdot 10^{-4}$.

4.3.2 Emission Above the Superconducting Gap

We now shift our focus to voltage bias values above the superconducting gap. We measure the evolution of the resonator population with junction bias at base temperature of the experiment, and compare the data with the two-mode classical master equation prediction. We highlight the difference in our approach compared to the description in terms of the junction tunneling shot noise used for calibrating microwave circuits. [72, 31, 33].

The power spectral density as function of frequency and junction bias measured at $T = 20\,\mathrm{mK}$ is shown in figure 4.12. For junction biases satisfying $eV < 2\Delta + \hbar\omega_1$ there is no discernable emission.

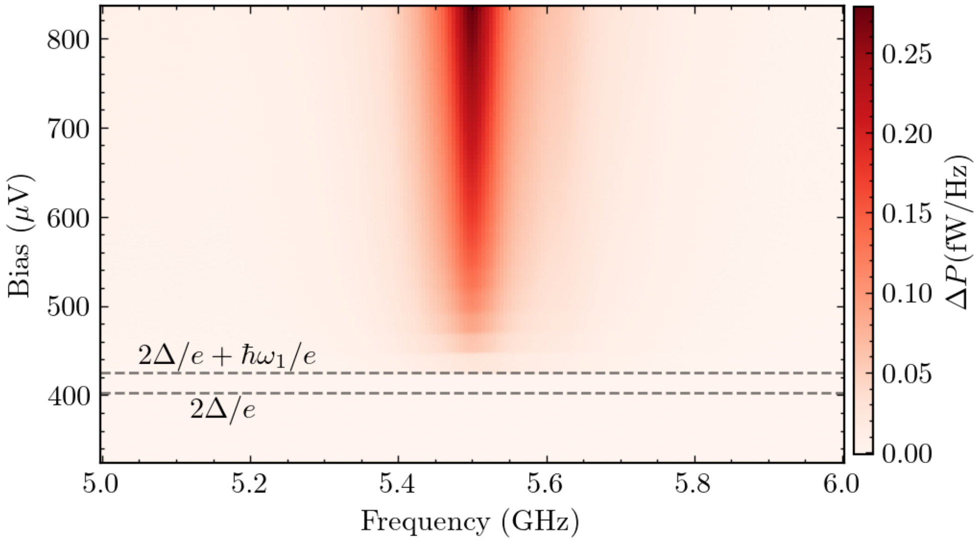

Figure 4.12: Excess PSD at $T = 20\,\mathrm{mK}$ as function of frequency and junction bias.

When the bias is increased above this value, the emission rises in series of steps, corresponding to different emission processes being energetically allowed. We fit each spectrum to the Lorentzian function

$$\Delta P(\omega) = \Delta P_{\max} \frac{\kappa^2/4}{\kappa^2/4 + (\omega - \omega_1)^2} \tag{4.32}$$

where $P_{\max}$ is the excess PSD at resonance, κ is the resonance width, and ω_1 is the resonance frequency. Several spectra, and the corresponding Lorentzian fits are shown in figure 4.13. With the exception of a small frequency range centered around 5.65 GHz, the spectra are well described by equation 4.32 for all bias voltages. The small deviation from Lorentzian shape is probably due to the resonator itself not being Lorentzian. The emission linewidth and peak emitted power extracted through fitting the spectra to the Lorentzian function for bias voltages $eV > 2\Delta + \hbar\omega_1$ are shown in figure 4.14. As the bias voltage is increased, the resonance width decreases in series of steps of width $\hbar\omega_1/e$, before saturating close to $\kappa = 2\pi \times 90\,\mathrm{MHz}$ for high bias voltages. Conversely, just above the superconducting gap, the peak emitted power increases in a step-like manner. Each step occurs at a voltage bias where an additional inelastic tunneling process involving photon emission becomes energetically allowed.

At high bias, the peak emitted power, and thus the mean population of the resonator (see equation 4.28) rises linearly with junction bias, similarly to the current flowing through the junction. We compare the evolution of resonator population and current with junction bias in figure 4.15a At sufficiently high junction bias, the resonator population is proportional to the shifted junction current-voltage characteristic $I(V - \hbar\omega_1/e)$. However, there is noticeable deviation in the 400 - 600 µeV bias range. We explore this discrepancy in more detail below. As we will see, it is a result

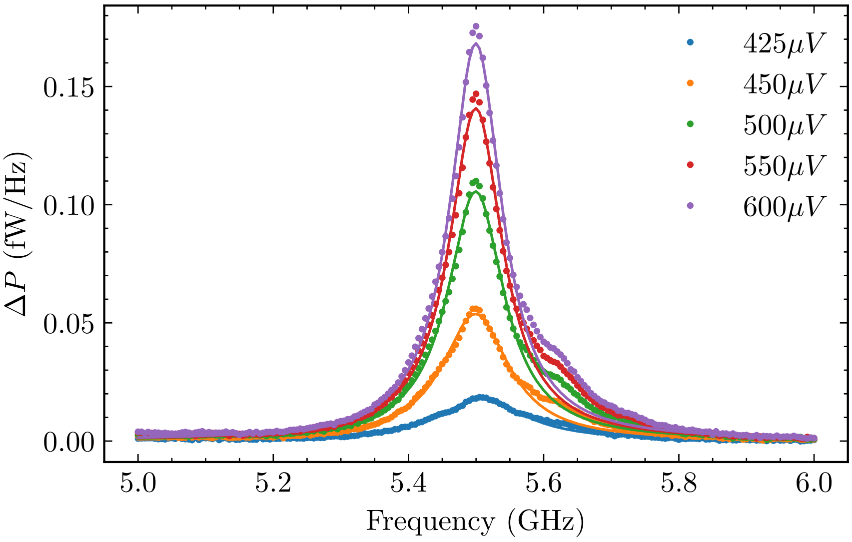

Figure 4.13: Excess PSD at $T = 20\,\text{mK}$ as function of frequency for different junction biases. The Lorentzian fits (equation 4.32) are shown in solid lines.

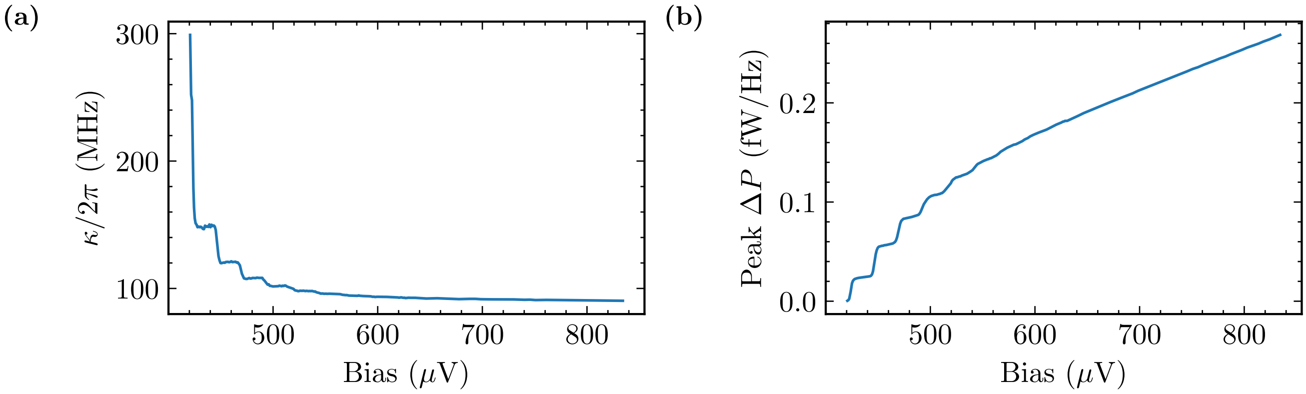

Figure 4.14: (a) Width of emission spectra as function of junction bias voltage (b) Excess PSD at resonance frequency as function of junction bias voltage

of multi-photon processes.

Resonator population at high bias: recovering the shot noise picture

For weak resonator-junction coupling $\lambda \ll 1$, and zero temperature, the resonator population can be calculated analytically at high junction bias. We start from the classical master equation 4.8, and neglect multi-photon processes. The inelastic tunneling rate corresponding to the transition $|n\rangle \to |n-1\rangle$ is

$$\kappa_{n,n-1} = n\lambda^2 I(V + \hbar\omega_1/e)/e \tag{4.33}$$

where we have used the identity $L_k^1(0) = k + 1$. Similarly, the photon emission rate $|n\rangle \to |n+1\rangle$ is given by

$$\kappa_{n,n+1} = (n+1)\lambda^2 I(V - \hbar\omega_1/e)/e. \tag{4.34}$$

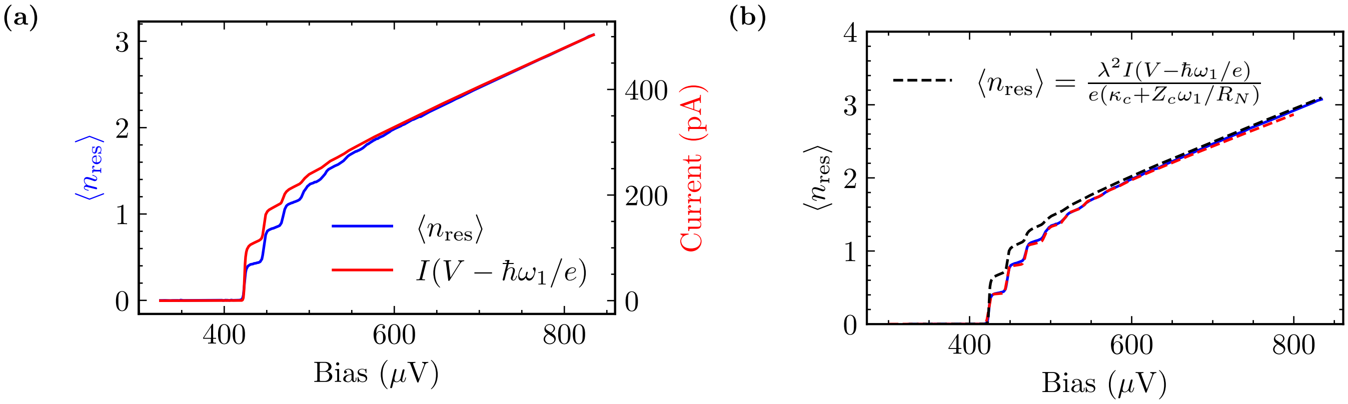

Figure 4.15: (a) Mean resonator population (blue) and current flowing through the junction shifted by $\hbar\omega_1/e$ (red) as functions of bias voltage (b) Mean resonator population at $T = 20\,\mathrm{mK}$ as a function of junction bias. Experimental data is shown in solid blue line, classical master equation calculation is in dashed red line, and the shot noise prediction (equation 4.39) is given by the black dashed line. At high bias, all three curves converge, and the shot noise picture is recovered.

Including the resonator damping κ_c, we can write:

$$\frac{\kappa_{n,n+1}}{\kappa_{n+1,n}} = \frac{\lambda^2 I(V - \hbar\omega_1/e)}{\lambda^2 I(V + \hbar\omega_1/e) + \kappa_c} \tag{4.35}$$

At high bias, we assume that the junction acts as an ohmic element, meaning that

$$I(V + \hbar\omega_1/e) = I(V - \hbar\omega_1/e) + \frac{2\hbar\omega_1}{eR_N} \tag{4.36}$$

where R_N is the normal state junction tunnel resistance. By inputting this result into equation 4.35 we recover the detailed balance

$$\frac{\kappa_{n,n+1}}{\kappa_{n+1,n}} = \frac{1}{1 + \frac{e(\kappa_c + Z_c\omega_1/R_N)}{\lambda^2 I(V - \hbar\omega_1/e)}}. \tag{4.37}$$

Therefore, at high bias, the resonator state is described by a Gibbs distribution

$$p(n) = \langle n_{\mathrm{res}} \rangle^n / (\langle n_{\mathrm{res}} \rangle + 1)^{n+1} \tag{4.38}$$

with the mean resonator population

$$\langle n_{\mathrm{res}} \rangle = \frac{\lambda^2 I(V - \hbar\omega_1/e)}{e\,(\kappa_c + Z_c\omega_1/R_N)} \tag{4.39}$$

where Z_c is the characteristic impedance of the resonator. Expression 4.39 exactly corresponds to the picture of the tunneling current shot noise being filtered by a resonator of characteristic impedance Z_c used for calibrating microwave circuits (see e.g. [31] or [72]).

In strong coupling case $\lambda \sim 1$, where multiphoton processes play a significant role, it is not possible to check the expression 4.39 analytically. Therefore, to verify its validity, we compare it to the experimental data, and the master equation calculation. The comparison is shown in figure

4.15b. At high junction bias, equation 4.39 aligns with the experimental data, confirming that the shot-noise prediction is recovered even for strong coupling. Therefore, we can use the tunnel junction as a calibrated source of shot noise to estimate the gain of our microwave circuit. The shot-noise based calibration is presented in section 2.3.2. However, as the high voltage bias needed to overcome the superconducting gap, and the high resulting current, combined with the strong coupling, bring the device far from equilibrium, we need to go to voltage biases $eV \approx 10\Delta$ to recover the shot noise picture with precision required for accurate calibration. However, just above the superconducting gap, in the 400 - 600 µeV range, the shot noise formula does not reproduce the experimental data, unlike the classical master equation model. As we will show in section 4.4, the resonator state is not thermal when the junction is biased in this voltage range.

4.3.3 Non-Lorentzian spectra at zero excess emission

As we have shown above, most of the measured spectra have a Lorentzian lineshape (equation 4.32). However, we have found that there is a very narrow bias voltage range where the spectrum deviates from a Lorentzian. This point is in the vicinity of $eV = 2\Delta + \hbar\omega_1$, and corresponds to the crossover to the bias range where more power is emitted than absorbed by the junction. As shown in figure (4.16), the non-Lorentzian spectra appear more clearly at high temperature but remain visible at low temperature. With changing junction bias, we observe that the absorption dip, which is observed when $eV < 2\Delta + \hbar\omega_1$, is centered at a higher frequency than the emission peak, which is observed when $eV > 2\Delta + \hbar\omega_1$. At the intermediate voltage, we observe a mixture of absorption and emission with slightly different centre frequencies, resulting in the non-Lorentzian lineshape. Figure 4.17 present the results of a Lorentzian fit of the spectra over a wider voltage range. When the mean excess emission crosses zero, the centre frequency diverges, similar to an avoided crossing, and the width drops. The variation of the centre frequency is responsible for the non-Lorentzian shape.

Reproducing the non-Lorentzian spectra

In order to compute the power spectral density $S_{\text{out}}(\delta)$, we have to determine the first order correlation functions $\langle a^\dagger(\tau)a(0)\rangle$ and $\langle a(0)a^\dagger(\tau)\rangle$, which are defined as [57]:

$$\begin{aligned} C_e(\tau) &= \langle a^\dagger(\tau)a(0)\rangle = \mathrm{Tr}\big[a^\dagger V_\tau\{a\rho_{\text{ss}}\}\big] && (4.40)\\ C_a(\tau) &= \langle a(0)a^\dagger(\tau)\rangle = \mathrm{Tr}\big[a^\dagger V_\tau\{\rho_{\text{ss}}a\}\big] && (4.41)\end{aligned}$$

where V_τ is the evolution operator for the density matrix for a duration τ. The e and a subscripts respectively stand for emission and absorption. The action of V_τ can be expressed as a Kraus map through $V_\tau\{\cdot\} = \sum_l E_{\tau,l} \cdot E^\dagger_{\tau,l}$, where the index l labels different quantum jump histories during the evolution. The steady state density matrix being diagonal, we can rewrite the two correlation functions as

$$\begin{aligned} C_e(\tau) &= \sum_{n=1}^{\infty} p(n)\,\sqrt{n}\,\langle n|a^\dagger_\tau|n-1\rangle && (4.42)\\ C_a(\tau) &= \sum_{n=1}^{\infty} p(n-1)\,\sqrt{n}\,\langle n|a^\dagger_\tau|n-1\rangle && (4.43)\end{aligned}$$

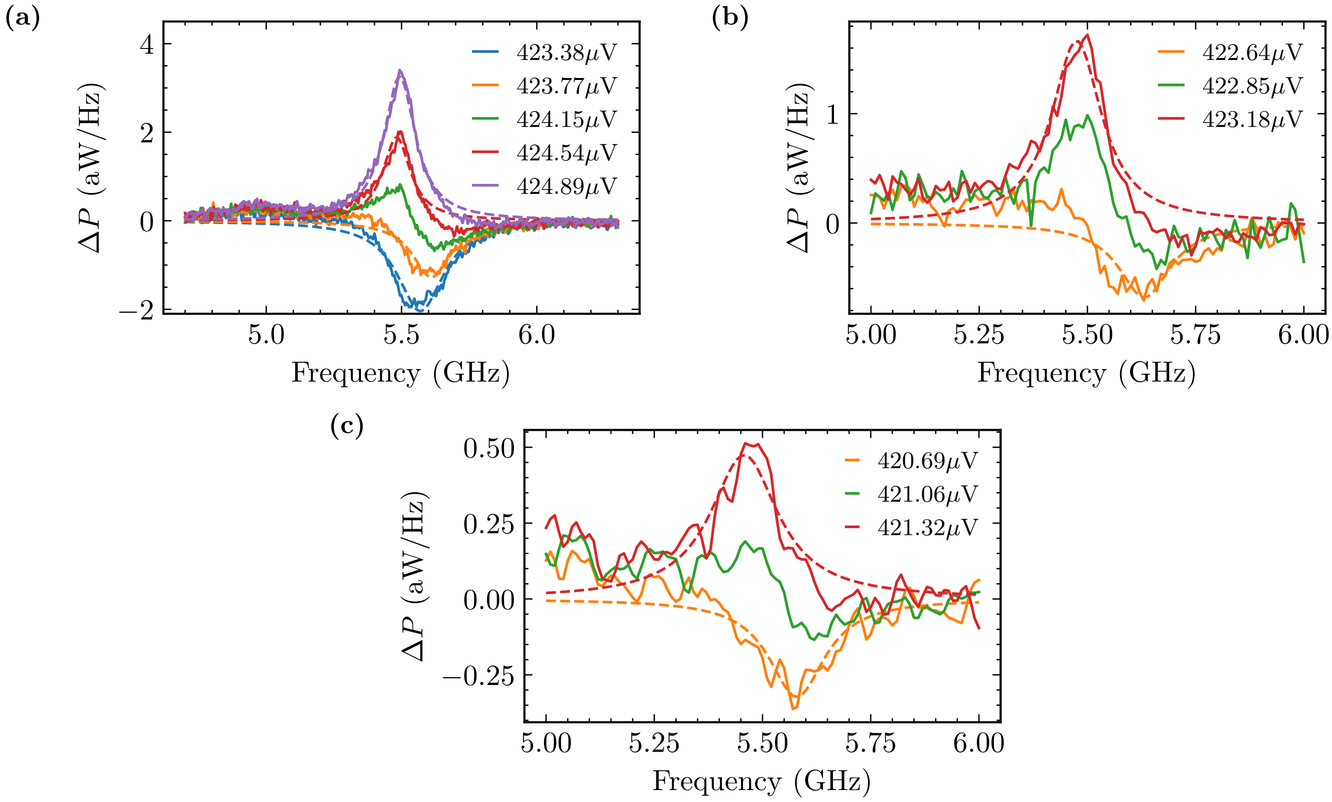

Figure 4.16: Excess PSD ΔP as function of frequency for three voltage biases close to $eV = 2\Delta + \hbar\omega_1$ and three temperatures. Dashed lines correspond to Lorentzian fits. (a) $T = 90$ mK (b) $T = 150$ mK (c) $T = 210$ mK. The green trace corresponds to the spectrum where the integrated excess PSD nearly vanishes. The spectrum is then a mixture of absorption and emission which are centered a slightly different frequencies.

where $a_\tau^\dagger = \sum_l E_{\tau,l}^\dagger a^\dagger E_{\tau,l}$. We introduce $S_n(\delta) = 2\sqrt{n}\int_0^\infty \mathrm{Re}\{\langle n|a_\tau^\dagger|n-1\rangle e^{-i\delta\tau}\}\,d\tau$, which allows us to write the Fourier transform of the absorption and emission correlation functions as

$$S_e(\delta) = \int_{-\infty}^{\infty} C_e(\tau)e^{-i\delta\tau}\,d\tau = \sum_{n=1}^{\infty} p(n)S_n(\delta) \tag{4.44}$$

$$S_a(\delta) = \int_{-\infty}^{\infty} C_a(\tau)e^{-i\delta\tau}\,d\tau = \sum_{n=1}^{\infty} p(n-1)S_n(\delta) \tag{4.45}$$

The output spectrum of the resonator (equation 4.21) is then given by

$$S_{\mathrm{out}}(\delta) = n_{\mathrm{BE}} + \kappa_c\left[(n_{\mathrm{BE}}+1)S_e(\delta) - n_{\mathrm{BE}}\,S_a(\delta)\right] \tag{4.46}$$

$$= n_{\mathrm{BE}} + \kappa_c\sum_{n=1}^{\infty}\left[(n_{\mathrm{BE}}+1)\,p(n) - n_{\mathrm{BE}}\,p(n-1)\right]S_n(\delta) \tag{4.47}$$

This expression is expected to be valid at any bias voltage, whether the steady state is close to a thermal state or not. In the specific case of a thermal state, for which $p(n) = e^{-\beta n\hbar\omega_1}/(e^{\beta\hbar\omega_1}-1)$,

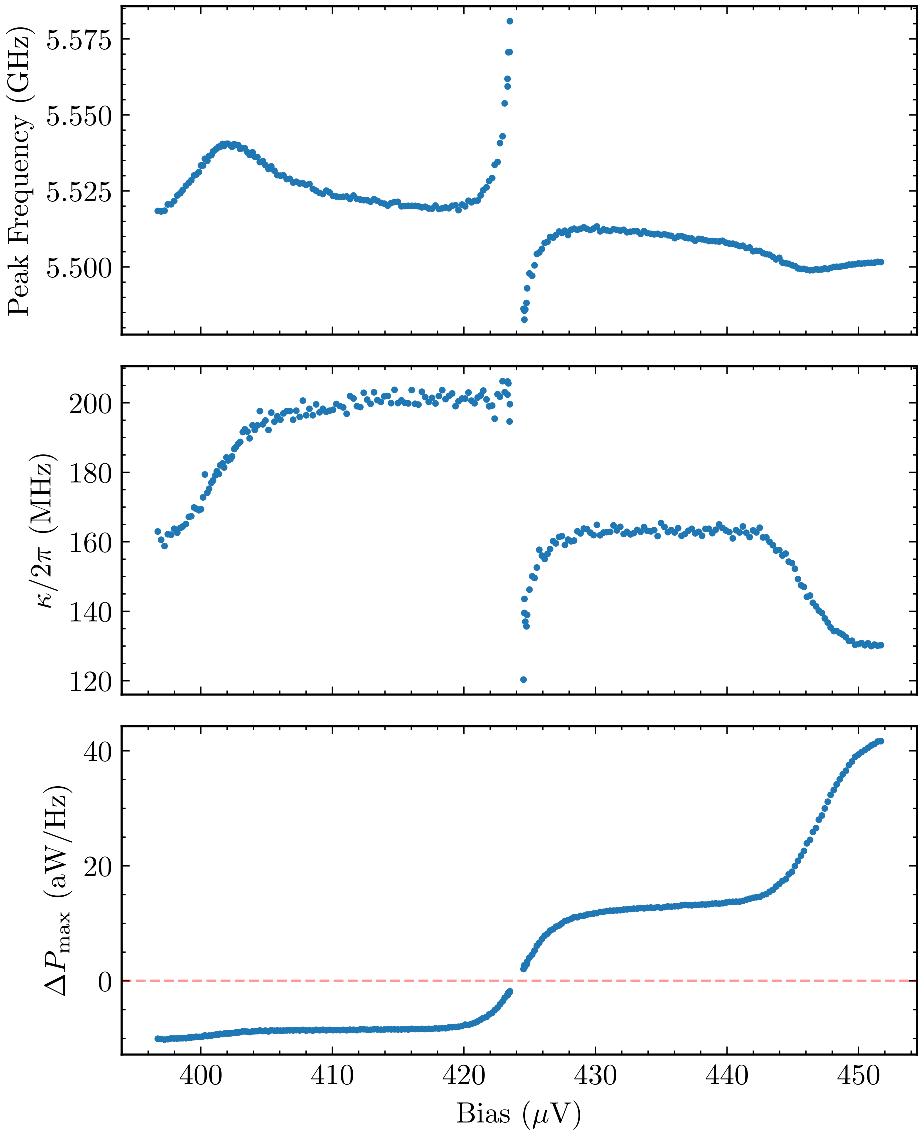

Figure 4.17: Lorentzian fit parameters for emission spectra measured at 210 mK. Top panel shows the centre frequency, middle panel the resonance width κ, and the bottom panel the excess PSD at the centre frequency $\Delta P_{\rm max}$. The red dashed line corresponds to zero peak excess emission. When $\Delta P_{\rm max}$ crosses zero, the peak frequency diverges and the spectra become non Lorentzian.

we recover the Kubo formula

$$S_e(\delta) = e^{-\beta\hbar\omega_1} S_a(\delta) = \frac{\langle n_{\rm res}\rangle}{\langle n_{\rm res}\rangle + 1} S_a(\delta) \tag{4.48}$$

And the output spectrum simplifies to

$$S_{\rm out}(\delta) = n_{\rm BE} + \kappa_c \frac{\langle n_{\rm res}\rangle - n_{\rm BE}}{\langle n_{\rm res}\rangle} S_e(\delta) \tag{4.49}$$

The previous formulae show that two criteria must be fulfilled in order to obtain non-Lorentzian spectra when the junction starts emitting more power than it absorbs. First, the steady state must be non thermal, otherwise (4.49) predicts a flat spectrum when $\langle n_{\mathrm{res}} \rangle = n_{\mathrm{BE}}$. Second, the resonator spectrum must be non-linear. In the case where the resonator spectrum is linear, the master equation in the rotating frame only contains jump terms and the function $\langle n|a_\tau^\dagger|n-1\rangle$ is a real function of τ, which decays with τ. If the only jump terms are the usual one photon absorption and emission processes, then $\langle n|a_\tau^\dagger|n-1\rangle$ is given by $n\exp(-\kappa\tau)$, where $\kappa = \kappa_c + \kappa_i$. We have numerically checked that this remains a very good approximation when we include the junction absorption and emission terms. Equation (4.47) then implies that the spectrum is Lorentzian with an amplitude given by $\langle n_{\mathrm{res}}\rangle(n_{\mathrm{BE}}+1) - (\langle n_{\mathrm{res}}\rangle+1)n_{\mathrm{BE}}$. Therefore, we conclude that the Lamb shift plays an essential role to explain the non-Lorentzian spectra by introducing a non-linearity in the spectrum as we have already observed in [59].

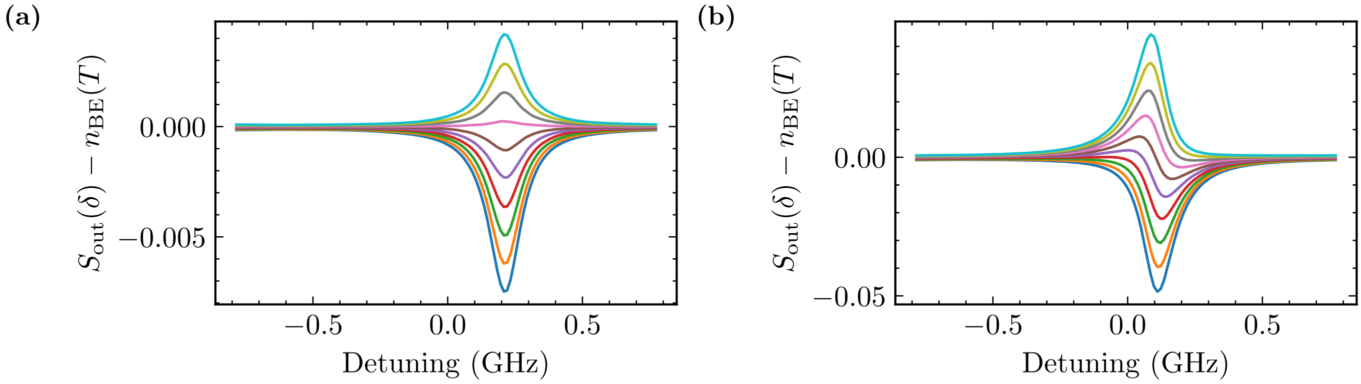

Figure 4.18: Power spectral density at $T = 210\,\mathrm{mK}$ with subtracted thermal radiation for bias voltage values in vicinity of emission zero-crossing. (a) Calculation with Lamb Shift neglected. There is a continuous change from absorption to emission and spectra are Lorentzian at all bias voltages. (b) Multi-photon Lamb shift is included. In this case, the shape of the spectra measured in the experiment are reproduced.

Including the Lamb shift and computing $S_n(\delta)$ from the Fourier transform of $\langle n|a_\tau^\dagger|n-1\rangle$, which we compute numerically using the quantum regression theorem, we obtain the curves shown in figure 4.18 for the expected spectrum at $T = 210\,\mathrm{mK}$. The figure also shows the results of a simulation without the Lamb shift, in which case the Lorentzian spectra are recovered. Our simulation also indicates that the state is close to thermal but not exactly thermal (see figure 4.19). The deviation of $p(n)$ from a thermal ensemble seems to be larger in the experiment than in our simulation, which results in a larger amplitude of the non-Lorentzian spectrum when $\langle n_{\mathrm{res}}\rangle \approx n_{\mathrm{BE}}$. In order to explain our data, we have to multiply the simulated power spectrum by roughly a factor 8.

To demonstrate that the cavity state at zero mean emission is not thermal, we compute its Wigner function, and compare it to the Wigner function

$$W_T(\alpha,\alpha^*) = \frac{2}{\pi}(1-\langle n_{\mathrm{res}}\rangle)e^{-2|\alpha|^2}\left(\frac{1}{1+\langle n_{\mathrm{res}}\rangle}e^{4|\alpha|^2\frac{\langle n_{\mathrm{res}}\rangle}{1+\langle n_{\mathrm{res}}\rangle}}\right) \tag{4.50}$$

of a thermal state with the same resonator population. As seen from equation 4.50, the thermal

Wigner function W_T is Gaussian. The difference in Wigner functions

$$W = \frac{W_{\text{res}} - W_T}{W_{\text{res}}(0,0)} \tag{4.51}$$

is shown in figure 4.19. Although the state is not exactly thermal, it is nearly thermal. The maximum deviation is approximately 3 %.

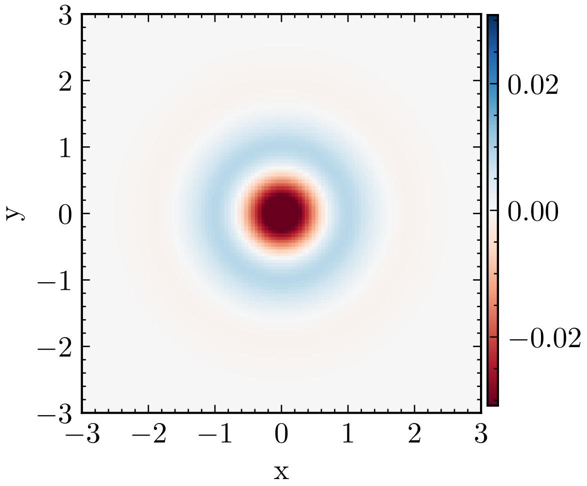

Figure 4.19: Difference between the Wigner function of the cavity state corresponding to the non-Lorentzian spectrum at 210 mK, and the Wigner function of a thermal state at fridge temperature. The maximum deviation is approximately 3 %.

4.4 Generating Non-thermal States in the Resonator

In the previous section, we have shown that the resonator state is non-thermal, when the junction crosses from absorbing more power to emitting. We now extend this analysis to the wider range of junction bias voltages. From the equation 4.38, we note that a thermal state satisfies

$$\frac{p(n+1)}{p(n)} = const \tag{4.52}$$

where the constant on the right side of the equation depends on the mean resonator population, and hence the junction bias. In figure 4.20, we plot the expression 4.52 for several junction bias voltages and two different coupling parameters — $\lambda = 0.1$ and $\lambda = 0.785$. For $\lambda = 0.1$ (dashed lines), the resonator distribution resembles a thermal state for all three bias voltage values, as expected from the analytical calculations presented above. However, for $\lambda = 0.785$ (solid lines), corresponding to our experiment, for the junction bias 430 µeV, slightly above $eV = 2\Delta + \hbar\omega_1$, the resonator state is far from satisfying the equation 4.52. The resonator state matches a thermal distribution only at high junction bias.

To show the non-thermal nature of the cavity state above the superconducting gap, we compare the Wigner function of the cavity state to the Wigner function of the thermal state with the

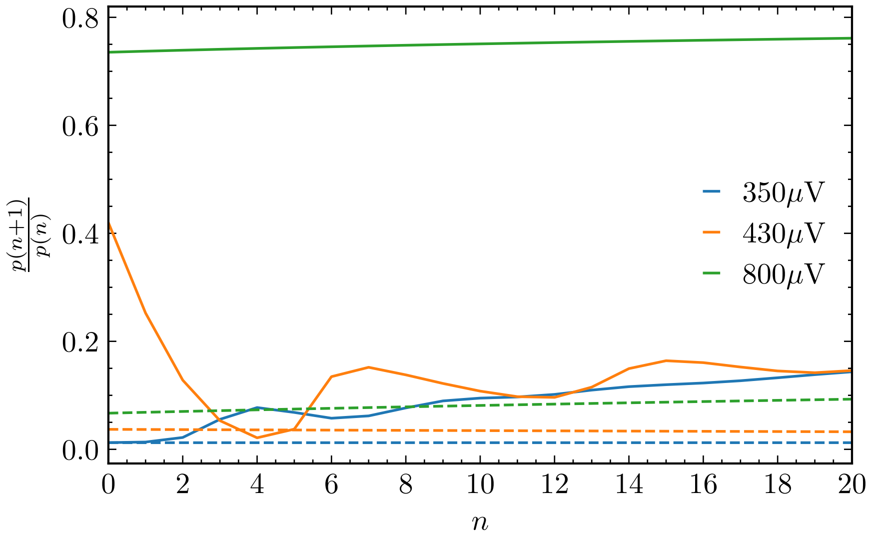

Figure 4.20: Population ratio $p(n+1)/p(n)$, for three different junction biases. Solid lines correspond to $\lambda = 0.785$, matching our experiment, while the dashed lines represent the weak coupling case $\lambda = 0.1$. For small coupling, the resonator distribution resembles a thermal state even just above the superconducting gap, while for $\lambda \sim 1$, the thermal distribution is recovered only at high bias.

identical mean resonator population. The normalized difference between the cavity and thermal Wigner functions (equation 4.51) is shown in figure 4.21 for different junction bias voltages, and the two coupling parameters discussed above. Well below the superconducting gap (panels (a) and (d)) the cavity is in a thermal state. Just above the gap, for $\lambda = 0.1$ (panel (e)) the cavity stays in a thermal state. However, for $\lambda = 0.785$, the cavity state deviates from the equivalent thermal state by more than 20 %. Far above the gap (panels (c) and (f)), the cavity is again in a thermal state regardless of λ.

The non-thermal states appear in the resonator due to different voltage bias thresholds corresponding to absorption and emission tunneling processes. Thus, when the junction is biased just above the superconducting gap, the multi-photon absorption is allowed, while the multi-photon emission is not, and the detailed balance cannot be established. When the junction bias is increased far above the gap, all inelastic processes become allowed, and the shot noise picture is recovered (equation 4.39).

In our experiment, we only measure the mean population of the resonator, but not the occupation probability of particular states. However, measuring the probability distribution of a resonator state is possible, e.g. by probing it with a qubit [71].

4.5 Conclusion

In this chapter, we have have presented the response of the sample to thermal radiation. We measured the thermal photo-assisted current and confirmed the high photon to electron conversion quantum efficiency estimated in Chapter 2. Due to the absence of coherence in the experiments, the quantum master equation model can be simplified to a classical rate equation description, allowing us to include multiple modes in calculation. The multi-mode rate equation model enables us to

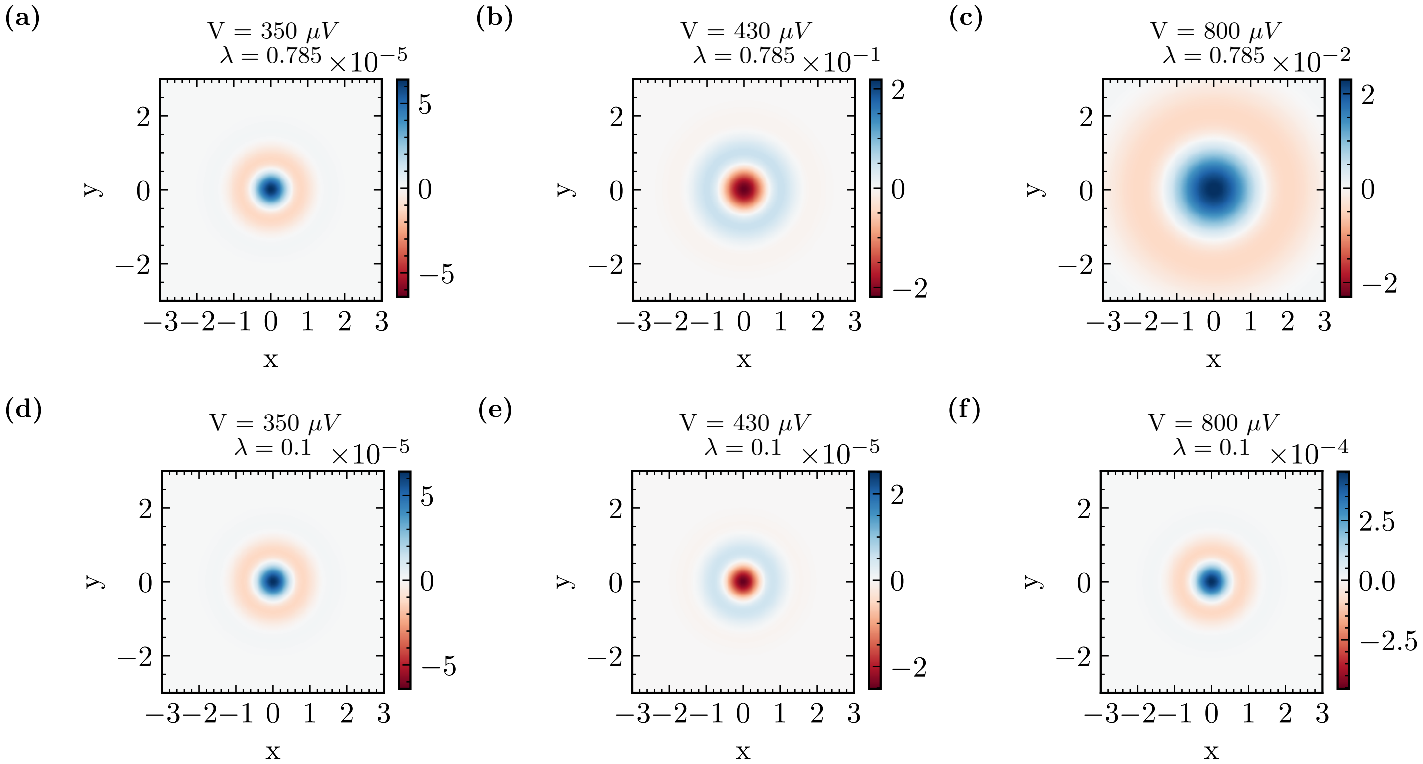

Figure 4.21: Difference between the cavity state Wigner function and the Wigner function of a thermal state with the same resonator population $\langle n_{\mathrm{res}} \rangle$ for different junction bias voltages and coupling parameters. Well below the superconducting gap (panels (a) and (d)) the cavity is in a thermal state. Just above the gap, for $\lambda = 0.1$ (panel (e)) the cavity stays in a thermal state. However, for $\lambda = 0.785$, the cavity state deviates from the equivalent thermal state by more than 20 %. Far above the gap (panels (c) and (f)), the cavity is again in a thermal state regardless of λ. Note the differences in color scale.

accurately estimate current for an arbitrary bias voltage. The theory is in quantitative agreement with the experimental data without any free parameters.

We also measure the out-of-equilibrium emission as function of temperature and junction bias. Through input-output theory, we show that measuring the power emitted by the sample allows us to estimate the mean resonator population. Below the superconducting gap, we measure the resonator population lower than in equilibrium, corresponding to the effective cooling of the resonator mode via photo-assisted tunneling. When junction bias crosses the gap, the resonator population rises with junction bias due to junction emission. With the help of classical master equation, we demonstrate that the resonator state in the bias range just above the superconducting gap is non-thermal when $\lambda \sim 1$ due to the imbalance between multi-photon absorption and emission rates. For high junction bias, the cavity state can again be described by an effective temperature directly proportional to current flowing through the junction even in the strong coupling case, and we show that the emission corresponds to the tunneling current shot noise. Therefore, the junction can be used as a calibrated source of microwaves, allowing for calibration of the microwave measurement chain gain.

For the bias voltage values close to $eV = 2\Delta + \hbar\omega_1$, the emission spectra are non-Lorentzian, indicating the non-thermal state of the resonator. To calculate the emission spectra, we use the quantum master equation formalism already outlined in Chapter 1, and apply the quantum regression theorem. The theory reproduces the shape of the spectra only if the multi-processes are allowed, and the cavity Lamb shift is taken into account, pointing to their crucial role in the dynamics of the system.

Chapter 5

Towards Single Photon Detection: RF-SET in a High Impedance Environment

---

We now turn to the experiments performed with the aim of making the photon detector presented in Chapters 1 and 2 compatible with charge counting techniques needed to resolve individual tunneling events. To this purpose, we realize a sample consisting of two capacitively coupled radio-frequency single-electron transistors (see figure 5). One RF-SET is used as a photon-to-electron converter, while the second one serves as a readout. Microwave photons are absorbed by the converter SET through inelastic quasiparticle tunneling, changing the charge of the transistor island. This change is detected by the capacitively coupled readout RF-SET, thus detecting the photon in real time.

We first perform reflection spectroscopy measurements, probing the photo-assisted processes in the two single-electron transistors independently. Regions in bias and gate voltages corresponding to high absorption are identified, similarly to the critical coupling case for the single tunnel junction.

The reflectometry measurements are used to extract the charging energies, as well as the junction asymmetry.

Since their first realization by Schoelkopf et al. [48], due to high bandwidth and sensitivity as low as $0.9 \cdot 10^{-6}\,\mathrm{e}/\sqrt{\mathrm{Hz}}$ [49], RF-SETs have been widely used as electrometers, including for real time measurement of electron tunneling in quantum dots (e.g. [74]), and monitoring the quasiparticle number in superconductors [75]. By measuring the evolution of reflected power with gate and bias voltages, we estimate the charge sensitivity of the readout RF-SET to be close to $5 \cdot 10^{-5}\,\mathrm{e}/\sqrt{\mathrm{Hz}}$, and discuss further improvements that could be made.

To understand the tunneling in a SET strongly coupled to a single-mode resonator, we monitor the microwave emission as a function of gate and bias voltages. As in the single junction case, by probing the emitted power, we probe the mean resonator population. However, in the RF-SET, we observe a non-monotonic increase in resonator population with rising junction bias observed in experimental data. To explain these measurements, we develop a model based on the classical rate equation, analogous to the one presented in section 4.1.2 for a resonator coupled to an SIS junction. In addition to the resonator state, the quasiparticle tunneling rates through the junctions also depend on the excess charge of the SET island. Thus the state of the system is described by the number of photons in the resonator, and the number of excess electrons on the island: (n_{ph}, n_e). Inelastic tunneling rates between these states are calculated in a similar manner to the single junction instance, and including the electrostatic energy considerations. We show good agreement between the experimental data and the rate equation model.

5.1 Quasiparticle Tunneling Through an RF-SET

We start by discussing the quasiparticle tunneling through a single SET. The SET equivalent circuit is shown in figure 5.1. It consists of two superconducting tunnel junctions separated by a small superconducting island. The central island is isolated from the rest of the circuit, except through the junction capacitors, and a capacitively coupled gate. Thus, the charge of the island is quantized: $Q_i = n_e e$, and adding or subtracting an electron from the island is followed by a change in its electrostatic energy. For n_e excess electrons on the island, its electrostatic energy is [40]:

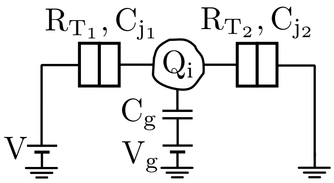

Figure 5.1: Equivalent circuit of a SET. The two junctions are separated by a small superconducting island of charging energy $E_C \ll k_{\mathrm{B}}T$. The chemical potential of the island can be tuned through a capacitively coupled gate electrode.

$$E_{n_e} = E_C(n_g - n_e)^2 \tag{5.1}$$

where $n_g = C_g V_g/e$ is a continuous variable representing the coupled gate charge (see figure 5.1), and E_C is the island charging energy:

$$E_C = \frac{e^2}{2C_\Sigma} \tag{5.2}$$

with C_Σ being the total island capacitance. For the circuit shown in figure 5.1, the total island capacitance is $C_\Sigma = C_{j_1} + C_{j_2} + C_g$. The electrostatic charging energy represents the energy needed to add one additional electron to the island. When it satisfies $E_C \gg k_\mathrm{B}T$, the electrostatic effects are no longer washed out by the thermal fluctuations, and need to be taken into account when calculating the current flowing through the SET. We present these calculations below, first only for the elastic process (section 5.1.1), and then including the photo-assisted tunneling (section 5.1.2). We only consider the sequential tunneling model, in which the tunneling events through the two junctions are independent of each other [40].

5.1.1 Elastic Tunneling

When we calculated the tunneling rates through a single superconducting junction (section 1.2), we showed that the tunneling is possible as soon as the junction bias voltage crosses the superconducting gap. In case of the SET, this is not the case. To demonstrate this, we consider the change in electrostatic energy corresponding to an addition of a quasiparticle to the island. From equation 5.1, we have

$$\Delta E_{el} = E_{n_e+1} - E_{n_e}. \tag{5.3}$$

Tunneling through a junction occurs only if, in addition to the energy 2Δ needed to split a Cooper pair, the energy supplied by the voltage source is sufficient to overcome the change in electrostatic energy. Therefore, quasiparticles tunnel into the island through junction i for bias voltages satisfying

$$\alpha_i eV \geq 2\Delta + E_{n_e+1} - E_{n_e}. \tag{5.4}$$

Coefficients α_1 and α_2 describe how the source voltage V is divided between the two junctions. For the asymmetric biasing scheme shown in figure 5.1, where one side of the SET is kept grounded, these coefficients are [40]:

$$\begin{aligned} \alpha_1 &= \frac{C_{j_2} + C_g}{C_\Sigma} \\ \alpha_2 &= \frac{C_{j_1}}{C_\Sigma}. \end{aligned} \tag{5.5}$$

In terms of the island charging energy, the tunneling conditions 5.4 are:

$$\alpha_i eV \geq 2\Delta + E_C(2n_e - 2n_g + 1). \tag{5.6}$$

Conditions for a quasiparticle tunneling off the island can be derived in a similar manner starting from $\Delta E_{el} = E_{n_e} - E_{n_e+1}$. These tunneling thresholds for a symmetric SET ($\alpha_1 = \alpha_2 = 0.5$) and $E_C = 1.4\Delta$ are shown in figure 5.2a. The structures seen in white are referred to as Coulomb diamonds. In these regions, the quasiparticle tunneling is prohibited and no current can flow through the junction. Each Coulomb diamond corresponds to a stable state island charge n_e. Outside of these regions, there are no stable charge configurations, and there is non-zero tunneling current. Solid black lines outlining the limits of Coulomb diamonds match the resonant tunneling through junction one, while the blue lines coincide with resonant tunneling through junction two. The ratio of their slopes is given by α_1/α_2. Quasiparticle tunneling energy diagram corresponding to three different points along these lines is shown in figure 5.2.

To quantify the tunneling rates in the SET, we can repeat the Fermi's golden rule calculation

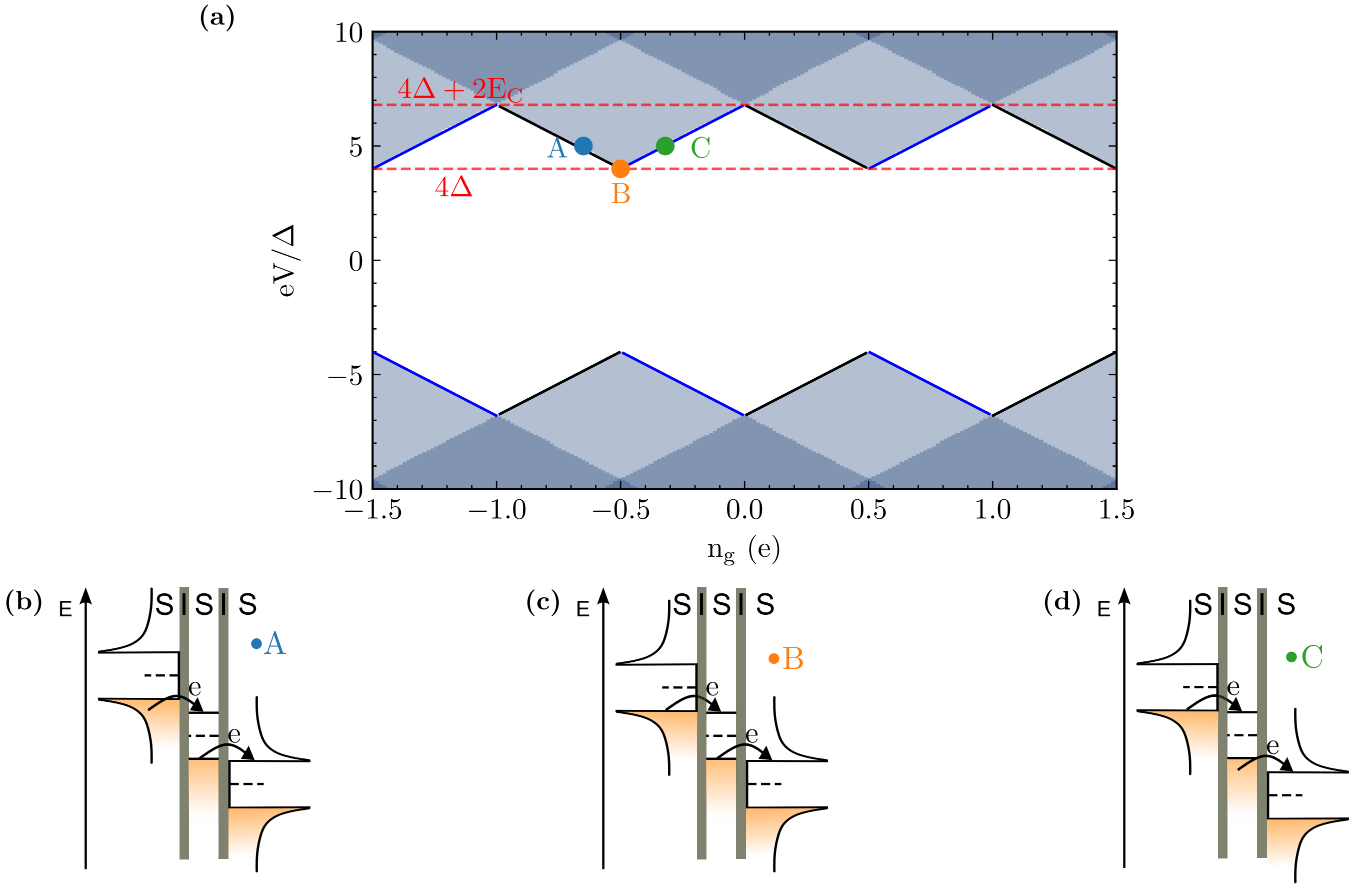

Figure 5.2: (a)Tunneling through a single electron transistor in a superconducting state for $\alpha_1 = \alpha_2 = 0.5$ and $E_C = 1.4\Delta$. In the white region, known as Coulomb diamonds, the tunneling is prohibited, and no current can flow through the SET. Black solid lines represent resonant tunneling through junction one, and blue solid lines through junction two. Quasiparticle tunneling corresponding to points A, B and C is shown in panels (b), (c) and (d) respectively.

presented in section 1.2.1, now including the electrostatic energy gain. Defining

$$\delta E^{\pm} = 2E_C(1/2 \pm (n_e - n_g)), \tag{5.7}$$

where δE^+ corresponds to the energy gain associated with adding a quasiparticle to the SET island and δE^- to removing it, the resulting forward tunneling rates through the two junctions are

$$\overrightarrow{\kappa_1}(V) = \gamma_1(\alpha_1 V - \delta E^+) \tag{5.8}$$

$$\overrightarrow{\kappa_2}(V) = \gamma_2(\alpha_2 V - \delta E^-) \tag{5.9}$$

where α_1 and α_2 are given by the equation 5.5, and

$$\gamma_i(V) = \frac{1}{e^2 R_{\mathrm{T_i}}} \int_{-\infty}^{\infty} \mathrm{d}E\, n_L(E) n_R(E + eV) f(E)(1 - f(E + eV)) \tag{5.10}$$

is the single junction forward tunneling rate discussed in section 1.2.1. Resistance $R_{\mathrm{T_i}}$ is the resistance of the particular junctions in the SET (see figure 5.1). The Fermi-Dirac distributions correspond to the two junction electrodes. In all the discussions in this thesis, we assume that all three SET electrodes are identical.

The tunneling rates depend on the number of excess electrons on the island n_e, and the gate charge n_g. Note that the forward tunneling through junction one (see figure 5.1) increases the number of quasiparticles on the island, while the forward tunneling through junction two decreases it. The reverse tunneling rates can be derived similarly, resulting in

$$\overleftarrow{\kappa_1}(V) = \gamma_1(-\alpha_1 V + \delta E^-) \tag{5.11}$$

$$\overleftarrow{\kappa_2}(V) = \gamma_2(-\alpha_2 V + \delta E^+). \tag{5.12}$$

The net current through junction i is then

$$I_i(V) = e(\overrightarrow{\kappa_i}(V) - \overleftarrow{\kappa_i}(V)). \tag{5.13}$$

However, we again restrict ourselves to positive bias voltages close to $4\Delta/e$. At these voltages, the reverse tunneling can be safely neglected, and the current is

$$I_i(V) = e\kappa_i(V) \tag{5.14}$$

where $\kappa_i = \overrightarrow{\kappa_i}$ and we drop the superscript. We apply this approximation throughout this chapter.

The tunneling through the SET, and particularly its dependence on gate charge has been measured in many experiments, starting with Fulton and Dolan [76]. At bias voltage $eV = 4\Delta$, for a symmetric superconducting SET, tunneling is allowed only when the gate offset charge satisfies $n_g = n/2, n \in \mathbb{N}$ (see figure 5.2). Thus, by fixing the junction bias voltage and gate charge to these values, and monitoring the current flowing it, one can measure very small changes in the charge surrounding the SET.

SET-based electrometers are widely utilized for single charge counting. However, these devices are limited by their slow operation speed, usually in the kHz range. To overcome this, a double junction is coupled to a resonator, resulting in a radio-frequency single-electron transistor (see figure 5). Instead of observing the DC current through the SET, reflected power at resonator frequency is measured, amounting to monitoring the differential conductance of the junction. In addition to allowing for faster detection, the high frequency measurements improve the charge sensitivity due to a reduction in $1/f$ noise. The RF-SET was first realized by Schoelkopf et al. [48], and has been commonly used in charge detection experiments, with bandwidths on the order of 100 MHz and sensitivity reaching $0.9 \cdot 10^{-6}\,\mathrm{e}/\sqrt{\mathrm{Hz}}$ [49], due to exceedingly large charging energy. However, the inelastic processes in RF-SETs have not gotten much attention. We give a brief theoretical description of these processes below, and explore them experimentally in more detail later in this chapter.

5.1.2 Inelastic Tunneling

To calculate the inelastic tunneling rates, we follow a similar procedure to the one presented in section 1.2.2. We assume that the single-electron transistor is coupled to a resonator of frequency ω, and characteristic impedance Z_c. The tunneling thresholds 5.6 become:

$$\alpha_i eV \geq 2\Delta + E_C(2n_e - 2n_g + 1) + l\hbar\omega \tag{5.15}$$

where l is the number of photons emitted into the resonator per tunnelled quasiparticle. These thresholds are shown in figure 5.3a. For the sake of simplicity, we only consider single-photon processes. The discussion involving multiple photons is analogous. We see a series of steps that are $2\hbar\omega/e$ wide in bias voltage. These steps correspond to the inelastic processes, where the quasiparticle tunneling is followed by single-photon emission or absorption. The prefactor 2 appears due to voltage division between the two junctions. The quasiparticle tunneling corresponding to three different bias and gate voltage combinations is shown in figures 5.3b-5.3d. At bias voltage $eV = 4\Delta - 2\hbar\omega$ (figure 5.3c), the tunneling is only possible at $n_g = n/2, n \in \mathbb{N}$, and only if both junctions absorb a photon. At $eV = 4\Delta - \hbar\omega$, the processes where tunneling involving photo-assisted tunneling through one junction, and elastic tunneling through the other are allowed (figures 5.3b and 5.3a).

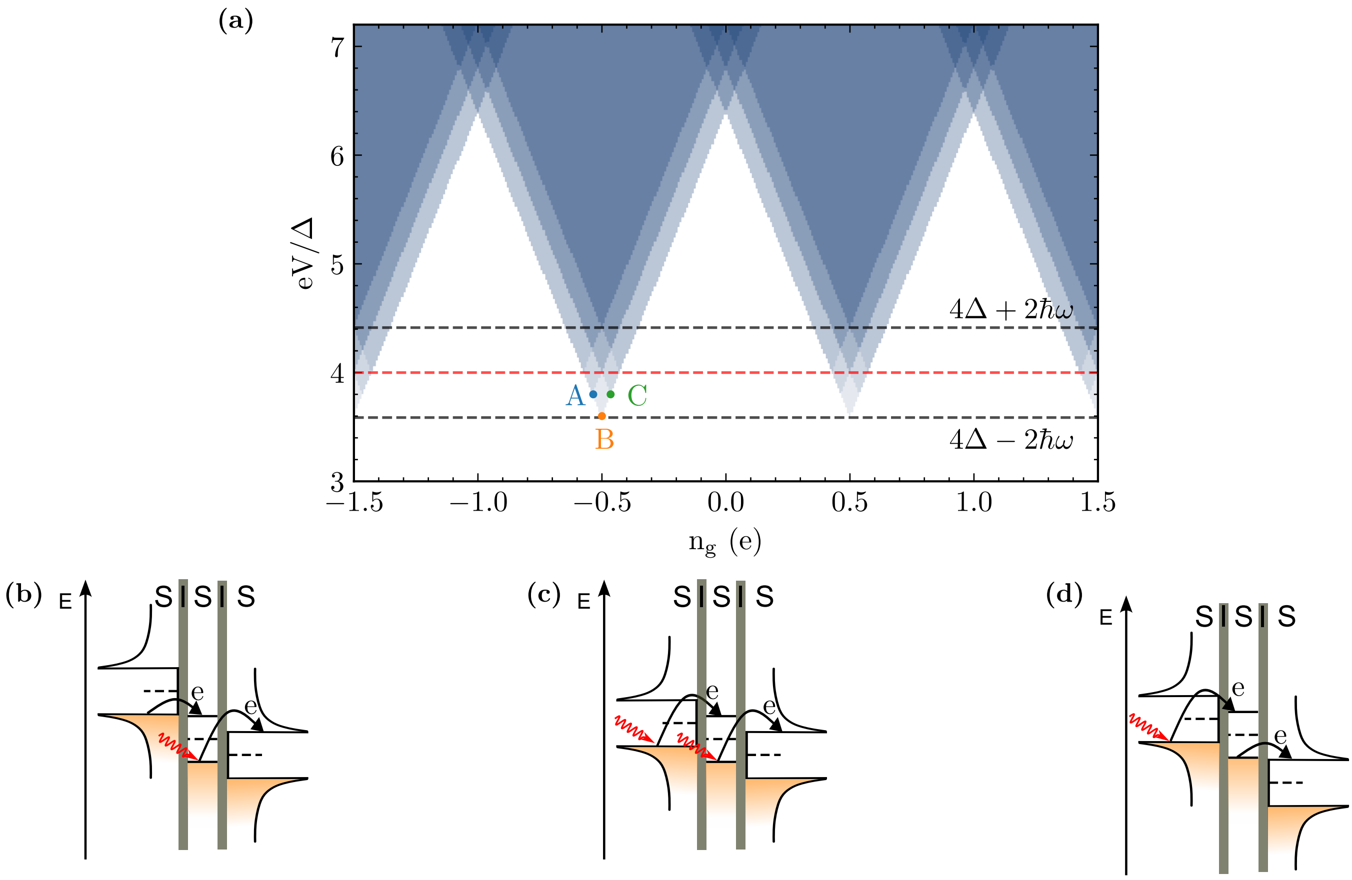

Figure 5.3: (a)Tunneling thresholds, including single-photon inelastic processes, for a single electron transistor in a superconducting state for $\alpha_1 = \alpha_2 = 0.5$, $E_C = 1.4\Delta$, and $\omega/\Delta = 0.2$. Quasiparticle tunneling corresponding to points A, B and C is shown in panels (b), (c) and (d) respectively.

The Fermi's golden rule calculation for the inelastic tunneling rates is analogous to the single junction case. For example, the forward tunneling rate through junction one, corresponding to a change in resonator state $|n_{ph}\rangle \rightarrow |n_{ph}+l\rangle$ is:

$$\overrightarrow{\kappa}_1^{n_{ph},n_{ph}+l}(V) = \left|\langle n_{ph}+l|\, e^{i\lambda_1(a+a^\dagger)}\, |n_{ph}\rangle\right|^2 \overrightarrow{\kappa}_1(V - l\hbar\omega/e) \tag{5.16}$$

where κ_1 is the elastic forward tunneling rate given by the equation 5.11, a and $a^\dagger$ are the resonator mode ladder operators, and λ_1 is the coupling parameter, which describes the coupling between the resonator and junction one. Using equation 5.11, the rate $\overrightarrow{\kappa}_1^{n_{ph},n_{ph}+l}$ can be rewritten in terms of the single junction forward tunneling rate $\gamma_1(V)$:

$$\overrightarrow{\kappa}_1^{n_{ph},n_{ph}+l}(V) = \left|\langle n_{ph}+l|\, e^{i\lambda_1(a+a^\dagger)}\, |n_{ph}\rangle\right|^2 \gamma_1(\alpha_1 V - \delta E^+ - l\hbar\omega/e). \tag{5.17}$$

Similarly, the forward tunneling rate through the second junction is

$$\overrightarrow{\kappa}_2^{n_{ph},n_{ph}+l}(V) = \left|\langle n_{ph}+l|\, e^{i\lambda_2(a+a^\dagger)}\, |n_{ph}\rangle\right|^2 \gamma_2(\alpha_2 V - \delta E^- - l\hbar\omega/e). \tag{5.18}$$

We again neglect reverse tunneling, and restrict the SET bias to positive values. Hence, we will drop the arrow superscript in $\overrightarrow{\kappa}_1^{n_{ph},n_{ph}+l}$ and $\overrightarrow{\kappa}_2^{n_{ph},n_{ph}+l}$, and write

$$\kappa_1^{n_{ph},n_{ph}+l}(V) = \left|\langle n_{ph}+l|\, e^{i\lambda_1(a+a^\dagger)}\, |n_{ph}\rangle\right|^2 I_1(\alpha_1 V - \delta E^+ - l\hbar\omega/e)/e \tag{5.19}$$

$$\kappa_2^{n_{ph},n_{ph}+l}(V) = \left|\langle n_{ph}+l|\, e^{i\lambda_2(a+a^\dagger)}\, |n_{ph}\rangle\right|^2 I_2(\alpha_2 V - \delta E^- - l\hbar\omega/e)/e \tag{5.20}$$

where $I_i(V) = e\gamma_i(V)$ is the single junction current-voltage characteristic in absence of the electromagnetic environment.

As described in detail in Chapter 1, the resonator-junction coupling parameter λ is proportional to the zero-point fluctuations of flux, and thus the ac voltage drop across the junction. Therefore, we expect the total SET-resonator coupling to be distributed across the two junctions of the SET in a manner analogous to the dc voltage:

$$\lambda_i = \alpha_i \lambda \tag{5.21}$$

where λ is the total resonator-SET coupling parameter given by $\lambda = \sqrt{\pi Z_c/R_K}$, with Z_c being the characteristic impedance of the resonator mode.

The discussion comparing the weak and strong coupling regime, detailed in section 1.2.2 also holds for the SET. As we are considering the junctions coupled to high-impedance resonators, the rates depend on the resonator state, and we have to take multi-photon processes into account when describing the dynamics of the system. Additionally, now we have to include the number of excess electrons on the SET island into the tunneling rate calculations. We do so to model the microwave emission of an RF-SET with the help of a classical master equation. The results are shown in section 5.5.1.

5.2 Sample and the Experimental Setup

In the previous section we have given a concise overview of quasiparticle tunneling in an RF-SET. We now turn to describing the device we have fabricated to study it, as well as the experimental setup. Firstly we describe the sample in 5.2.1. We then briefly outline the low temperature experimental setup in section 5.2.2, and extract the resonance frequencies, junction-SET coupling parameters, and the SET tunneling resistances in section 5.2.3.

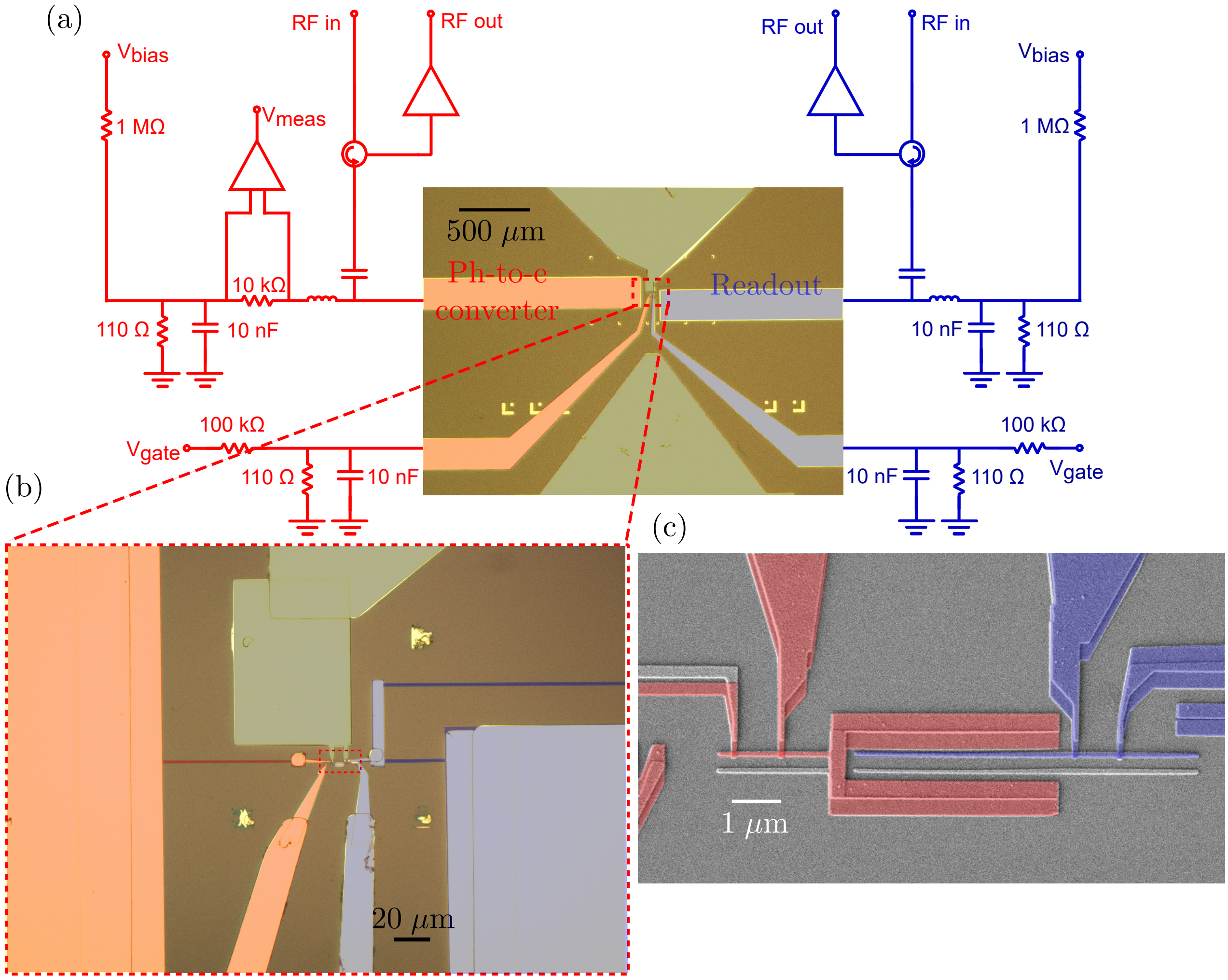

Figure 5.4: (a) A simplified scheme of the experimental setup for the double RF-SET experiment with an optical image of the sample. Photon-to-electron converter and the circuit connected to it are in red, while the readout RF-SET, and the corresponding circuit are in blue. Horizontal waveguides incoming from the left and the right are 50 Ω transmission lines connecting the RF-SETs to the rest of the setup. Gate electrodes, one for each transistor, commence from the bottom right and bottom left hand corners. Ground plane is visible in the top and the bottom of the picture, colored grey. (b) Area outlined by the red dashed rectangle in panel (a). Photon to electron converter RF-SET is shown in the left of the picture, with the grAl resonator terminated by a SISIS double junction. In contrast, in the readout RF-SET seen on the right, the junction is placed close to the end of the resonator coupled to the feedline, in order to reduce the junction-resonator coupling. Red dashed rectangle represents the area of the sample shown in panel (c). Scanning electron micrograph corresponding to the area outlined by the red dashed rectangle in panel (b).

5.2.1 Sample Description

The sample is fabricated an oxidised silicone chip using standard electron-beam lithography and evaporation techniques. Fabrication details can be found in Appendix B. The image of the sample is shown in figure 5.4(a).

The sample consists of two capacitively coupled RF-SETs. The converter SET (on the left), and the readout SET (on the right). To detect photons of energy $\hbar\omega_c$, a SET is coupled to a quarter-wavelength resonator with fundamental mode ω_c, constituting the photon to electron converter shown in red in figure 5.4(b). The resonance frequency is chosen to be in the upper end of 4 - 12 GHz band, where the microwave measurements are possible. Higher frequency enables us to operate the detector at bias voltages further away from the superconducting gap, thus reducing the potential dark current. The SET is connected to the end of the resonator with the help of an aluminium patch. The converter RF-SET is capacitively coupled to the readout RF-SET, colored blue. In contrast to the photon to electron converter, the junction is placed 30 µm from the beginning of the 255 µm resonator, reducing the impedance seen by the junction, and thus decreasing the coupling between the SET and the resonator. The readout resonator is designed so that the fundamental frequency is slightly above 4 GHz, to be in range suitable for reflection measurements, and to increase the distance from the converter RF-SET resonance frequency as much as possible.

All transmission lines are fabricated in a microstrip geometry. Two horizontal waveguides, on either side of the picture, correspond to the 50 Ω waveguides connecting the RF-SET resonators to the rest of the experimental setup. Leads commencing from the bottom right and bottom left corners are the gate electrodes of the readout and the converter respectively. The ground plane, colored grey, is visible in the top and the bottom. Zoom of the area outlined by a red dashed rectangle is shown in figure 5.4(b). Two grAl nanowires are visible. The shorter horizontal nanowire on the left hand side, colored red, is the converter resonator, while the Π shaped resonator, on the right, in blue, is a part of the readout RF-SET. The resonators are galvanically coupled to the transmission lines, enabling voltage biasing of the single-electron transistors. Granular aluminium is used in fabrication of both resonators. Using a high kinetic inductance material, such as grAl, for resonator fabrication in an RF-SET eliminates the need for lumped-element resonant circuits used in the first RF-SETs [48, 77], or separate fabrication of tank circuits (see e.g. [75]). In addition to more straightforward fabrication, higher quality factors are achievable, leading to potential improvements in charge sensitivity. The characteristic impedance seen by the SET can also be easily controlled by choosing the position of the junction along the resonator. This enables us to balance between the higher impedance needed for better power transfer between the junction and the resonator, and lower impedance needed to reduce the influence of inelastic processes on charge detection. We exploit this tunability by placing the junction close to the beginning of the resonator in the readout RF-SET. As outlined in detail in section 5.2.3, this reduces the characteristic impedance seen by the SET compared to the photon-to-electron converter, while using the grAl is of approximately the same sheet resistance.

Scanning electron micrograph of the two SETs, seen in the centre of the picture, is shown in figure 5.4(c). Circuit coloured blue corresponds to the readout single-electron transistor, consisting of two junctions. The junctions share one electrode — a superconducting island 7 µm long and approximately 120 nm wide. The left junction is grounded on one side, while the right one is connected to the resonator via an aluminium patch. Gate electrode is visible to the right of the island. The SET utilized for photon to electron conversion is shown in red. Its central island is shaped as a tuning fork, in order to increase the coupling to the readout circuit. Right hand side junction of the converter transistor is grounded, while the left is attached to the high impedance resonator.

The equivalent circuit of the sample described above, with the relevant parameters highlighted is shown in figure 5.5. We characterize the sample below, starting by determining the resonance frequencies ω_c and ω_{ro}, and resonator-SET coupling parameters λ_c and λ_{ro} in sectioin 5.2.3.

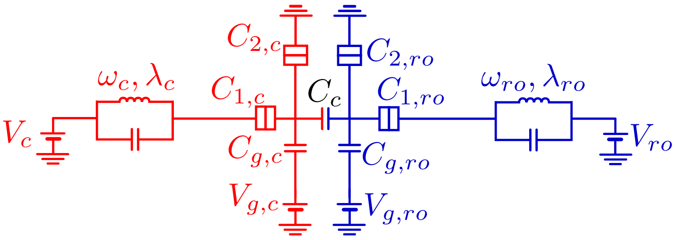

Figure 5.5: Scheme of the double RF-SET sample, with relevant parameters highlighted.

5.2.2 Experimental Setup

The sample described in the preceding section is glued to a sample holder (figure 5.6), which is then tightly closed, anchored to the mixing chamber plate of a dilution refrigerator with base temperature of 20 mK, and connected to the rest of the experimental setup. The low temperature part of the experimental setup is shown in figure 5.7. It is similar to the single junction experiment setup described in Chapter 3. The circuits for readout and photon-to-electron converter RF-SETs are analogous. Both the input and output RF lines consist of 50 Ω coaxial cables, with the total attenuation of −70 dB per line. Upon the reflection of the RF-SET, the microwave excitation is directed to the detection line via Low Noise Factory double-junction circulators. The signal is then amplified by HEMT amplifiers anchored at the 3 K stage of the dilution fridge, and then amplified again at room temperature. The measurement frequency bands are set by the choice of circulators and low noise amplifiers. The converter circuit is connected to the 4 - 12 GHz circulator, and the LNF-LNC0.3_14B amplifier, while the readout RF-SET is connected to the 4 - 8 GHz circulator and LNF-LNC4_8F amplifier.

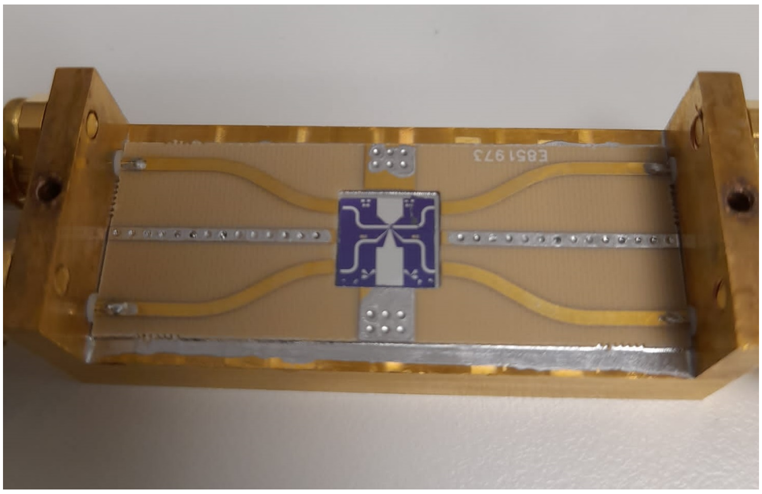

Figure 5.6: Sample holder containing the coupled RF-SET device. The two transmission lines at the top of the picture are used for biasing the RF-SETs, while the two lines in the bottom are bonded to the two gate electrodes. The box is connected to the rest of the setup through SMA ports.

The dc circuit consists of four voltage dividers for setting the two gate and two bias voltages. Additionally, a 10 kΩ resistor is placed in series with the converter RF-SET voltage divider. The current flowing through the photon-to-electron converter is measured by monitoring the voltage

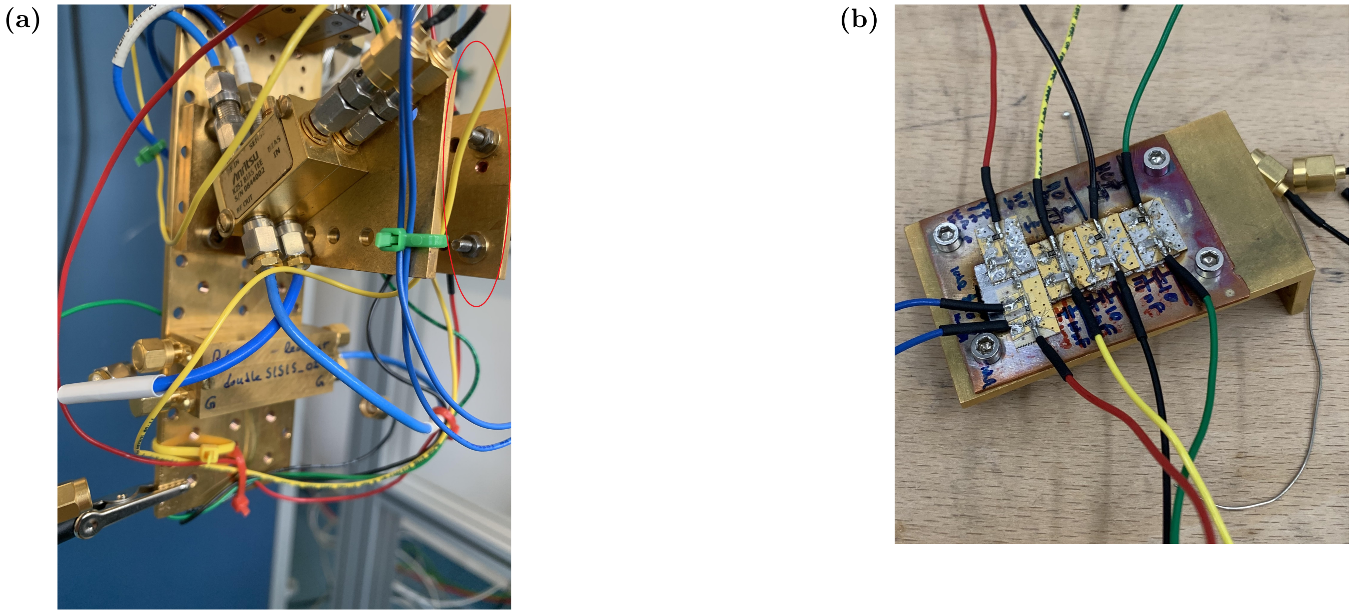

Figure 5.7: (a) Mixing chamber of the dilution fridge. The sample holder box is anchored to the bottom of the plate. Above, two bias-tees are visible. Blue Mini-Circuits coaxial cables are used for the high-frequency circuit, while the copper wire cables are used to connect the dc components. (b) The plate with low temperature dc components circled in red in panel (a). The circuit consists of four resistors used for voltage division, with capacitors added in parallel for filtering the high-frequency noise. A 10 kΩ resistor is soldered in series with one of the dividers. The current flowing through the photon-to-electron converter is monitored by measuring the voltage drop across this resistor

drop across this resistor. All dc components placed at low temperature are soldered to a metal plate shown in figure 5.7b. The plate is then fixed to the fridge mixing chamber. The dc and microwave excitations are combined before reaching the sample using bias-tees anchored to the mixing chamber plate of the fridge,

5.2.3 RF-SET Characterization

We now turn to characterizing the two RF-SETs independently. To begin with, we determine the junction-resonator coupling parameters using the transfer matrix model. Then, we show the evolution of reflection spectra with junction bias for the two resonators, and extract the loss rates in the readout circuit.

Determining junction-resonator coupling

The coupling parameters for the two transistors are extracted from 1D model simulation of the resonators. The grAl kinetic inductance used in simulations is obtained from measuring the sheet resistance of nanowires placed next to the sample. The grAl sheet resistance is $R_\square = 620\,\Omega/\square$. From equation 1.81, we calculate the kinetic inductance to be $L_\square \approx 400\,\mathrm{pH}/\square$. The same value is used for both resonators. The capacitance per unit length is deduced from Sonnet simulations.

Converter RF-SET — The converter RF-SET resonator is 62.5 µm long and 350 nm wide. To simplify the calculations, the nanowire is terminated by a single capacitor representing the capacitance of the pad used for patching, as well as the total equivalent capacitance of the single-electron transistor. The capacitance needed to reproduce the resonance frequency $\omega_c = 2\pi \times 10.86\,\mathrm{GHz}$ of the fundamental resonator mode determined from reflection spectra (see figures 5.9a and 5.10a) is 2.2 fF, in agreement with the expectations based on patch size, as well as anticipated junction capacitance. The spatial dependence of the fundamental resonator mode is shown in figure 5.8a. Characteristic impedance of the mode seen by the junction, calculated from equation 1.19 is 4.7 kΩ. The total coupling between the transistor-circuit and the resonator is $\lambda_\mathrm{c} = 0.76$.

Readout RF-SET — The readout resonator consists of two grAl nanowires, 350 nm wide and 30 µm and 185 µm long, separated by a layer of aluminium 40 µm long and 5 µm wide (see the right hand side of figure 5.4(b)). Although the resonator structure is not one-dimensional, we neglect the geometric effects and use the same transfer matrix model to calculate the mode properties. As noted above, the grAl inductance is calculated from the nanowire resistivity measurements, while the aluminium inductance and all capacitances are extracted from Sonnet simulations. In contrast to the photon-to-electron converter, the readout SET is not placed at the end of the resonator. Rather, the SET is connected to the aluminium layer, at the end of the first grAl portion of the structure. As the junction-mode coupling is proportional to the voltage seen by the junction, placing the SET close to the 50 Ω feedline effectively reduces λ. For the fundamental mode resonance frequency and characteristic impedance, we obtain $\omega_\mathrm{ro} = 2\pi \times 4.88\,\mathrm{GHz}$ and $Z_{ro} = 0.4\,\mathrm{k\Omega}$, resulting in the coupling parameter value of $\lambda_\mathrm{ro} = 0.21$. This weak coupling between the mode and the transistor is desirable to reduce the impact of photo-assisted processes on the charge detection The extracted resonance frequency is very close to the experimentally measured value of $\omega_{ro} = 2\pi \times 4.815\,\mathrm{GHz}$ (see figures 5.9b and 5.10b). The minor disagreement can be assigned to the systematic uncertainty in sample parameters. However, the coupling rate cannot be estimated using the transfer matrix model. It is measured to be $2\pi \times 16\,\mathrm{MHz}$, several times lower than the model estimate of $s\pi \times 88\,\mathrm{MHz}$. Again, it is believed that this disagreement stems from the width mismatch between the feedline and the grAl nanowire (220 µm compared to 350 nm), especially since the resonator is placed close to the corner of the feedline (see figure 5.4(b)).

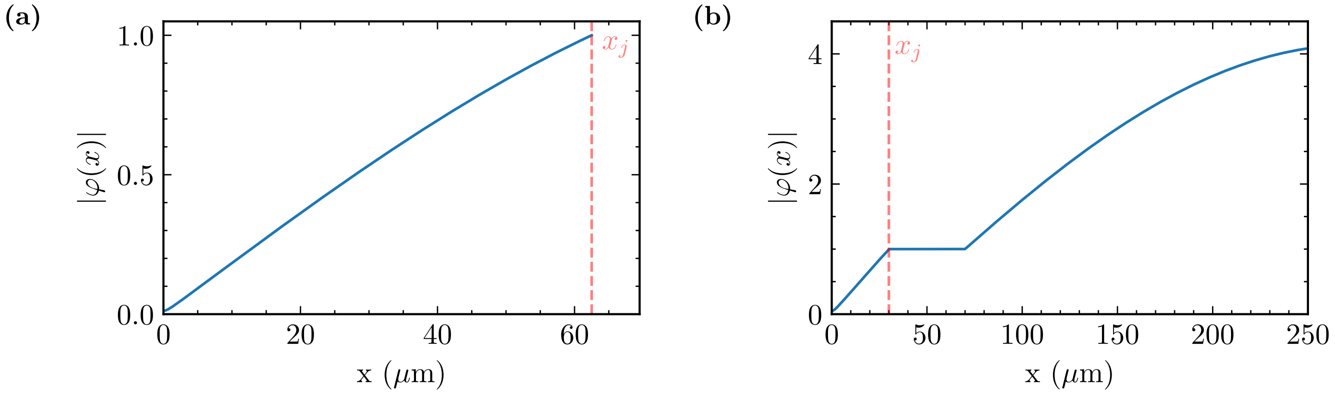

Figure 5.8: Spatial dependence of fundamental resonator modes normalized such that $|\varphi(x_j)| = 1$ (a) Photon-to-electron converter resonator (b) Readout resonator

Estimating SET tunneling resistance

The tunneling resistance of the photon-to-electron converter SET at low temperature is $R_\mathrm{c} = 980\,\mathrm{k\Omega}$.The measurement configuration did not allow dc-measurement of the readout SET at 20 mK.

However, based on the room temperature resistance measurements (800 kΩ compared to the 610 kΩ for the converter SET) we expect it to be in the 1.1 - 1.2 MΩ range.

RF-SET Reflection Spectra

To further characterize the sample, we rely on high-frequency measurements. We start by showing, in figure 5.9, the reflection spectra of the two resonators as functions of junction bias. The gate voltage is fixed to $V_{g,c} = V_{g,ro} = 0$ for the duration of the measurement.

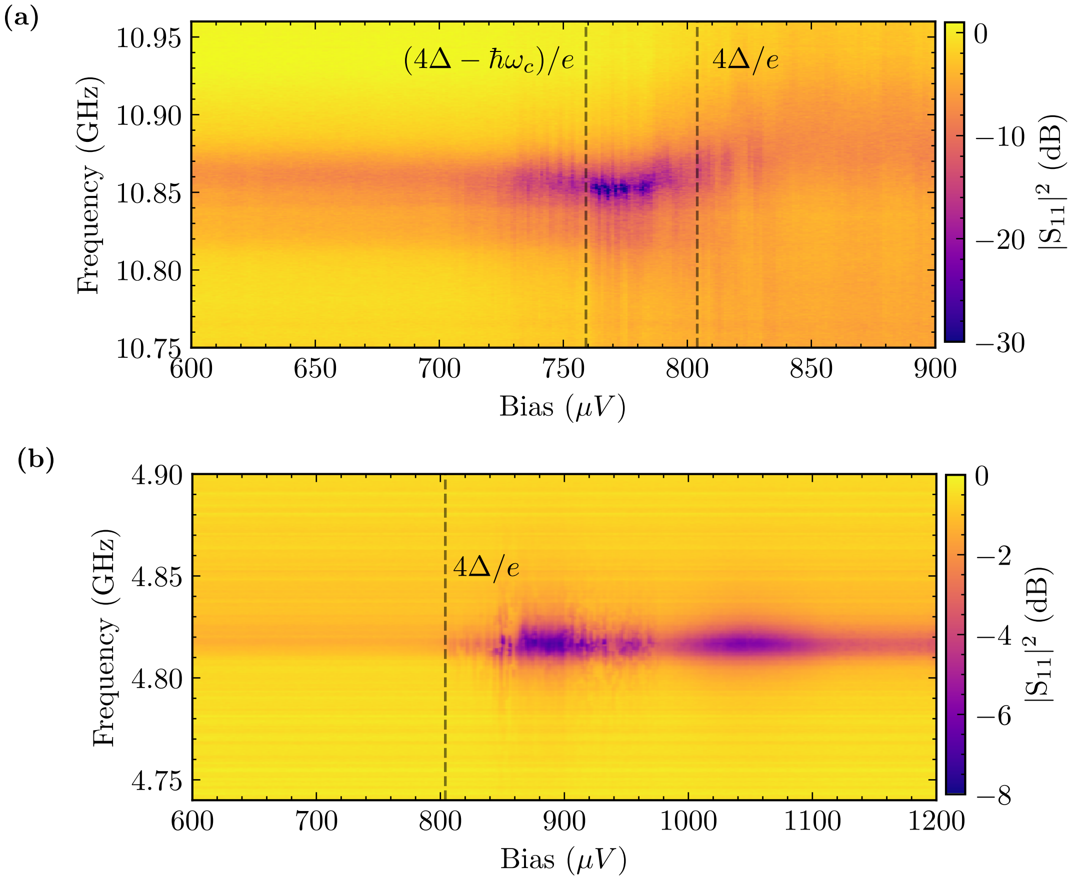

Figure 5.9: Reflection spectra as function of SET bias voltage for zero gate voltage. (a) Converter resonator. (b) Readout resonator

Converter RF-SET — First, let us consider the converter RF-SET (figure 5.9a). Similarly to the single junction case, we observe in the bias range close to the superconducting gap where microwave reflection is low. We find a resonance at $\omega_c = 2\pi \times 10.86\,\mathrm{GHz}$ well below the superconducting gap. The resonance slightly shifts lower in frequency when approaching the gap, as expected due to the Lamb shift. The bias voltage values corresponding to this range should vary periodically with gate charge between $eV = 4\Delta - 2\hbar\omega_c$ and $eV = 4\Delta - 2\hbar\omega_c + 2E_{C_c}$, where E_{C_c} is the charging energy of the SET. Resonance spectra for two different bias voltages — one well below the superconducting gap, and one close to $eV = 4\Delta$ are shown in figure 5.10a. The drop in reflection between the two bias voltages is greater than 20 dB. The spectra do not conform to the expected Lorentzian shape, and the fit to the equation 1.72 does not converge, meaning that we are unable to determine the loss rates precisely. However, rough estimates are $\kappa_{c,c} \approx 2\pi \times 40\,\mathrm{MHz}$, and $\kappa_{i,c} \approx 2\pi \times 15\,\mathrm{MHz}$.

Readout RF-SET — We now direct our attention to the readout resonator (figure 5.9b). We notice the resonance at $\omega_{ro} = 2\pi \times 4.815\,\mathrm{GHz}$. There is no discernable Lamb shift, in agreement with smaller coupling parameter λ_{ro}. The area of increased microwave absorption close to the superconducting gap is still noticeable. From the two spectra shown in figure 5.10b, we conclude that the absorption is not as high as in the photon-to-electron converter SET. To obtain the resonator loss rates, we fit the resonance spectra to equation 1.72. The coupling to the transmission line is given by $\kappa_{c,ro} = 2\pi \times 16\,\mathrm{MHz}$, and stays constant with changing junction bias. The intrinsic losses well below the gap are estimated to be $\kappa_{i,ro} = 2\pi \times 0.6\,\mathrm{MHz}$, resulting in the intrinsic quality factor of $Q_i \approx 8 \cdot 10^3$. Total junction loss rate κ_j stays below $2\pi \times 6\,\mathrm{MHz}$ in the full bias range.

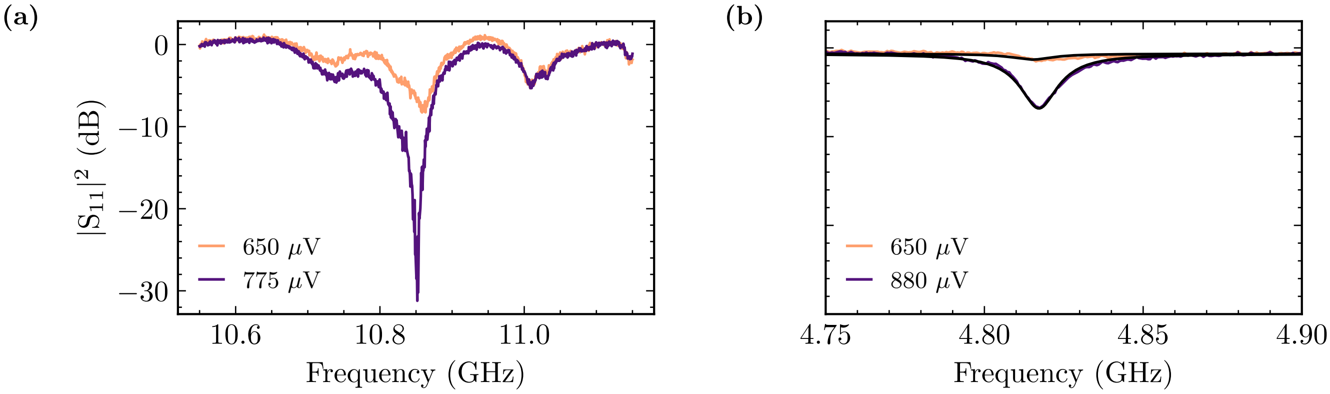

Figure 5.10: Reflection spectra for two different bias voltages. (a) Converter RF-SET, showing critical coupling (b) Readout RF-SET. Black solid lines represent the circle fits to equation 1.72.

5.2.4 Conclusion

To recapitulate, we have fabricated a device consisting of two capacitively coupled RF-SETs, a photon-to-electron converter RF-SET where the resonator is strongly coupled to the junction to boost the inelastic tunneling, and a readout RF-SET with lower resonator-SET coupling to optimize charge detection. The resonator parameters are summarized in table 5.1.

Parameter	Converter	Readout
$\omega/2\pi$ (GHz)	10.86	4.815
$\kappa_c/2\pi$ (MHz)	≈ 40	16
$\kappa_i/2\pi$ (MHz)	≈ 15	0.6
λ	0.76	0.21
R_T (MΩ)	0.98	≈ 1.1

Table 5.1: Parameters of the two RF-SETs.

To further characterize the sample, and determine the parameters such as charging energies, coupling capacitance between the two SETs or asymmetry in the transistor junctions, we measure the evolution of microwave absorption and emission with gate voltage. To avoid low frequency gate noise due to movement of background charges, we fix the microwave frequency to resonance, and perform the measurements in the continuous wave mode, while constantly sweeping the gate and bias voltages.

5.3 Reflection Spectroscopy

In this section, we present the reflection measurements carried out on the two RF-SETs. The shown measurements are performed at the base fridge temperature of 20 mK, and in continuous wave mode at resonance frequency unless otherwise noted. First, we present the reflectometry measurements on the readout (section 5.3.1), and the converter (section 5.3.2) separately. We then show how the readout RF-SET can be used to measure the tunneling through the converter SET, and extract the coupling capacitance between the two SETs, C_c (section 5.3.3). We are able to detect charge flow through the converter SET, but not the individual tunneling events, because the converter tunneling rates are too high.

5.3.1 Spectroscopy of the Readout RF-SET

First, we consider the readout RF-SET. The reflected power at resonance frequency $\omega_{ro} = 2\pi \times 4.816\,\mathrm{GHz}$ as function of SET bias and gate voltages is shown in figure 5.11. The applied microwave pump power is $P = -119\,\mathrm{dBm}$, which is equivalent to the resonator population of $\langle n_{\mathrm{res}} \rangle \approx 16$ well below the superconducting gap. We observe several copies of Coulomb diamonds due to different

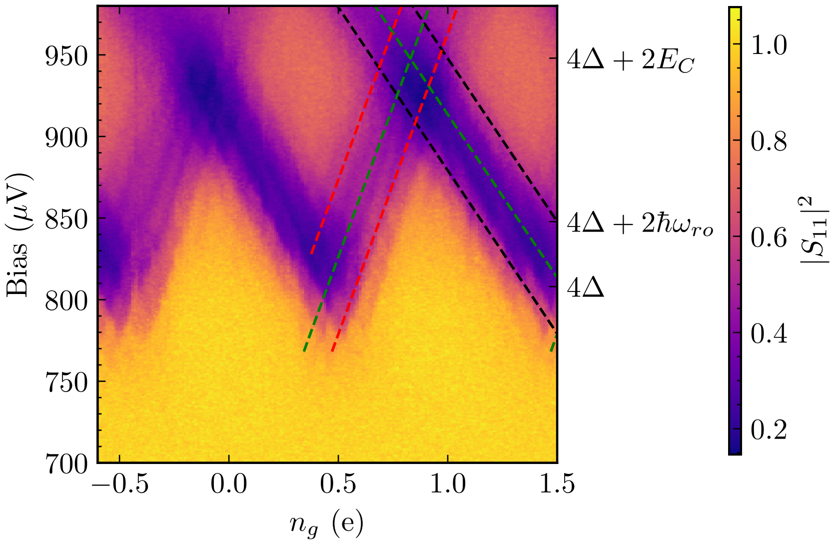

Figure 5.11: Reflection at resonance as function of gate and bias voltages for the readout RF-SET. Several copies of Coulomb diamonds are visible, corresponding to inelastic tunneling processes. Green dashed lines are the Coulomb diamonds delimiting elastic tunneling thresholds. From the slope of these lines we extract the SET asymmetry: $\alpha_{1,ro} = 0.58, \alpha_{2,ro} = 0.42$. The black dashed lines represent the inelastic tunneling thresholds fo the first junction, and they are offset by $\pm\hbar\omega_{ro}/\alpha_{1,ro}$ in bias compared to the elastic tunneling threshold. Similarly, the red dashed lines correspond to inelastic tunneling through the second junction, and are offset by $\pm\hbar\omega_{ro}/\alpha_{2,ro}$ compared to the green line.

inelastic processes outlined in section 5.1.2. The structure is periodic in gate voltage, with the period of $\Delta V_{g,ro} = 5.8\,\mathrm{mV}$, indicating that the gate capacitance is $C_{g,ro} = e/\Delta V_{g,ro} \approx 30\,\mathrm{aF}$. The elastic Coulomb diamonds are outlined by the green dashed lines. The charging energy of the readout SET, obtained from estimating the height of the Coulomb diamond is

$$E_{C,ro} \approx 65\,\mathrm{\mu eV}, \tag{5.22}$$

corresponding to the total island capacitance of

$$C_{\Sigma,ro} = \frac{e^2}{2E_{C,ro}} = 1.2\,\mathrm{fF} \tag{5.23}$$

From the slopes of elastic Coulomb diamonds, we extract the SET asymmetry described by

$$\alpha_{1,ro} = 0.58 \tag{5.24}$$

$$\alpha_{2,ro} = 0.42. \tag{5.25}$$

From the equation 5.5, the junction capacitance is $C_{1,ro} = 0.5\,\mathrm{fF}$. Based on the SEM images of the sample (see figure 5.4), we assume that the two junctions are equal in size, and that the asymmetry is present due to the island ground capacitance, which is included only in $\alpha_{2,ro}$, but not in $\alpha_{1,ro}$. Thus, $C_{2,ro} = C_{1,ro} = 0.5\,\mathrm{fF}$, and the ground capacitance of the island is $C_{gr,ro} = 0.2\,\mathrm{fF}$. The size of the two junctions is similar, and it is approximately $100 \times 120\,\mathrm{nm}^2$. Thus, we get for the junction capacitance $C_j = 40\,\mathrm{fF/\mu m^2}$.

Based on the equation 5.21, the resonator coupling parameters for the individual junctions in the readout SET are

$$\lambda_{1,ro} = \alpha_1\lambda_{ro} = 0.12 \tag{5.26}$$

$$\lambda_{2,ro} = \alpha_2\lambda_{ro} = 0.09. \tag{5.27}$$

This small variation in the coupling parameters is responsible for the difference in absorption observed between the two slopes of the Coulomb diamonds corresponding to the inelastic tunneling through the first or the second junction.

In addition to the quasiparticle current, other processes involving tunneling of Cooper pairs, such as Josephson-quasiparticle (JQP) and double Josephson-quasiparticle cycles (DJQP) [78, 79, 80, 81], are possible in a superconducting single-electron transistor. However these processes were not observed in our sample due to the charging energy being too low.

5.3.2 Spectroscopy of the Converter RF-SET

We now move on to the photon-to-electron converter circuit. We use the reflectometry data to determine the charging energy, and discuss photo-assisted processes in the strong coupling regime.

Measurements on the converter RF-SET are performed off-resonance, at the frequency of 10.73 GHz to better resolve the different processes, and avoid the areas where absorption is close to zero due to the intrinsic losses of the resonator. Reflection as function of the transistor bias and gate voltages is shown in figure 5.12. As expected, several Coulomb diamond structures are visible. Similarly to the readout case, from the period in gate voltage, we extract the converter gate capacitance of $C_{g,c} \approx 80\,\mathrm{aF}$. However, the asymmetry in Coulomb diamond slopes (black dashed lines) is much

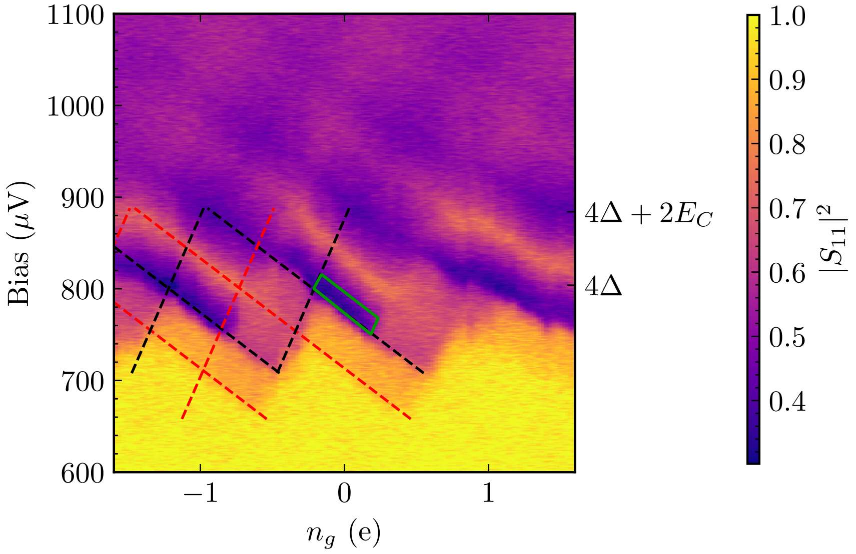

Figure 5.12: Reflection as function of gate and bias voltages for the converter RF-SET at 10.73 GHz, and $P = -109$ dBm. As in the readout circuit, several copies of Coulomb diamonds are visible, corresponding to inelastic tunneling processes. The elastic Coulomb diamonds are shown in green dashed lines, and the SET asymmetry determined from their slope is $\alpha_{1,c} = 0.75, \alpha_{2,c} = 0.25$. The red lines are offset by $\hbar\omega_c/\alpha_{1,c}$ corresponding to the width of the photo-assisted step for the first junction.

more pronounced, due to higher capacitance of the SET island to ground. The island capacitance is increased compared to the readout circuit due to its bigger size (see figure 5.4). From the data in figure 5.12, we have

$$\alpha_{1,c} = 0.75 \tag{5.28}$$
$$\alpha_{2,c} = 0.25, \tag{5.29}$$

and the charging energy is

$$E_{C,c} \approx 40\,\mu\text{eV} \tag{5.30}$$

corresponding to the total capacitance of the readout SET island:

$$C_{\Sigma,c} = \frac{e^2}{2E_{C,c}} = 2\,\text{fF} \tag{5.31}$$

Assuming that the additional capacitance compared to the readout RF-SET is due to the ground capacitance, we obtain the same value for the junction capacitance of 0.5 fF, and the ground capacitance of the converter SET island of $C_{gr,c} = 1$ fF.

The SET asymmetry is pronounced in the photo-assisted processes as well. From equation 5.21, we get

$$\begin{aligned} \lambda_{1,c} &= 0.8\lambda_c = 0.57 \\ \lambda_{2.c} &= 0.2\lambda_c = 0.19 \end{aligned} \tag{5.32}$$

Hence, we expect the asymmetry to be reflected in subgap absorption.

We indeed conclude that there is high absorption for bias voltages corresponding to values just below the resonant tunneling condition for the first junction in figure 5.12. This area in junction and bias voltages (green rectangle in figure 5.12) is the potential operating point for photon-to-electron detection.

5.3.3 Converter-readout Coupling

In the previous sections, we have discussed the two RF-SETs independently, not exploiting the fact that they are capacitively coupled. Furthermore, we have tried to suppress the mutual influence of the SET-s by biasing the non-measured SET well below the superconducting gap, to reduce the charge noise. Now we explore the coupling between the two circuits in more detail. We bias the readout SET at $V_{ro} = 785\,\mu\mathrm{V}$, where it is charge sensitive, and measure the reflection. At this bias value, the reflected signal is very sensitive to changes in gate charge (see figure 5.11). We then sweep the two SET gates. The results are shown in figure 5.13. For $V_c = 22\,\mu\mathrm{eV}$ (panel (a)), we observe a series of dips in reflection, corresponding to a change in the charge of the readout SET island, similarly to the measurement presented in section 5.3.1. However, no response is observed when the charge on the converter SET island changes. In contrast, when the converter SET is biased close to the superconducting gap (panel (b)), we observe a change in the readout reflection when the tunneling through the detector SET is allowed. The dip in reflected signal traces a series of hexagons, with each hexagon corresponding to a stable charge configuration $n_{e,c}$, $n_{e,ro}$. From the position in the $(V_{g,ro}, V_{g,c})$ plane of the points where three charge states are stable — triple points (red and green dots in figure 5.13b), we determine the coupling capacitance between the two SETs:

$$C_c = \frac{\Delta V_{\text{triple}}}{\Delta V_{g,ro}} C_{\Sigma,ro} = 0.09 C_{\Sigma,ro} = 110\,\mathrm{aF}. \tag{5.33}$$

Thus, the coupling capacitance C_c is approximately 10 % of the total readout capacitance, making it very sensitive to changes in the converter SET island. However, this is achieved at the expense of the converter charging energy due to the increase in the size of the island.

5.3.4 Discussion: Towards Photon Detection

We have shown above the reflectometry measurements of the converter and readout RF-SETs. These measurements were used to obtain several SET parameters such as charging energies, gate capacitances, as well as the coupling capacitance between the two SETs. These parameters are summarized in table 5.2.

We have detected the current flowing through the converter SET by measuring the readout reflection. However, the individual tunneling events were not observed, because the lifetime of the quasiparticle on the converter island too short. To increase it, the charging energy of the converter SET needs to be increased, especially above $2\hbar\omega_c = 90\,\mu\mathrm{eV}$, so that the quasiparticle cannot be removed from the island by absorbing a photon. This could allow us to observe single photo-assisted tunneling events in these devices. Additionally, the coupling rate of the converter resonator needs to be decreased, in order to reduce the dark photon rate below our measurement bandwidth set by the readout charge noise discussed below (see discussion on dark current in our photon-to-electron converter in section 2.4.1). This work is in progress in the group.

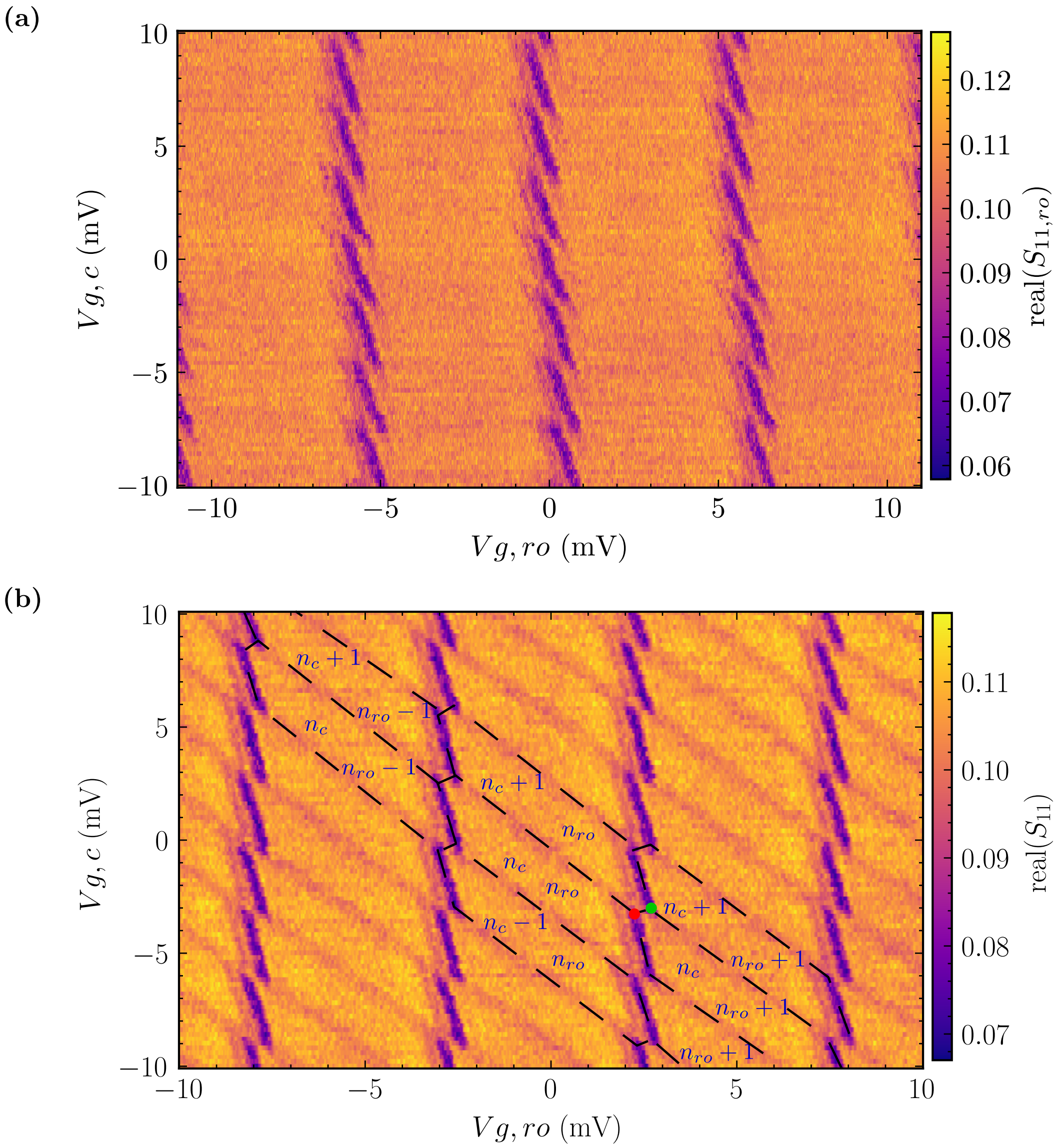

Figure 5.13: Charge stability diagrams for two different converter bias voltages: (a) $V_c = 22\,\mu\text{eV}$ (b) $V_{ro} = 800\,\mu\text{eV}$. For low detector bias we detect only the tunneling through the readout SET, while for the bias at the superconducting gap (panel (b)), we see a response in the readout reflection when the tunneling through the converter SET is allowed. The distance in gate voltage between the two triple points (red and green dots in panel (b)) is used to measure the coupling capacitance between the two SETs.

5.4 Readout Charge Noise

In the previous section we have shown how the charge flowing through the converter SET can be detected with the readout SET. We now estimate the charge noise of the readout, and vary the applied microwave drive power, and the SET bias to find the optimal operation working point.

Parameter	Converter	Readout
E_C (µeV)	40	65
C_Σ (fF)	2	1.2
C_g (aF)	80	30
α_1	0.75	0.58
α_2	0.25	0.42
λ_1	0.12	0.57
λ_2	0.09	0.16
C_c (aF)	110	

Table 5.2: SET charging energies, capacitances ans individual junction-resonator coupling parameters.

5.4.1 Gate Charge Susceptibility

The charge sensitivity is estimated from the reflection measurements versus junction bias and gate voltages, analogous to those shown in the previous section. We discuss an example of such a measurement below, and extract the detection sensitivity. The applied microwave drive power is fixed to −116 dBm, the frequency to 4.816 GHz, and the measurement bandwidth to $BW = 100\,\mathrm{kHz}$. The two gate sweeps of the readout reflection corresponding to the SET bias values of 600 µeV, well below $eV = 4\Delta$, and 800 µeV, close to $eV = 4\Delta$, are shown in the complex plane in figure 5.14. The data is rotated to maximize the information in the real quadrature. At 600 µeV (blue dots), the reflection shows no dependence on gate voltage. In contrast, at 800 µeV (red dots), there is a clear shift in reflection, corresponding to the gate voltages where the tunneling is allowed. We show this data as function of gate voltage in figure 5.15. We extract the change in the reflection with gate voltage by fitting a Lorentzian (solid black line) to the real quadrature data (blue trace), and

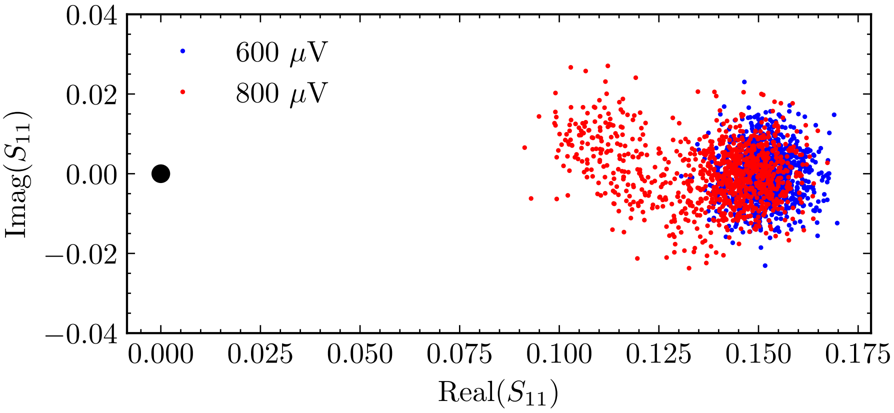

Figure 5.14: Evolution of the readout reflection with gate voltage in the complex plane for SET bias values of 600 µeV (blue dots) and 800 µeV (red dots). The applied microwave drive power is fixed to −116 dBm, and frequency to 4.816 GHz. At 600 µeV, the reflection shows no dependence on gate voltage. In contrast, at 800 µeV — just below $eV = 4\Delta$, there is a clear shift in reflection when the tunneling through the junction is allowed. At this bias voltage, the SET can be operated as a charge detector.

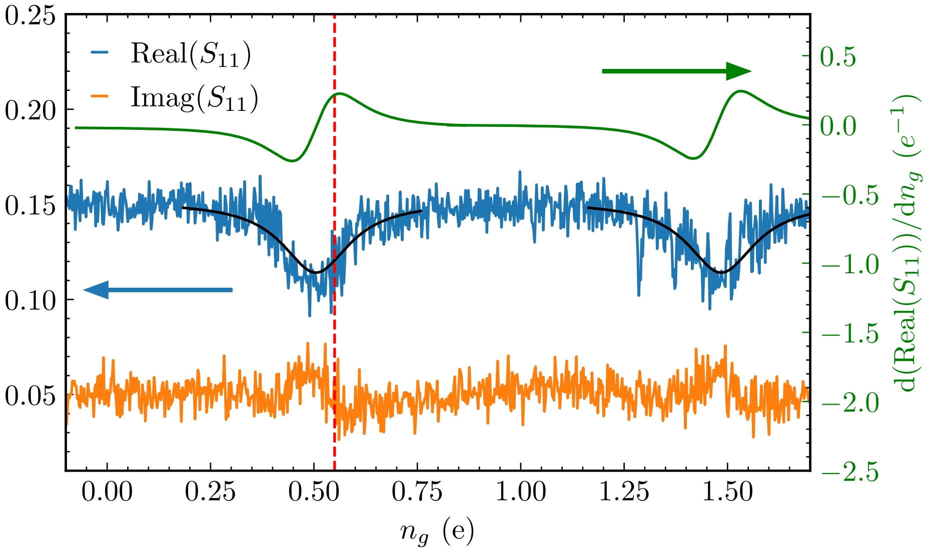

Figure 5.15: Real and imaginary parts of reflected signal as function of gate charge for SET bias of 800 µeV (red dots in figure 5.14). The peaks in real part of the reflected signal are fitted to a Lorentzian (black solid line), and the derivative of this curve (green solid line) represents the photon detection signal. The operating point of the detector is at the signal maximum highlighted by the red dashed line.

taking its derivative $\mathrm{d}(\mathrm{Real}(S_{11}))/\,\mathrm{d}n_g$, representing the gate charge susceptibility of our detector shown in green in figure 5.15. The operating point of the detector is at the maximum of charge susceptibility, highlighted by the red dashed line. The noise N is given by the Fourier transform of the trace. The charge noise is then determined from the equation

$$\delta q = \frac{N}{\mathrm{d}(\mathrm{Real}(S_{11}))/\,\mathrm{d}n_g \times BW} \tag{5.34}$$

where BW is the measurement bandwidth. The same procedure is repeated for different SET bias voltages. The evolution of charge noise with bias voltage is for three different measurement tone powers shown in figure 5.16. The charge noise is lowest close to $eV = 4\Delta - \hbar\omega_{ro}$. Above this value, we observe a periodic structure, with the period of $2E_{C,ro}$. As the power is increased, the optimal detector working point moves to lower bias voltage due to multi-photon absorption. Additionally, the minimal charge noise rises with rising power.

5.4.2 Power Dependence of the Charge Noise

To measure the power dependence of the charge noise, we fix the SET bias voltage to $eV = 4\Delta - \hbar\omega_{ro}$, where we expect the detector to have best overall charge noise. The evolution of charge noise with applied power is shown in figure 5.17. First, when the power is increased, the charge noise decreases due to better signal to noise ratio. However, close to −114 dBm, the charge noise saturates, and starts rising rapidly when the power is above −110 dBm. At high powers, the optimal working point shifts to lower bias voltage. However, even at the optimal SET bias, the charge noise rises with rising power (see figure 5.16).

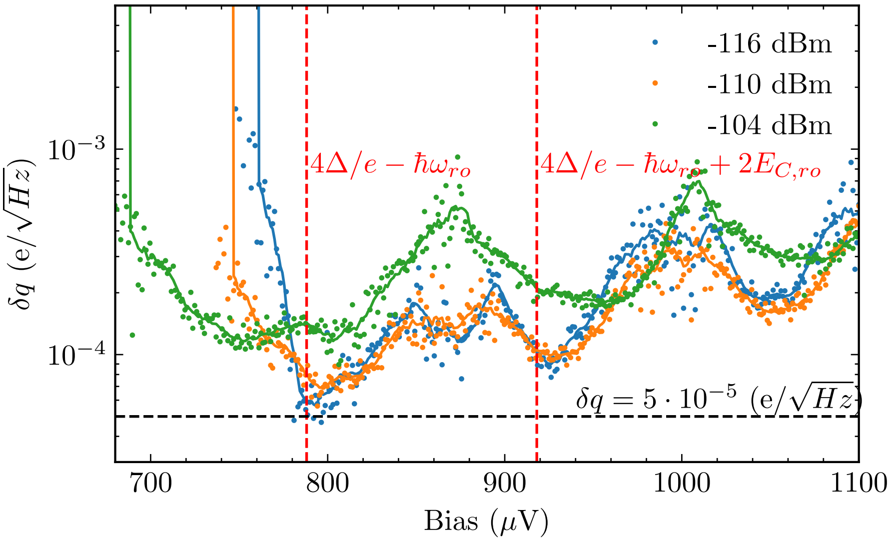

Figure 5.16: Charge sensitivity of the readout RF-SET as function of voltage for drive frequency of 4.816 GHz and three different microwave tone powers. The charge sensitivity is maximal close to $eV = 4\Delta - \hbar\omega_{ro}$, represented by the red dashed line, and shows periodicity in bias voltage, with the period set by the charging energy. As the power is increased, the optimal working point of the detector moves to lower bias voltage due to multi-photon absorption, and the charge noise increases.

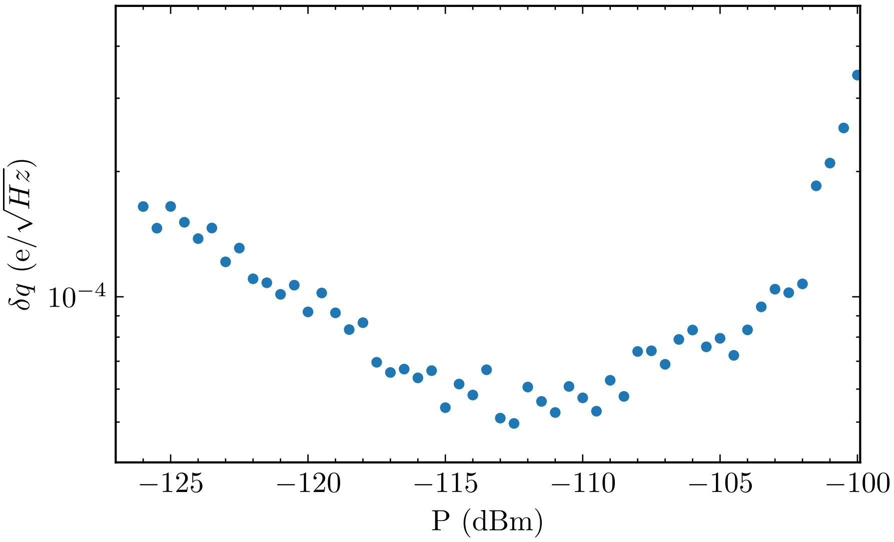

Figure 5.17: Charge sensitivity as a function of the applied power. The readout bias is fixed to 790 µeV, and the frequency of the tone to 4.816 GHz. The optimal working point of the detector -113 dBm.

The minimal charge noise measured in this experiment is $5 \cdot 10^{-5}\,\mathrm{e}/\sqrt{\mathrm{Hz}}$, corresponding to the SET bias of 790 µeV, and the applied microwave power of -113 dBm. This charge noise is an order of magnitude higher than what is achievable with an RF-SET. However, there are several ways in which the readout could be improved. Increasing charging energy beyond $2\Delta/3 \approx 135\,\mu\text{eV}$ would enable observation of processes involving Cooper-pair tunneling, including the the DJQP process. Operating the superconducting RF-SET at DJQP point shows superior properties compared to the quasiparticle current [82, 81]. The dominant contribution to SET charging energy is due to the junction capacitance. This capacitance can be reduced by decreasing junction size through better controlling the evaporation angle (see Appendix B for fabrication details). Parametric amplifiers could also be used to reduce the measurement noise, as the detector operating point is below the parametric amplifier saturation power [83, 84, 85]. A JPA has already been used to improve the RF-SET readout, increasing the charge sensitivity by a factor of 20 [75].

The role of high characteristic impedance for readout is not yet fully understood. As discussed at length in Chapter 1, the use of strong coupling allows for impedance matching at higher bandwidth, which is beneficial for charge detection. However, the strong coupling also induces multi-photon absorption, which limits the power that can be applied to the SET, before the charge noise increases due to inferior matching. We have shown in figure 5.16 that multi-photon processes displace the optimal junction bias, and increase charge noise. Thus, a more systematic study is needed before concluding on the optimal device parameters for charge detection.

5.5 Microwave Emission

To gain more understanding of the tunneling through a SET in a high impedance environment, we measure the power emitted by the RF-SET as a function of gate and bias voltages. This experiment is simpler compared to measuring the microwave reflection with a VNA, as we are able to observe the photon emission only, but not the photo-assisted tunneling. We present the results for the readout circuit only. Data for the photon-to-electron converter are not shown because the amplifier noise washes out the significant features in the emission.

As shown in Chapter 4, provided that the resonator loss rates are known, and assuming that the emission is Lorentzian, measuring the power emitted at resonance allows us to calculate the mean resonator population. Using the loss rates estimated in the previous section, and calculate the resonator population from

$$\langle n_{\text{res}} \rangle = \frac{\kappa_{\text{tot}} P_{em}}{4\kappa_c \hbar\omega_{ro} \times BW \times G} \tag{5.35}$$

where BW is the measurement bandwidth, and G is the gain of the microwave chain taken to be the same as in single junction experiments presented in the previous chapters.

The evolution of resonator population with bias and gate voltages is shown in figure 5.18. As in the reflectometry data presented in section 5.3.1, we observe the Coulomb diamonds, together with the several steps in bias voltage due to the inelastic emission. However, unlike in the single junction case, the resonator population does not rise monotonically with increasing bias voltage. Rather, when additional island charge states become available, the resonator population drops slightly, as seen in additional diamond-like structures in figure 5.18. To reproduce this phenomenon, we rely on a classical rate equation model, similar to one outlined in section 4.1.2.

5.5.1 RF-SET Classical Master Equation

We have seen in Chapter 4 that the emission experiments can be explained by a classical master equation model, in which the tunneling rates depend on the resonator state. We now apply analogous reasoning to the case of inelastic tunneling through a single-electron transistor. In addition to the

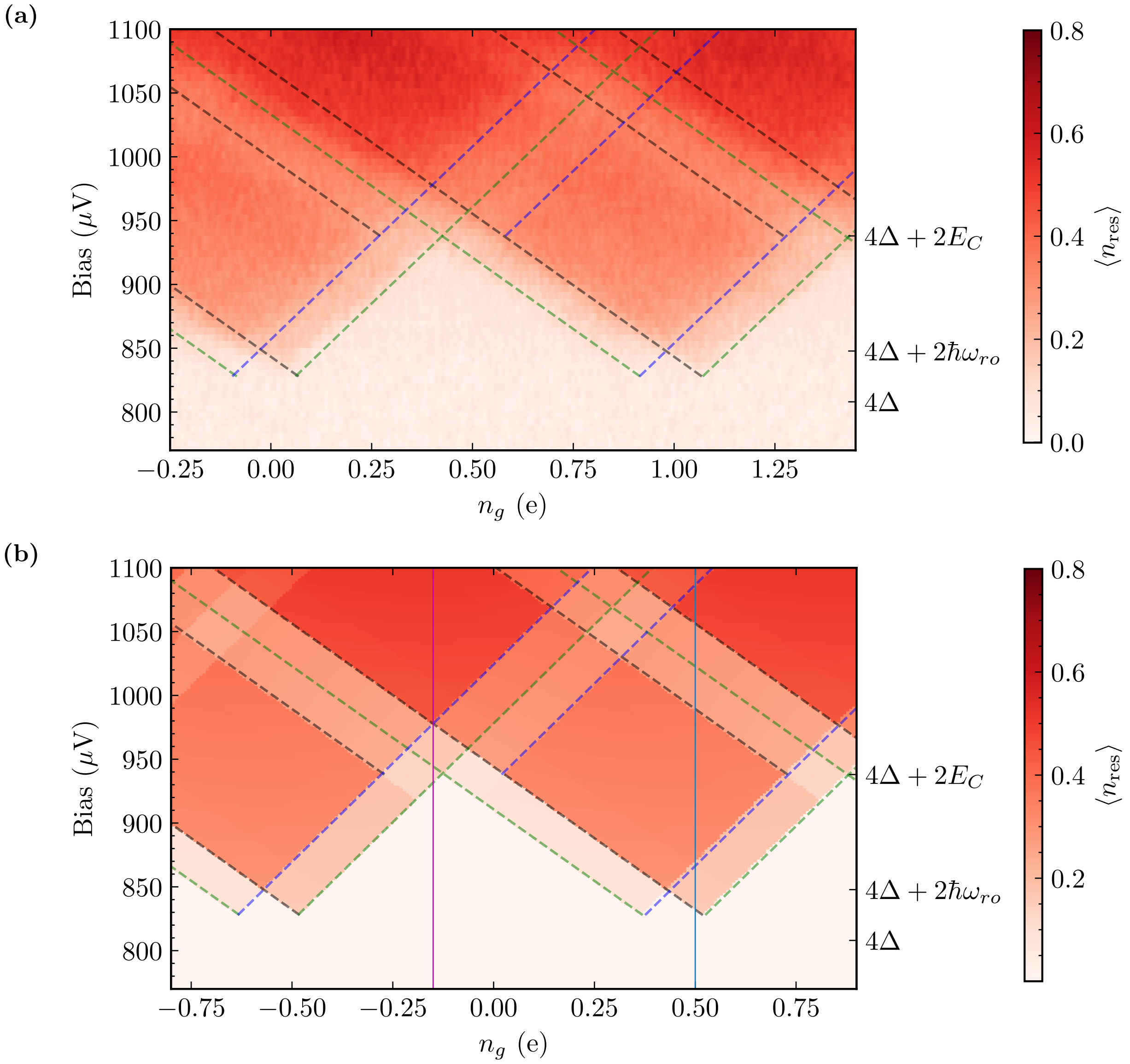

Figure 5.18: Readout resonator population as function of the junction bias voltage and gate voltages (a) Population calculated from the measured emission at resonance frequency using equation 5.35. Green dashed current lines represent the Coulomb diamonds corresponding to the elastic tunneling. Black dashed lines represent the inelastic tunneling through junction one, and the blue through junction two. (b) Classical master equation calculation result. Dashed lines are same as in panel (a). Magenta and blue solid lines represent the linecuts shown in figure 5.20.

resonator state, the tunneling rates through the SET junctions depend on the central island charge. Thus, we describe the state of the system by a tuple (n_{ph}, n_e), where n_{ph} is number of photons in the single resonator mode that we consider, and n_e is the number of excess electrons on the SET island. The tunneling rates are derived in detail in section 5.1.2. For the forward tunneling, they are given by

$$\kappa_1^{n_{ph},n_{ph}+l}(V) = \left|\langle n_{ph}+l|\, e^{i\lambda_1(a+a^\dagger)}\, |n_{ph}\rangle\right|^2 I_1(\alpha_1 V - \delta E^+ - l\hbar\omega/e)/e \tag{5.36}$$

$$\kappa_2^{n_{ph},n_{ph}+l}(V) = \left|\langle n_{ph}+l|\, e^{i\lambda_2(a+a^\dagger)}\, |n_{ph}\rangle\right|^2 I_2(\alpha_2 V - \delta E^- - l\hbar\omega/e)/e \tag{5.37}$$

with

$$\delta E^\pm = 2E_C(1/2 \pm (n_e - n_g)) \tag{5.38}$$

where n_g is the gate charge, and $I_i = e\gamma_i(V)$ is the single junction current-voltage characteristic. We present the calculations for the readout SET only, so we will drop the subscript $_{ro}$ in this section to simplify the notation. For the sample parameters, we take the values extracted in sections 5.2.3 and 5.3.1. The remaining two parameters to determine are the junction resistances. We assume that the junctions are equal, and set the tunneling resistance to $R_1 = R_2 = 550\,\mathrm{k\Omega}$. The single junction voltage characteristic $I_1(V) = I_2(V)$ is then calculated using equation 1.24 with $\Delta = 202\,\mathrm{\mu eV}$ and $\Gamma = 10\,\mathrm{neV}$.

After fixing all the parameters, we calculate the rates and construct the rate matrix. We consider the 9 lowest resonator states, and set the island charge states $n_e = -4, \ldots, 4$. Only the transitions between the neighbouring island charge states are allowed. The tunneling through junction one (equation 5.36) increases the number of excess quasiparticles on the island by one, while the tunneling through junction two (equation 5.37) decreases it by one. Thus, for example, the transition from state $(0,0)$ to $(2,1)$, corresponding to adding the quasiparticle to the island, while two photons are emitted into the resonator mode, is given by

$$\kappa_1^{0,2}(V) = \left|\langle 2|\, e^{i\lambda_1(a+a^\dagger)}\, |0\rangle\right|^2 I_1(\alpha_1 V - \delta E^+ - 2\hbar\omega/e)/e. \tag{5.39}$$

The full master equation is then given by

$$\begin{aligned}\dot{p}(n_{ph}, n_e) =& \sum_l \kappa_1^{n_{ph}+l,n_{ph}}(V) p(n_{ph}+l, n_e-1) + \kappa_2^{n_{ph}+l,n_{ph}}(V) p(n_{ph}+l, n_e+1)\\ &- \sum_l \left(\kappa_1^{n_{ph},n_{ph}+l}(V) + \kappa_2^{n_{ph},n_{ph}+l}(V)\right) p(n_{ph}, n_e)\\ &+ \kappa_c n_{\mathrm{th}} p(n_{ph}-1, n_e) + \kappa_c(n_{\mathrm{th}}+1) p(n_{ph}+1, n_e) - \kappa_c(2n_{\mathrm{th}}+1) p(n_{ph}, n_e)\end{aligned} \tag{5.40}$$

The steady state master equation solutions for four different gate and bias voltage combinations (minimal and maximal bias voltage at the magenta and blue vertical lines in figure 5.18b) are given in figure 5.19. As expected, below the superconducting gap ($V_{bias} = 770\,\mathrm{\mu eV}$), the resonator is empty, and there is a well defined charge state of the SET island. For the higher bias voltage, there is no stable charge configuration, and the current can flow through the SET.

After obtaining the steady state master equation solution, the mean photon number in the resonator is calculated from

$$\langle n_{\mathrm{res}}\rangle = \sum_{n_{ph}} n_{ph} \sum_{n_e} p(n_{ph}, n_e). \tag{5.41}$$

The evolution of the resonator population with gate and bias voltages is shown in figure 5.18b. Two linecuts, corresponding to the two solid vertical lines in the figure 5.18b are shown in figure 5.20. The classical master equation model reproduces well the non-monotonic increase in the resonator

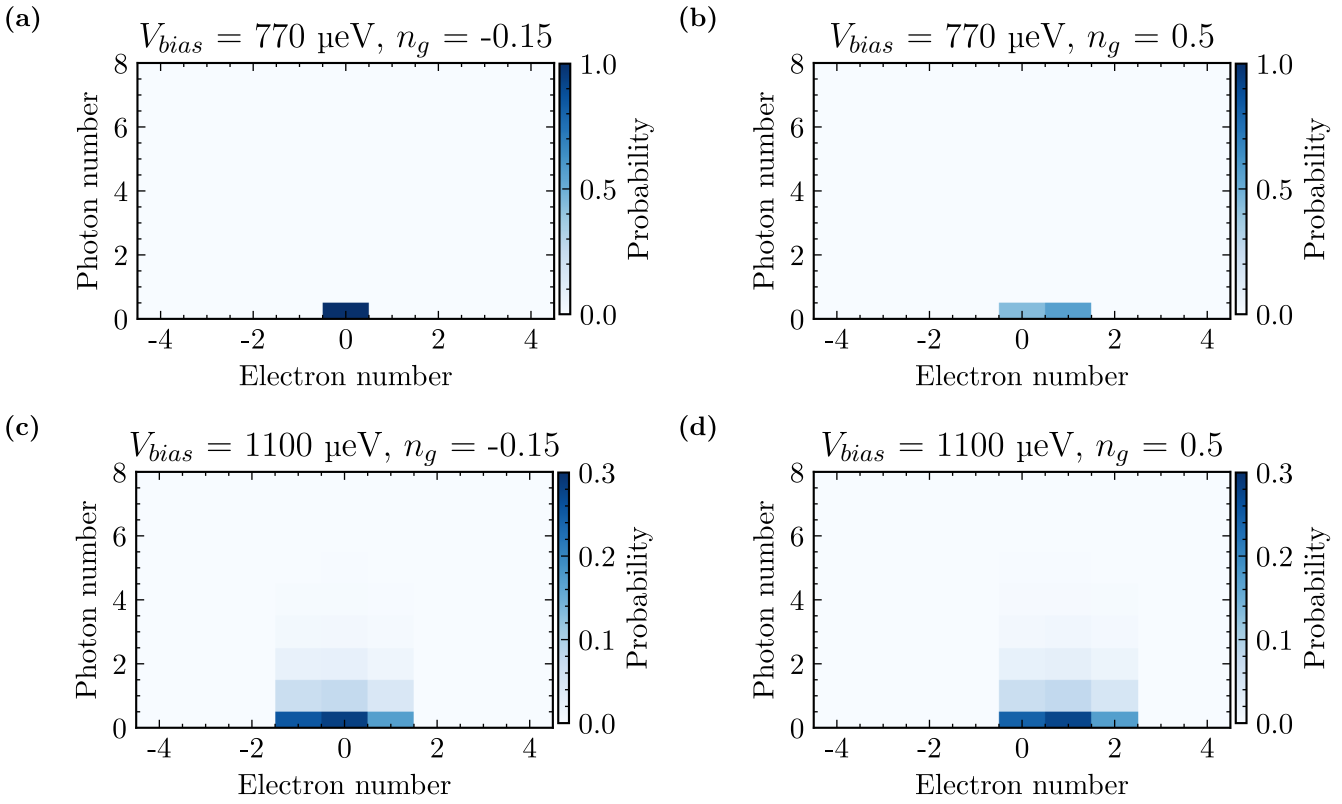

Figure 5.19: Probability distributions for resonator state and island states in the steady state for different combinations of junction bias and gate voltages.

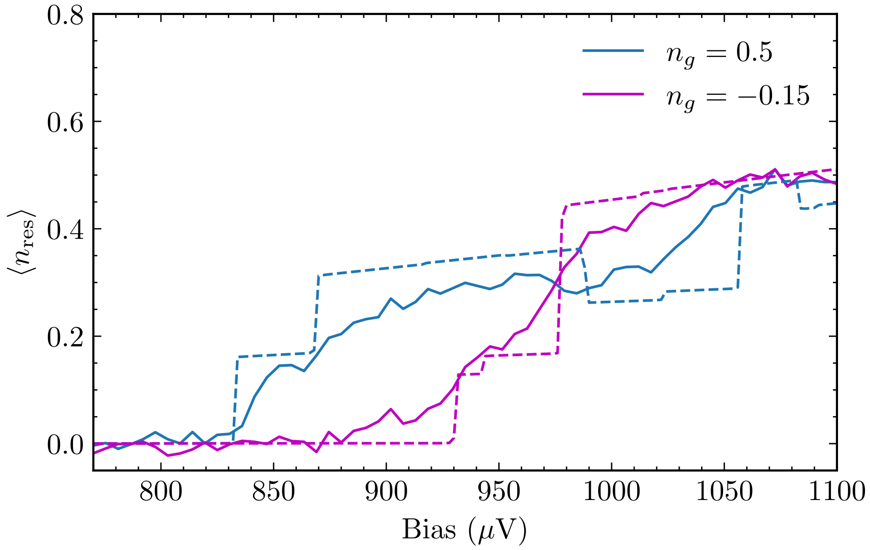

Figure 5.20: Two linecuts of maps shown in figure 5.18 for fixed gate voltages. Solid lines are the experimental data, while the dashed lines are classical master equation solutions.

population with rising junction bias observed in the experimental data. This phenomenon arises due to the mismatch in tunneling thresholds for photon emission and photon absorption: when the absorption processes through excited charge states of the island become allowed, the resonator population drops, before rising again, when the emission through the excited states is also allowed.

To achieve better agreement between the theory and the experimental data, one would need to thoroughly measure the sample parameters, such as the junction resistance and junction loss rate, as well as perform a precise calibration of the microwave measurement chain.

5.6 Conclusion

In this chapter, we have presented the preliminary experiments performed with the aim of building a detector based on inelastic quasiparticle tunneling able to resolve single microwave photons. The implemented sample consists of two capacitively coupled radio-frequency single-electron transistors — a photon-to-electron converter RF-SET, and a readout RF-SET. Resonators in both RF-SETs are fabricated in grAl, allowing for compact design. The converter circuit is designed to achieve strong coupling between the resonator and the junction to boost the inelastic tunneling, while the readout resonator-SET coupling is reduced, to decrease the back-action of photo-assisted processes on charge detection.

When measuring reflection as a function of SET bias and gate voltages, several copies of Coulomb diamond structure are observed, corresponding to the inelastic processes. We discuss the differences between the converter and the readout due to the variation in the coupling parameter λ, and show that for suitable gate and bias voltages, there are areas of high absorption. Thus we can expect high photon-to-electron conversion efficiency. Additionally, we have demonstrated that the charge flow through the converter SET could be detected by measuring the reflectometry of the readout. However, we were unable to detect single tunneling events due to high barrier transparency.

The spectroscopy measurements were used to determine the readout RF-SET charge noise as well. We varied SET bias voltage and the power of the applied microwave tone to find the optimal operating point for the charge detector. Obtained charge noise is as low as $\delta q = 5 \cdot 10^{-5}\,\mathrm{e}/\sqrt{\mathrm{Hz}}$. Different possible approaches to improving the charge sensitivity such as increasing the charging energy, decreasing the SET resistance, or utilizing parametric amplifiers are also considered.

The power emitted by the readout RF-SET was measured to gain more insight into the inelastic tunneling through cavity coupled islands. The Coulomb diamonds periodic in gate charge were observed. Furthermore, step-like structure due to dynamical Coulomb blockade was identified. To explain the experimental data, we have developed a master equation model analogous to one described in detail in Chapter 4 for tunneling through a single junction. The state of the system is characterized by the number of photons in the resonator, and the number of excess quasiparticles on the SET island. The transition rate matrix was constructed from tunneling rates between different states, and the resulting master equation steady state solution is used to determine the resonator population. This model aligns well with the data, and reproduces the observed non-monotonic increase in resonator population with rising junction bias due to a mismatch in absorption and emission tunneling through excited island charge states.

Conclusion and Perspective

This thesis covers the work done towards building a single microwave photon detector relying on inelastic quasiparticle tunneling. As a step towards detecting individual photons, we have designed and implemented a microwave photon-to-electron converter based on tunneling through a single SIS junction. We have then conducted the preliminary experiments towards detecting single charges on a device consisting of two coupled RF-SETs, showing promising results.

To convert the photons of energy $\hbar\omega_1$ to electrons, we couple the junction to the resonator with the fundamental mode frequency ω_1, and bias the junction at $eV = 2\Delta - \hbar\omega_1/2$, where Δ is the superconducting gap. As the junction is biased below the superconducting gap, there is virtually no current flowing through it as long as the resonator is empty. When the photons are present in the resonator, they supply the energy needed to overcome the gap, inducing photo-assisted current. By monitoring this photo-current, we detect the incident microwave photons. The photo assisted current has been widely used to detect electromagnetic radiation. However, in this work, we push the limits in frequency of detected radiation, and quantum efficiency of the conversion thanks to strong coupling between the junction and the resonator.

The resonator is fabricated using granular aluminium, a high kinetic inductance disordered superconductor, resulting in a characteristic impedance close to $5\,\mathrm{k}\Omega$, an order of magnitude higher compared to conventional resonators made of aluminium or niobium. The high characteristic impedance increases the coupling between the junction and the resonator, boosting the inelastic tunneling rates.

In high coupling regime, multi-photon processes, and in particular the dependence of their rates on the resonator state need to be taken into account to accurately describe the dynamics of the resonator-junction system. Under these circumstances, the $P(E)$ theory, usually used to calculate the tunneling current through a junction embedded in an electromagnetic environment fails. Instead, we have treated the junction electrodes as equilibrium baths for the resonator mode, and derived a quantum master equation describing the resonator evolution (Chapter 1).

We have then used the quantum master equation framework to design a microwave photon detector. The design is described in Chapter 1. We have pointed out the crucial role of the ratio of the coupling rate — the rate at which the photons enter the resonator, to the rate at which the photons are absorbed by the junction in determining the photon-to-electron conversion quantum efficiency. When these two rates are equal, the quantum efficiency is equal to one, if the internal losses of the resonator are small. This rate matching condition is equivalent to impedance matching maximizing the power transfer to a load in electric circuits. The coupling rate is fixed by the sample geometry. Thus, to satisfy the rate matching condition, we tune the photon absorption rate by choosing the suitable target junction resistance. The tunneling resistance needed to fulfil the matching condition is two orders of magnitude higher in strong coupling regime, when compared to the junctions coupled to conventional resonators. The high junction resistance is beneficial for reducing the dark electron rate, given by the subgap current flowing through the junction in absence of any incoming photons.

In Chapter 2, we have presented the experiments evaluating the figures of merit of the implemented photon detector. From reflection spectroscopy measurements, we estimate the quantum efficiency of 0.87 — significantly higher than in other photon detectors based on inelastic tunneling [36]. This value was confirmed by measuring the evolution of photo-assisted current with the power of the applied microwave drive. We have measured the photo-assisted current due to two, three, and four-photon processes. By fitting all four current-power curves to the quantum master equation model, with the attenuation between the sample and the room temperature microwave source being the lone free parameter, we have determined the incident power at the sample stage. There is an excellent agreement between the experimental data and the model, allowing for the precise calibration of the measurement chain, and thus the precise knowledge of quantum efficiency of $\chi = (0.83 \pm 0.05)$.

The lowest measured dark current of the detector is 26 fA, corresponding to the electron rate of $160\,\mathrm{ks}^{-1}$. The origin of the dark current is not fully understood. However it is not due to the rounding of the current-voltage characteristic of the junction, but rather can be explained by the residual resonator population of $5 \cdot 10^{-4}$.

In Chapter 4, by varying the fridge temperature, we have measured the photo-assisted tunneling current due to the thermal radiation in the resonator. The current-temperature dependence reaffirms high quantum efficiency of photon-to-electron conversion. Concomitantly, as a consequence of the photon absorption by the junction, the resonator population is expected to be lower than the equilibrium value given by the Bose-Einstein occupation factor, giving rise to effective cooling. We have measured the power radiated by the sample as a function of junction bias and fridge temperature, and deduced the resonator population from input-output theory. When the junction is biased below the superconducting gap, we observe the effective cooling of the resonator mode, as expected. The resonator population is approximately half its equilibrium value. The cooling power could be further improved by decreasing the junction resistance. However, this would lower the photon-to-electron conversion efficiency, negatively impacting the photon detection, which was the main interest when designing the sample.

Above the superconducting gap, the population of the resonator rises due to photon emission by the junction. Far above the superconducting gap, we measure the tunneling current shot noise filtered by the resonator. Measuring the photon emission in this regime is widely used for calibrating the microwave chain in circuit QED experiments [31, 33]. We have shown that this approach is remains valid for $\lambda \sim 1$. However, in the intermediate junction bias range, just above the superconducting gap, we observe a significant deviation from the shot noise picture presented in [72]. The disagreement arises due to high bias voltages needed to overcome the superconducting gap, coupled with the long photon lifetime in the cavity, as well as the strong resonator-junction coupling boosting the multi-photon process rates, bringing the system far from equilibrium. At these intermediate bias voltages, the detailed balance condition for the transition rates between different resonator states is not satisfied, and thus the effective temperature of the system cannot be defined. In contrast to the shot noise model [86], the master equation calculation is in quantitative agreement with the experimental data for all bias voltages and temperatures. We have calculated the Wigner functions of the resonator state, and show that the resonator states just above the superconducting gap are not thermal. Combining the non-thermal states with the resonator Lamb shifts caused by the junction results in non-Lorentzian spectra in a narrow voltage bias range around $eV = 2\Delta + \hbar\omega_1$. The non-Lorentzian spectra were directly observed. The Wigner function was however not evaluated experimentally.

The transition to photon counting requires detecting single electrons resulting from microwave photon-to-electron conversion. Thus, we propose and implement a device consisting of two capacitively RF-SETs. One RF-SET acts as a photon-to-electron converter, and the second one is used for the readout. The incident photons are absorbed by the junction, changing the charge of the converter island by e. This change is then detected by the readout. Preliminary experiments performed on a double RF-SET sample are presented in Chapter 5. We have performed the spectroscopy measurements on both RF-SETs, and shown that for suitable gate and bias voltages, there is high photon-absorption due to inelastic tunneling, pointing to high photon-to-electron conversion quantum efficiency. We have demonstrated that the readout RF-SET is sensitive to charge flow through the converter. However, the single tunneling events were not detected due to the tunneling rates being too high. To better understand the SET behaviour in a high impedance environment, we have measured the power emitted by the readout as function of gate and bias voltages. Unlike the single junction case (Chapter 4), the power emitted by the SET does not increase monotonically with rising junction bias due to a mismatch in the tunneling rates through excited island states corresponding to photon absorption and emission. We compare the data to a classical master equation model, finding good agreement.

Further perspective

In this work, we have demonstrated efficient microwave photon-to-electron conversion, and built a photon detector based on inelastic quasiparticle tunneling that is able to measure a sustained microwave photon flux with high efficiency (83 %), and low dark counts ($160\,\mathrm{ks}^{-1}$). In the future, it would be interesting to extend this detection mechanism to single photon detection. We have performed preliminary experiments with this aim by pairing the photon-to-electron converter with an RF-SET used for charge readout. The readout charge noise is $5 \cdot 10^{-5}\,\mathrm{e}/\sqrt{\mathrm{Hz}}$. Even though the charge noise is low, there is still room for improvement compared to state-of-the-art RF-SET charge noise of $0.9 \cdot 10^{-6}\,\mathrm{e}/\sqrt{\mathrm{Hz}}$ [49]. The overall performance of the detector could be improved by reducing the charging energy of both the readout and the converter. The charging energies are limited by the junction capacitance. Hence, reducing their size is a straightforward way towards increasing the charging energy, and thus better controlling the tunneling rates through the SET, or moving to tunneling through quantum dots [36].

The readout was fabricated using high impedance resonators, enabling a compact design, and easier fabrication compared to separate tank circuits commonly used in RF-SETs. High impedance allows us to realize impedance matching at higher bandwidths, speeding up the charge measurement, but it also limits the power used for the readout before the appearance of multi-photon processes which reduce the detector performance. Thus, a more systematic study is needed before concluding on the optimal resonator characteristic impedance for charge detection.

However, based on the charge noise in state of the art RF-SETs, and the coupling achieved between the converter and the readout, we are confident that the single photons could be measured at a rate of 100 kHz. Therefore, the dark count of the detector needs to be significantly lower than this rate. The obvious way to reduce the dark count would be to decrease the resonance width. The recent work in [27] shows that dark count rates as low as $100\,\mathrm{s}^{-1}$ can be reached in a narrow band detector. The resonator width can be reduced by using a Bragg structure [59] to keep the galvanic contact for biasing the junction, and controlling the coupling rate through a separate capacitively coupled feedline. To keep the high quantum efficiency in a narrow band resonator, the intrinsic losses need to be reduced compared to the device presented in the thesis. High quality granular aluminium resonators ($Q_i = 10^5$) have already been fabricated [60], and we do not consider this requirement to be a fundamental limiting factor for transition to single photon detection. As the resonator width is reduced, the dark rate due to subgap current will make a significant share of the total dark counts. Thus, the scaling of the dark count with resonator width needs to be checked experimentally. High kinetic inductance materials, such as granular aluminium will play a crucial role in building these narrow band detectors, as they enable use of more resistive junctions while keeping high quantum efficiency, thus limiting the subgap dark current. We envision that such detectors will have a crucial role in advancing microwave quantum optics, sensing, and many more areas of research, such as axion detection.

Appendix A

Resonator Coupled to a Bath: Input-Ouput Theory

To measure its properties, the system under consideration needs to be coupled to a measurement setup. The measurement setup is usually modelled as a bath of harmonic oscillators, and the derived formalism is called input-output theory. We consider the harmonic oscillator as the system under test, and derive some of the formulas used in the main text. The derivation shown here is standard in literature and largely follows [57] and the supplementary information of [87].

The total Hamiltonian we consider is

$$H = H_{\text{sys}} + H_{\text{B}} + H_{\text{int}} \tag{A.1}$$

where

$$H_{\text{sys}} = \hbar\omega_0 a^\dagger a \tag{A.2}$$

is the system hamiltonian,

$$H_{\text{B}} = \hbar \int_{-\infty}^{\infty} \mathrm{d}\omega \omega b^\dagger(\omega) b(\omega) \tag{A.3}$$

is the bath Hamiltonian, and the interaction Hamiltonian is

$$H_{\text{int}} = i\hbar \int_{-\infty}^{\infty} \mathrm{d}\omega \gamma(\omega)(b^\dagger(\omega)a - a^\dagger b(\omega)). \tag{A.4}$$

Bath operators satisfy bosonic commutation relation $[b(\omega), b^\dagger(\omega')] = \delta(\omega - \omega')$. We have applied the rotating wave approximation in the interaction Hamiltonian. Additionally, this approximation allows us to extend the integration to negative frequencies for bath and interaction Hamiltonians, as there are no resonant terms in this frequency range, but the calculations are greatly simplified. The equations of motion for bath and system operators are then

$$\dot{b}(\omega) = -i\omega b(\omega) + \gamma(\omega) a \tag{A.5}$$

$$\dot{a} = -i\omega_0 a - \int_{-\infty}^{\infty} \mathrm{d}\omega \gamma(\omega) b(\omega) \tag{A.6}$$

By solving the equation of motion for the bath operator, we get

$$b(\omega) = e^{-i\omega(t-t_0)}b_0\omega + \gamma(\omega)\int_{t_0}^{t} e^{-i\omega(t-t')}a(t')\,\mathrm{d}t' \tag{A.7}$$

where $b_0(\omega)$ is $b(\omega)$ evaluated at $t = t_0$ in the past. By substituting this solution in A.6, we get for the resonator operator

$$\dot{a} = -i\omega_0 a - \int_{-\infty}^{\infty} \mathrm{d}\omega\gamma(\omega)e^{-i\omega(t-t_0)}b_0(\omega) - \int_{t_0}^{t} \mathrm{d}\omega(\gamma(\omega))^2 e^{-i\omega(t-t')}a(t'). \tag{A.8}$$

Now we apply the Markov approximation

$$\gamma(\omega) = \sqrt{\kappa/2\pi} \tag{A.9}$$

and define an input field $b_{\text{in}}(t)$ as

$$b_{\text{in}}(t) = \frac{1}{\sqrt{2\pi}}\int_{-\infty}^{\infty} \mathrm{d}\omega e^{-i\omega(t-t_0)}b_0(\omega). \tag{A.10}$$

The equation of motion then becomes

$$\dot{a} = -i\omega_0 a - \frac{\kappa}{2}a - \sqrt{\kappa}b_{\text{in}}(t). \tag{A.11}$$

If we consider some future time t_1 such that $t_1 > t$ analogously to the input field, we can define the output field as

$$b_{\text{out}}(t) = \frac{1}{\sqrt{2\pi}}\int_{-\infty}^{\infty} \mathrm{d}\omega e^{-i\omega(t-t_1)}b_1(\omega) \tag{A.12}$$

where $b_1(\omega)$ is the bath operator evaluated at time t_1. Now we can write the equation of motion A.6 in terms of the output field as

$$\dot{a} = -i\omega_0 a + \frac{\kappa}{2}a - \sqrt{\kappa}b_{\text{out}}(t). \tag{A.13}$$

By combining A.11 and A.13 we get the relation between the input and output fields:

$$b_{\text{out}}(t) = b_{\text{in}}(t) + \sqrt{\kappa}a(t). \tag{A.14}$$

We can easily extend the equation A.11 to the case where there are several inputs and outputs:

$$\dot{a} = -i\omega_0 a - \sum_l(\frac{\kappa_l}{2}a + \sqrt{\kappa_l}b_{\text{in}}(l,t)). \tag{A.15}$$

We identify κ_l as different loss rates, e.g. the coupling rate which describes the leakage of the photons between the resonator and the measurement setup, or the intrinsic loss rate which accounts for the finite quality factor of the resonator. We will now use the equation of motion A.11 to derive different quantities we measure.

Reflection Spectrum of the Resonator

To experimentally characterize the resonator, we measure the reflection coefficient

$$S_{11}(\omega) = \frac{b_{\text{out}}(\omega)}{b_{\text{in}}(\omega)} \tag{A.16}$$

To derive the reflection coefficient formula, we Fourier transform the equation A.15. We assume that the resonator is coupled to two baths. One corresponds to the transmission line leading to the rest of the experimental setup, and the corresponding coupling rate is κ_c. The second bath represents the intrinsic losses in the resonator. It is described by loss rate κ, and we consider the corresponding input field to always be in vacuum. The equation A.15 is then

$$-i\omega a(\omega) = -i\omega_0 a(\omega) - \frac{\kappa_c + \kappa}{2} a(\omega) - \sqrt{\kappa_c} b_{\text{in}}(\omega) \tag{A.17}$$

By substituting A.14 we get

$$\frac{b_{\text{out}}(\omega) - b_{\text{in}}(\omega)}{\sqrt{\kappa_c}} = -\frac{\sqrt{\kappa_c}}{\frac{\kappa_c+\kappa}{2} + i(\omega_0 - \omega)} \tag{A.18}$$

The reflection coefficient is then

$$S_{11}(\omega) = 1 - \frac{\kappa_c}{\frac{\kappa_{\text{tot}}}{2} + i\delta} \tag{A.19}$$

where $\kappa_{\text{tot}} = \kappa_c + \kappa$ are total resonator losses, and δ is detuning.

Mean Resonator Population

We now calculate the mean population of a resonator driven at a frequency $\omega_D = \omega_0 + \delta$. The equation of motion in the frame rotating at ω_D becomes

$$\dot{a} = i\delta a - \frac{\kappa_{\text{tot}}}{2} a - \sqrt{\kappa_c} b_{\text{in}} \tag{A.20}$$

Mean values $\bar{a}$ and $\bar{b}_{\text{in}}$ in the steady state satisfy the equation

$$\bar{a} = -\frac{\sqrt{\kappa_c}}{\frac{\kappa_{\text{tot}}}{2} - i\delta} \bar{b}_{\text{in}} \tag{A.21}$$

The input field is

$$\bar{b}_{\text{in}} = \sqrt{\phi} \tag{A.22}$$

where ϕ is the incident photon flux. The mean resonator population $n = |\bar{a}|^2$ is then

$$n = \frac{4\eta^2}{\kappa_{\text{tot}}^2 + 4\delta^2} \tag{A.23}$$

where $\eta = \sqrt{\phi \kappa_c}$ is the microwave pumping strength. We note that this is equivalent to setting the system Hamiltonian to

$$H_D = i\eta(a - a^\dagger) - \delta a^\dagger a \tag{A.24}$$

This Hamiltonian is used in the main text to describe the microwave drive.

Appendix B

Sample fabrication

Both samples presented in this thesis are fabricated using the standard e-beam lithography and evaporation techniques.

Resonator-SIS Sample

First we describe the fabrication process for the photon detector sample discussed in chapters 1–4. The process is divided into several steps shown in figure B.1:

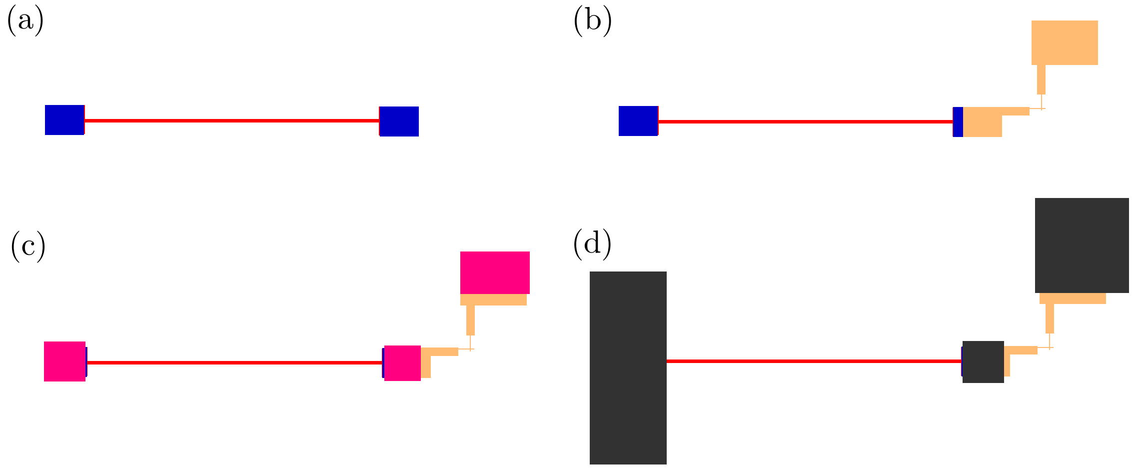

Figure B.1: Different fabrication steps. (a) Deposition of the grAl resonator (red). (b) Deposition of the Al/AlOx/Al tunnel junction (orange). (c) Argon etching to remove the oxide (pink). (d) Depositing aluminium (grey) for transmission lines, ground plane, and the patch connecting the junction and the resonator. See the text for details.

(a) The sample is fabricated on an oxidised silicone wafer. The first step is fabricating the grAl resonator with e-beam lithography. The chip is spin-coated with three layers of the electron-sensitive resist: the bottom layer is PMMA 495 A6, while the top two layers are PMMA 950 A6. Each layer is spin-coated at 4000 RPM for 60 s, and then baked for 2 min at 180 °C. The mask shown in figure B.1(a) is patterned with a dose of 450 µC/cm^2. The resonator is 180 µm long and 700 nm wide. At both ends of the resonator, there is a 10 µm × 10 µm square, used for connecting the resonator to the rest of the circuit. The mask is then developed in 1:3 MIBK/IPA solution at $\approx 20\,^\circ\mathrm{C}$. The deposition is done in two layers:

- 20 nm of grAl is deposited at 0° angle. The oxygen pressure during the evaporation was $p_{O_2} = 1.15 \cdot 10^{-5}\,\mathrm{mbar}$.
- 25 nm of Al is deposited at 45° angle.

Due to the high angle, aluminium is only deposited at the patches (blue squares in figure B.1(a)). After the deposition, the lift-off is done in DMSO at $80\,^\circ\mathrm{C}$ for 45 minutes.

(b) The junction is fabricated using Manhattan technique in a separate lithography and deposition (figure B.1(b)). The chip is spin-coated with a PMMA 495 A6/ PMMA 950 A3 resist bi-layer (bottom to top). The spin-coating was done at 4000 RPM for 60 s, and followed by baking for 2 min at $180\,^\circ\mathrm{C}$ for each layer. The mask shown in orange in figure B.1(b) was patterned using a dose of $400\,\mu\mathrm{C/cm^2}$, and developed using the same procedure as in step (a). To achieve high resistance, triple oxidation is performed. The deposition and oxidation steps are as follows:

- 25 nm of Al is deposited at 45° angle.
- Oxidation 15 min at $p_{O_2} = 10\,\mathrm{mbar}$.
- 0.2 nm of Al is deposited at 45° angle.
- Oxidation 15 min at $p_{O_2} = 10\,\mathrm{mbar}$.
- 0.2 nm of Al is deposited at 45° angle.
- Oxidation 15 min at $p_{O_2} = 10\,\mathrm{mbar}$.
- Sample holder is rotated by 90°.
- 50 nm of Al is deposited at 45° angle.

The lift-off is done in DMSO at $80\,^\circ\mathrm{C}$ for 45 minutes.

(c) We connect the junction and the resonator by etching the oxide layer using an Ar gun, and an Al patch. The $50\,\Omega$ transmission lines are fabricated in the same step. The patch and transmission line mask is patterned using optical lithography. The sample is spin-coated with a layer of AZ514 resist, baked for 1 min at $110\,^\circ\mathrm{C}$, and exposed using the dose of $110\,\mathrm{mJ/cm^2}$. The sample is then placed in vacuum, and a layer of oxide is removed from the areas colored in pink in figure B.1(c) using the Ar gun.

(d) Without exposing to air, the 100 nm of Al is deposited after the Ar etching was performed for transmission lines, the ground plane, and the patch connecting the resonator and the junction (grey area in figure B.1(d)). The lift-off is again done in DMSO at $80\,^\circ\mathrm{C}$ for one hour.

The sample is shown in figure 3.8 in the main text.

Double RF-SET Sample

We now switch to the Double RF-SET sample presented in Chapter 5. Similarly to the previous sample, the sample is fabricated in two e-beam lithographies — the first for the grAl resonators, and the second for the two SETs. The lithography mask is shown in figure B.2. The detailed dimensions

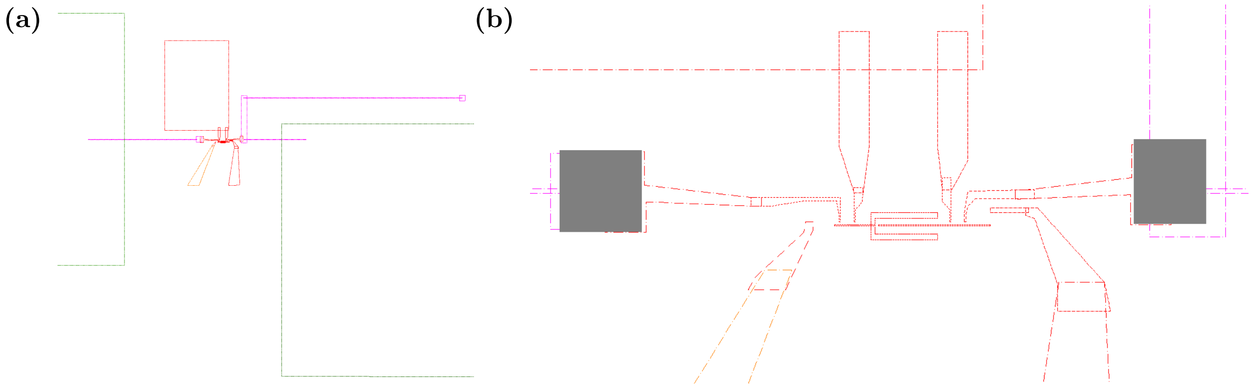

Figure B.2: (a) E-beam lithography mask. Transmission lines extending beyond the shown area are shown in green. GrAl resonators are in pink, and the two SETs are shown in red. (b) Zoom on the central area of the sample showing the two SETs. The two patches connecting the resonator and the junctions are in grey.

of the sample are given in section 5.2. In the first lithography, we pattern the grAl resonators shown in pink, and the transmission lines shown in green. The sample is spin coated with a PMMA 495 A6/ PMMA 950 A6/ PMMA 950 A6 resist triple layer (bottom to top). Each layer is spin-coated at 4000 RPM for 60 s, and then baked for 2 min at 180 °C. The mask is then patterned with a dose of 460 µC/cm^2, and developed in a 1:3 MIBK/IPA solution for 1 min. The deposition is as follows:

- 20 nm of grAl is deposited at 0° angle. The oxygen pressure during the evaporation was $p_{O_2} = 1.2 \cdot 10^{-5}$ mbar.
- 25 nm of Al is deposited at 45° angle.

After the deposition, the lift-off is performed in hot DMSO, at 80 °C for one hour.

To fabricate the junctions, we spin coat a resist bi-layer. The bottom layer is PMMA/MAA copolymer, spin-coated at 2000 RPM for 60 s and then baked for 2 min at 180 °C. The top layer is PMMA 950 A3 spin-coated at 4000 RPM for 60 s and then baked for 2 min at 180 °C. The patterned mask is shown in red in figure B.2. The dose was 350 µC/cm^2. The mask was developed in a 1:3 MIBK/IPA solution for 45 s. The deposition and oxidation steps are following:

- 25 nm of Al is deposited at $-14°$ angle.
- Oxidation 20 min at $p_{O_2} = 20$ mbar.
- 50 nm of Al is deposited at 14° angle.

The lift-off was done in DMSO at 80 °C for 45 min.

The last step is the deposition of the transmission lines, the ground plane, and the patching of the resonators and the junctions. The procedure is identical to the previous sample. An optical lithography is performed to pattern the lines, the ground plane, and the patches. The two patches are shown in grey in figure B.2b. The sample is then placed under vacuum, and the surface layer of oxide is removed using the Ar gun to ensure good contact. A 100 nm thick layer of Al is then deposited at zero angle for the patch and the transmission lines. The sample is shown in figure 5.4 of the main text.

Appendix C

Transfer Matrix Method

The simulated circuits consist of lossless transmission lines and tunnel junctions. Assuming the electromagnetic field in each section of the circuit occupies the fundamental transverse mode which can be described analytically, greatly simplifying and speeding up the circuit design. We represent the circuit we want to simulate as a cascade of two-port networks, and use the transfer matrix method. Each circuit component is characterized by transfer matrix T. Voltage and current at two component nodes are then given by:

$$\begin{bmatrix} V_2 \\ I_2 \end{bmatrix} = T \begin{bmatrix} V_1 \\ I_1 \end{bmatrix} \tag{C.1}$$

The transfer matrix T that describes a circuit consisting of several components in a cascade is given by the product of transfer matrices T_l of individual components:

$$T = \prod_l T_l \tag{C.2}$$

For a transmission line of length L, and characteristic impedance Z, the transfer matrix is given by:

$$T = \begin{bmatrix} \cos(kL) & iZ\sin(kL) \\ iY\sin(kL) & \cos(kL) \end{bmatrix} \tag{C.3}$$

where $k = \omega/v_p$, and $v_p = 1/\sqrt{lc}$ is the phase velocity of light.

The junction is modelled as a capacitance C_j, described by the transfer matrix T_j

$$T_j = \begin{bmatrix} 1 & 0 \\ i\omega C_j & 1 \end{bmatrix} \tag{C.4}$$

We place one port at $x = 0$, and the other port at the position of the junction $x = x_j$. After calculating the transfer matrix T of our system, and eliminating the junction port using the boundary condition:

$$\begin{bmatrix} V(x_j) \\ I(x_j) \end{bmatrix} = \begin{bmatrix} 1 \\ 0 \end{bmatrix} \tag{C.5}$$

which corresponds to an open circuit, we have:

$$\begin{bmatrix} V(0) \\ I(0) \end{bmatrix} = T \begin{bmatrix} V(x_j) \\ I(x_j) \end{bmatrix}. \tag{C.6}$$

We can now calculate the reflection spectrum at $x = 0$:

$$S_{11} = \frac{V(0) - Z_0 I(0)}{V(0) + Z_0 I(0)} \tag{C.7}$$

The excitation frequency f is swept, and resonant mode frequencies are determined by finding the local minima of $S_{11}(f)$. The spatial dependence of the mode ω_n is then calculated from equation 1.7. If the simulated system consists of several different transmission lines, the spatial dependence of the mode is a piecewise function analogous to equation 1.7 (see [51] for details).

When the spatial dependence of the mode is known, its characteristic impedance is calculated from the equation 1.19.

Appendix D

Summary in English

In the optical domain, the photoelectric effect is the method of choice to build single photon detectors covering a wide frequency spectrum with large quantum efficiency and low dark current. Reducing the photon energy down to microwave frequencies ($\sim 10\,\mathrm{GHz}$), while fulfilling the requirements for single photon detection, is experimentally challenging because of the absence of semiconducting or superconducting materials with a sufficiently low energy gap. However, an efficient microwave detector would be of substantial utility in microwave quantum optics [15], quantum cryptography [16], sensing [17, 18], and axion search [19, 20, 21]. Therefore, realizing microwave photon detectors remains an intense area of research. There have been several recent efforts exploiting superconducting quantum circuits [22] in different ways — whether by entangling the microwave photon with a qubit [23, 24], utilizing quantum criticality [25] or a Josephson mixer [26, 27].

Photon-to-Electron Conversion via Inelastic Tunneling

In recent years, realizing single microwave photon detectors based on inelastic tunneling has been an active area of research, and noticeable progress has been made, particularly using photo-assisted tunneling through double quantum dots [36, 37, 38]. Although the experiments are promising, these devices suffer from low quantum efficiency, caused by the mismatch between the photo-assisted tunneling rate and the photon input rate.

In this work, we build on the idea of a microwave photon detector based on the photoelectric effect. Rather than relying solely on the energy of the incident photon to break the Cooper pairs in a superconductor, our detector is based on photo-assisted tunneling through a superconducting tunnel junction biased just below the superconducting gap. Thus, the difference in energy between the microwave photon, and the gap, is provided by the voltage source.

When the junction is irradiated by photons, the current-voltage characteristic of the junction is modified by an onset of inelastic processes, in which a quasiparticle gains the energy to tunnel across the junction by absorbing photons [39]. This process, and the resulting current voltage characteristic are shown in figure D.1. We observe that the current below the superconducting gap appears only if the electromagnetic radiation is present. We exploit this fact by utilizing the tunneling current for photon detection. Photo-assisted tunneling through a tunnel junction has already been harnessed for detecting electromagnetic radiation, e.g. through the use of SIS mixers in astronomy, at frequencies on the order of $100\,\mathrm{GHz}$ [41], or for noise measurements at microwave frequencies [42]. In this work, we lower the operation frequency of quasiparticle tunneling based detectors to the 4 - $8\,\mathrm{GHz}$ band, and design the detector with the eventual goal of single microwave photon detection in mind. The scheme of our proposed detector is shown in figure D.2. It consists of a resonator galvanically

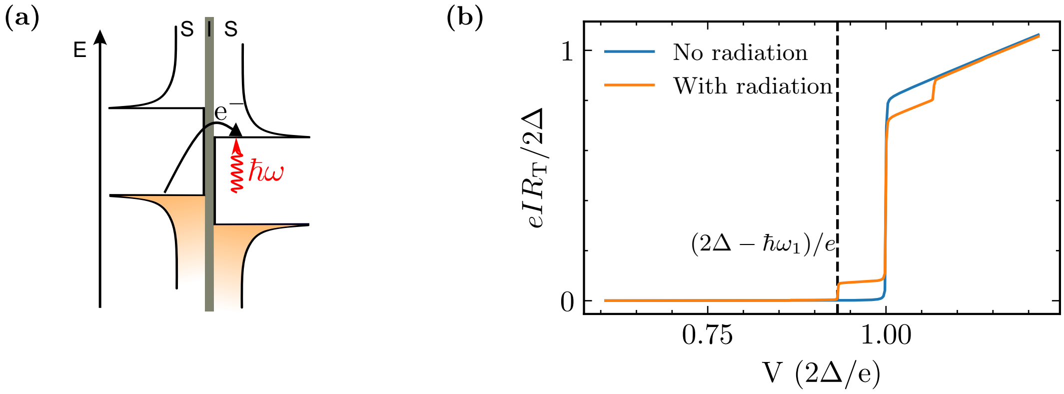

Figure D.1: (a) Photo-assisted quasiparticle tunneling across an SIS junction (b) Calculated current-voltage characteristics of an SIS junction of resistance R_{T}: current in absence of electromagnetic radiation is shown in blue. Current through the junction irradiated by light of frequency ω_1 is in orange

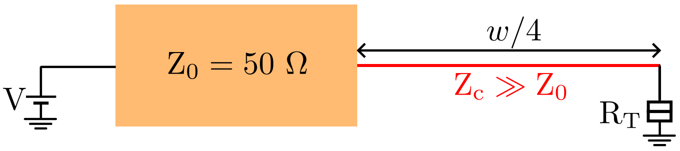

Figure D.2: Photon to electron converter scheme. To detect photons of wavelength w, a $w/4$ resonator, shown in red, is terminated on one side by a voltage biased superconducting tunnel junction. Characteristic impedance Z_c of the resonator is comparable to the quantum of resistance. The resonator is galvanically coupled to the rest of the circuit through a $50\,\Omega$ line

coupled to a $Z_0 = 50\,\Omega$ transmission line, which is then connected to the rest of the experimental setup. To detect photons of wavelength w, the resonator length is set to $w/4$. It is terminated by a voltage biased superconducting tunnel junction of tunneling resistance R_{T}. The junction is biased such that the absorption of incident photons through photo-assisted tunneling is energetically permitted, but no current flows in absence of microwaves. These conditions are fulfilled for bias voltages $eV \in [2\Delta - \hbar\omega_1, 2\Delta]$. The characteristic impedance Z_c of the resonator is comparable to the quantum of resistance, so that the coupling parameter satisfies $\lambda = \sqrt{\pi Z_c/R_K} \sim 1$, in order to increase the inelastic tunneling rate. To achieve high characteristic impedance, the resonator is fabricated using granular aluminium, a high kinetic inductance disordered superconductor.

The quasiparticle tunneling in junctions coupled to an electromagnetic environment, such as a resonator mode is usually described by $P(E)$ theory [40]. In this theory, the environment influence is calculated from quantum fluctuations of the phase at junction electrodes. $P(E)$ has been widely successful in predicting inelastic tunneling rates [46, 47]. However, one of the core assumptions in $P(E)$ theory is that electromagnetic modes stays in thermal equilibrium. As we consider strong coupling to modes of high quality factor, this assumption cannot be made. In this case, rates of different processes start to depend on the state of the resonator, and a comprehensive description of the system must take this fact into account. If we assume that the initial state of the resonator is $|n\rangle$, and the final state is $|n+l\rangle$, the tunneling rate corresponding to this process given by the

Fermi's golden rule is

$$\kappa_{n,n+l} = \left| \langle n+l | \, e^{i\lambda(a+a^\dagger)} \, |n\rangle \right|^2 I(V - l\hbar\omega_1/e)/e \tag{D.1}$$

where $\lambda = \sqrt{\pi Z_c/R_K}$ is the resonator-junction coupling constant, $I(V)$ is the current-voltage characteristic of the junction in absence of the high impedance environment, and ω_1 is the frequency of the resonator mode coupled to the junction. Photon absorption corresponds to $l < 0$, while the emission corresponds to $l > 0$.

To calculate the net current flowing through the junction, we treat it as a Markovian bath at equilibrium, and derive the quantum master equation governing the time evolution of the reduced density operator of the resonator. The obtained steady state resonator density matrix is then used to calculate the current in presence of a coherent microwave drive. When the mean number of photons in the resonator is significantly less than one, and for junction bias voltages in range $eV \in [2\Delta - \hbar\omega_r, 2\Delta]$, photo-assisted current is proportional to resonator population, and the device can be used for photon detection.

The quantum efficiency of the photon-to-electron conversion is given by the ratio of the resulting electron flux ϕ_e to the incident photon flux ϕ:

$$\chi = \frac{\phi_e}{\phi} = \frac{I_{\mathrm{PAT}}}{e\phi}. \tag{D.2}$$

In our detector, it writes

$$\chi = \frac{4\kappa_j\kappa_c}{(\kappa_i + \kappa_j + \kappa_c)^2}, \tag{D.3}$$

where

$$\kappa_j = \lambda^2 e^{-\lambda^2} I(V + \hbar\omega_1/e) \tag{D.4}$$

is the single-photon junction absorption rate, κ_c is the coupling rate between the resonator and the feedline, and κ_i describes the spurious losses in the resonator. Quantum efficiency has a maximum at $\kappa_j = \kappa_c + \kappa_i$, which is equivalent to an impedance matching condition for maximizing the power transfer to the load in electric circuits. The coupling rate κ_c is fixed by the sample geometry, so the rate matching condition is satisfied by tuning the junction resistance, and the detector bias voltage. The use of high coupling enables using higher junction resistance, while fulfilling the rate matching condition, thus minimizing the dark electron rate set by the subgap current at the detector operating bias.

Experimental Characterisation of the Photon-to-Electron Converter

After fabricating the device described in the previous section, we cool it down to 20 mK in a dilution fridge. Firstly, we perform spectroscopy of the cavity by measuring the reflection spectra at different junction biases close to the superconducting gap. The measurements are shown in figure D.3a. We observe a resonance at $\omega_1 = 2\pi \times 5.5\,\mathrm{GHz}$, corresponding to the fundamental mode of the resonator. At low bias there is a slight dip in the reflected signal, meaning that the losses are small. As the junction bias approaches the superconducting gap, there is a sharp drop in reflection at resonance, and for bias voltages $V > (2\Delta - \hbar\omega_1)/e = 379\,\mu\mathrm{V}$, we have almost perfect absorption. To extract the different loss rates, we fit each spectrum to

$$S_{11} = 1 - \frac{\kappa_c}{\frac{\kappa+\kappa_c}{2} + i(\omega - \omega_r)} \tag{D.5}$$

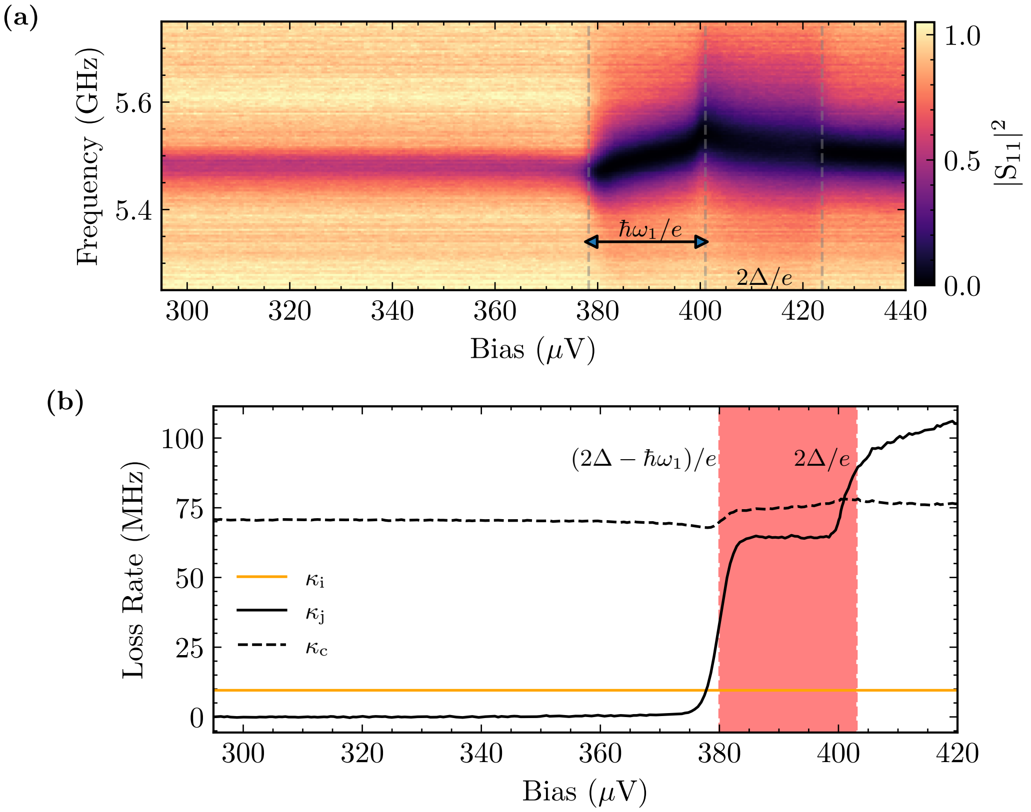

Figure D.3: (a) Absolute value of reflected signal as function of junction bias and frequency. Microwave excitation power is $P = -142\,\mathrm{dBm}$. (b) The loss rates κ_c, κ_j and κ_i as functions of bias voltage.

where κ_c is the coupling loss, while κ describes all the other losses present in the system. The coupling loss rate is weakly dependent on the junction bias, and its value is $\kappa_c = 2\pi \times 71\,\mathrm{MHz}$. The other loss rate κ is constant below the gap. At bias voltage $eV = 2\Delta - \hbar\omega_1$ it rises from $2\pi \times 9.5\,\mathrm{MHz}$ to $2\pi \times 75\,\mathrm{MHz}$, and then stays constant in the bias range $2\Delta - \hbar\omega_1 < eV < 2\Delta$. This loss rate has two contributions — junction induced losses κ_j, and internal losses of the resonator κ_i:

$$\kappa = \kappa_i + \kappa_j. \tag{D.6}$$

We expect κ_j to be negligible well below the superconducting gap. Thus, we attribute this loss rate to voltage independent internal resonator losses κ_i. The bias voltage dependence of these loss rates are shown in figure D.3b. After obtaining the three resonator loss rates κ_c, κ_j and κ_i, we calculate the microwave absorption

$$1 - |S_{11}(0)|^2 = \frac{4(\kappa_i + \kappa_j)\kappa_c}{(\kappa_i + \kappa_j + \kappa_c)^2} \tag{D.7}$$

and the expected quantum efficiency of microwave photon-to-electron conversion

$$\chi = \frac{4\kappa_j\kappa_c}{(\kappa_i + \kappa_j + \kappa_c)^2}. \tag{D.8}$$

The absorption probability and quantum efficiency for different junction biases are shown in figure D.4. Inside the gap, the absorption is approximately 0.4 due to the internal resonator losses. For voltages $eV > 2\Delta - \hbar\omega_1$, where the photo-assisted quasiparticle tunneling is allowed, absorption increases to unity. At the same bias voltage, quantum efficiency rises from 0 to 0.85. Especially, over the whole bias voltage range $eV \in [2\Delta - \hbar\omega_1, 2\Delta]$, we expect quantum efficiency $\chi > 0.85$ and low dark counts.

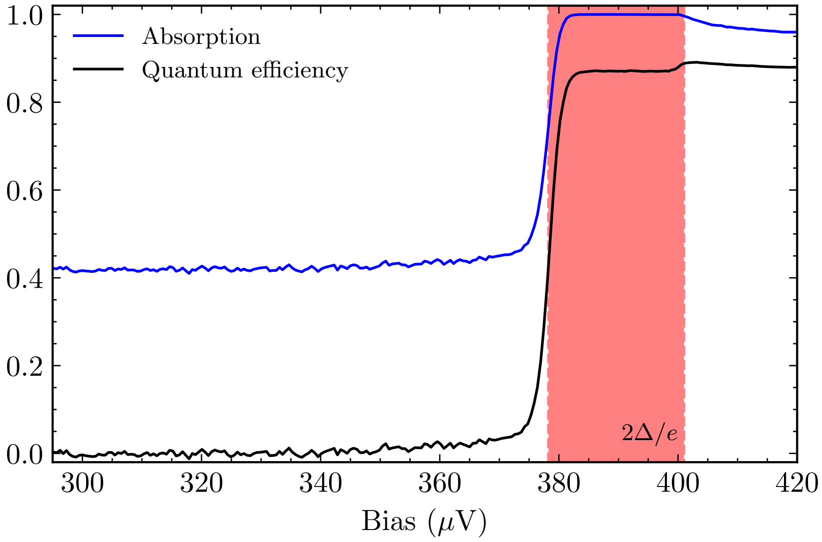

Figure D.4: Absorption (blue) and expected quantum efficiency (black) as functions of junction bias. The range of voltage biases suitable for photon detection experiments, characterized by high quantum efficiency and low dark count, are shaded in red.

To verify the quantum efficiency estimate, we measure the photo-assisted current as function of applied microwave drive power at bias voltages $eV = 2\Delta - (2n-1)\hbar\omega_1/2, b = 1, 2, 3, 4$, corresponding to one, two, three and four-photon absorption processes (figure D.5) When the resonator population is low, the photo-assisted current due to single-photon absorption rises linearly with applied power. At high power the photo-assisted current saturates due to multi-photon absorption. This saturation is quantified by 1 dB and 3 dB compression points. For our detector, these compression points are $P_{1\,\mathrm{dB}} = 340\,\mathrm{Mph/s}$ and $P_{3\,\mathrm{dB}} = 1\,\mathrm{Gph/s}$. By fitting all four current-power curves to the quantum master equation model at the same time, with the attenuation between the sample and the microwave source as the lone free parameter, we calibrate the incident power at the sample stage. In the theoretical calculations, the sample parameters are fixed to their ab initio values. The junction-resonator coupling parameter is $\lambda = 0.785$. Resonator damping rate $\kappa_c + \kappa_i = 2\pi \times 80.5\,\mathrm{MHz}$ is taken from the microwave spectroscopy measurements, and the junction resistance is $R_\mathrm{T} = 1.75\,\mathrm{M\Omega}$. After the incident power is calibrated, the quantum efficiency is calculated from the variation of single-photon absorption current with power. The obtained result is

$$\chi = (0.83 \pm 0.05) \tag{D.9}$$

In addition to the response to coherent excitation, the current due to thermal radiation in the resonator is measured by changing the temperature of the fridge, and the quantum efficiency result is verified.

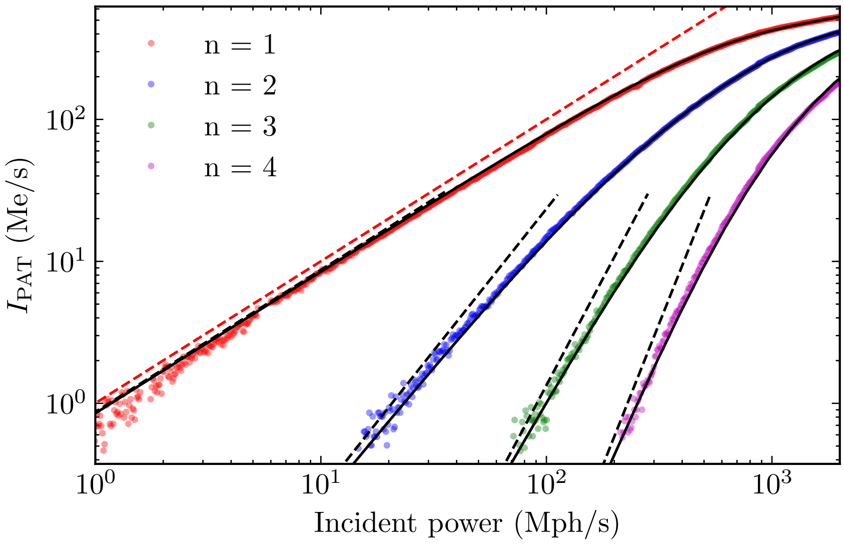

Figure D.5: Photo-assisted tunneling current as function of microwave power measured at junction bias $eV = 2\Delta - (2n-1)\hbar\omega_1/2, n = 1, 2, 3, 4$, and resonant drive. Dashed black lines represent the weak pumping limit quantum master equation solutions, while the solid black lines are the predictions obtained by solving the quantum master equation numerically. The dashed red line represents the ideal photon to electron conversion, with quantum efficiency equal to one. The sample parameters are set to their ab initio values, and it is assumed that the incident power at the sample stage is known.

To determine the dark current, we measure the current flowing through the junction at the detector operating point without any microwave drive. The measured dark current is $I_{\mathrm{dark}} = (26 \pm 4)\,\mathrm{fA}$. Although the precise origin of the dark current is not known, it is not caused by the rounding of the junction $I(V)$, but is due to a non-equilibrium population of the resonator corresponding to $\langle n_{\mathrm{res}} \rangle = 5 \cdot 10^{-4}$.

Out-of-Equilibrium Noise Spectroscopy

Furthermore, we measure the power emitted by the sample as a function of junction bias and fridge temperature. Measuring the emission gives us access to resonator population. Its evolution with junction bias for different temperatures is given in figure D.6. Full lines are the experimental data, while the dashed lines are master equation predictions taking into account the two lowest resonator modes. We observe an excellent agreement between the theory and the data.

Below the superconducting gap, we measure the resonator population lower than in equilibrium, corresponding to effective cooling of the resonator mode via photo-assisted tunneling. In the junction bias range $eV \in [2\Delta - \hbar\omega_1, 2\Delta]$ corresponding to maximum cooling power, the resonator population is approximately half its equilibrium value. When junction bias crosses the gap, the resonator population rises with junction bias due to junction emission. With the help of a classical master equation, we demonstrate that the resonator state in the bias range just above the superconducting gap is non-thermal when $\lambda \sim 1$ due to the imbalance between multi-photon absorption and emission rates. For high junction bias, the cavity state can again be described by an effective temperature directly proportional to the current flowing through the junction even in the strong coupling case,

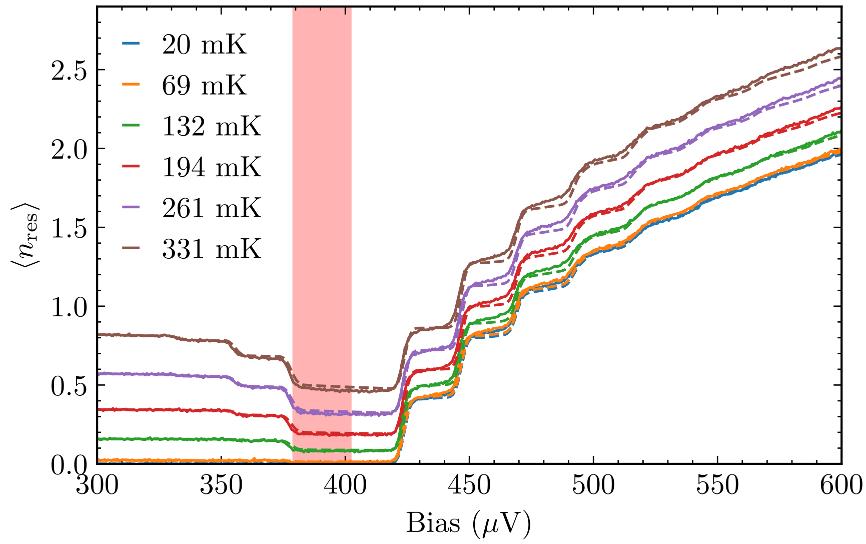

Figure D.6: Mean resonator population as function of junction bias voltage for different temperatures. The solid lines represent the experimental data, while the dashed lines are master equation predictions for ab initio sample parameters. Subgap voltage bias span $eV \in [2\Delta - \hbar\omega_1, 2\Delta]$ corresponding to maximum cooling power is highlighted in red.

and we show that the emission corresponds to the tunneling current shot noise. Therefore, the junction can be used as a calibrated source of microwaves, allowing for calibration of the microwave measurement chain gain [31, 33]. For the bias voltage values close to $eV = 2\Delta + \hbar\omega_1$, the emission spectra are non-Lorentzian. To compare the measured spectra with theory, we use the quantum master equation formalism, and apply the quantum regression theorem. The theory reproduces the shape of the spectra only if the multi-processes are allowed, and the cavity Lamb shift is taken into account, pointing to their crucial role in the dynamics of the system.

Towards the single photon detection: RF-SET in a High Impedance Environment

The work on photon detection presented above is devised as a step towards fabricating a single photon detector. The transition to photon counting requires shifting away from measuring the photo-assisted current to detecting single electrons resulting from microwave photon-to-electron conversion. Thus, we propose and implement a device consisting of two capacitively RF-SETs. One RF-SET acts as a photon-to-electron converter, and the second one is used for the readout. The incident photons are absorbed by the junction, changing the charge of the central SET island by e. This change is then detected by the readout. The device scheme is shown in figure D.7.

When measuring the reflection as function of SET bias and gate voltages, several copies of the Coulomb diamond structure are observed, corresponding to inelastic processes, both in the readout (figure D.8), and the converter (figure D.9). Similarly to the photon-to-electron converter shown above, there are areas of high absorption corresponding to suitable gate and bias voltages. Thus we can expect high photon-to-electron conversion efficiency. However, the dc measurements were too noisy to compare the expectations with experimental data.

The reflection measurements were used to determine the readout RF-SET charge noise as well. The readout charge noise is $5 \cdot 10^{-5}\,\mathrm{e}/\sqrt{\mathrm{Hz}}$. Even though the charge noise is low, there is still room

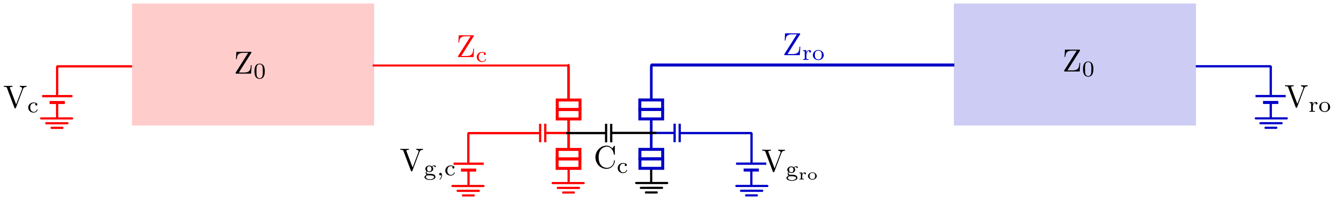

Figure D.7: Single microwave photon detector design based on two capacitively couple RF-SETs. One RF-SET, shown in red, is used as a photon to electron converter relying on inelastic quasiparticle tunneling. When the incident photon enters the converter resonator, it is absorbed by the junction, resulting in the change of the SET island charge. This change is detected by the capacitively coupled readout RF-SET shown in blue.

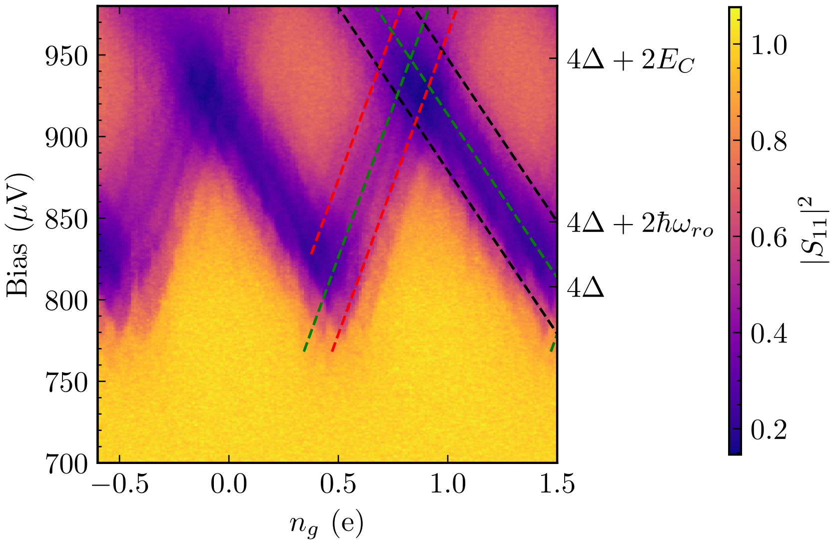

Figure D.8: Reflection at resonance frequency $\omega_{ro} = 2\pi \times 4.816\,\text{GHz}$ as function of gate and bias voltages for the readout RF-SET. Several copies of Coulomb diamonds are visible, corresponding to inelastic tunneling processes. Green dashed lines are the Coulomb diamonds delimiting elastic tunneling thresholds. The black dashed lines represent the inelastic tunneling thresholds fo the first junction. Similarly,the red dashed lines correspond to inelastic tunneling through the second junction.

for improvement compared to state-of-the-art RF-SET charge noise of $0.9 \cdot 10^{-6}\,\text{e}/\sqrt{\text{Hz}}$[49]. The overall performance of the detector could be improved by increasing the charging energy of both the readout and the converter. The charging energies are limited by the junction capacitance. Hence, reducing their size is a straightforward way towards increasing the charging energy, and thus better controlling the tunneling rates through the SET.

The readout was fabricated using a high impedance resonator, enabling a compact design, and easier fabrication compared to separate tank circuits commonly used in RF-SETs. High impedance allows us to realize impedance matching at higher bandwidths, speeding up the charge measurement, but it also limits the power used for the readout before the appearance of multi-photon processes limits the detector performance. Thus, a more systematic study is needed before concluding on the

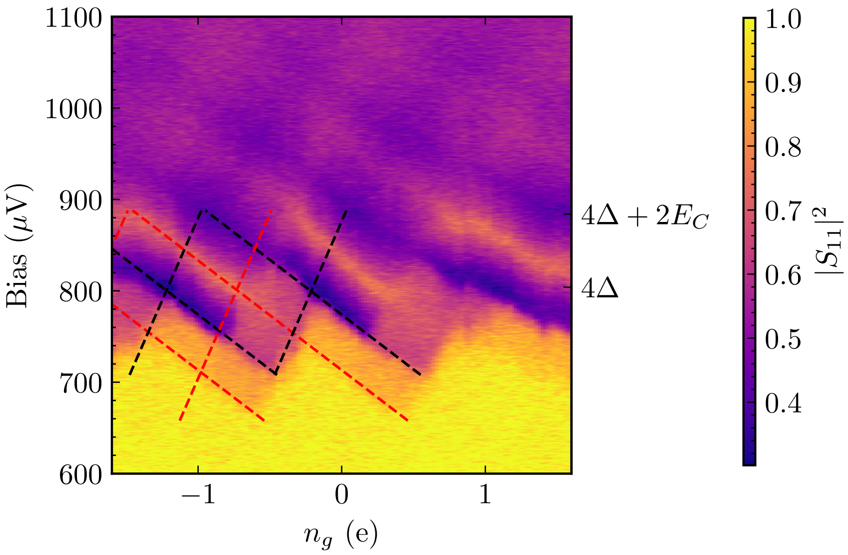

Figure D.9: Reflection as function of gate and bias voltages for the converter RF-SET at $2\pi \times 10.73\,\mathrm{GHz}$, and $P = -109\,\mathrm{dBm}$. As in the readout circuit, several copies of Coulomb diamonds are visible, corresponding to the inelastic tunneling processes. The elastic Coulomb diamonds are shown in green dashed lines. The red lines correspond to the width of the photo-assisted step for the first junction. Photo-assisted tunneling through the second junction is not visible due to low charging energy

optimal resonator characteristic impedance for charge detection.

The power emitted by the readout RF-SET is also measured and the Coulomb diamonds periodic in gate charge are observed (figure D.10). Furthermore, a step-like structure due to the dynamical Coulomb blockade is identified. To explain the experimental data, we develop a master equation model for tunneling through a single junction. The state of the system is characterized by the number of photons in the resonator, and the number of excess quasiparticles on the SET island. The transition rate matrix was constructed from the tunneling rates between different states, and the resulting master equation steady state solution is used to determine the resonator population. This model aligns well with the data, and reproduces the observed non-monotonic increase in resonator population with rising junction bias.

We have demonstrated that the charge flow through the converter SET could be detected by through the reflectometry of the readout. However, we were unable to detect single tunneling events due to low charging energy and resistance of the converter SET. In the future, the charging energies can be increased by better controlling the junction size.

We are confident that the single photons could be measured at a rate of $100\,\mathrm{kHz}$. Therefore, the dark count of the detector needs to be significantly lower than this value. The obvious way to reduce the dark count would be to decrease the resonator width. The recent work in [27] shows that dark count rates as low as $100\,\mathrm{s}^{-1}$ can be reached in a narrow band detector. The resonator width can be reduced by using a Brag structure [59] to keep the galvanic contact for biasing the junction, and controlling the coupling rate through a separate capacitively coupled feedline. To keep the high quantum efficiency in a narrow band resonator, the intrinsic losses need to be reduced compared to the device presented in the thesis. High quality granular aluminium resonators ($Q_i = 10^5$)

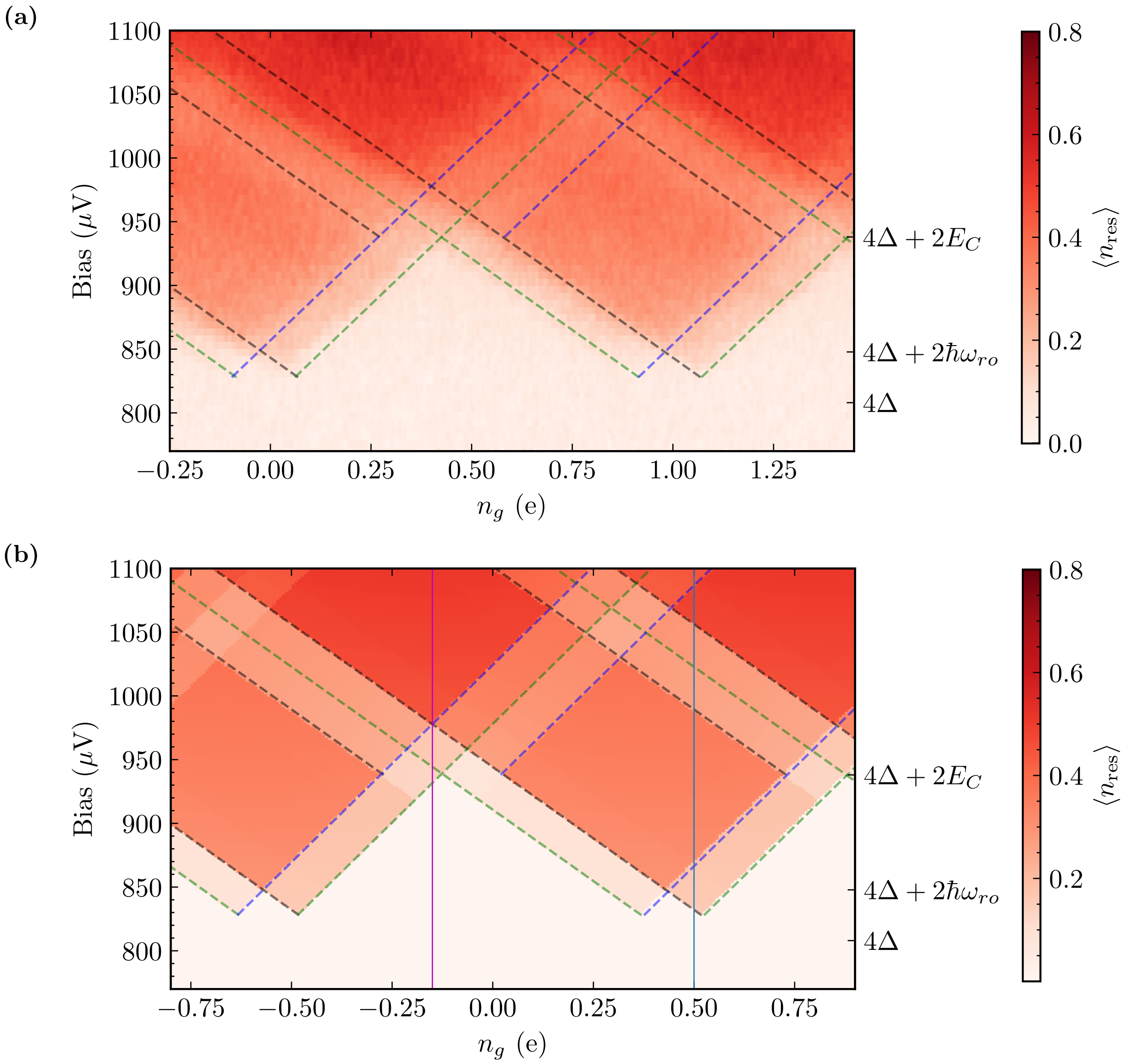

Figure D.10: Readout resonator population as function of the junction bias voltage and gate voltages (a) Experimental data. Green dashed current lines represent the Coulomb diamonds corresponding to elastic tunneling. Black dashed lines represent the inelastic tunneling through junction one, and the black through junction two. (b) Classical master equation calculation result. Dashed lines are same as in panel (a).

have already been fabricated [60], and we do not consider this requirement to be a fundamental limiting factor for transition to single photon detection. As the resonator width is reduced, the dark rate due to the subgap current will make a significant share of the total dark counts. Thus, the scaling of the dark count with resonator width needs to be checked experimentally. High kinetic inductance materials, such as granular aluminium will play a crucial role in building these narrow band detectors, as they enable use of more resistive junctions while keeping high quantum efficiency, thus limiting the subgap dark current. We envision that such detectors will have a crucial role in advancing microwave quantum optics, sensing, and many more areas of research, such as axion detection.

Appendix E

Résumé en français

Dans le domaine optique, l'effet photoélectrique est la méthode de choix pour construire des détecteurs de photons uniques couvrant un large spectre de fréquences avec une grande efficacité quantique et un faible courant d'obscurité. La réduction de l'énergie des photons aux fréquences micro-ondes ($\sim 10\,\mathrm{GHz}$) répondant aux exigences de la détection de photons uniques, est un défi expérimental important en raison de l'absence de matériaux semi-conducteurs ou supraconducteurs de bande interdite suffisamment faible. Un détecteur micro-ondes efficace aurait cependant une utilité importante en optique quantique micro-ondes [15], en cryptographie quantique [16], détection de spin [17, 18]ou encore pour la recherche d'axion [19, 20, 21]. Par conséquent, le développement de détecteurs de photons micro-ondes reste un domaine de recherche intense. Plusieurs efforts récents ont exploité les circuits quantiques supraconducteurs [22] de différentes manières — que ce soit en intriquant le photon hyperfréquence avec un qubit [23, 24], en utilisant la criticalité quantique [25] ou encore en utilisant l'effet Josephson dans les mélangeurs supraconducteurs [26, 27].

Conception d'un convertisseur photon-électron

Dans cette thèse, nous développons l'idée d'un détecteur de photons à micro-ondes basé sur l'effet photoélectrique. Plutôt que de compter uniquement sur l'énergie du photon incident pour briser les paires de Cooper du supraconducteur, notre détecteur est basé sur l'effet tunnel photo-assisté à travers une jonction tunnel supraconductrice polarisée juste en dessous du gap supraconducteur. Ainsi, la différence d'énergie entre le photon micro-onde et le gap est fournie par une source de tension. Ces dernières années, la réalisation de détecteurs de photons micro-ondes uniques basés sur l'effet tunnel inélastique a été un domaine de recherche actif, et des progrès notables ont été réalisés, notamment en utilisant l'effet tunnel photo-assisté au travers des doubles boites quantiques semi-conductrices [36, 37, 38]. Bien que ces expériences soient prometteuses, ces dispositifs souffrent d'une faible efficacité quantique, due à l'inadéquation entre le taux d'effet tunnel photo-assisté et le taux d'arrivée des photons.

Dans notre approche, lorsque la jonction tunnel supraconductrice est irradiée par des photons, la caractéristique courant-tension de la jonction est modifiée par le processus tunnel inélastique, au cours duquel une quasiparticule acquiert l'énergie nécessaire pour traverser la jonction en absorbant un photon [39]. Ce processus est illustré dans la figure E.1 ensemble avec la modification de la caractéristique courant-tension. Nous observons que le courant sous le gap supraconducteur n'apparaît que si le rayonnement électromagnétique est présent. C'est cet effet que nous avons exploité pour la détection de photons. L'effet tunnel photo-assisté à travers les jonctions a déjà été exploité dans le passé pour détecter des rayonnements électromagnétiques, par exemple grâce à

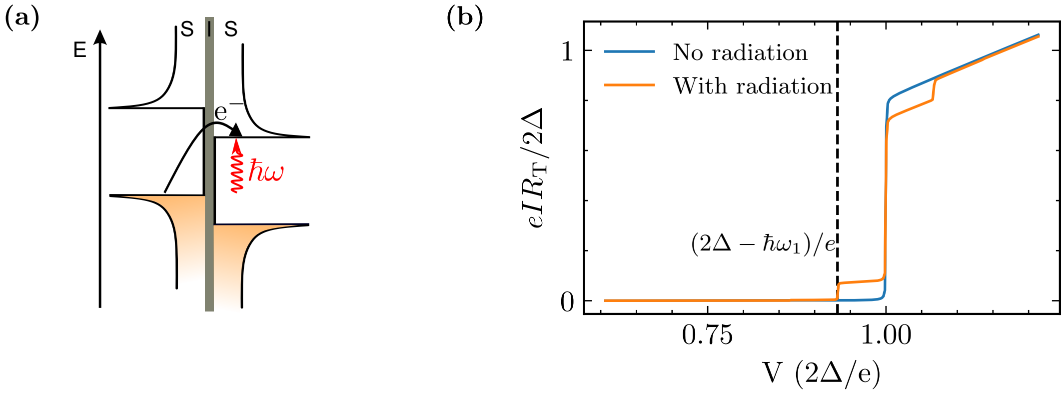

Figure E.1: (a) Tunnel de quasiparticules photo-assisté à travers une jonction SIS (b) Caractéristiques courant-tension calculées d'une jonction SIS de résistance R_{T} : le courant en l'absence de rayonnement électromagnétique est représenté en bleu. Le courant à travers la jonction irradiée par une lumière de fréquence ω_1 est en orange.

l'utilisation de mélangeurs SIS en astronomie, à des fréquences de l'ordre de 100 GHz. [41], ou pour les mesures de bruit à des fréquences micro-ondes [42]. Dans ce travail, nous abaissons la fréquence de fonctionnement des détecteurs basés sur l'effet tunnel des quasiparticules à la bande 4 - 8 GHz, et repoussons les limites de l'efficacité grâce à l'utilisation de matériaux supraconducteurs désordonnés qui amplifie le couplage lumière matière de manière significative. L'objectif final étant la détection de photons micro-ondes uniques avec la meilleure efficacité. Le schéma du détecteur que nous proposons est illustré par la figure E.2. Il se compose d'un résonateur couplé galvaniquement à une ligne de transmission $Z_0 = 50\,\Omega$, qui est ensuite connectée au reste du dispositif expérimental. Pour détecter les photons de longueur d'onde w, la longueur du résonateur est fixée à $w/4$. Il est terminé par une jonction tunnel supraconductrice polarisée en tension dont la résistance tunnel est R_{T}. La jonction est polarisée de telle sorte que l'absorption des photons incidents par effet tunnel photo-assisté est énergétiquement permise, mais qu'aucun courant ne circule en l'absence de micro-ondes. Ces conditions sont remplies pour des tensions de polarisation $eV \in [2\Delta - \hbar\omega_1, 2\Delta]$. L'impédance caractéristique Z_c du résonateur est comparable au quantum de résistance, de sorte que le paramètre de couplage satisfait $\lambda = \sqrt{\pi Z_c/R_K} \sim 1$, afin d'augmenter le taux d'effet tunnel inélastique. Pour obtenir une impédance caractéristique élevée, le résonateur est fabriqué en aluminium granulaire, un supraconducteur désordonné à inductance cinétique élevée.

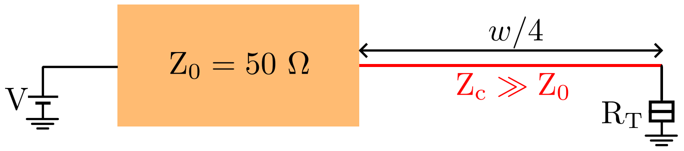

Figure E.2: Schéma d'un convertisseur de photons en électrons. Pour détecter les photons de longueur d'onde w, un résonateur $w/4$, représenté en rouge, est terminé d'un côté par une jonction tunnel supraconductrice polarisée en tension. L'impédance caractéristique Z_c du résonateur est comparable au quantum de la résistance. Le résonateur est couplé galvaniquement au reste du circuit par une ligne de transmission d'impédance caractéristique 50 Ω.

L'effet tunnel de quasiparticules dans les jonctions couplées à un environnement électromagnétique comme le mode d'un résonateur, est généralement décrit par la théorie $P(E)$ [40]. Dans cette théorie, l'influence de l'environnement est calculée à partir des fluctuations quantiques de la phase aux électrodes de jonction. Le modèle $P(E)$ s'est avéré très efficace pour prédire les taux d'effet tunnel inélastique [46, 47]. Cependant, l'une des hypothèses fondamentales de la théorie standard $P(E)$ est que les modes électromagnétiques restent à l'équilibre thermique. Comme nous considérons un couplage fort avec des modes à facteur de qualité élevé, cette hypothèse ne peut pas être satisfaite. Dans ce cas, les taux des différents processus dépendent de l'état du résonateur, et la description complète du système doit tenir compte de ce fait. Si nous supposons que l'état initial du résonateur est $|n\rangle$, et que l'état final est $|n+l\rangle$, le taux d'effet tunnel correspondant à ce processus, donné par la règle d'or de Fermi, est:

$$\kappa_{n,n+l} = \left|\langle n+l|\, e^{i\lambda(a+a^\dagger)}\, |n\rangle\right|^2 I(V - l\hbar\omega_1/e)/e \tag{E.1}$$

où $\lambda = \sqrt{\pi Z_c/R_K}$ est la constante de couplage résonateur-jonction, $I(V)$ est la caractéristique courant-tension de la jonction en l'absence d'environnement, et ω_1 est la fréquence du mode de résonateur couplé à la jonction.

Pour calculer le courant net circulant à travers la jonction, nous la traitons comme un bain markovien à l'équilibre et dérivons l'équation maîtresse quantique régissant l'évolution temporelle de l'opérateur de densité réduite du résonateur. La matrice de densité du résonateur obtenue à l'état d'équilibre est ensuite utilisée pour calculer le courant en présence d'une impulsion micro-onde cohérente. Lorsque le nombre moyen de photons dans le résonateur est significativement inférieur à un, et pour des tensions de polarisation de la jonction $eV \in [2\Delta - \hbar\omega_r, 2\Delta]$, le courant photo-assisté est proportionnel à la population du résonateur, et le dispositif peut être utilisé pour la détection de photons.

L'efficacité quantique de la conversion photon-électron est donnée par le rapport entre le flux d'électrons résultant ϕ_e et le flux de photons incident ϕ:

$$\chi = \frac{\phi_e}{\phi} = \frac{I_{\mathrm{PAT}}}{e\phi}. \tag{E.2}$$

Dans notre expérience, il s'écrit comme

$$\chi = \frac{4\kappa_j\kappa_c}{(\kappa_i + \kappa_j + \kappa_c)^2}, \tag{E.3}$$

où

$$\kappa_j = \lambda^2 e^{-\lambda^2} I(V + \hbar\omega_1/e) \tag{E.4}$$

est le taux d'absorption de la jonction à photon unique, κ_c est le taux de couplage entre le résonateur et la ligne de transmission, et κ_i décrit les pertes parasites dans le résonateur. L'efficacité quantique est maximale à $\kappa_j = \kappa_c + \kappa_i$, ce qui équivaut à une condition d'adaptation de l'impédance pour maximiser le transfert de puissance vers la charge dans les circuits électriques. Le taux de couplage κ_c est fixé par la géométrie de l'échantillon, de sorte que la condition d'adaptation du taux est satisfaite en ajustant la résistance de jonction. L'utilisation d'un taux de couplage élevé permet d'utiliser une résistance de jonction plus élevée, tout en remplissant la condition d'adaptation du taux, minimisant ainsi le taux d'électrons sombres fixé.

Caractérisation expérimentale du convertisseur photon-électron

Après avoir fabriqué le dispositif décrit dans la section précédente, nous le refroidissons à 20 mK dans un réfrigérateur à dilution. Tout d'abord, nous mesurons les spectres de réflection à différentes polarisations de jonction proches du gap supraconducteur. Les mesures sont présentées dans la figure E.3a. Nous observons une résonance à $\omega_1 = 2\pi \times 5.5\,\mathrm{GHz}$, correspondant au mode fondamental du résonateur. A faible polarisation, il y a un léger creux dans le signal réfléchi, ce qui signifie que les pertes sont faibles. Lorsque la polarisation de la jonction s'approche du gap supraconducteur, on observe une chute brutale de la réflexion à la résonance, et pour des tensions de polarisation $V > (2\Delta - \hbar\omega_1)/e = 379\,\mu\mathrm{V}$, nous avons une absorption presque parfaite. Pour extraire les différents taux de perte, nous ajustons chaque spectre à l'équation

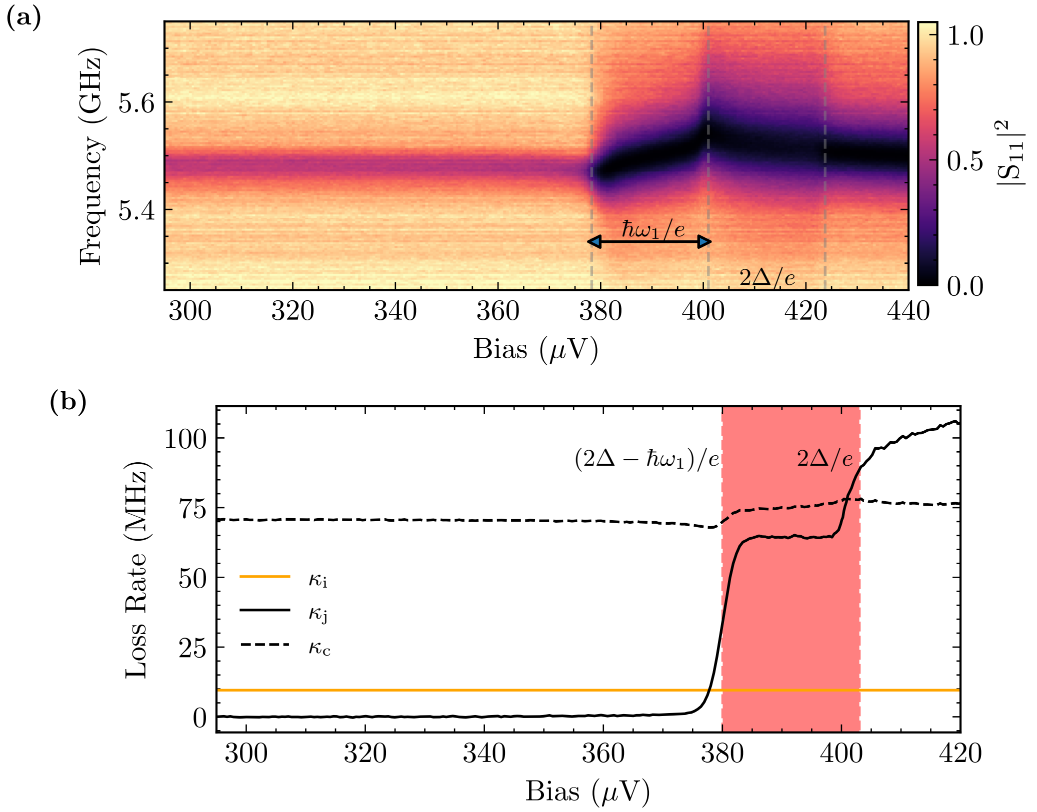

Figure E.3: (a) Valeur absolue du signal réfléchi en fonction de la polarisation de la jonction et de la fréquence. La puissance d'excitation micro-ondes est $P = -142\,\mathrm{dBm}$. (b) Taux de perte κ_c, κ_j et κ_i en fonction de la tension de polarisation.

$$S_{11} = 1 - \frac{\kappa_c}{\frac{\kappa+\kappa_c}{2} + i(\omega - \omega_r)} \tag{E.5}$$

où κ_c est la perte de couplage, tandis que κ décrit toutes les autres pertes présentes dans le système. Le taux de perte de couplage dépend faiblement de la polarisation de la jonction, et sa valeur est $\kappa_c = 2\pi \times 71\,\mathrm{MHz}$. L'autre taux de perte κ est constant en dessous du gap. À la tension de polarisation $eV = 2\Delta - \hbar\omega_1$, il passe de $2\pi \times 9.5\,\mathrm{MHz}$ à $2\pi \times 75\,\mathrm{MHz}$, puis reste constant dans la plage de polarisation $2\Delta - \hbar\omega_1 < eV < 2\Delta$. Ce taux de perte a deux contributions — les pertes induites par la jonction κ_j, et les pertes internes du résonateur κ_i:

$$\kappa = \kappa_i + \kappa_j. \tag{E.6}$$

Nous nous attendons à ce que κ_j soit négligeable bien en dessous du gap supraconducteur. Nous attribuons donc ce taux de perte aux pertes du résonateur interne indépendantes de la tension κ_i. La figure D.3b montre la dépendance en tension de ces taux de perte. Après avoir obtenu les trois taux κ_c, κ_j et κ_i, nous calculons l'absorption des micro-ondes

$$1 - |S_{11}(0)|^2 = \frac{4(\kappa_i + \kappa_j)\kappa_c}{(\kappa_i + \kappa_j + \kappa_c)^2} \tag{E.7}$$

et l'efficacité quantique attendue de la conversion des photons en électrons

$$\chi = \frac{4\kappa_j\kappa_c}{(\kappa_i + \kappa_j + \kappa_c)^2}. \tag{E.8}$$

La probabilité d'absorption et l'efficacité quantique sont présentées dans la figure E.4 pour différentes polarisations de jonction. À l'intérieur du gap, l'absorption est d'environ 0.4 en raison des pertes internes du résonateur. Pour des tensions $eV > 2\Delta - \hbar\omega_1$, où l'effet tunnel des quasiparticules photo-assisté est autorisé, l'absorption augmente jusqu'à atteindre l'unité. À la même tension de polarisation, l'efficacité quantique passe de 0 à 0.85. En particulier, sur l'ensemble de la plage de tension de polarisation $eV \in [2\Delta - \hbar\omega_1, 2\Delta]$, nous prévoyons une efficacité quantique $\chi > 0.85$ et de faibles comptes d'obscurité.

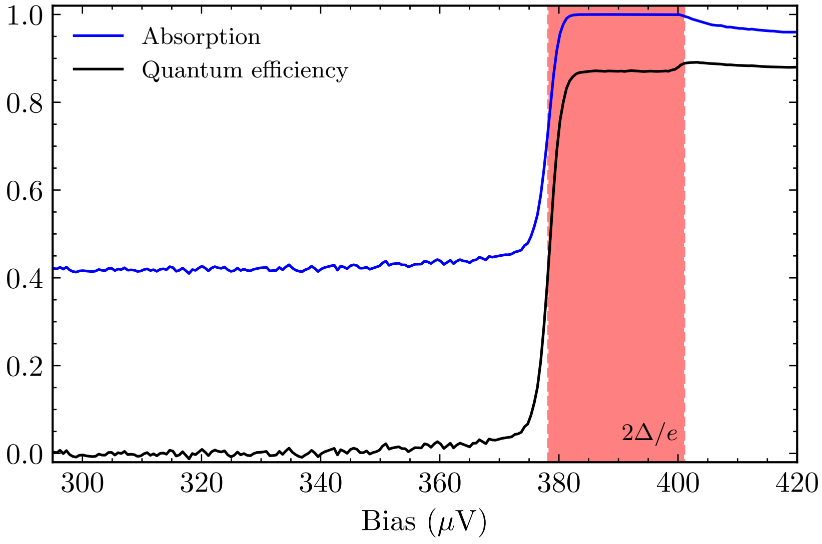

Figure E.4: Absorption (bleu) et efficacité quantique attendue (noir) en fonction de la polarisation de la jonction. La gamme des polarisations de tension adaptées aux expériences de détection de photons, caractérisées par une efficacité quantique élevée et un faible taux d'obscurité, est ombrée en rouge.

Pour vérifier cette estimation de l'efficacité quantique, nous mesurons le courant photo-assisté en fonction de la puissance micro-ondes appliquée à des tensions de polarisation $eV = 2\Delta - (2n -$

$1)\hbar\omega_1/2, b = 1, 2, 3, 4$, correspondant à des processus d'absorption à 1, 2, 3 et 4 photons (figure E.5). Lorsque la population du résonateur est faible, le courant photo-assisté dû à l'absorption de

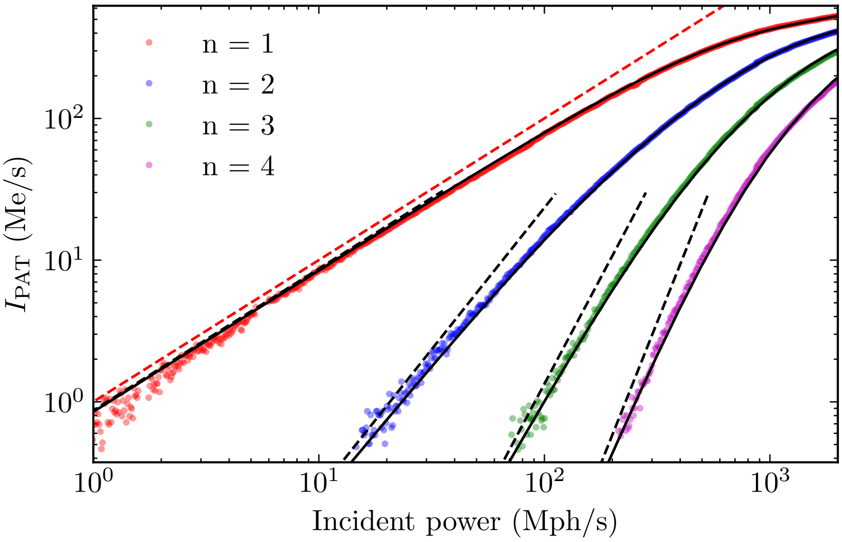

Figure E.5: Courant photo-assisté en fonction de la puissance des micro-ondes mesurée aux tensions $eV = 2\Delta - (2n-1)\hbar\omega_1/2, n = 1, 2, 3, 4$, à résonance. Les lignes noires en pointillé représentent les solutions de l'équation maîtresse quantique dans la limite de pompage faible, tandis que les lignes noires pleines sont les prévisions obtenues en résolvant numériquement l'équation maîtresse quantique. La ligne rouge en pointillés représente la conversion idéale du photon en électron, avec une efficacité quantique égale à un. Les paramètres de l'échantillon sont fixés à leurs valeurs ab initio, et l'on suppose que la puissance incidente à l'étage de l'échantillon est connue.

photons uniques augmente linéairement avec la puissance appliquée. À puissance élevée, le courant photo-assisté sature en raison de l'absorption multiphotonique. Cette saturation est quantifiée par des points de compression à 1 dB et 3 dB. Pour notre détecteur, ces points de compression sont $P_{1\,\mathrm{dB}} = 340\,\mathrm{Mph/s}$ et $P_{3\,\mathrm{dB}} = 1040\,\mathrm{Mph/s}$. En ajustant les quatre courbes courant-puissance au modèle d'équation maîtresse quantique en même temps, avec l'atténuation entre l'échantillon et la source de micro-ondes comme seul paramètre libre, nous calibrons la puissance incidente à l'entrée de l'échantillon. Dans les calculs théoriques, les paramètres de l'échantillon sont fixés à leurs valeurs ab initio. Le paramètre de couplage jonction-résonateur est $\lambda = 0.785$. Le taux d'amortissement du résonateur $\kappa_c + \kappa_i = 2\pi \times 80.5\,\mathrm{MHz}$ est tiré des mesures de spectroscopie micro-ondes, et la résistance de jonction est $R_\mathrm{T} = 1.75\,\mathrm{M\Omega}$. Une fois la puissance incidente calibrée, l'efficacité quantique est calculée à partir de la variation du courant d'absorption du photon unique en fonction de la puissance. Le résultat obtenu est

$$\chi = (0.83 \pm 0.05) \tag{E.9}$$

En plus de la réponse à une excitation cohérente, le courant dû au rayonnement thermique dans le résonateur a aussi été mesuré en changeant la température du réfrigérateur. Les résultats obtenus confirment l'efficacité quantique obtenue par pompage.

Pour déterminer le courant d'obscurité, nous avons mesuré le courant traversant la jonction au point de fonctionnement du détecteur sans aucune irradiation micro-onde. Le courant d'obscurité mesuré est $I_{\text{dark}} = (26 \pm 4)\,\text{fA}$. Bien que l'origine précise du courant d'obscurité ne soit pas connue, il n'est pas causé par l'arrondissement de la jonction $I(V)$, mais est dû à une population hors-équilibre du résonateur correspondant à $\langle n_{\text{res}} \rangle = 5 \cdot 10^{-4}$.

Spectroscopie du bruit hors d'équilibre

Nous avons mesuré la puissance émise par l'échantillon en fonction de la polarisation de la jonction et de la température du réfrigérateur. La mesure de l'émission nous donne accès à la population du résonateur. Son évolution en fonction de la polarisation de la jonction pour différentes températures est donnée en figure E.6. Les lignes pleines sont les données expérimentales, tandis que les lignes pointillées sont les prédictions de l'équation maîtresse prenant en compte les deux modes les plus bas du résonateur. Nous observons un excellent accord entre la théorie et les données.

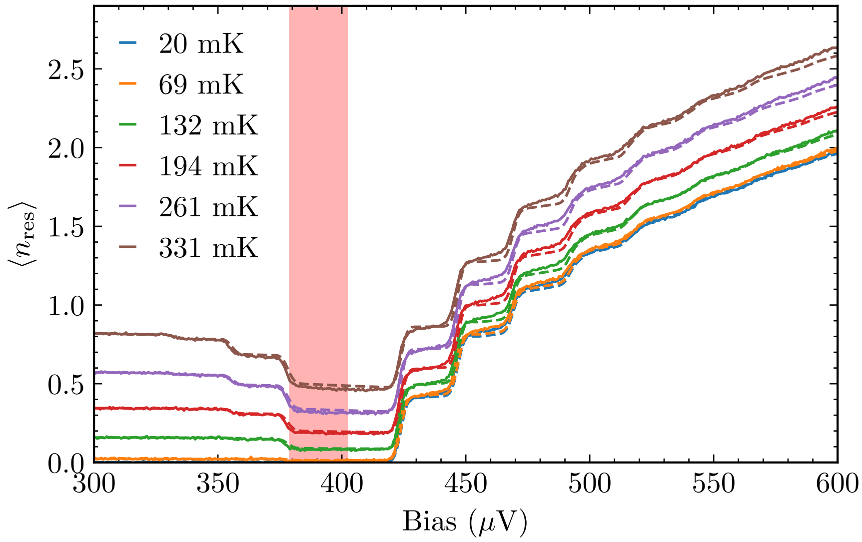

Figure E.6: Population moyenne du résonateur en fonction de la tension de polarisation de la jonction pour différentes températures. Les lignes pleines représentent les données expérimentales, tandis que les lignes pointillées sont des prédictions de l'équation maîtresse pour les paramètres de l'échantillon ab initio. La gamme de tension de polarisation $eV \in [2\Delta - \hbar\omega_1, 2\Delta]$ correspondant à la puissance de refroidissement maximale est surlignée en rouge.

En dessous du gap supraconducteur, nous mesurons la population du résonateur plus basse qu'à l'équilibre, ce qui correspond à un refroidissement effectif du mode du résonateur par effet tunnel photo-assisté. Dans la plage de polarisation de la jonction $eV \in [2\Delta - \hbar\omega_1, 2\Delta]$ correspondant à la puissance de refroidissement maximale, la population du résonateur est approximativement la moitié de sa valeur d'équilibre. Lorsque la polarisation de la jonction traverse le gap, la population du résonateur augmente avec la polarisation de la jonction en raison de l'émission de la jonction. À l'aide de l'équation maîtresse classique, nous démontrons que l'état du résonateur dans la plage de polarisation juste au-dessus du gap supraconducteur est non thermique lorsque $\lambda \sim 1$ en raison du déséquilibre entre les taux d'absorption et d'émission multiphotonique. Pour une polarisation élevée de la jonction, l'état de la cavité peut à nouveau être décrit par une température effective directement proportionnelle au courant traversant la jonction, même dans le cas d'un couplage fort, et nous montrons que l'émission correspond au bruit de grenaille du courant d'effet tunnel. Par conséquent, la jonction peut être utilisée comme une source calibrée de micro-ondes, permettant l'étalonnage du gain de la chaîne de mesure des micro-ondes [31, 33]. Pour les valeurs de tension de polarisation proches de $eV = 2\Delta + \hbar\omega_1$, les spectres d'émission sont non-lorentziens. Pour comparer les spectres mesurés avec la théorie, nous utilisons le formalisme de l'équation maîtresse quantique et appliquons le théorème de régression quantique. La théorie ne reproduit la forme des spectres que si les processus multiphotoniques sont autorisés, et si le décalage de Lamb de la cavité est pris en compte, ce qui met en évidence leur rôle crucial dans la dynamique du système.

Vers la détection d'un photon unique : RF-SET dans un environnement à haute impédance

Les travaux sur la détection des photons présentés ci-dessus sont conçus comme une étape vers la fabrication d'un détecteur à photon unique. La transition vers le comptage de photons nécessite de passer de la mesure du courant photo-assisté à la détection d'électrons uniques résultant de la conversion photon-électron par micro-ondes. Nous proposons ici, et mettons en œuvre, un dispositif composé de deux RF-SET couplés capacitivement. Un RF-SET sert de convertisseur photon-électron et le second est utilisé pour la lecture. Les photons incidents sont absorbés par la jonction, ce qui modifie la charge de l'îlot du SET convertisseur de e. Ce changement est ensuite détecté par le SET détecteur de charge. Le schéma du dispositif est illustré dans la figure E.7.

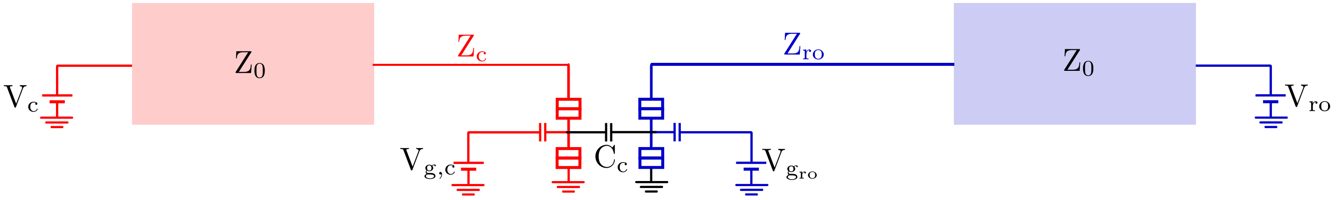

Figure E.7: Conception d'un détecteur de photons à micro-ondes unique basé sur deux RF-SET haute impédance couplé capacitivement. Un RF-SET, représenté en rouge, est utilisé comme convertisseur de photons en électrons en s'appuyant sur l'effet tunnel inélastique de quasiparticules. Lorsque le photon incident pénètre dans le résonateur du convertisseur, il est absorbé par la jonction, ce qui entraîne une modification de la charge de l'îlot du SET. Ce changement est détecté par le lecteur de charge couplé capacitivement et représenté en bleu.

En mesurant la réflexion micro-ondes en fonction de la polarisation en tension et des tensions de grille des SETs, on observe plusieurs copies de la structure en diamant de Coulomb, correspondant à des processus inélastiques, à la fois pour le SET de lecture (figure E.8) et le convertisseur (figure E.9). Comme dans le cas du convertisseur photon-électron illustré ci-dessus, il existe des zones de forte absorption correspondant à des tensions de grille et de polarisation appropriées. On peut donc s'attendre à une efficacité élevée de la conversion photon-électron.

Les mesures de réflexion ont également été utilisées pour déterminer le bruit de charge du RF-SET de lecture. Le bruit de charge est de $5 \cdot 10^{-5}\,\mathrm{e}/\sqrt{\mathrm{Hz}}$. Même si le bruit de charge est faible, il peut encore être amélioré par rapport au bruit de charge RF-SET de pointe de $0.9 \cdot 10^{-6}\,\mathrm{e}/\sqrt{\mathrm{Hz}}$[49]. Les performances globales du détecteur pourraient être améliorées en augmentant l'énergie de charge de la lecture et du convertisseur. Les énergies de charge sont limitées par la capacité de jonction. Par conséquent, la réduction de leur taille est un moyen direct d'augmenter l'énergie de charge, et donc de mieux contrôler les taux d'effet tunnel à travers le SET.

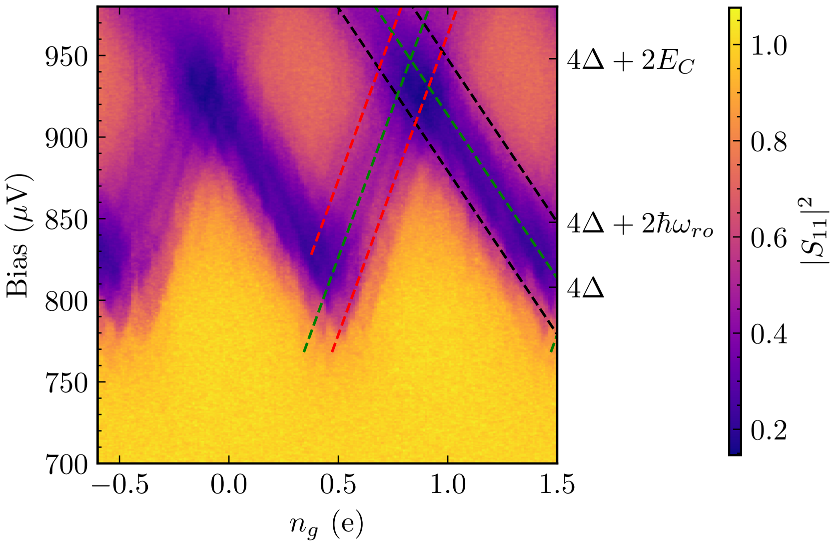

Figure E.8: Réflexion micro-onde à la fréquence de résonance $\omega_{ro} = 2\pi \times 4.816\,\mathrm{GHz}$ en fonction des tensions de grille et de polarisation source-drain pour le RF-SET de lecture. Plusieurs copies de diamants de Coulomb sont visibles, correspondant à des processus d'effet tunnel inélastique. Les lignes pointillées vertes sont les diamants de Coulomb délimitant les seuils d'effet tunnel élastique. Les lignes pointillées noires représentent les seuils d'effet tunnel inélastique de la première jonction. De même, les lignes pointillées rouges correspondent à l'effet tunnel inélastique à travers la deuxième jonction.

Le RF-SET de lecture a été fabriqué à l'aide de résonateurs à haute impédance, ce qui permet une conception compacte et une fabrication plus facile par rapport aux circuits bouchons couramment utilisés dans les RF-SET. Une impédance caractéristique élevée nous permet de réaliser une adaptation d'impédance pour des résistances tunnels plus élevées, ce qui accélère la mesure de la charge. En revanche, elle limite la puissance utilisée pour la lecture avant que l'apparition de processus multiphotoniques ne limite les performances du détecteur.

Afin de mieux cerner la physique du SET couplé à un résonateur haute impédance, nous avons mesuré la puissance émise par le RF-SET de lecture. Des diamants de Coulomb périodiques en tension de grille sont observés (figure E.10). Des structures en escalier dues à un blocage de Coulomb dynamique sont identifiées. Afin d'expliquer les données expérimentales, nous développons un modèle d'équation maîtresse pour l'effet tunnel à travers une jonction unique. L'état du système est caractérisé par le nombre de photons dans le résonateur et le nombre de quasiparticules en excès sur l'îlot métallique. La matrice des taux de transition a été construite à partir des taux d'effet tunnel entre les différents états, et la solution d'état stable de l'équation maîtresse qui en résulte est utilisée pour déterminer la population du résonateur. Ce modèle correspond bien aux données et reproduit l'augmentation non monotone observée de la population du résonateur avec l'augmentation de la polarisation de la jonction.

Nous avons démontré que le flux de charge à travers le convertisseur SET pouvait être détecté par la réflectométrie de la lecture. Cependant, nous n'avons pas été en mesure de détecter des événements tunnel unique en raison de la faible énergie de charge et de la résistance du convertisseur SET. À l'avenir, les énergies de charge pourront être augmentées en contrôlant mieux la taille de la

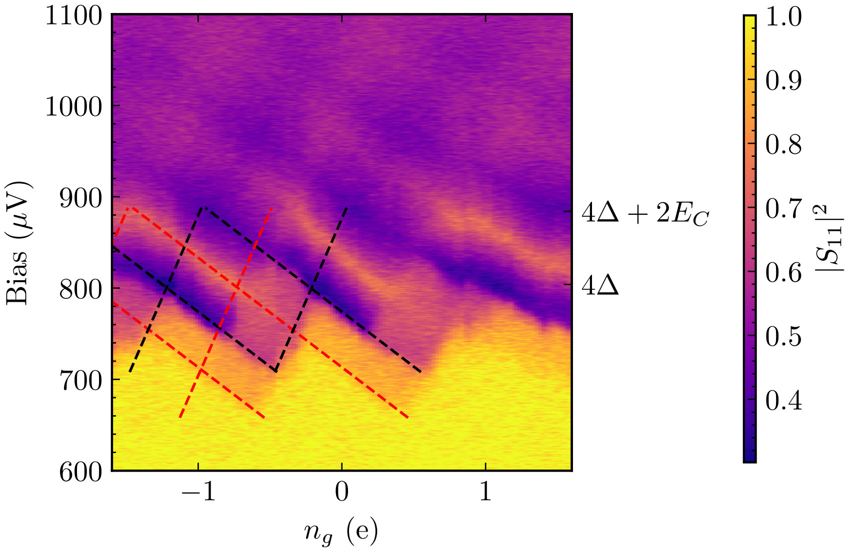

Figure E.9: Réflexion micro-onde en fonction des tensions de grille et de polarisation source-drain pour le convertisseur RF-SET à $2\pi \times 10.73\,\mathrm{GHz}$, et $P = -109\,\mathrm{dBm}$. Comme dans le circuit de lecture, plusieurs copies de diamants de Coulomb sont visibles, correspondant à des processus d'effet tunnel inélastique. Les diamants de Coulomb élastiques sont représentés par des lignes pointillées vertes. Les lignes rouges correspondent à la largeur de l'étape photo-assistée pour la première jonction. L'effet tunnel photo-assisté à travers la deuxième jonction n'est pas visible en raison de la faible énergie de charge.

jonction.

Nous sommes convaincus que les photons uniques pourraient être mesurés à un taux de 100 kHz. Par conséquent, le taux d'obscurité du détecteur doit être nettement inférieur à cette valeur. La façon la plus évidente de réduire le taux d'obscurité serait de diminuer la largeur de bande du résonateur. Les travaux récents de [27] montrent que des taux de comptage d'obscurité aussi bas que $100\,\mathrm{s}^{-1}$ peuvent être atteints dans un détecteur à bande étroite. La largeur du résonateur peut être réduite en utilisant une structure de miroir de Bragg [59] pour conserver le contact galvanique afin de polariser la jonction, et en contrôlant le taux de couplage par le biais d'une ligne d'alimentation séparée à couplage capacitif. Pour conserver le rendement quantique élevé d'un résonateur à bande étroite, les pertes intrinsèques doivent être réduites par rapport au dispositif présenté dans la thèse. Des résonateurs en aluminium granulaire de haute qualité ($Q_i = 10^5$) ont déjà été fabriqués [60], et nous ne considérons pas cette exigence comme un facteur limitant fondamental pour la transition vers la détection de photons uniques. Au fur et à mesure que la largeur du résonateur est réduite, le taux d'obscurité constituera une part importante des comptes d'obscurité totaux. Il convient donc de vérifier expérimentalement l'évolution du taux d'obscurité en fonction de la largeur du résonateur. Les matériaux à haute inductance cinétique, tels que l'aluminium granulaire, joueront un rôle crucial dans la construction de ces détecteurs à bande étroite, car ils permettent d'utiliser des jonctions plus résistives tout en conservant une efficacité quantique élevée, limitant ainsi le courant d'obscurité.

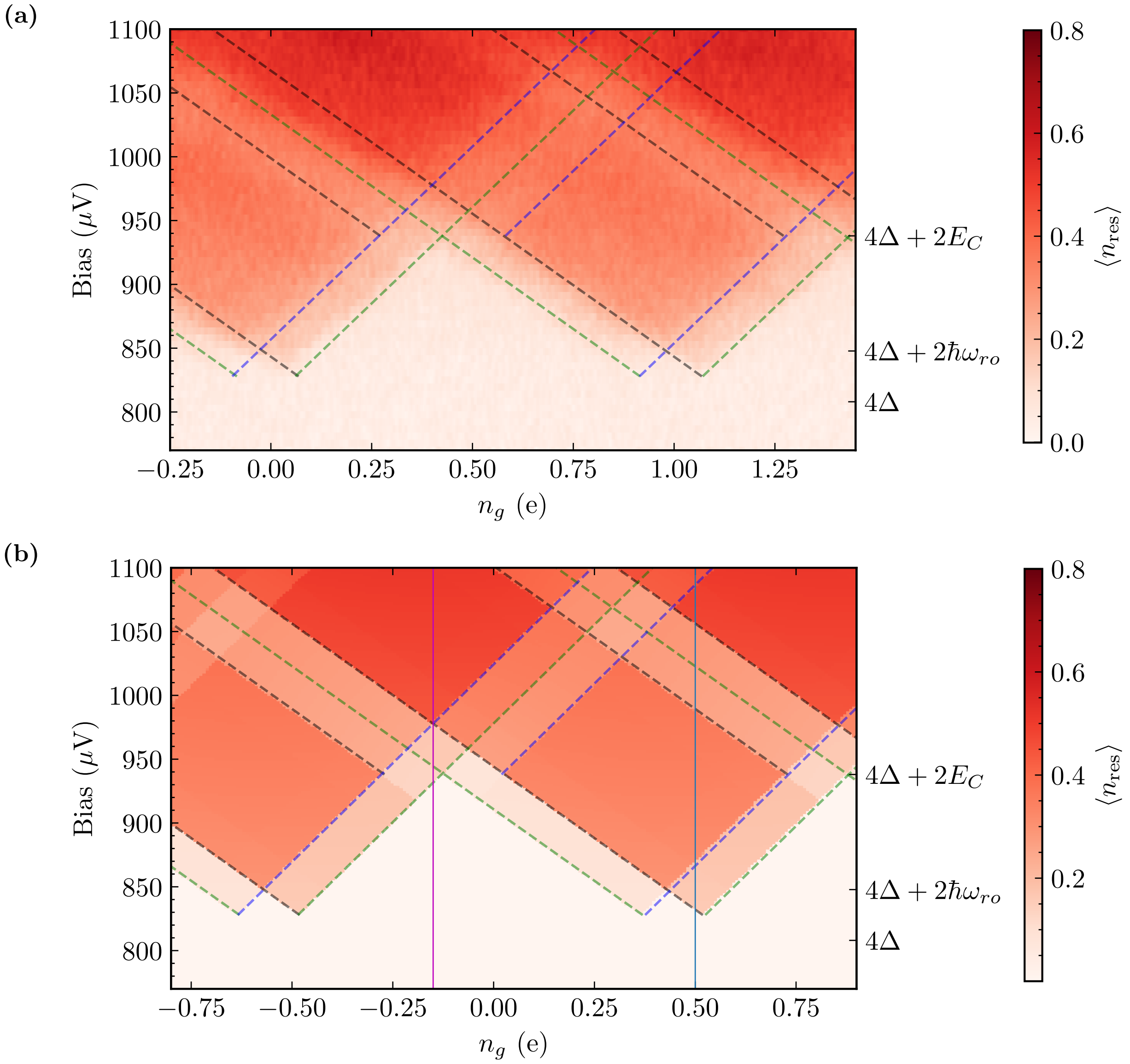

Figure E.10: Population du résonateur couplé au SET de lecture en fonction de la tension de polarisation de la jonction et de la tensions de grille (a) Données expérimentales. Les lignes de courant en pointillés verts représentent les diamants de Coulomb correspondant à l'effet tunnel élastique. Les lignes pointillées noires représentent l'effet tunnel inélastique à travers la jonction un, et les lignes noires à travers la jonction deux. (b) Résultat du calcul de l'équation maîtresse classique. Les lignes en pointillé sont les mêmes que dans le panneau (a).

Bibliography

[1] R. Foord, R. Jones, C. J. Oliver, and E. R. Pike. The Use of Photomultiplier Tubes for Photon Counting. *Applied Optics*, 8(10):1975–1989, October 1969. ISSN 2155-3165. doi: 10.1364/AO.8.001975.

[2] P. Cushman and R. Rusack. A photomultiplier tube incorporating an avalanche photodiode. *Nuclear Instruments and Methods in Physics Research Section A: Accelerators, Spectrometers, Detectors and Associated Equipment*, 333(2-3):381–390, September 1993. ISSN 01689002. doi: 10.1016/0168-9002(93)91180-U.

[3] S. Cova, M. Ghioni, A. Lacaita, C. Samori, and F. Zappa. Avalanche photodiodes and quenching circuits for single-photon detection. *Applied Optics*, 35(12):1956, April 1996. ISSN 0003-6935, 1539-4522. doi: 10.1364/AO.35.001956.

[4] D. Renker. Geiger-mode avalanche photodiodes, history, properties and problems. *Nuclear Instruments and Methods in Physics Research Section A: Accelerators, Spectrometers, Detectors and Associated Equipment*, 567(1):48–56, November 2006. ISSN 0168-9002. doi: 10.1016/j.nima.2006.05.060.

[5] D. Renker and E. Lorenz. Advances in solid state photon detectors. *Journal of Instrumentation*, 4(04):P04004, April 2009. ISSN 1748-0221. doi: 10.1088/1748-0221/4/04/P04004.

[6] Xiao-Hui Li, Yi-Xuan Guo, Yujie Ren, Jia-Jun Peng, Ji-Shu Liu, Cong Wang, and Han Zhang. Narrow-bandgap materials for optoelectronics applications. *Frontiers of Physics*, 17(1):13304, July 2021. ISSN 2095-0470. doi: 10.1007/s11467-021-1055-z.

[7] K. D. Irwin. An application of electrothermal feedback for high resolution cryogenic particle detection. *Applied Physics Letters*, 66(15):1998–2000, April 1995. ISSN 0003-6951, 1077-3118. doi: 10.1063/1.113674.

[8] A. Peacock, P. Verhoeve, N. Rando, A. van Dordrecht, B. G. Taylor, C. Erd, M. a. C. Perryman, R. Venn, J. Howlett, D. J. Goldie, J. Lumley, and M. Wallis. Single optical photon detection with a superconducting tunnel junction. *Nature*, 381(6578):135–137, May 1996. ISSN 1476-4687. doi: 10.1038/381135a0.

[9] Alex D. Semenov, Gregory N. Gol'tsman, and Alexander A. Korneev. Quantum detection by current carrying superconducting film. *Physica C Superconductivity*, 351:349–356, April 2001. ISSN 0921-4534. doi: 10.1016/S0921-4534(00)01637-3.

[10] G. N. Gol'tsman, O. Okunev, G. Chulkova, A. Lipatov, A. Semenov, K. Smirnov, B. Voronov, A. Dzardanov, C. Williams, and Roman Sobolewski. Picosecond superconducting single-photon

optical detector. *Applied Physics Letters*, 79(6):705–707, August 2001. ISSN 0003-6951. doi: 10.1063/1.1388868.

[11] Peter K. Day, Henry G. LeDuc, Benjamin A. Mazin, Anastasios Vayonakis, and Jonas Zmuidzinas. A broadband superconducting detector suitable for use in large arrays. *Nature*, 425(6960): 817–821, October 2003. ISSN 0028-0836, 1476-4687. doi: 10.1038/nature02037.

[12] Iman Esmaeil Zadeh, J. Chang, Johannes W. N. Los, Samuel Gyger, Ali W. Elshaari, Stephan Steinhauer, Sander N. Dorenbos, and Val Zwiller. Superconducting nanowire single-photon detectors: A perspective on evolution, state-of-the-art, future developments, and applications. *Applied Physics Letters*, 118(19):190502, May 2021. ISSN 0003-6951, 1077-3118. doi: 10.1063/5.0045990.

[13] P. Szypryt, S. R. Meeker, G. Coiffard, N. Fruitwala, B. Bumble, G. Ulbricht, A. B. Walter, M. Daal, C. Bockstiegel, G. Collura, N. Zobrist, I. Lipartito, and B. A. Mazin. Large-format platinum silicide microwave kinetic inductance detectors for optical to near-IR astronomy. *Optics Express*, 25(21):25894, October 2017. ISSN 1094-4087. doi: 10.1364/OE.25.025894.

[14] K. S. Karkare, P. S. Barry, C. M. Bradford, S. Chapman, S. Doyle, J. Glenn, S. Gordon, S. Hailey-Dunsheath, R. M. J. Janssen, A. Kovács, H. G. LeDuc, P. Mauskopf, R. McGeehan, J. Redford, E. Shirokoff, C. Tucker, J. Wheeler, and J. Zmuidzinas. Full-Array Noise Performance of Deployment-Grade SuperSpec mm-Wave On-Chip Spectrometers. *Journal of Low Temperature Physics*, 199:849–857, February 2020. ISSN 1063-777X0022-2291. doi: 10.1007/s10909-020-02407-4.

[15] Xiu Gu, Anton Frisk Kockum, Adam Miranowicz, Yu-xi Liu, and Franco Nori. Microwave photonics with superconducting quantum circuits. *Physics Reports*, 718–719:1–102, November 2017. ISSN 0370-1573. doi: 10.1016/j.physrep.2017.10.002.

[16] Nicolas Gisin, Grégoire Ribordy, Wolfgang Tittel, and Hugo Zbinden. Quantum cryptography. *Reviews of Modern Physics*, 74(1):145–195, March 2002. doi: 10.1103/RevModPhys.74.145.

[17] Emanuele Albertinale, Léo Balembois, Eric Billaud, Vishal Ranjan, Daniel Flanigan, Thomas Schenkel, Daniel Estève, Denis Vion, Patrice Bertet, and Emmanuel Flurin. Detecting spins by their fluorescence with a microwave photon counter. *Nature*, 600(7889):434–438, December 2021. ISSN 1476-4687. doi: 10.1038/s41586-021-04076-z.

[18] Z. Wang, L. Balembois, M. Rančić, E. Billaud, M. Le Dantec, A. Ferrier, P. Goldner, S. Bertaina, T. Chanelière, D. Esteve, D. Vion, P. Bertet, and E. Flurin. Single-electron spin resonance detection by microwave photon counting. *Nature*, 619(7969):276–281, July 2023. ISSN 1476-4687. doi: 10.1038/s41586-023-06097-2.

[19] Akash V. Dixit, Srivatsan Chakram, Kevin He, Ankur Agrawal, Ravi K. Naik, David I. Schuster, and Aaron Chou. Searching for Dark Matter with a Superconducting Qubit. *Physical Review Letters*, 126(14):141302, April 2021. doi: 10.1103/PhysRevLett.126.141302.

[20] Pierre Sikivie. Invisible axion search methods. *Reviews of Modern Physics*, 93(1):015004, February 2021. doi: 10.1103/RevModPhys.93.015004.

[21] A. L. Pankratov, L. S. Revin, A. V. Gordeeva, A. A. Yablokov, L. S. Kuzmin, and E. Il'ichev. Towards a microwave single-photon counter for searching axions. *npj Quantum Information*, 8 (1):1–7, May 2022. ISSN 2056-6387. doi: 10.1038/s41534-022-00569-5.

[22] Alexandre Blais, Arne L. Grimsmo, S. M. Girvin, and Andreas Wallraff. Circuit quantum electrodynamics. *Reviews of Modern Physics*, 93(2):025005, May 2021. doi: 10.1103/RevModPhys.93.025005.

[23] S. Kono, K. Koshino, Y. Tabuchi, A. Noguchi, and Y. Nakamura. Quantum non-demolition detection of an itinerant microwave photon. *Nature Physics*, 14(6):546–549, June 2018. ISSN 1745-2481. doi: 10.1038/s41567-018-0066-3.

[24] Jean-Claude Besse, Simone Gasparinetti, Michele C. Collodo, Theo Walter, Philipp Kurpiers, Marek Pechal, Christopher Eichler, and Andreas Wallraff. Single-Shot Quantum Nondemolition Detection of Individual Itinerant Microwave Photons. *Physical Review X*, 8(2):021003, April 2018. ISSN 2160-3308. doi: 10.1103/PhysRevX.8.021003.

[25] Kirill Petrovnin, Jiaming Wang, Michael Perelshtein, Pertti Hakonen, and Gheorghe Sorin Paraoanu. Microwave photon detection at parametric criticality, December 2023.

[26] Raphaël Lescanne, Samuel Deléglise, Emanuele Albertinale, Ulysse Réglade, Thibault Capelle, Edouard Ivanov, Thibaut Jacqmin, Zaki Leghtas, and Emmanuel Flurin. Irreversible Qubit-Photon Coupling for the Detection of Itinerant Microwave Photons. *Physical Review X*, 10(2): 021038, May 2020. ISSN 2160-3308. doi: 10.1103/PhysRevX.10.021038.

[27] L. Balembois, J. Travesedo, L. Pallegoix, A. May, E. Billaud, M. Villiers, D. Estève, D. Vion, P. Bertet, and E. Flurin. Cyclically Operated Microwave Single-Photon Counter with Sensitivity of ${10}^{\ensuremath{-}22}\phantom{\rule{0.2em}{0ex}}\mathrm{W}/\sqrt{\mathrm{Hz}}$. *Physical Review Applied*, 21(1):014043, January 2024. doi: 10.1103/PhysRevApplied.21.014043.

[28] Yuriy Makhlin, Gerd Schön, and Alexander Shnirman. Quantum-state engineering with Josephson-junction devices. *Reviews of Modern Physics*, 73(2):357–400, May 2001. ISSN 0034-6861, 1539-0756. doi: 10.1103/RevModPhys.73.357.

[29] Jens Koch, Terri M. Yu, Jay Gambetta, A. A. Houck, D. I. Schuster, J. Majer, Alexandre Blais, M. H. Devoret, S. M. Girvin, and R. J. Schoelkopf. Charge-insensitive qubit design derived from the Cooper pair box. *Physical Review A*, 76(4):042319, October 2007. doi: 10.1103/PhysRevA.76.042319.

[30] N. Bergeal, F. Schackert, M. Metcalfe, R. Vijay, V. E. Manucharyan, L. Frunzio, D. E. Prober, R. J. Schoelkopf, S. M. Girvin, and M. H. Devoret. Phase-preserving amplification near the quantum limit with a Josephson ring modulator. *Nature*, 465(7294):64–68, May 2010. ISSN 1476-4687. doi: 10.1038/nature09035.

[31] C. Rolland, A. Peugeot, S. Dambach, M. Westig, B. Kubala, Y. Mukharsky, C. Altimiras, H. le Sueur, P. Joyez, D. Vion, P. Roche, D. Esteve, J. Ankerhold, and F. Portier. Antibunched Photons Emitted by a dc-Biased Josephson Junction. *Physical Review Letters*, 122(18):186804, May 2019. doi: 10.1103/PhysRevLett.122.186804.

[32] A. Grimm, F. Blanchet, R. Albert, J. Leppäkangas, S. Jebari, D. Hazra, F. Gustavo, J.-L. Thomassin, E. Dupont-Ferrier, F. Portier, and M. Hofheinz. Bright On-Demand Source of Antibunched Microwave Photons Based on Inelastic Cooper Pair Tunneling. *Physical Review X*, 9(2):021016, April 2019. ISSN 2160-3308. doi: 10.1103/PhysRevX.9.021016.

[33] G. C. Ménard, A. Peugeot, C. Padurariu, C. Rolland, B. Kubala, Y. Mukharsky, Z. Iftikhar, C. Altimiras, P. Roche, H. Le Sueur, P. Joyez, D. Vion, D. Esteve, J. Ankerhold, and F. Portier. Emission of Photon Multiplets by a dc-Biased Superconducting Circuit. *Physical Review X*, 12 (2):021006, April 2022. ISSN 2160-3308. doi: 10.1103/PhysRevX.12.021006.

[34] A. Peugeot, G. Ménard, S. Dambach, M. Westig, B. Kubala, Y. Mukharsky, C. Altimiras, P. Joyez, D. Vion, P. Roche, D. Esteve, P. Milman, J. Leppäkangas, G. Johansson, M. Hofheinz, J. Ankerhold, and F. Portier. Generating Two Continuous Entangled Microwave Beams Using a dc-Biased Josephson Junction. *Physical Review X*, 11(3):031008, July 2021. doi: 10.1103/PhysRevX.11.031008.

[35] R. Albert, J. Griesmar, F. Blanchet, U. Martel, N. Bourlet, and M. Hofheinz. Microwave Photon-Number Amplification. *Physical Review X*, 14(1):011011, February 2024. doi: 10.1103/PhysRevX.14.011011.

[36] Waqar Khan, Patrick P. Potts, Sebastian Lehmann, Claes Thelander, Kimberly A. Dick, Peter Samuelsson, and Ville F. Maisi. Efficient and continuous microwave photoconversion in hybrid cavity-semiconductor nanowire double quantum dot diodes. *Nature Communications*, 12(1): 5130, August 2021. ISSN 2041-1723. doi: 10.1038/s41467-021-25446-1.

[37] Subhomoy Haldar, Drilon Zenelaj, Patrick P. Potts, Harald Havir, Sebastian Lehmann, Kimberly A. Dick, Peter Samuelsson, and Ville F. Maisi. Microwave power harvesting using resonator-coupled double quantum dot photodiode, June 2023.

[38] Subhomoy Haldar, David Barker, Harald Havir, Antti Ranni, Sebastian Lehmann, Kimberly A. Dick, and Ville F. Maisi. Continuous microwave photon counting by semiconductor-superconductor hybrids, January 2024.

[39] A. H. Dayem and R. J. Martin. Quantum Interaction of Microwave Radiation with Tunneling Between Superconductors. *Physical Review Letters*, 8(6):246–248, March 1962. ISSN 0031-9007. doi: 10.1103/PhysRevLett.8.246.

[40] Gert-Ludwig Ingold and Yu. V. Nazarov. Charge Tunneling Rates in Ultrasmall Junctions. In Hermann Grabert and Michel H. Devoret, editors, *Single Charge Tunneling: Coulomb Blockade Phenomena In Nanostructures*, NATO ASI Series, pages 21–107. Springer US, Boston, MA, 1992. ISBN 978-1-4757-2166-9. doi: 10.1007/978-1-4757-2166-9_2.

[41] John R. Tucker and Marc J. Feldman. Quantum detection at millimeter wavelengths. *Reviews of Modern Physics*, 57(4):1055–1113, October 1985. ISSN 0034-6861. doi: 10.1103/RevModPhys.57.1055.

[42] Julien Basset, Hélène Bouchiat, and Richard Deblock. Emission and Absorption quantum noise measurement with an on-chip resonant circuit. *Physical Review Letters*, 105(16):166801, October 2010. ISSN 0031-9007, 1079-7114. doi: 10.1103/PhysRevLett.105.166801.

[43] Carles Altimiras, Olivier Parlavecchio, Philippe Joyez, Denis Vion, Patrice Roche, Daniel Esteve, and Fabien Portier. Tunable microwave impedance matching to a high impedance source using a Josephson metamaterial. *Applied Physics Letters*, 103(21):212601, November 2013. ISSN 0003-6951. doi: 10.1063/1.4832074.

[44] S. Frasca, I.N. Arabadzhiev, S.Y. Bros de Puechredon, F. Oppliger, V. Jouanny, R. Musio, M. Scigliuzzo, F. Minganti, P. Scarlino, and E. Charbon. NbN films with high kinetic inductance for high-quality compact superconducting resonators. *Physical Review Applied*, 20(4):044021, October 2023. doi: 10.1103/PhysRevApplied.20.044021.

[45] Lukas Grünhaupt, Martin Spiecker, Daria Gusenkova, Nataliya Maleeva, Sebastian T. Skacel, Ivan Takmakov, Francesco Valenti, Patrick Winkel, Hannes Rotzinger, Wolfgang Wernsdorfer, Alexey V. Ustinov, and Ioan M. Pop. Granular aluminium as a superconducting material for high-impedance quantum circuits. *Nature Materials*, 18(8):816–819, August 2019. ISSN 1476-4660. doi: 10.1038/s41563-019-0350-3.

[46] T. Holst, D. Esteve, C. Urbina, and M. H. Devoret. Effect of a Transmission Line Resonator on a Small Capacitance Tunnel Junction. *Physical Review Letters*, 73(25):3455–3458, December 1994. ISSN 0031-9007. doi: 10.1103/PhysRevLett.73.3455.

[47] Max Hofheinz, Fabien Portier, Quentin Baudouin, Philippe Joyez, Denis Vion, Patrice Bertet, Patrice Roche, and Daniel Esteve. The Bright Side of Coulomb Blockade. *Physical Review Letters*, 106(21):217005, May 2011. ISSN 0031-9007, 1079-7114. doi: 10.1103/PhysRevLett.106.217005.

[48] R. J. Schoelkopf, P. Wahlgren, A. A. Kozhevnikov, P. Delsing, and D. E. Prober. The Radio-Frequency Single-Electron Transistor (RF-SET): A Fast and Ultrasensitive Electrometer. *Science*, 280(5367):1238–1242, May 1998. ISSN 0036-8075, 1095-9203. doi: 10.1126/science.280.5367.1238.

[49] Henrik Brenning, Sergey Kafanov, Tim Duty, Sergey Kubatkin, and Per Delsing. An ultrasensitive radio-frequency single-electron transistor working up to 4.2 K. *Journal of Applied Physics*, 100(11):114321, 2006. ISSN 00218979. doi: 10.1063/1.2388134.

[50] S. M. Girvin. Circuit QED: Superconducting qubits coupled to microwave photons. In Michel Devoret, Benjamin Huard, Robert Schoelkopf, and Leticia F. Cugliandolo, editors, *Quantum Machines: Measurement and Control of Engineered Quantum Systems*, pages 113–256. Oxford University Press, June 2014. ISBN 978-0-19-968118-1. doi: 10.1093/acprof:oso/9780199681181.003.0003.

[51] Gianluca Aiello. *Quantum Dynamics of a High Impedance Microwave Cavity Strongly Coupled to a Josephson Junction.* These de doctorat, université Paris-Saclay, December 2020.

[52] Michael Tinkham. *Introduction to Superconductivity.* Courier Corporation, January 2004. ISBN 978-0-486-13472-7.

[53] J. P. Pekola, V. F. Maisi, S. Kafanov, N. Chekurov, A. Kemppinen, Yu. A. Pashkin, O.-P. Saira, M. Möttönen, and J. S. Tsai. Environment-Assisted Tunneling as an Origin of the Dynes Density of States. *Physical Review Letters*, 105(2):026803, July 2010. ISSN 0031-9007, 1079-7114. doi: 10.1103/PhysRevLett.105.026803.

[54] O.-P. Saira, A. Kemppinen, V. F. Maisi, and J. P. Pekola. Vanishing quasiparticle density in a hybrid Al/Cu/Al single-electron transistor. *Physical Review B*, 85(1):012504, January 2012. doi: 10.1103/PhysRevB.85.012504.

[55] Jérôme Estève, Marco Aprili, and Julien Gabelli. Quantum dynamics of a microwave resonator strongly coupled to a tunnel junction. *arXiv:1807.02364 [cond-mat, physics:quant-ph]*, July 2018.

[56] K. E. Cahill and R. J. Glauber. Ordered Expansions in Boson Amplitude Operators. *Physical Review*, 177(5):1857–1881, January 1969. ISSN 0031-899X. doi: 10.1103/PhysRev.177.1857.

[57] Crispin Gardiner and Peter Zoller. *Quantum Noise: A Handbook of Markovian and Non-Markovian Quantum Stochastic Methods with Applications to Quantum Optics*. Springer Science & Business Media, August 2004. ISBN 978-3-540-22301-6.

[58] Matti Silveri, Shumpei Masuda, Vasilii Sevriuk, Kuan Y. Tan, Máté Jenei, Eric Hyyppä, Fabian Hassler, Matti Partanen, Jan Goetz, Russell E. Lake, Leif Grönberg, and Mikko Möttönen. Broadband Lamb shift in an engineered quantum system. *Nature Physics*, 15(6):533–537, June 2019. ISSN 1745-2473, 1745-2481. doi: 10.1038/s41567-019-0449-0.

[59] Gianluca Aiello, Mathieu Féchant, Alexis Morvan, Julien Basset, Marco Aprili, Julien Gabelli, and Jérôme Estève. Quantum bath engineering of a high impedance microwave mode through quasiparticle tunneling. *Nature Communications*, 13(1):7146, November 2022. ISSN 2041-1723. doi: 10.1038/s41467-022-34762-z.

[60] Lukas Grünhaupt, Nataliya Maleeva, Sebastian T. Skacel, Martino Calvo, Florence Levy-Bertrand, Alexey V. Ustinov, Hannes Rotzinger, Alessandro Monfardini, Gianluigi Catelani, and Ioan M. Pop. Loss Mechanisms and Quasiparticle Dynamics in Superconducting Microwave Resonators Made of Thin-Film Granular Aluminum. *Physical Review Letters*, 121(11):117001, September 2018. doi: 10.1103/PhysRevLett.121.117001.

[61] G. Deutscher, H. Fenichel, M. Gershenson, E. Grünbaum, and Z. Ovadyahu. Transition to zero dimensionality in granular aluminum superconducting films. *Journal of Low Temperature Physics*, 10(1):231–243, January 1973. ISSN 1573-7357. doi: 10.1007/BF00655256.

[62] D. C. Mattis and J. Bardeen. Theory of the Anomalous Skin Effect in Normal and Superconducting Metals. *Physical Review*, 111(2):412–417, July 1958. ISSN 0031-899X. doi: 10.1103/PhysRev.111.412.

[63] S. Probst, F. B. Song, P. A. Bushev, A. V. Ustinov, and M. Weides. Efficient and robust analysis of complex scattering data under noise in microwave resonators. *Review of Scientific Instruments*, 86(2):024706, February 2015. ISSN 0034-6748, 1089-7623. doi: 10.1063/1.4907935.

[64] J.R. Johansson, P.D. Nation, and Franco Nori. QuTiP: An open-source Python framework for the dynamics of open quantum systems. *Computer Physics Communications*, 183(8):1760–1772, August 2012. ISSN 00104655. doi: 10.1016/j.cpc.2012.02.021.

[65] J. R. Johansson, P. D. Nation, and Franco Nori. QuTiP 2: A Python framework for the dynamics of open quantum systems. *Computer Physics Communications*, 184(4):1234–1240, April 2013. ISSN 0010-4655. doi: 10.1016/j.cpc.2012.11.019.

[66] Y. Jin, Q. Dong, A. Cavanna, U. Gennser, L. Couraud, and C. Ulysse. Ultra-low noise HEMTs for deep cryogenic low-frequency and high-impedance readout electronics. In *2014 12th IEEE International Conference on Solid-State and Integrated Circuit Technology (ICSICT)*, pages 1–4, October 2014. doi: 10.1109/ICSICT.2014.7021379.

[67] Cyril Vaneph. *Observation Du Phénomène de Blocage Anormal de Photon Dans Le Domaine Micro-Onde*. These de doctorat, Paris 6, November 2017.

[68] Matti Silveri, Hermann Grabert, Shumpei Masuda, Kuan Yen Tan, and Mikko Möttönen. Theory of quantum-circuit refrigeration by photon-assisted electron tunneling. *Physical Review B*, 96(9):094524, September 2017. ISSN 2469-9950, 2469-9969. doi: 10.1103/PhysRevB.96.094524.

[69] Timm Fabian Mörstedt, Arto Viitanen, Vasilii Vadimov, Vasilii Sevriuk, Matti Partanen, Eric Hyyppä, Gianluigi Catelani, Matti Silveri, Kuan Yen Tan, and Mikko Möttönen. Recent Developments in Quantum-Circuit Refrigeration. *Annalen der Physik*, 534(7):2100543, 2022. ISSN 1521-3889. doi: 10.1002/andp.202100543.

[70] V. Vadimov, A. Viitanen, T. Mörstedt, T. Ala-Nissila, and M. Möttönen. Single-junction quantum-circuit refrigerator. *AIP Advances*, 12(7):075005, July 2022. ISSN 2158-3226. doi: 10.1063/5.0096849.

[71] Arto Viitanen, Timm Mörstedt, Wallace S. Teixeira, Maaria Tiiri, Jukka Räbinä, Matti Silveri, and Mikko Möttönen. Quantum-circuit refrigeration of a superconducting microwave resonator well below a single quantum, August 2023.

[72] Carles Altimiras, Olivier Parlavecchio, Philippe Joyez, Denis Vion, Patrice Roche, Daniel Esteve, and Fabien Portier. Dynamical Coulomb Blockade of Shot Noise. *Physical Review Letters*, 112(23):236803, June 2014. doi: 10.1103/PhysRevLett.112.236803.

[73] Vivek Maurya, Haimeng Zhang, Daria Kowsari, Andre Kuo, Darian M. Hartsell, Clark Miyamoto, Jocelyn Liu, Sadman Shanto, Evangelos Vlachos, Azarin Zarassi, Kater W. Murch, and Eli M. Levenson-Falk. On-Demand Driven Dissipation for Cavity Reset and Cooling. *PRX Quantum*, 5(2):020321, April 2024. doi: 10.1103/PRXQuantum.5.020321.

[74] Wei Lu, Zhongqing Ji, Loren Pfeiffer, K. W. West, and A. J. Rimberg. Real-time detection of electron tunnelling in a quantum dot. *Nature*, 423(6938):422–425, May 2003. ISSN 1476-4687. doi: 10.1038/nature01642.

[75] E. T. Mannila, P. Samuelsson, S. Simbierowicz, J. T. Peltonen, V. Vesterinen, L. Grönberg, J. Hassel, V. F. Maisi, and J. P. Pekola. A superconductor free of quasiparticles for seconds. *Nature Physics*, 18(2):145–148, February 2022. ISSN 1745-2473, 1745-2481. doi: 10.1038/s41567-021-01433-7.

[76] T. A. Fulton and G. J. Dolan. Observation of single-electron charging effects in small tunnel junctions. *Physical Review Letters*, 59(1):109–112, July 1987. ISSN 0031-9007. doi: 10.1103/PhysRevLett.59.109.

[77] A. Aassime, D. Gunnarsson, K. Bladh, P. Delsing, and R. Schoelkopf. Radio-frequency single-electron transistor: Toward the shot-noise limit. *Applied Physics Letters*, 79(24):4031–4033, December 2001. ISSN 0003-6951, 1077-3118. doi: 10.1063/1.1424477.

[78] T. A. Fulton, P. L. Gammel, D. J. Bishop, L. N. Dunkleberger, and G. J. Dolan. Observation of combined Josephson and charging effects in small tunnel junction circuits. *Physical Review Letters*, 63(12):1307–1310, September 1989. ISSN 0031-9007. doi: 10.1103/PhysRevLett.63.1307.

[79] Alec Maassen Van Den Brink, Gerd Schön, and L. J. Geerligs. Combined single-electron and coherent-Cooper-pair tunneling in voltage-biased Josephson junctions. *Physical Review Letters*, 67(21):3030–3033, November 1991. ISSN 0031-9007. doi: 10.1103/PhysRevLett.67.3030.

[80] P. Hadley, E. Delvigne, E. H. Visscher, S. Lähteenmäki, and J. E. Mooij. $3e$ tunneling processes in a superconducting single-electron tunneling transistor. *Physical Review B*, 58(23): 15317–15320, December 1998. doi: 10.1103/PhysRevB.58.15317.

[81] W. W. Xue, Z. Ji, Feng Pan, Joel Stettenheim, M. P. Blencowe, and A. J. Rimberg. Measurement of quantum noise in a single-electron transistor near the quantum limit. *Nature Physics*, 5(9):660–664, September 2009. ISSN 1745-2481. doi: 10.1038/nphys1339.

[82] Benjamin Anthony Turek. Precision Measurements with the Single Electron Transistor: Noise and Backaction in the Normal and Superconducting state. May 2007.

[83] C. Eichler, Y. Salathe, J. Mlynek, S. Schmidt, and A. Wallraff. Quantum-Limited Amplification and Entanglement in Coupled Nonlinear Resonators. *Physical Review Letters*, 113(11):110502, September 2014. ISSN 0031-9007, 1079-7114. doi: 10.1103/PhysRevLett.113.110502.

[84] C. Macklin, K. O'Brien, D. Hover, M. E. Schwartz, V. Bolkhovsky, X. Zhang, W. D. Oliver, and I. Siddiqi. A near–quantum-limited Josephson traveling-wave parametric amplifier. *Science*, 350(6258):307–310, October 2015. doi: 10.1126/science.aaa8525.

[85] Luca Planat, Rémy Dassonneville, Javier Puertas Martínez, Farshad Foroughi, Olivier Buisson, Wiebke Hasch-Guichard, Cécile Naud, R. Vijay, Kater Murch, and Nicolas Roch. Understanding the Saturation Power of Josephson Parametric Amplifiers Made from SQUID Arrays. *Physical Review Applied*, 11(3):034014, March 2019. ISSN 2331-7019. doi: 10.1103/PhysRevApplied.11.034014.

[86] D Rogovin and D. J Scalapino. Fluctuation phenomena in tunnel junctions. *Annals of Physics*, 86(1):1–90, July 1974. ISSN 0003-4916. doi: 10.1016/0003-4916(74)90430-8.

[87] A. A. Clerk, M. H. Devoret, S. M. Girvin, Florian Marquardt, and R. J. Schoelkopf. Introduction to quantum noise, measurement, and amplification. *Reviews of Modern Physics*, 82(2): 1155–1208, April 2010. ISSN 0034-6861, 1539-0756. doi: 10.1103/RevModPhys.82.1155.

Titre: Un détecteur à haute inductance cinétique de photon micro-onde

Mots clés: Supraconducteur desordonnee, Physique quantique, Jonction tunnel, Hyperfrequences

Résumé: Les détecteurs de photons uniques à des fréquences visibles ont été des outils essentiels dans de nombreux domaines de la technologie quantique, tels que la distribution de clés quantiques ou l'optique quantique. Cependant, la réalisation de détecteurs de photons uniques micro-ondes continus et hautement efficaces reste un défi. Dans cette thèse, nous proposons et mettons en œuvre un détecteur de photons micro-ondes basé sur une jonction tunnel supraconductrice couplée à une cavité micro-ondes. Les photons incidents à la fréquence du résonateur sont absorbés par la jonction via un effet tunnel inélastique des quasiparticules, ce qui entraîne un courant de tunnel photo-assisté mesurable. Pour augmenter le taux d'effet tunnel inélastique, le résonateur est fabriqué en aluminium granulaire, ce qui conduit à une impédance caractéristique du mode de l'ordre du quantum de résistance. En mesurant le courant dû aux processus d'ordre supérieur, nous calibrons le détecteur et estimons l'efficacité quantique à 0,83 — un ordre de grandeur plus élevé que celui rapporté dans la littérature pour les détecteurs basés sur l'effet tunnel photo-assisté. En plus du courant photo-assisté, la puissance émise par l'échantillon est mesurée, et il est démontré que le même dispositif pourrait être utilisé pour refroidir efficacement les circuits supraconducteurs. Nous discutons de la compatibilité du détecteur de photons mis en œuvre avec les techniques de comptage de charge nécessaires pour discerner les électrons individuels, tels que les RF-SET. Nous réalisons un RF-SET à l'aide d'un résonateur granulaire en aluminium à haute impédance, et nous montrons une forte absorption de photons pour des tensions de polarisation et de grille appropriées. En outre, nous mesurons la sensibilité à la charge de ce dispositif à un niveau aussi bas que 5e-5 e/sqrt(Hz). Ainsi, les expériences de ce travail montrent que la combinaison d'un transistor radiofréquence à électron unique avec un convertisseur photon-électron à haute efficacité basé sur l'effet tunnel inélastique pourrait conduire à un compteur de photons micro-ondes unique pratique.

ÉCOLE DOCTORALE
Physique en
Île-de-France (PIF)

Title: High kinetic inductance-based microwave photon detection

Keywords: Disordered superconductors, Quantum physics, Tunnel junctions, Microwaves

Abstract: Single photon detectors at visible frequencies have been essential tools in many areas of quantum technology, such as quantum key distribution or quantum optics. However, realizing highly efficient continuous single microwave photon detectors remains challenging. In this thesis, we propose and implement a microwave photon detector based on a superconducting tunnel junction coupled to a microwave cavity. Incident photons at resonator frquency are absorbed by the junction via inelastic quasiparticle tunneling, resulting in measurable photo-assisted tunneling current. To increase the inealstic tunneling rate, the resonator is fabricated in granular aluminium, leading to the mode characteristic impedance on the order of quantum of resistance. By measuring the current due to higher order processes, we calibrate the detector and estimate the quantum efficiency to be 0.83 — an order of magnitude higher than reported in literature for detectors based on photo-assisted tunneling. In addition to the photo-assisted current, the power emitted by the sample is measured, and it is shown that the same device could be utilized to effectively cool superconducting circuits. We discuss the compatibility of the implemented photon detector-with charge counting techniques required for discerning individual electrons, such as RF-SETs. We relize an RF-SET using a high-impedance granular aluminum resonator, and show high photon absorption for suitable bias and gate voltages. Additionally, we measure the charge sensitivity of this device as low as 5e-5 e/sqrt(Hz). Thus, the experiments in this work show that combining a radio-frequency single-electron transistor with a high efficiency photon to electron converter based on inelastic tunneling could lead to a practical single microwave photon counter.